NMR-Dose Response Studies of the Gels Used for 3-D Radiation Dosimetry by Magnetic Resonance Imaging

by

Chantal Audet
Department of Physics
McGill University, Montréal
September, 1995

A thesis submitted to the Faculty of Graduate Studies and Research in partial fulfillment of the degree of Doctor of Philosophy.

ISBN 0-612-12326-X

Abstract

In the past ten years, three dimensional radiation dosimetry techniques based on the dose response of the Nuclear Magnetic Resonance (NMR) spin relaxation of the water protons in gels have been developed. The studies in this work focus on **1)** the dose response of the spin-lattice relaxation rate, R_1, of the ferrous sulfate-doped gelatin dosimeter and **2)** the dose response of the spin-spin relaxation rate, R_2, of the BANG (Bis Acrylamide Nitrogen Gelatin) polymer gel dosimeter.

When the ferrous sulfate gelatin dosimeter is irradiated ferrous ions are converted to ferric ions. A model is proposed for the R_1-dose response of the dosimeter. The model includes such parameters as the ferric ion yield and the ion relaxivities which measure the ability of the ions to enhance the spin-lattice relaxation of water protons. The effects of gelatin and sulfuric acid concentration on the ferric ion yield and ion relaxivities are studied. The ferric ion relaxivity is shown to vary because of the complexing of the ferric ions resulting from gelatin-induced pH changes or pH changes arising from variations in sulfuric acid concentration. A modified version of the R_1-dose response model accounting for ferric ion complexing is presented and tested spectrophotometrically. The results are also examined for possible ways of optimizing the dosimeter.

The BANG dosimeter is based on the radiation-induced polymerization of the Bis and acrylamide monomers in the gelatin. Studies on the reproducibility of the R_2-dose response of small volume BANG polymer gel dosimeters show that there are post-irradiation reactions and that sufficient time delays must elapse before the value of R_2 stabilizes. A preliminary fast exchange model for the R_2-dose response of BANG dosimeters involving the polymer yield and polymer spin-spin relaxivity is presented. Results of the effects of gelatin, Bis and acrylamide concentration, and the NMR measurement temperature on the R_2-dose response are presented. The results are used to determine the dosimeter compositions and NMR measurement temperatures providing the best NMR-dose response. Also, the results are interpreted in terms of the polymer yield and relaxivity to better understand the physical and chemical mechanisms governing the R_2-dose response of BANG dosimeters.

Résumé

Depuis les dix dernières années, des techniques de radiodosimétrie en trois dimensions ont été dévelopées. Les techniques sont basées sur l'éffet de la dose sur la relaxation Résonance Magnétique Nucléaire (RMN) des protons d'eau trouvés dans les dosimètres de gels radiosensibles. Les études présentées regardent 1) la relation dose-effet du taud de relaxation spin-réseau, R_1, du dosimètre contenant des ions ferreux et de la gélatine et 2) la relation dose-effet du taud de relaxation spin-spin, R_2, du dosimètre polymérique BANG (Bis Acrylamide Nitrogen Gelatin).

Quand le premier dosimètre est irradié les ions ferreux sont convertis en ions ferriques. Un modèle représentant la relation dose-effet de R_1 du dosimètre est proposé. Le modèle inclu deux paramètres d'importance, le rendment d'ion ferrique et les relaxivités qui sont une mésure de l'abilité des ions de promouvoir la relaxation spin-réseau des protons d'eau. Les effets de la concentration de gélatine et d'acide sulférique sur le rendement d'ion ferrique et les relaxivités sont investigés. Il est démontré que la relaxivité de l'ion ferrique est affectée par la formation de complexes des ion ferriques. Cette formation est induit par les changements de pH apportés par la gélatine ou la concentration d'acide sulférique. Une version modifiée du modèle prennant compte de la formation des complexes est présentée et verifiée en utilisant des méthodes de spectrophotométrie. Les résultats sont aussi examinés pour les manières possible d'améliorer la relation dose-effet.

Le dosimètre BANG est basé sur la polymérization, induite par la radiation, des monomères de Bis et d'acrylamide qui se trouvent dans la gélatine. Les études sur la reproduction des relations dose-effets de R_2 pour des dosimètres BANG démontre qu'il y'a des reactions qui procèdent après l'irradiation du dosimètre et qu'il faut attendre un certain temps avant que la valeur de R_2 stabilise. Un modèle préliminaire pour la relation dose-effet de R_2 du dosimètre BANG est présenté. Le modèle comprend un paramètre de rendment de polymère et un de relaxivité spin-spin. Les résultats des éffets de les concentrations de gélatine, Bis et acrylamide et de la température de la mesure de R_2 sur la relation dose-effet de R_2 sont présentés. Ils sont utilisés pour déterminer les compositions du dosimètre BANG et les temperatures de mesures qui produisent les meilleurs relations dose-effect de la relaxation RMN. Les résultats sont aussi interpretés en termes de rendement de polymère et de relaxivité spin-spin pour mieux comprendre les méchanisms physique et chimique gouvernant la relation dose-effet de R_2.

Acknowledgments

The research for this thesis has been performed for the most part at the Department of Medical Physics of the Montréal General Hospital, Montréal, Québec, in requirement for the Ph.D. program offered by the Department of Physics at McGill University, Montréal. Also, a research term of six months to study BANG gel dosimeters was spent with NMR Research Group at Yale University, New Haven CT. Both experiences have been very positive and rewarding, not only professionally but personally. They have given me the opportunity to pursue interesting research and meet many wonderful friends and colleagues.

I am very grateful for having had the opportunity to work under the supervision of Dr. L. John Schreiner at McGill University. His guidance and assistance in producing this thesis have been invaluable. The freedom he gave me to pursue my different research ideas was very supportive and is much appreciated. The support of Dr. E.B. Podgorsak (McGill U.), especially his pep talks, is also very appreciated. I would like to thank Joe Larkin (Montreal General Hospital) for his technical assistance with setting up the lab at the start of my studies.

I would like to thank Dr. M.J. Maryanski and Dr. J.C. Gore for giving me the opportunity to pursue interesting research at Yale University. I am very grateful for the direct supervision and support of Dr. Maryanski. I would also like to thank MGS Research Inc. for providing me with the funds necessary for me to attend and present at this year's AAPM conference.

The support offered to me and the help invested in this thesis by Cristelle Audet, Adam Mar. and Corey Zankowski is extremely appreciated. I would like to thank my parents for the moral support and inspiration which have been crucial in contributing indirectly to the completion of this thesis.

Financial assistance obtained from FCAR funding agency of Québec is acknowledged.

Table of Contents

CHAPTER THREE
Gel Dosimeters

CHAPTER FOUR
Methods and Materials

CHAPTER FIVE
Results and Discussion: Ferrous Sulfate-Doped Gels

CHAPTER SIX
Results and Discussion: BANG Polymer Gels

CHAPTER SEVEN
Conclusions

List of Figures

List of Tables

CHAPTER ONE

Introduction

In radiotherapy, the primary objective is to deliver a prescribed dose of radiation to a tumour or lesion within a patient while minimizing the dose delivered to the surrounding healthy tissue. Conformal therapies are currently being developed with this goal in mind. However, the implementation of conformal therapies has been limited in part by the unavailability of adequate three dimensional (3-D) radiation dosimetry techniques having high spatial resolution in all dimensions. Established dosimetry techniques and their shortcomings will be discussed. A 3-D radiation dosimetry technique proposed in 1984 by Gore *et al.* and currently being developed, combines the use of radiation sensitive gels and magnetic resonance imaging (MRI). The goals of the work described in this thesis are twofold. First, it is hoped that the work will lead to a better understanding of the physical and chemical processes governing the Nuclear Magnetic Resonance (NMR) response of existing dosimeter gels to dose. Second, the studies are aimed at improving the NMR dose response of the gels.

1.1 Motivation for a Three Dimensional Radiation Dosimetry

Usually when treating a patient, a compromise is made between tumour control and complications arising from normal tissue irradiation. One measure of this compromise, the therapeutic ratio, is defined as the radiation dose producing complications in 50% of patients divided by the dose providing tumour control in 50% of the patients (Johns and Cunningham, 1953). The therapeutic ratio depends on the radiobiological characteristics of the cancerous tissue and surrounding healthy tissues and on the radiation dose distribution achieved by the radiotherapy treatment.

Traditional radiotherapy treatments usually involve simple external or internal irradiations of a tumour. External irradiations are normally achieved in the clinic with photon beams produced by high energy linear accelerators (linacs) or ^{60}Co units. The photon beams are collimated into regular shapes as they emerge from the treatment head of the unit. The treatment head is supported by a gantry that can be rotated isocentrically to any position (see Fig. 1a). A discrete number of photon beams with different angles of incidence that intersect at the isocenter are used to produce a region of high dose around the tumour volume (positioned at the isocenter). Simple internal irradiations are accomplished by implanting a few radioactive brachytherapy sources in and around the tumour or lesion. Such irradiations are characterized by very high doses local to the tumour.

It is generally believed that the therapeutic ratio can be minimized by optimizing the conformation of the radiation dose distribution to the tumour volume (Kutcher *et al.*, 1991). This is difficult with traditional radiotherapy techniques since they do not produce dose distributions which adequately cover tumour volumes of complex shapes and sizes while sparing normal

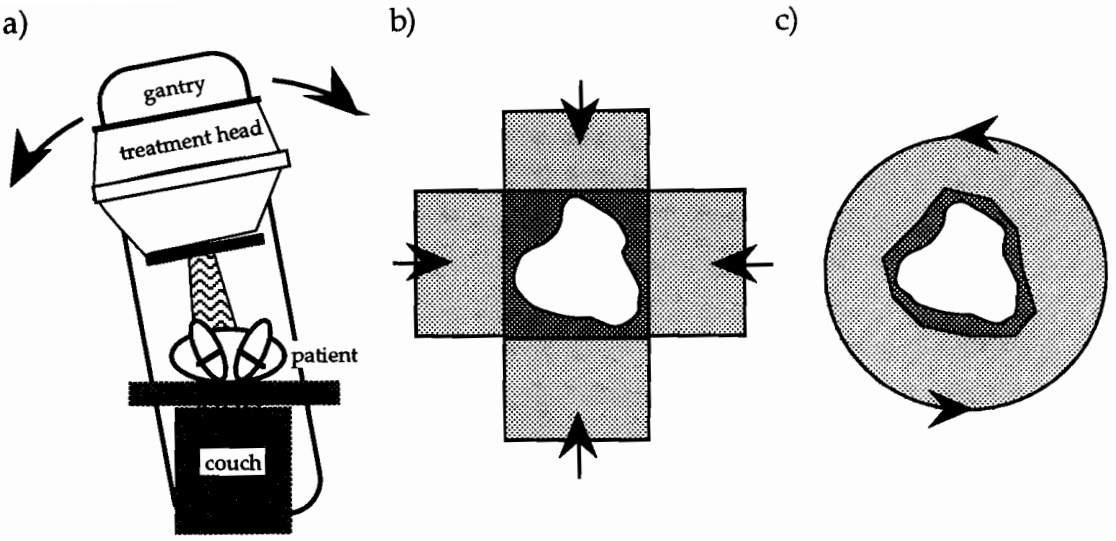

Figure 1.1 a) Schematic of the frontal view of a linear accelerator or ^{60}Co unit. The gantry rotates about the isocenter placed within the tumour volume found in the patient; all beams intersect at the isocenter. b) Schematic of an irregularly-shaped tumour area irradiated by 4 rectangularly collimated beams. c) Schematic of an irregularly-shaped area given a conformal therapy treatment.

tissue. The situation is further complicated if the normal tissues are critical organs or are particularly sensitive to radiation. Radiotherapy techniques employed to obtain a closer conformation of the dose distribution to the tumour volume are referred to as *conformal* radiotherapy techniques (Webb, 1993). Note that since the tumours being treated extend throughout some volume, conformal therapy is inherently three dimensional (3-D) in nature. Figure 1.1b illustrates a tumour (white area) encompassed by a high-dose region (darkly shaded) produced by a standard 4-field box treatment with regions of low dose (lightly shaded) extending beyond the target area. Figure 1.1c shows the same tumour treated with a generic conformal therapy technique. The high-dose region around the tumour area follows the contour of the tumour more accurately than in the previous example such that more healthy tissue is spared.

Many technological advances have taken place over the past twenty years that would facilitate the conformal radiotherapy of complex tumour volumes. For example, 3-D imaging techniques such as x-ray Computed Tomography (CT) and Magnetic Resonance Imaging (MRI) provide the 3-D anatomical information required to determine the extent, shape and localization (relative to other anatomical sites) of the tumour. This 3-D information can in turn be used in radiotherapy treatment planning to select the position and geometry of a number of beams, so that the resulting dose distribution conforms to the tumour volume. More powerful computers used in treatment planning allow for more precise determination of the dose distributions by permitting the use of improved dose calculation models. Improved algorithms can calculate 3-D dose distributions while taking into account tissue inhomogeneities and patient contours as defined by CT anatomical information (Sontag and Purdy, 1991 as cited in Webb, 1993). Advances have also been made in the delivery of treatments. For external beam therapy they involve beam shaping using multileaf collimators (Webb, 1993; Mohan, 1993; Powlis *et al.*, 1991; Galvin *et al.*, 1993; LoSasso *et al.*, 1991), the use of non-coplanar beams achieved by couch rotation in dynamic therapy (McLaughlin *et al.*, 1994; Podgorsak *et al.*, 1988; Ramani *et al.*, 1994) and the automatic modulation of beam intensity (Bortfeld and Schlegel, 1993; Mackie *et al.*, 1993). In brachytherapy, improvements have involved the development of High Dose Rate (HDR) remote after-loading techniques whereby an HDR radioactive source at the end of a steel cable is mechanically drawn in and out of catheters imbedded in the tumour (Glasgow *et al.*, 1993; Chiu-Tsao *et al.*, 1994). The source is positioned at various locations in the tumour bed for different dwell times so that complex dose distributions can be achieved.

The clinical implementation of conformal therapy has been delayed by limitations in 1) the verification of complex conformal treatments during its delivery to the patient and 2) the verification of conformal dose distributions calculated by the treatment planning systems prior to the irradiation of the patient (Perez and Purdy, 1992). Verification of the treatment during delivery involves monitoring the treatment unit settings (i.e., gantry angles, collimator settings) (Powlis *et al.*, 1991) and on-line beam monitoring provided by portal imaging systems. Portal imaging involves the imaging of the radiation field transmitted through the patient; there has been considerable progress in this area with the development of on-line portal imaging systems (Michalski *et al.*, 1993; Wong *et al.*, 1993).

Difficulties in the verification of dose distributions has limited the development of conformal therapy (Perez and Purdy, 1992). There are two aspects of conformal therapy that complicate dose verification. First, to achieve the dose distributions conforming to complex three dimensional volumes, high dose gradients arise in the treatment volume. Second, most conformal therapies are dynamic, thus the total dose at a given point is the dose integrated over the entire treatment time as the radiation source follows a complicated dynamic path. These aspects require that practical dose measurement (dosimetric) techniques be able to integrate dose over time and easily measure dose distributions in 3-D with high spatial resolution. Traditional dosimeters (see Section 1.3) do not fulfill these requirements adequately; their shortcomings are discussed in more detail in Section 1.4.

A potential 3-D dosimetry technique involving a gel dosimeter in which dose distributions could be determined using MRI techniques (see Section 1.3.5 below) was first proposed by Gore *et al.* (1984). This thesis is concerned with studies of the dose responses of the two existing gel

dosimeters: the ferrous sulfate-doped gels (Gore *et al.*, 1984) and the polymer gels (Maryanski *et al.*, 1993).

1.2 Basic Concepts in Radiation Dosimetry

The basic concepts in radiation dosimetry are well reviewed in the literature (Greening, 1981; Johns and Cunningham, 1953; Khan, 1984; Attix, 1986). While a comprehensive review of radiation dosimetry is beyond the scope of this thesis, some pertinent aspects will be discussed in this section. The determination of the dose to tissue in clinical dosimetry is described in Section 1.2.2. Different dosimeters respond to radiation dose differently. Section 1.2.3 describes how a general dose response may be characterized and optimized for different applications in terms of various parameters.

1.2.1 Absorbed Dose

Estimations of the radiation doses used for the first treatments in radiotherapy by x-rays or γ-rays were very crude and qualitative. For instance, the skin erythema dose, was defined as the amount of x or γ rays required to instigate reddening of human skin (Kahn, 1994). More quantitative measurements of ionizing radiation were then made in terms of exposure, a measure of radiation intensity based on the ionization produced in a specified volume of air by photons. Exposure was a popular measure because of the ease of measurement using ion chambers and electrometers (Greening, 1981). However, exposure can only be measured in air for photons having an energy

less than 3 MeV. A more general quantity, the 'absorbed dose' can be determined for any absorbing medium, energy and ionizing radiation (including neutrons, protons and electrons). The absorbed dose is the average energy absorbed per unit mass of material from ionizing radiation. The SI unit for absorbed dose is therefore measured in J/kg and denoted as the Gray (Gy).

Energy is absorbed by the medium through the collision of charged particles with atoms and molecules which become ionized or excited. Charged particles such as electrons and protons may constitute the primary radiation field or they may be secondary radiation products originating from the interaction of photons or neutrons with matter. Hence, photons and neutrons are considered indirectly ionizing radiations. Because of the predominant use of photons and electrons in the clinic, only interactions involving photons and electrons with matter will be considered.

Photons

There are six main interactions that photons of typical clinical energies (<10 MeV) undergo as they traverse a material: coherent scattering, the photoelectric effect, the Compton effect, pair and triplet production and photo-disintegration. Although the last two interactions occur for clinical energies their probability of occuring is negligible.

For coherent or Rayleigh scattering a photon interacts coherently with an atom and is scattered elastically in a different direction. The photon energy is not changed and no ionization of the atom occurs. Since no energy is transferred during the interaction, coherent scattering does not contribute to the dose absorbed by the medium.

The photoelectric effect involves the ejection of a bound electron from an atom by a photon whose energy is completely transferred to the electron. The final kinetic energy of the photoelectron is the difference between the incident photon energy and the binding energy of the electron. The probability of the photoelectric interaction occurring is greatest when the photon energy is approximately equal to the binding energy of the electron. Otherwise it varies roughly as the inverse cube of the photon energy. Furthermore, the probability of a photoelectric event occuring when a single photon passes through a layer of material containing one atom per m^2 varies approximately as Z^4 (where Z is the atomic number of the absorbing material) for high Z materials and as $Z^{4.8}$ for low Z materials. An effective atomic number, Z_{eff}, for a medium consisting of several elements, i, can be defined for the photoelectric interaction as follows (Attix, 1986):

$$Z_{eff} = \left[\sum_i \frac{f_i (Z/A)_i}{\sum_j f_j (Z/A)_j} Z_i^a \right]^{1/a} , \qquad (1.1)$$

where f is the weight fraction of element i or j and A is the atomic weight. For the photoelectric effect 'a' is empirically determined to be 2.94 (McCullough and Holmes, 1985).

In Compton interactions, the energy of the photon is much greater than the binding energy of the electrons and so the electrons can be considered to be free. The photon is scattered by the free electron and some of its energy is transferred to the kinetic energy of the electron. The energy of the scattered photon is a function of the incident photon energy and its scattering angle. Low incident photon energies and small scattering angles correspond to small energy transfers to the electron. The probability of the

Compton effect occurring is proportional to the electron density of the absorbing medium and the inverse of the incident photon energy.

For pair production, the photon interacts with the Coulomb force field of a nucleus and gives up all of its energy to the process of creating an electron-positron pair. Since the rest mass of an electron and positron is 0.511 MeV, a photon must possess a threshold energy of 1.02 MeV for pair production to occur. The excess photon energy goes into the kinetic energy of the electron and positron. A similar interaction is triplet production where an electron-positron pair is produced in the electric field of an electron. The probability of triplet production occurring is much less than that of pair production for the photon energies typically encountered in radiotherapy (<10 MeV).

The probability of a photon interaction occurring is related to the total linear attenuation coefficient, μ, which is the sum of the individual basic linear attenuation coefficients related to the cross sections for each interaction:

$$\mu = \sigma^{coh} + \tau + \sigma^{c} + \kappa\,, \tag{1.2}$$

where σ^{coh}, τ, σ^{c} and κ are the linear attenuation coefficients for coherent scattering, photoelectric effect, Compton effect and pair production, respectively. The attenuation coefficient depends on photon energy and the atomic number and density of the absorbing material. The relative importance of the three main photon interactions is depicted in Fig. 1.2 for different atomic numbers and photon energies. The curves in Fig. 1.2 represent the values of Z and photon energy for which the two bordering interactions are equal.

The energy that contributes to absorbed dose in a particular interaction is that which is transferred to the kinetic energy of a charged particle. Hence,

a quantity more related to absorbed dose is the energy absorption attenuation coefficient, μ_{ab}, given by,

$$\mu_{ab} = \frac{\overline{E}_{ab}}{h\nu}\mu \qquad (1.3)$$
$$= \tau_{ab} + \sigma^{c}_{ab} + \kappa_{ab},$$

where $\overline{E}_{ab}$ is the average energy absorbed by the medium and $h\nu$ is the incident photon energy. The $\overline{E}_{ab}$ is equivalent to $\overline{E}_{tr}(1\text{-}g)$ where $\overline{E}_{tr}$ is the average energy transferred into the kinetic energy of charged particles per interaction and g is the fraction of the kinetic energy of charged particles lost as bremsstrahlung (the photon radiation produced by the deceleration of the particles). Coherent scattering does not factor into Eq. 1.3 because no photon energy is transferred to charged particles. The dependence of μ_{ab} on the density of the absorbing medium, ρ, may be factored out to give the mass energy absorption attenuation coefficient, (μ_{ab}/ρ).

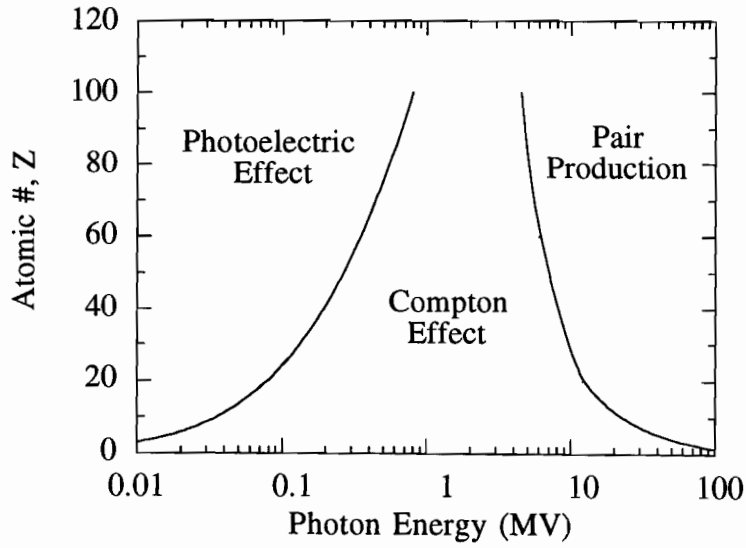

Figure 1.2 Relative importance of the three main photon interactions for different atomic numbers of the absorbing material and different initial photon energies (Adapted from Evans (1955)). The labels indicate regions in which the different interactions dominate, and the curves show the values of Z and photon energy where the two bordering effects are equal.

Electrons

Electrons traveling through a medium can undergo a number of Coulombic interactions with the nuclei or electrons in the medium. These interactions can be either inelastic or elastic collisions. The kinetic energy of the electron-medium system is conserved during elastic collisions. For inelastic interactions, some of the electron kinetic energy is lost to the ionization or excitation of atoms or molecules in the medium or to radiation production. It has been determined that electrons with kinetic energy of 10 and 30 MeV lose ~ 4 and 12% of their energy, respectively, by radiative losses (Greening, 1981).

The kinetic energy lost per unit distance traveled by the electron in a medium, dE/dl, is known as the linear stopping power of that medium and is given by

$$S = \left(\frac{dE}{dl}\right)_{col} + \left(\frac{dE}{dl}\right)_{rad}, \qquad (1.4)$$
$$= S_{col} + S_{rad},$$

where the subscripts 'col' and 'rad' refer to the collisional and radiation losses of the electron kinetic energy, respectively. The dose absorbed by a medium from energetic electrons is related to the collisional stopping power since this describes the transfer of energy to the medium. The radiative stopping power describes the electron energy lost to photon radiation or bremsstrahlung as it deccelerates, and does not contribute to the absorption of dose.

The collisional linear stopping power depends on the density (ρ) and electron density (N_e) of the absorbing medium as well as on the electron energy as follows (Johns and Cunningham, 1953):

$$S_{col} = 2\pi r_o^2 \rho N_e \frac{\mu_o}{\beta^2}\left[\ln\frac{E^2(E+2\mu_o)}{2\mu_o I^2} + \frac{E^2/8 - (2E+\mu_o)\mu_o \ln 2}{(E+\mu_o)^2}\right. \qquad (1.5)$$

$$\left. + 1 - \beta^2 - \delta\right]$$

where $\beta=v/c$ is the ratio of the electron velocity to the speed of light, E is the kinetic energy of the electron, I is the mean excitation energy for the atoms of the absorbing medium, μ_o is the rest energy of the electron (m_oc^2), r_o is the classical electron radius and δ is a correction factor accounting for the polarization of atoms by the electric field of incident electrons. The mass stopping power is defined as the stopping power divided by the density of the absorbing medium, S/ρ.

More precisely, the absorbed dose is related to the restricted collisional stopping power,

$$\left(\frac{L}{\rho}\right) = \left(\frac{S}{\rho}\right)_{col,\,\Delta} \qquad (1.6)$$

where Δ represents an upper limit to the energy of secondary electrons. The limit restricts the dose deposition (a local variable) to electrons whose energies are locally absorbed rather than carried away by energetic secondary electrons (delta rays).

1.2.2 Clinical Dose Measurements

Clinical dose measurements are usually made by placing a dosimeter in a volume of material called a phantom. In radiotherapy, one is concerned with the dose absorbed by tissue, thus dose measurements are usually made in a phantom material that absorbs and scatters ionizing radiations similarly to tissue. Such a material is referred to as being tissue equivalent. Water,

being tissue equivalent, provides the ideal phantom material (Task Group 21, 1983; Khan *et al.*, 1991; Andreo *et al.*, 1987) since it is readily available. In fact, the terms tissue equivalence and water equivalence are often used interchangeably in practice. Specialized dose measurements may be made in anthropomorphic phantoms that simulate the human body more closely.

In photon and electron dosimetry, for example, the tissue equivalence between the dose absorption of a dosimeter in a medium is maintained if the density, mass energy absorption attenuation coefficients, (μ_{ab}/ρ), and the restricted collision stopping powers, (L/ρ), of the two media are equivalent for all energies (Constantinou, 1978 as cited in Olsson, 1991). These requirements may be met by matching the composition and density of the dosimeter in terms of the weight fractions of the different elements to that of the phantom medium.

The tissue equivalence of any material can be verified by a number of methods. The μ_{ab}/ρ and L/ρ may be calculated at different energies for different materials using elemental values of μ_{ab}/ρ and L/ρ and a mixture rule. The calculated values can then be compared to the values for water. Similarly, the dose to a material for photon or electron irradiations may be measured or calculated for different beam energies and compared to those for water. For instance, Monte Carlo simulation may be used to calculate absorbed dose for different materials. Published applications of these methods to the gel dosimeters used for 3-D radiation dosimetry using MRI are reviewed in Section 3.2.4.

The accuracy of a dose measurement made with a non-tissue equivalent dosimeter needs to be carefully examined, because the dosimeter may perturb the dose delivery to the phantom and/or it may absorb dose differently than the phantom material. Such dose measurements may need

to be corrected. Dose corrections are possible when the basic physical energy absorption processes of dosimetry are considered.

There are various types of clinical dose measurements that are made in phantoms. For example, the calibration of the output of a treatment unit is made at a certain depth in phantom. Also, beam data for standard sets of treatment beams are required for the computation of dose distributions produced by computer treatment planning systems for different clinical setups. Beam data may include percent depth doses (PDDs) and beam profiles for different beam sizes. The PDD characterizes the depth dependence of the doses absorbed in a medium along the central axis of the beam. Beam profiles measure the dose deposition at a particular depth along a line perpendicular to the beam axis.

1.2.3 Dose Response Optimization

In general, a radiation dosimeter measures some quantity M which varies with dose, D. The general variation of M with D is illustrated in Fig. 1.3. There are three regions apparent on the graph: a low dose region in which the response may be slow (the toe), a region in which M varies significantly with dose and a high dose region in which the response saturates (the shoulder). A linear response of M to dose is preferred since relative values of M would give the relative values of dose directly. (The normalizations of M or D are usually performed with respect to their maximum values, M_{max} and D_{max}, respectively). However, the response of M to dose need not be linear, but then the entire response curve has to be calibrated. In determining the utility of a dosimeter, three variables are of particular interest: the dose range (D_{max}-D_o) over which useful

measurements can be made, the dynamic range (M_{max}-M_o) indicating the extent that M changes over the dose range, and the dose sensitivity, d, which defines the extent by which M changes per unit dose.

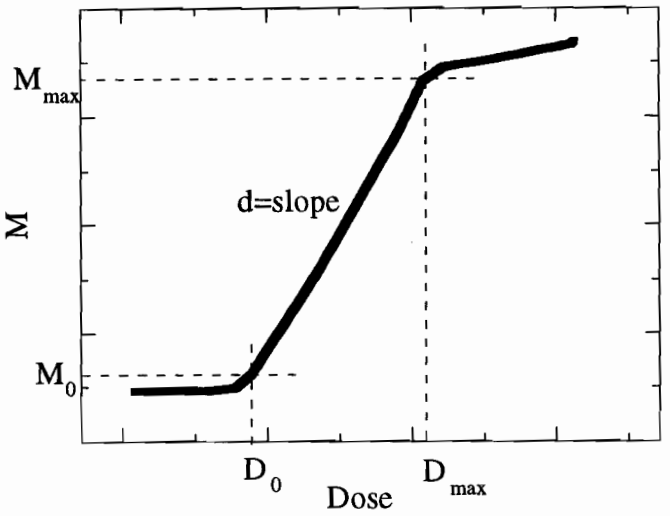

Figure 1.3 General dose response for a variable M with a practical linear region.

An optimal response of M to dose has the lowest minimum detectable dose and provides the best resolution for an absolute or relative dose determination. Also, the best dose resolution provides the highest contrast and signal to noise ratios for an image whose intensity is related to M. The minimum dose is that dose for which the measurement M can be differentiated from the background noise of the measuring system. For this reason, it is often defined as the dose, D, equivalent to 3 times the absolute dose resolution defined below (ICRU Report No. 22, 1972). For the purpose of simplifying the following discussion, the values of M_o and D_o shown in Fig. 1.3 are assumed to be zero. The resolution for the absolute dose and the relative dose differ. For an absolute dose determination given by,

$$D = \frac{M}{d}, \tag{1.6}$$

the resolution in D, according to error propagation rules (Bevington and Robinson, 1992), is,

$$\sigma_D^2 = \sigma_M^2 \left(\frac{1}{d}\right)^2 + \sigma_d^2 \left(\frac{-M}{d^2}\right)^2, \tag{1.7}$$

where σ_M is the resolution in the measurement M and σ_d is the resolution in d. For a relative dose determination given by,

$$\%x = 100 \frac{D}{D_{max}} = 100 \frac{M}{M_{max}}, \tag{1.8}$$

the resolution in %x is,

$$\sigma_{\%x}^2 = \sigma_M^2 \left(\frac{100}{M_{max}}\right)^2 + \sigma_{M_{max}}^2 \left(\frac{-100\,M}{M_{max}^2}\right)^2, \tag{1.9}$$

where σ_M and σ_{Mmax} are the resolutions in M and M_{max}, respectively. The two resolutions, σ_M and σ_{Mmax}, are equivalent. By comparing Eq. 1.7 with Eq. 1.9 it is evident that the best resolution in an absolute dose measurement, and hence the lowest minimum detectable dose, is achieved for the smallest σ_M and the greatest dose sensitivity, whereas the best resolution in a relative dose measurement is achieved for the smallest σ_M and the greatest M_{max} regardless of the dose sensitivity. Of course the irradiation time required to produce a response M_{max} must be within practical limits.

Aside from resolution considerations, a large dose range is preferred for practical reasons because it would accommodate more applications. For example, a large dose range would allow for a better assessment of the high doses produced in the vicinity of brachytherapy sources. In summary, an optimal dose response has the greatest dose sensitivity, dynamic range (in so far as it is related to M_{max}) and dose range.

1.3 Practical Dosimetry Techniques

There are four types of dosimeters generally used for measuring radiation dose distributions: ionization chambers, diode detectors, thermoluminescent dosimeters (TLD) and radiographic film. These dosimeters are well suited for the various types of clinical dose measurements (see Section 1.2.2). For example, the radiation output of therapy modalities is almost exclusively calibrated by ion chamber measurements made in phantom. Diode detectors and ion chambers are often used in current mode to quickly acquire relative dose information such as PDD and dose profile data (see Section 1.2.2). For static radiation beams these detectors are displaced automatically along a line through a tank of water. For symmetric beams, only PDDs and profiles need be measured. To measure more complex asymmetric 2-D dose distributions planes through the distribution can be adequately scanned in raster fashion. TLD dosimeters and radiographic film are also used to determine relative dose information from relative readings. Dose measurements can also be made in more complex anthropomorphic phantoms containing tissue inhomogeneities using TLDs.

The physical basis and the practical uses of the dosimeters are well presented in most basic texts on radiation dosimetry (Attix, 1986; Johns and Cunningham, 1953). However, the dosimeters are reviewed briefly below prior to describing their suitability for 3-D radiation dosimetry in Section 1.4.

1.3.1 Ionization Chambers

There are many varieties of ionization chambers used in clinical practice, but generally they are all comprised of a gas-filled chamber

containing electrodes that collect the ions produced in the gas by the ionizing radiation. For example, a standard thimble-type chamber is cylindrical or spherical in shape. The wall is composed of plastic or graphite and is thick enough to provide electronic equilibrium. That is, it is greater than the range of the highest energy secondary electrons so that all the electrons that traverse the cavity are produced from within the chamber wall. The wall is either conducting or lined with a thin layer of conducting material to which a high voltage is applied. The collector electrode placed in the center of the chamber is connected to an electrometer input near ground potential. The chamber/electrometer setup can be used to measure the charge or current produced by the ionizing radiation. The charge or current can in turn be related to the absorbed dose or dose rate, respectively. Some features of the relationship between the measurement reading and the dose to water are illustrated below.

When the ion chamber is introduced into a phantom for dose measurements, the cavity introduced into the phantom perturbs the dose deposition in the phantom and the perturbation must be accounted for. For example the dose to water is derived from M_{corr} the reading from the ionization chamber/reader combination as follows (TG21, 1983):

$$D_{water} = M_{corr} N_{gas} \left(\frac{\bar{L}}{\rho}\right)_{gas}^{water} P_{factor}\,, \qquad (1.10)$$

where N_{gas} is the cavity-gas calibration factor relating M_{corr} to the dose absorbed by the gas and $(\bar{L}/\rho)_{gas}^{med}$ is the ratio of the mean restricted mass stopping power of the phantom material to that of the chamber gas. The quantity, P_{factor}, is a product of three factors accounting for 1) the ion collection efficiency of the chamber, 2) the change in photon fluence resulting from the replacement of the medium by the ion chamber wall and cavity, and

3) the differences in the composition of the medium and the chamber wall. Equation 1.10 is based on the Spencer-Attix modification (Spencer and Attix, 1955) of the Bragg-Gray cavity theory (Bragg, 1912; Gray, 1929 and 1936) which states that under suitable conditions, the ratio of the dose absorbed by water to that absorbed by the gas in the ion chamber is equivalent to the ratio of the restricted stopping powers for the two media. If the dose to muscle is of interest rather than the dose to water, then the following expression could be used:

$$D_{muscle} = D_{water} \left(\frac{\mu_{ab}}{\rho} \right)_{water}^{muscle}, \qquad (1.11)$$

where $(\mu_{ab}/\rho)_{water}^{muscle}$ is the ratio of the mass energy absorption attenuation coefficient for muscle to that for water.

1.3.2 Diode Detectors

Diode detectors measure the ionization produced by ionizing radiation in solid semiconductors instead of in gas. A typical diode detector consists of a silicon p-n junction where the p-region contains an excess of holes and the n-region contains an excess of electrons. Applying a reverse bias potential across the p-n junction (i.e., V_n-V_p>0) causes enhancement (relative to no bias condition) of the depletion region at the p-n junction. Ionizing radiation traverses the depletion region producing electron-hole pairs. These electrons and holes are swept to the n and p sides of the junction, respectively, where they become mobile majority carriers. The resulting current can be detected, amplified and related to absorbed dose.

1.3.3 Thermoluminescent Dosimeters

The emission of light by certain irradiated crystalline materials when they are heated is known as thermoluminescence. Thermoluminscence occurs because of imperfections in the crystalline lattice produced by impurities that create energy traps. When the crystals are irradiated energy is absorbed, and some charge carriers become excited and then trapped in the higher energy levels. Subsequent heating of the crystals may provide trapped charge carriers with enough energy to escape the energy traps. Released charge carriers such as electrons may recombine with holes at a luminescent centers, and the excess energy is emitted as visible or ultraviolet light. The light output can be measured using an apparatus containing a photomultiplier tube. The total amount of light emitted is proportional to the absorbed dose. Crystals used for this dosimetry technique are known as thermoluminescent dosimeters or TLDs. TLDs are available in powder format, as a powder compressed in a binding material or as small solid crystals. TLDs can be used to measure 3-D dose distributions by placing them in a grid of compartments machined in thin layers of solid, tissue-equivalent phantom.

1.3.4 Radiographic Film

Radiographic film contains an emulsion of gelatin and silver bromide (AgBr) grains. When the film is irradiated ion pairs are created that convert some of the Ag^+ ions on a grain to Ag atoms. In the development process the bromine is removed and all the Ag^+ ions in any grain containing a few Ag atoms are converted to Ag atoms. What remains are opaque grains of silver.

The variations in density of these grains throughout the film produces variations in optical density which form the image. The optical density of radiographic film can be measured using a densitometer, and related to dose using a calibration curve of the optical density to dose.

1.3.5 Recent Developments

Two recent developments in dosimetry techniques involve radiochromic film and plastic scintillator sheets. Radiochromic film (McLaughlin and Chalkey, 1965; Chiu-Tsao, S.T. *et al.* 1994) is colorless and turns blue upon irradiation, and it has the advantage that it doesn't require development or processing. Prior to analysis, one must wait several days for the film's radiation response to stabilize. Radiochromic film is relatively insensitive to dose with the more sensitive types requiring doses of the order of 10-50 Gy for an appropriate response. Also, difficulties in achieving a uniform dose response over the entire surface of the film are encountered leading to errors of about 5% in the doses determined (Zhu *et al.*, 1995; Meigooni *et al.*, 1995). The optical density of radiochromic film is best analysed using specialized densitometer equipment. Both radiographic and radiochromic film can be used to measure 2-D dose distributions by placing it between layers of tissue equivalent plastic phantom.

Scintillation is the emission of visible or near-visible light by a material when the material absorbs energy from ionizing radiation. The plastic scintillator sheet dosimeter (Chawla *et al.*, 1995; Dorner, 1995; Perera *et al.*, 1992) emits amounts of light over its surface that are proportional to the doses absorbed locally over the surface. A sheet can be placed in a light-tight water tank and connected to a charge coupled device (CCD) camera whose

signal is converted to a 2-D dose distribution shortly after the completion of an irradiation sequence. Several 2-D distributions can be obtained by displacing the sheet through the radiation field in the tank. Three dimensional dose distributions can then be determined by stacking the 2-D data.

1.3.6 3-D Dosimetry Using Gels and MRI

While most of the dosimetry techniques discussed thus far are adequate for current clinical dose measurements, the conformal techniques being developed require dosimetry techniques with 3-D capabilities and high spatial resolution. The combined use of radiation sensitive gels and MRI shows potential for such a dosimetry technique.

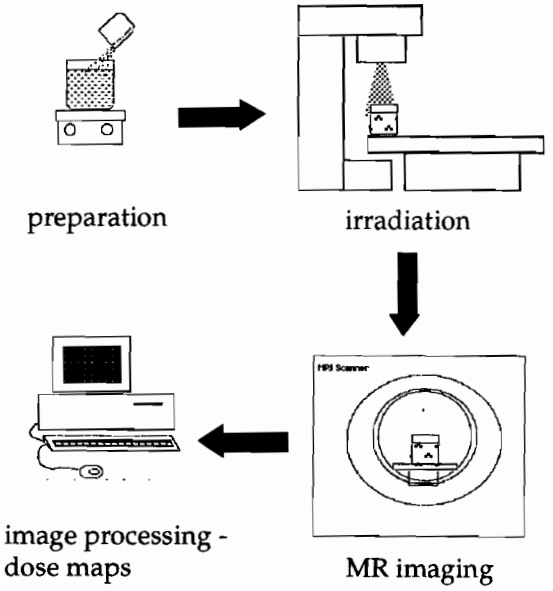

Figure 1.4 The general procedure for 3-D radiation dosimetry using gels and MR imaging. First the gel is prepared. Then it is irradiated so that a dose distribution is formed within its volume. The gel is then scanned and the resulting cross sectional MR images are processed by computer to produce dose maps.

The general procedure for measuring radiation dose distributions in 3-D using radiation sensitive gels and Magnetic Resonance Imaging (MRI) is outlined in Fig. 1.4. The gel dosimeter phantom is prepared, and then it is

irradiated so that a specific 3-D dose distribution is produced within the gel volume. Cross-sectional MR images of the gel are then acquired, and the intensity distribution in the images are analyzed to produce maps of the dose distributions.

Figures 1.5 and 1.6 are examples of MR images of the two existing types of gel dosimeters: a ferrous sulfate-doped gel and a polymer gel, respectively (see below). Figure 1.5a (Schreiner, Parker, Evans, Audet, Roman and Donath, 1994) shows the MR image of an axial cut through a ferrous sulfate-doped gelatin gel irradiated by displacing an HDR ^{192}Ir source through five catheters implanted into the gel. The image is T_1-weighted and the high dose regions appear bright; the gray scale corresponds to the raw MR signal intensity. Figure 1.5b shows the dose data obtained from the image in Fig. 1.5a binned into five ranges (>40 Gy, 30-39 Gy, 20-29 Gy, 10-19 Gy, 5-9 Gy and <5 Gy). The lines bordering the ranges are the isodose contours predicted by a treatment plan generated by the McGill Planning System (Pla 1989 and 1994). There is very good agreement between the contours and the corresponding limits of the dose bins. Figure 1.6 shows two 3-D views of an irradiated BANG (Bis Acrylamide Nitrogen Gelatin) polymer gel consisting of thirty 3 mm thick slices. The gel was irradiated with four 1 cm^2, 10 MV photon beams with a surface to skin distance of 100 cm. The white bars in Fig. 1.6a, going counter clockwise, indicate separate irradiations with peak doses of 8, 6, 4 and 2 Gy deposited at the depth of dose maximum (~2.5 cm). Figure 1.6b shows an expanded view of the gel that is rotated 90° counter clockwise. These two images are T_2-weighted images in which the high dose regions appear dark.

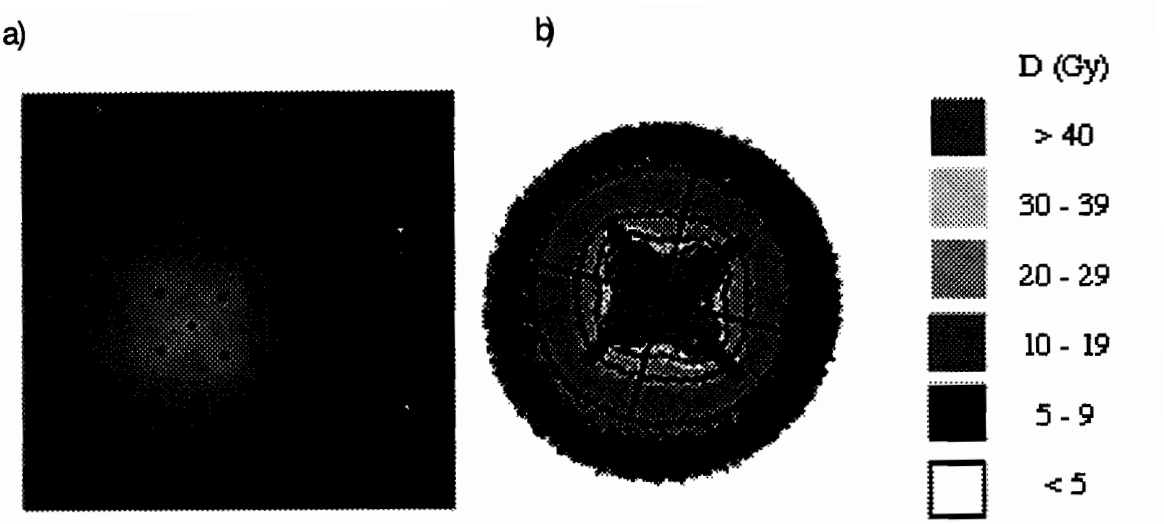

Figure 1.5 a) MR image of an axial cut through a ferrous sulfate gelatin dosimeter irradiated by displacing an HDR ^{192}Ir source through five catheters implanted into the gel (Schreiner, Parker, Evans, Audet, Roman and Donath, 1994). The image is a T_1-weighted image in which the high dose regions appear bright and the gray scale corresponds to the raw MR signal intensity. b) The dose data obtained from the image in a) binned into five ranges (>40 Gy, 30-39 Gy, 20-29 Gy, 10-19 Gy, 5-9 Gy and <5 Gy). The lines bordering the ranges are the isodose contours predicted by an MPS treatment plan (Pla 1989 and 1994).

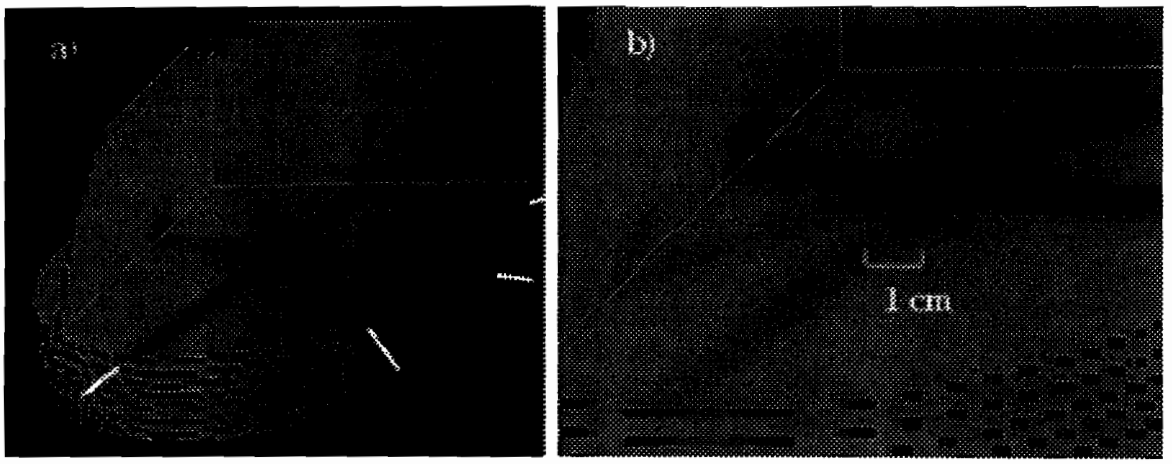

Figure 1.6 Two 3-D views of an irradiated BANG polymer gel consisting of thirty 3 mm thick slices. The gel was irradiated with four 1 cm^2, 10 MV photon beams with a surface to skin distance of 100 cm. The white bars in a), going counter clockwise, indicate separate irradiations with peak doses of 8, 6, 4 and 2 Gy deposited at the depth of dose maximum (~2.5 cm). b) An expanded view of the gel that is rotated 90° counter clockwise. These two images are T_2-weighted images in which the high dose regions appear dark.

The basis for 3-D gel dosimetry using MRI can be divided into three main areas:

1) *Response of the gels to dose*

The gel dosimeters presently used for 3-D MRI radiation dosimetry are chemical dosimeters, a radiation sensitive material in which the radiation induces certain chemical reactions. The concentration of radiation products can be detected by experimental means and related to the radiation dose (Attix, 1986).

The two types of gel dosimeters used with MRI are the ferrous sulfate-doped gels (Gore *et al.*, 1984) and the polymer gels (Maryanski *et al.*, 1993). Both dosimeters consist of an aqueous environment dispersed in a gel matrix. The aqueous environment of the ferrous sulfate gel contains ferrous (Fe^{2+}) ions which are oxidized upon irradiation to ferric (Fe^{3+}) ions. The aqueous environment of the polymer gel contains monomers that polymerize and crosslink into polymer macromolecules upon irradiation of the gel. The gel matrix is typically composed of agarose or gelatin; the purpose of the matrix is to prevent the reaction products in the liquid environment from mixing, and maintains the integrity of the spatial distribution of dose information. This is only partially achieved for the ferrous sulfate-doped gel dosimeters in which the ions still diffuse slowly (Schulz *et al.*, 1990). After irradiation, the concentration of radiation products within the gel will vary throughout the volume of the dosimeter according to the distribution of absorbed dose. The agarose and the gelatin may also participate in the radiation reactions (Appleby *et al.*, 1988; Olsson, 1991; Maryanski *et al.*, 1994). The gel dosimeters and their radiation chemistry will be reviewed in more detail in Chapter 3.

2) *Response of NMR Spin Relaxation to Dose*

An equilibrium magnetization associated with the nuclear spins in a material exists when a material is placed in an external magnetic field, such as when a gel dosimeter is placed in the magnetic field of an MR imager. The equilibrium magnetization can be perturbed by irradiating the material with radio frequency energy. After perturbation the magnetization returns to its equilibrium value by way of spin relaxation processes characteristic of the dynamics and structure of the molecules in the material. Of particular interest is the spin relaxation for the hydrogen nuclei or protons of water molecules in the gel dosimeters which are mainly composed of water ($\geq$ 90% by weight). It has been established that water proton spin relaxation of the gel dosimeters is sensitive to the radiation-induced chemical changes in the dosimeters (see Sections 3.2.4 and 3.3.3). Hence, the proton spin relaxation of the dosimeters can be used to monitor the dose absorbed by the dosimeter. The studies presented in Chapters 5 and 6 are concerned with the response of spin relaxation to dose for the ferrous sulfate-doped gel dosimeter and polymer gel dosimeter, respectively.

3) *Response of image intensity to dose*

The intensity of a pixel in an MR image is a measure of the magnetization at that pixel (Kaldoudi and Williams, 1993). The position of the detected magnetization in a subject is determined by using magnetic field gradients that spatially encode the data. Cross sectional images are obtained from the detected, encoded magnetization data using reconstruction algorithms. It is beyond the scope of this thesis to explain how images are produced from an MRI scanner. However, it is important

to realize that the intensities in an image depend on NMR relaxation parameters and hence on dose (Parker, 1995).

1.4 Utility of Dosimeters for 3-D Dosimetry

Established clinical dosimetric techniques are not well suited for acquiring dose to tissue or water information in a 3-D volume with a high spatial resolution. A recent report (Masterson *et al.*, 1991) indicates that intensive labour is required even to monitor dose distributions produced by simple beam arrangements at a few points with ion chambers or TLDs. The main requirements of a 3-D dosimetry technique and how they are fulfilled by current dosimeters are discussed below.

1.4.1 Tissue Equivalence

Although radiographic film, diode detectors and TLDs are not tissue equivalent, their perturbation of the dose deposition in a phantom is usually considered negligible especially when the dosimeters are present in sparse quantities. However, the effective atomic numbers (see Eq. 1.1) of these dosimeters, being greater than those of tissue, causes their response to dose to increase at low photon energies where the Z-dependent photoelectric effect has a greater probability of occurring.

The perturbations of dose deposition by an ion chamber must be accounted for when converting an ion chamber reading to the dose absorbed by the phantom. The correction factors used to do so may introduce an error

of about ± 1.5% in the dose determination (Harrison, 1993; Curtin-Savard, 1995). The radiochromic film, scintillator sheets and gel dosimeters are largely tissue equivalent, and hence, the dose measured by these dosimeters is equivalent to the dose that would be absorbed by human tissue. However, only for gel dosimeters can it be said that the dosimeter itself constitutes the phantom, and that there are no correction factors required to correct for perturbation of dose absorption in the medium. The tissue equivalence for ferrous sulfate doped gel dosimeters is discussed in Section 3.2.4 whereas that for polymer gel dosimeters is discussed in Section 3.3.3.

1.4.2 Dose Integration

The complex dose distributions required for conformal therapy are created with multiple beam setups or dynamic treatments in which the dose is delivered over an extended period of time. Therefore, a practical dosimeter must be able to integrate the dose at each position of interest over the whole time course of the irradiation. All the dosimeters described in Section 1.3 have this capacity. However, a 3-D dose distribution can no longer be probed by scanning an ion chamber or diode detector through a water tank during a dynamic irradiation since the correlation between dose and position of the dosimeter is lost. Hence, the entire irradiation must be repeated for each point in the volume. This dosimetry technique is time consuming and inappropriate for measuring complex 3-D dose distributions.

Similar drawbacks, although less severe, are encountered for plastic scintillation sheet detectors. Irradiations must be reperformed for each new

position of the sheet in the water tank, however, at least a whole plane of information is being acquired for each irradiation.

1.4.3 Tissue Inhomogeneities

Variations in absorbed dose arising from tissue inhomogeneities and body shape can be accounted for by using anthropomorphic phantoms that closely mimic the composition of the body in terms of radiation absorption properties. Lung and bone represent two types of tissue inhomogeneities since their density and average atomic number vary greatly from that of soft tissue like muscle. Some dosimetry techniques lend themselves more easily to measurements in anthropomorphic phantoms than others. TLDs and film can be easily placed in or between the layers of solid anthropomorphic phantoms.

The method of measuring dose distributions in water tanks with detectors such as ion chambers, diodes or scintillation sheets cannot easily be adapted to account for tissue inhomogeneities. The insertion of objects mimicking tissue inhomogeneities in the tank would interfere with the positioning of the detector.

One of the advantages of gel dosimeters is that they can easily be used in the design of anthropomorphic phantoms. They could be set into molds of any shape, and objects of varying shape and composition could be placed within the molds (Hiraoka *et al.*, 1992).

1.4.4 Spatial Resolution In 3-D

Spatial resolution is very important for measuring areas of high dose-gradients which are characteristic of the dose distributions produced by conformal therapies. For dosimeters such as diode detectors, ion chambers and TLDs the spatial resolution is limited by the size of the dosimeter. For most detectors the spatial resolution that can be achieved in 3-D is limited by the tediousness of probing a 3-D volume with detectors that integrate doses at points only (diode detectors, ion chambers and TLDs) or in planes (film, scintillation sheets). For instance, to measure the dose every 5 mm in a 1 liter volume, more than 1000 TLDs would be needed. Because each TLD has a slightly different radiation response, each TLD must be calibrated and its identity maintained throughout its usage. To do this for a thousand TLDs is very tedious and requires a lot of book-keeping. Also, TLDs are not soft tissue equivalent, and if too many are present, the measured dose will not accurately represent that absorbed by phantom. This problem can be circumvented by using fewer TLDs but repeating the procedure for different sets of TLDs in different positions is a more time consuming alternative.

Film possesses the highest spatial resolution in 2-D (~1 μm). To measure 3-D dose distributions, additional films need only be placed between extra layers of phantom. The width of a layer, and hence the vertical resolution, is however, as with TLDs, limited by the fact that radiographic film is not tissue equivalent and cannot be present at too high a density. Again, an alternative procedure may be to use fewer films, and repeat the irradiations for sets of films at different spacings. Scintillation sheet detectors have a lower spatial resolution in 2-D of about 0.6 mm. As mentioned

previously, the drawback of scintillation sheet detectors is that the irradiation must be performed for each repositioning of the sheet in the water tank.

The gel dosimeters can detect integrated dose data in 3-D. High spatial resolution is possible in all dimensions because gel dosimetry does not involve the finite displacement of probe through a detector. In a sense, a gel dosimeter acts as a 3-D photographic emulsion. However, the spatial resolution determined by that of the acquisition technique, MRI, is typically limited to ~1 mm (in a plane) for a 24x24 cm^2 field of view and a 256x256 pixel matrix. The resolution may be improved by decreasing the field of view and increasing the pixel matrix size. The spatial resolution in MR images is not as good as that for film, but will only improve with time as the field of MRI continues to experience tremendous growth and development. Furthermore, it is very simple to analyze dose distributions in any plane because MRI units can readily produce cross sectional images along any axis. Film on the other hand, cannot easily be setup in an arbitrary direction because of the way in which phantom layers are oriented.

CHAPTER TWO
Nuclear Magnetic Resonance and Relaxation

Nuclear Magnetic Resonance (NMR) has been very useful in the study of the structure and molecular dynamics of materials. Of particular interest is the nuclear magnetic relaxation of the magnetization arising from the water protons (hydrogen nuclei) in the two gel dosimeters, the ferrous sulfate-doped gelatin gel and the BANG polymer gel. Changes in the molecular dynamics of the solutes in the BANG gel and in the paramagnetic species in the ferrous sulfate gel can be induced by exposing the gels to radiation. Since proton relaxation parameters are sensitive to these changes, they can be related to the dose absorbed by the dosimeters. Three dimensional mappings of dose depositions in gels may be obtained by acquiring proton relaxation data throughout the gel using MRI. While a complete review of NMR theory is beyond the scope of this thesis the principal concepts pertinent to the studies presented are covered. Basic NMR theory is well reviewed in the literature (Slichter, 1990; Abragam, 1961; Callaghan, 1991).

2.1 Magnetization

Nuclear magnetism is observable for atomic nuclei with angular momentum, $\hbar\mathbf{I}$, and an associated magnetic moment, $\vec{\mu} = \gamma\hbar\mathbf{I}$, where γ is the gyromagnetic ratio specific to a particular nucleus, $\hbar$ is Planck's constant divided by 2π and $\mathbf{I}$ (= (I_x, I_y, I_z)) is the spin operator. The state of a nucleus can be specified by the simultaneous eigenfunction, $|Im\rangle$, of operators I^2 and

I_z which yield eigenvalues of $I(I+1)$ and m, respectively, when they act upon $|Im\rangle$ (i.e., $I^2 |Im\rangle = I(I+1)|Im\rangle$ and $I_z|Im\rangle = m|Im\rangle$ where $m = -I, -I+1...I$; note that the symbols for eigenvalues are italicized). The value normally quoted as the spin of a nucleus is that of I. For spin 1/2 nuclei, $I = 1/2$ and $m = \pm 1/2$.

In an applied homogeneous, static magnetic field, $\mathbf{H} = (0,0,H_0)$, oriented by convention along the z-axis the nuclear magnetic moment interacts with H_0 via the Zeeman Hamiltonian, $\mathcal{H}_0$ (Slichter, 1990):

$$\mathcal{H}_0 = \vec{\mu} \cdot \mathbf{H} = -\gamma \hbar H_0 I_z . \tag{2.1}$$

Hence, the energy eigenvalues of the Zeeman Hamiltonian are $E_m = -\gamma \hbar H_0 m$ where $m = -I, -I+1...I$.

The expectation value of a time-dependent magnetic moment given in terms of the time-dependent spin operator $\mathbf{I}(t)$ is,

$$\langle \vec{\mu}(t) \rangle = \int \psi'^* \, \vec{\mu}(t) \, \psi \, d\tau = \gamma \hbar \langle \psi' | \mathbf{I}(t) | \psi \rangle , \tag{2.2}$$

where Ψ is the generalized wave function describing an arbitrary state of the nucleus. The generalized wave function is a linear combination of the basis states, $|m\rangle$ (the I in $|Im\rangle$ has been omitted for convenience):

$$\Psi = \sum_m a_m |m\rangle , \tag{2.3}$$

where the coefficients a_m have both magnitude and phase. For a single magnetic moment experiencing the Zeeman interaction equation of motion for the spin operators is,

$$\frac{d\mathbf{I}(t)}{dt} = \frac{i}{\hbar} [\mathcal{H}_0, \mathbf{I}(t)] , \tag{2.4}$$

where i = x, y, z and the square brackets represent the commutation of the arguments. For a time-independent Hamiltonian such as $\mathcal{H}_o$ the solution to Eq. 2.4 is,

$$\mathbf{I}(t) = \exp\left(-i\mathcal{H}_o t/\hbar\right)\ \mathbf{I}(0)\ \exp\left(i\mathcal{H}_o t/\hbar\right). \tag{2.5}$$

Substituting Eq. 2.3 and Eq. 2.5 into Eq. 2.2, the following expression for the expectation value of the magnetic moment is obtained:

$$\left\langle \Psi' \middle| \vec{\mu}(t) \middle| \Psi \right\rangle = \gamma\hbar \sum_{m,\,m'} a^*_{m'}\, a_m \exp\left(i\left(E_m - E_{m'}\right) t / \hbar\right) \left\langle m' \middle| \mathbf{I}(0) \middle| m \right\rangle , \tag{2.6a}$$

where the * denotes the complex conjugate. This expression reduces to the following for the z-component,

$$\left\langle \mu_z(t) \right\rangle = \gamma\hbar \sum_{m=-I}^{I} |a_m|^2 . \tag{2.6b}$$

To determine μ_x and μ_y the operators I_x and I_y are written in terms of the raising and lowering operators I_+ and I_- (i.e., $I_\pm |m\rangle = \left(I(I+1) - m(m\pm1) \right)^{1/2} |m\pm1\rangle$). That is $I_x = \frac{1}{2}\left(I_+ + I_- \right)$ and $I_y = -\frac{1}{2}i\left(I_+ - I_- \right)$. The expression for $\langle\mu_x\rangle$ is then:

$$\left\langle \mu_x(t) \right\rangle = \frac{\gamma\hbar}{2} \sum_{m=-I}^{I} \left(\sqrt{I(I+1) - m(m+1)}\ \ a^*_{m+1}\, a_m \exp\left(i\,\gamma H_o t\right) + \right.$$
$$\left. \sqrt{I(I+1) - m(m-1)}\ \ a^*_{m-1}\, a_m \exp\left(-i\,\gamma H_o t\right) \right). \tag{2.6c}$$

A similar expression is obtained for $\langle\mu_y\rangle$ with a 90° phase shift . It is evident from Eq.'s 2.6 that the expectation values of the transverse components of the magnetic moment, $\langle\mu_x\rangle$ and $\langle\mu_y\rangle$, have oscillatory time dependence whereas $\langle\mu_z\rangle$ is static. This result concurs with the classical description in which $\langle\vec{\mu}\rangle$ precesses about the z-axis at the Larmor frequency of $\omega_o = \gamma H_o$ (i.e., with a static component parallel to H_o and a transverse component rotating in the

xy-plane). For a given field H_o, different nuclei each characterized by a different γ will have a different Larmor frequency corresponding to the energy difference between levels. For example, for hydrogen nuclei or protons, $\gamma = 267$ rad s^{-1} T^{-1} and for deuterons, $\gamma = 41$ rad s^{-1} T^{-1} where T is the magnetic field strength in Tesla.

The above discussion has been limited to a single spin only, yet in most materials the nuclei are usually present in large quantities. Once the material is in the external field, a net equilibrium macroscopic magnetization given by:

$$M_i = N \overline{\langle \mu_i \rangle} , \tag{2.7a}$$

can be observed, where i designates the axis (i = x, y, z), N is the number of spins and the bar denotes the average over all the spins. According to Eq. 2.6b the z-component of the average magnetic moment is proportional to the populations of the eigenstates, $\overline{|a_m|}^2$, given as follows by the Boltzmann factors (Slichter, 1990):

$$\overline{|a_m|}^2 = \frac{\exp\left(\frac{\gamma\hbar H_o m}{kT}\right)}{\sum_{m=-I}^{I} \exp\left(\frac{\gamma\hbar H_o m}{kT}\right)} , \tag{2.7b}$$

These populations imply that there are more spins aligned along the direction of the magnetic field ($m > 0$ and $E_m = -\gamma\hbar m H_o < 0$) than against it ($m < 0$ and $E_m = -\gamma\hbar m H_o > 0$). The following is obtained for the longitudinal magnetization when in the high temperature regime with $\mu H_o/kT \ll 1$ (an approximation for typical fields of ~1 Tesla and room temperature):

$$\begin{aligned} M_z &= N\gamma\hbar \sum_{m=-I}^{I} \overline{|a_m|}^2 , \\ &= \frac{N\gamma^2\hbar^2 I\,(I+1)}{3kT} H_o . \end{aligned} \tag{2.8}$$

The expectation values of the transverse magnetic moments, $\langle \mu_x \rangle$ and $\langle \mu_y \rangle$, on the other hand are proportional to $a^*_{m\pm1} a_m$. The coefficients, a_m, have arbitrary phase, α_m, and the product $a^*_{m\pm1} a_m$ depends on the phase difference between the states ($= |a_{m\pm1}| \, |a_m| \exp(-i(\alpha_m - \alpha_{m\pm1}))$). Since, at equilibrium, no phase coherence exists between spins, i.e., the phases are randomly distributed, the average values of $\langle \mu_x \rangle$ and $\langle \mu_y \rangle$ are zero, and no net transverse magnetization, M_{xy}, is observed. Thus, the equilibrium magnetization of the ensemble of spins is given by $\mathbf{M} = (0, 0, M_o)$.

2.2 Magnetization Dynamics

As previously described, when a material is placed in an external magnetic field an equilibrium magnetization $\mathbf{M} = (0, 0, M_o)$ is established. If the material is irradiated with a time-dependent magnetic field or radiofrequency (rf) energy oscillating at the Larmor frequency, ω_o, the equilibrium magnetization may be perturbed so that $\mathbf{M}$ becomes time-dependent, and $M_z \neq M_o$ and $M_{xy} \neq 0$. Because of the resonance condition imposed by ω_o, different nuclei characterized by unique values for γ can be selectively irradiated, i.e., only protons will absorb rf energy of 25 MHz in a 0.6 T field. The coupling between the rf energy and the spins creates non-zero transition probabilities between the eigenstates. Thus, the absorption of rf can affect the populations of the eigenstates and hence the average $\langle \mu_z \rangle$ (see Eq. 2.7b). The coupling also creates phase coherence in the time dependence of the average $\langle \mu_x \rangle$ and $\langle \mu_y \rangle$ making the average magnetic moments non-zero.

Once the perturbing rf is removed, the magnetization will begin to return to its equilibrium value $\mathbf{M} = (0, 0, M_0)$, and the system is said to relax. The relaxation proceeds by two different processes involving the components of magnetization along **H** (i.e., the longitudinal magnetization M_z) and in the plane orthogonal to **H** (the transverse magnetization M_{xy}). The longitudinal magnetization evolves as the consequence of the redistribution of the spin population among the different energy levels until the initial Boltzmann distribution is re-established. In this process the spin reservoir exchanges energy with the lattice (i.e., with the energy reservoir associated with non-spin degrees of freedom). The relaxation of the longitudinal magnetization is therefore termed spin-lattice relaxation. The transverse magnetization decays back to its zero equilibrium value as the transverse components of the magnetic moments of the spins lose coherence. The loss in coherence results from spin-spin interactions which cause the spins to precess at slightly different Larmor frequencies, and does not involve the transitions of spins between the different energy levels. The decay of the transverse magnetization is therefore termed spin-spin relaxation.

The transitions required to establish the equilibrium Boltzmann population distribution once the perturbation is removed must be driven by relaxation processes. Spontaneous emission is not effective in causing transitions from higher to the lower energy levels since the probability of transitions at typical NMR frequencies are extremely low (one transition per 10^{13} years; Dixon *et al.*, 1986). As will soon be shown, it is this requirement which enables one to use the characterization of the NMR spin-lattice relaxation properties to investigate the physical properties of materials.

2.2.1 Bloch Equations

The evolution of the macroscopic magnetization described above can be described by the phenomenological Bloch equations:

$$\frac{dM_z}{dt} = \gamma(\mathbf{M} \times \mathbf{H})_z + \frac{M_o - M_z}{T_1}, \text{ and} \qquad (2.9a)$$

$$\frac{dM_{x,y}}{dt} = \gamma(\mathbf{M} \times \mathbf{H})_{x,y} - \frac{M_{x,y}}{T_2}. \qquad (2.9b)$$

The first terms on the right-hand side of Eq.'s 2.9 describes the motion of the macroscopic magnetization in the presence of an applied field, **H**. The applied field of interest is given by $\mathbf{H} = (H_1\cos\omega t, -H_1\sin\omega t, H_o)$ where the z term is the static field and the x and y terms constitute the perturbing rf field rotating at a frequency ω. If the rf frequency is taken to be the resonant frequency ω_o and if the system is viewed in a frame of reference which rotates about the z-axis at ω_o, then in this frame of reference $\mathbf{H} = (H_1, 0, 0)$ where H_1 is arbitrarily assigned to the rotating x-axis.

The second term on the right-hand side of each of Eq.'s 2.9 account for the relaxation of the magnetization. The time constants T_1 and T_2 are the constants characterizing the time evolution of the magnetization by the spin relaxation processes. T_1 is called the spin-lattice (or longitudinal) relaxation time; T_2 is the spin-spin (or transverse) relaxation time.

The Bloch equations can be used to establish the time behaviour(s) of the macroscopic magnetization in two limits of interest: 1) the perturbation of $\mathbf{M} = (0, 0, M_o)$ under the influence of an rf pulse and 2) the relaxation of the magnetization **M** back to $(0, 0, M_o)$ when the perturbation is removed. First,

the determination of the evolution of the magnetization in a rotating frame in the presence of an applied rf pulse $\mathbf{H} = (H_1, 0, 0)$ is simplified since, at least in the studies considered in this thesis, the rf pulses are of such short duration that spin-relaxation need not be considered and the last terms in Eq. 2.9 may be neglected. The solutions of the Bloch equations in the rotating frame (indicated by the prime) are then:

$$M_y' = M_0 \sin(\gamma H_1 t), \tag{2.10a}$$

$$M_z' = M_0 \cos(\gamma H_1 t). \tag{2.10b}$$

It is evident from Eq.'s 2.10 that applying a transverse rf field will cause **M** to rotate away from the z-axis at a frequency $\omega_1 = \gamma H_1$. The angle of the rotation of **M** is determined by $\theta = \gamma H_1 t_p$ where t_p is the duration of the rf pulse (Ferrar and Becker, 1971).

Second, once the perturbation rf is removed, the Bloch equations become:

$$\frac{dM_z'}{dt} = \frac{M_0 - M_z'}{T_1}, \tag{2.11}$$

$$\frac{dM_{x,y}'}{dt} = -\frac{M_{x,y}'}{T_2}, \tag{2.12}$$

with only the relaxation terms remaining. Equation 2.11 indicates that the longitudinal magnetization, M_z, once perturbed, will grow exponentially to its equilibrium value M_o with a characteristic time T_1. Likewise, Eq. 2.12 indicates that the transverse magnetization, $M_{x,y}$, decays exponentially to zero with a characteristic time T_2.

2.2.2 Spin Relaxation

While the Bloch equations describe the time evolution of the macroscopic magnetization, they do not connect the relaxation of the magnetization to the physics of a material. A number of approaches exist that one can take to determine the processes which cause relaxation (Bloembergen *et al.*, 1948; Abragam, 1961; Slichter, 1990). A semi-classical approach to describe the evolution of the quantum mechanical operators associated with macroscopic magnetization (i.e., recall $M_i = N\overline{\langle \mu_i \rangle}$) is sufficient for the work presented in this thesis.

For a general spin interaction $\mathcal{H}_1(t)$, the equation of motion for the spin operator, I_i (where i = x, y or z), is:

$$\frac{\partial I_i(t)}{\partial t} = \frac{i}{\hbar}\left[I_i(t),\ \mathcal{H}_0 + \mathcal{H}_1(t)\right] . \qquad (2.13)$$

The time-dependent portion of the Hamiltonian associated with the spin interaction is in general much smaller than the time-independent Zeeman Hamiltonian, $\mathcal{H}_0$, and may be treated as a perturbation (Note: the specific example of dipolar spin interactions will be addressed later in this chapter). In order to solve Eq. 2.13 for the slow motion of I_i arising from $\mathcal{H}_1(t)$ rather than for the fast motion of I_i arising from $\mathcal{H}_0$, it is useful to transform I_i and $\mathcal{H}_1(t)$ into the interaction representation (Abragam, 1961; Slichter, 1990):

$$I_i^*(t) = e^{i\mathcal{H}_0 t/\hbar}\, I_i(t)\, e^{-i\mathcal{H}_0 t/\hbar} , \qquad (2.14)$$

where the * denotes the interaction representation unless otherwise specified.

This transformation is equivalent to working in a reference frame rotating about the z-axis at ω_o. The equation of motion is then:

$$\frac{\partial I_i^*(t)}{\partial t} = \frac{i}{\hbar}\left[I_i^*(t),\ \mathcal{H}_1^*(t)\right]. \qquad (2.15)$$

It is evident from Eq. 2.15 that in the absence of perturbing interactions ($\mathcal{H}_1^*(t) = 0$) I_i^* is constant, and relaxation does not occur. The solution of Eq. 2.15, approximated using second order time-dependent perturbation theory, is as follows (Abragam, 1961; Slichter, 1990):

$$\frac{dI_i^*(t)}{dt} = \frac{i}{\hbar}\left[I_i^*(0),\ \mathcal{H}_1^*(t)\right] + \left(\frac{i}{\hbar}\right)^2 \int_0^t \left[\left[I_i^*(0),\ \mathcal{H}_1^*(t')\right],\ \mathcal{H}_1^*(t)\right] dt'. \qquad (2.16)$$

The first and second terms on the right hand side are first and second order contributions to the dynamics of I_i, respectively. In general, a spin interaction can be expressed in the following form:

$$\mathcal{H}_1^*(t) = \sum_q e^{-iq\omega_o t}\ S^{(q)}(t)\ A^{(q)}. \qquad (2.17)$$

The $S^{(q)}(t)$ are the spatial time-dependent operators which can be written classically and the $A^{(q)}$ are the spin operators. The q represent the difference in the states Δm joined by the operator $A^{(q)}$ (i.e., q = +1, -1 for I_+ and I_-, respectively). The exponential in Eq. 2.17 results from working in the interaction representation. According to Eq.'s 2.16 and 2.17, spin relaxation for a component q of the perturbing interaction (i.e., $dI_i^*(t)/dt \neq 0$) is only observed under two conditions. First, the commutator, $[A^{(q)}, I_i^*]$, has to be nonzero; a condition that is always met unless q=0 (i.e., $A^{(0)} \alpha I_z$) and $I_i=I_z$. Second, the $S^{(q)}(t)$'s must have a time dependence that counters that of the rapidly varying exponential of Eq. 2.17 (i.e., $\exp(iq\omega_o t)$), because the

contribution of terms in Eq. 2.16 containing such exponentials averages to zero.

The perturbing Hamiltonians $\mathcal{H}_1$ representing the interactions responsible for magnetization relaxation are random operators that vary from spin to spin. When the equations of motion for the I_i (Eq. 2.16) are averaged over the different H_1's, the first term goes to zero and the equations for like spins become (Abragam, 1961):

$$\frac{dI_i^*(t)}{dt} = \frac{-i}{2\hbar^2} \sum_{qq'} e^{i(q'\omega_o + q\omega_o)t} \left[\left[I_i^*(0), A^{(q')} \right], A^{(q)} \right] J_q(q\omega_o). \qquad (2.18)$$

The $J_q(q\omega_o)$ are the spectral density functions which contain the time integrals of the time-dependent spatial operators factored out from Eq. 2.16 (see below). The terms in the above summation only contribute to the dynamics of $I_i^*(t)$ when the exponent of the rapidly varying exponential reduces to zero, i.e., if $q = -q'$. Although it is not obvious from direct inspection, the right hand side of Eq. 2.18 is proportional to I_i^* for most perturbing spin interactions, $\mathcal{H}_1$. Thus, Eq 2.18 is a first order differential equation and the $I_i^*(t)$ relax exponentially as noted previously in the macroscopic Bloch equations. The utility of Eq. 2.18 is that the relaxation is expressed in terms of the spectral densities which encompass the contribution of molecular dynamics to spin relaxation.

Spatial operators and J_q

The spectral density functions, $J_q(q\omega_o)$, represent the Fourier transform of the auto-correlation function $G^{(q)}$ of the spatial operators, that is (Bloembergen *et al.*, 1948; Abragam, 1961):

$$J_q(q\omega_o) = \int_{-\infty}^{\infty} \overline{S^{(q)}(t)\, S^{(-q)}(t+\tau)}\, e^{-iq\omega_o\tau}\, d\tau\,,$$

$$= \int_{-\infty}^{\infty} G^{(q)}(\tau)\, e^{-i\, q\omega_o\tau}\, d\tau\,, \qquad (2.19)$$

where the bar denotes the average over the different $\mathcal{H}_1$ which only depend on times, t and t', through a their difference, τ (=t-t'), the correlation time. The correlation time takes into account the finite duration of the perturbation, and $G^{(q)}(\tau)$ gives the temporal persistence of any particular arrangement of spins relative to each other. Because molecular motions are thermally activated processes, the following Arrhenius relation is often assumed for the correlation times:

$$\tau = \tau_o \exp(E_a/kT)\,, \qquad (2.19b)$$

where E_a is the activation energy for the motion associated with τ and k is Boltzman's constant. Temperature studies of relaxation times, such as those presented in Chapter 6 for BANG polymer gel dosimeters, can be used to investigate the activation energies, correlation times and hence the molecular motions describing a system of spins.

The correlation times and functions, and thus the spectral density functions, are specific to the type of motion experienced by the spins. Furthermore, the magnitudes of the spectral density functions at the frequencies $q\omega_o$ indicate the power made available for relaxation by the spins' motions. For example, if the magnitudes are low then the motions are

ineffective at promoting relaxation and the relaxation times are long. Examples of spectral density functions will be shown below for the specific cases of protons on water undergoing isotropic reorientation (bulk water) and anisotropic reorientation (hydration water) and for protons on polymers.

Spin Operators, $A^{(q)}$

The effect of spin interactions on magnetization relaxation was discussed in Section 2.2.1. It is instructive to further consider how spin interactions contribute to the relaxation of M_{xy} and M_z through the different $A^{(q)}$'s (see Eq. (2.18)). The $A^{(0)}$ operator is responsible for spin-spin interactions that do not cause energy transitions ($q = \Delta m = 0$) and conserve energy. It does not commute with $I_{i=x,y}$, and thus, is partially responsible for the relaxation of M_{xy}. However, it does commute with I_z so that M_z remains constant under the influence of $A^{(0)}$. Thus, the spin-spin operators contribute to the relaxation of M_{xy} or spin-spin relaxation characterized by the spin-spin relaxation time T_2.

The $A^{(q\neq0)}$ operators on the other hand describe the transitions between energy levels ($q = \Delta m \neq 0$) that couple the spin reservoir and the lattice (i.e., permits energy exchange or transitions between eigenstates). The spin-lattice coupling allows the equilibrium populations of eigenstates to be reestablished. Since the $A^{(q\neq0)}$ do not commute with I_z, they promote the longitudinal relaxation of M_z or spin-lattice relaxation characterized by the longitudinal or spin-lattice relaxation time, T_1. The $A^{(q\neq0)}$ also do not commute with the $I_{x,y}$, and thus, are partially responsible for a spin-lattice contribution to transverse relaxation. Because of the additional spin-spin

contribution to transverse relaxation, T_2^{-1} is always greater than or equal to T_1^{-1}.

Spin Interactions

There are a number of possible spin interactions which can cause relaxation: spin-rotational, anisotropic chemical shift, scalar, quadrupolar and dipole-dipole (Noack, 1971; Pfeifer, 1972; Farrar and Becker, 1971; Abragam, 1961). The importance of each depends on the spin environment being considered. The spin-rotational interaction involves the coupling between a nuclear spin and the magnetic moment produced by the electron distribution of a rotating molecule on which the spin exists. It is strongest for small, symmetric molecules in liquids, with water at room temperature, being one of the exceptions (Schreiner, 1978). The anisotropic chemical shift interaction occurs in molecules in which the spin is shielded from H_0 by the chemical environment of the spin (i.e., $H_z = H_0 + \delta H_0$). If the shielding is asymmetric, the spins will see a time-dependent fluctuation in H_z as the molecule rotates and this can drive spin relaxation. While the interaction may be significant in high magnetic fields, it is not important for the aqueous systems and low magnetic field (≤ 0.6 T) used in this work. The scalar interaction is an indirect coupling between intra-molecular nuclear spins mediated through their interactions with the electrons within the molecule. Quadrupole interactions are electric interactions which only occur for nuclei possessing a quadrupolar moment, i.e., with $I>\frac{1}{2}$. Such spins interact with local electric field gradients surrounding the spin. For spin systems consisting of hydrogen nuclei or protons on water molecules and polymers, there is only one spin interaction which is important in determining the spin-relaxation properties: the dipole-dipole interaction between the spins themselves.

2.3 Relaxation Via the Dipole-Dipole Interaction

As outlined in Section 2.2.2, the theory relating T_1 and T_2 to the dynamics and structural properties of a material is developed using a semi-classical analysis of the spin interaction. The analysis considers the pairwise coupling of two spins. The perturbing Hamiltonian representing the interaction between two spins with magnetic moments μ_1 and μ_2 is:

$$\mathcal{H}_1 = \frac{\vec{\mu}_1 \cdot \vec{\mu}_2}{r^3} - \frac{3(\vec{\mu}_1 \cdot \vec{r})(\vec{\mu}_2 \cdot \vec{r})}{r^5}, \tag{2.20}$$

where $\vec{r}$ is the vector between two spins. This can be written in the form of Eq. 2.17 with the time dependent spatial operators and spin operators (Abragam, 1961):

$$\begin{aligned}
S^{(0)} &= \frac{(1-3\cos^2\theta)}{r^3}, & A^{(0)} &= \frac{3}{2}\gamma^2\hbar\left(\frac{2}{3}I_{1z}I_{2z} + \frac{1}{6}\left(I_{1+}I_{2-} + I_{1-}I_{2+}\right)\right) \\
S^{(1)} &= S^{(-1)*} = \frac{\sin\theta\cos\theta\, e^{-i\phi}}{r^3}, & A^{(1)} &= A^{(-1)\dagger} = \frac{3}{2}\gamma^2\hbar\left(I_{1z}I_{2+} + I_{1+}I_{2z}\right), \\
S^{(2)} &= S^{(-2)*} = \frac{\sin^2\theta\, e^{-i2\phi}}{r^3}, & A^{(2)} &= A^{(-2)\dagger} = \frac{3}{4}\gamma^2\hbar\, I_{1+}I_{2+}.
\end{aligned} \tag{2.21}$$

The S^* and $A^\dagger$ represent the complex and hermitian conjugates of S and A, respectively, and the subscripts of I_1 and I_2 refer to each of the two spins. The equations of motion of the I_i's can be derived by substituting Eq.'s 2.21 into Eq. 2.18 (recall that Eq. 2.18 relates the time derivative of $I_i^*(t)$ to $A^{(q)}$ and $J_q(q\omega_o)$). Then, for two like spins (Abragam, 1961):

$$\frac{d}{dt}\overline{\langle I_{1z} + I_{2z}\rangle^*} = -\frac{1}{T}\left(\overline{\langle I_{1z} + I_{2z}\rangle^*} - \overline{\langle I_{1z} + I_{2z}\rangle_o^*}\right), \text{ and} \tag{2.22}$$

$$\frac{d}{dt}\overline{\langle I_{1x} + I_{2x}\rangle^*} = -\frac{1}{T'}\left(\overline{\langle I_{1x} + I_{2x}\rangle^*}\right), \tag{2.23}$$

where * denotes the interaction representation. The inverse of the relaxation time constants (i.e., the relaxation rates) are given by:

$$\frac{1}{T} = \frac{3}{2}\gamma^4\hbar^2 I(I+1)\{J_1(\omega_o) + J_2(2\omega_o)\}, \text{ and} \tag{2.24}$$

$$\frac{1}{T'} = \gamma^4\hbar^2 I(I+1)\left\{\frac{3}{8}J_0(0) + \frac{15}{4}J_1(\omega_o) + \frac{3}{8}J_2(2\omega_o)\right\}. \tag{2.25}$$

The last term in Eq. 2.22, $\overline{\langle I_{1z}+I_{2z}\rangle^*_o}$, is the equilibrium value of the spin operators and I in Eq.'s 2.24 and 2.25 is the total spin (= I_1 = I_2). By comparing Eq.'s 2.22 and 2.23 to the Bloch equations, Eq.'s 2.11 and 2.12, and recalling that the macroscopic magnetizations are proportional to the averaged expectation values of the spin operators, one can identify $T = T_1$ and $T' = T_2$ directly.

As mentioned earlier, the spectral density functions, $J_q(q\omega_o)$, contain the dependence of the relaxation times on the relative motions of the spins and the Larmor frequency. This dependence is discussed in further detail.

2.4 Dipolar Relaxation and Molecular Motions

In this section we will illustrate the connection between spin relaxation and molecular dynamics by considering specific examples relevant to this thesis, i.e., the relaxation of protons on water molecules in the bulk (Section 2.4.1) and hydrating large molecules (Section 2.4.2) and of protons on polymer molecules (Section 2.4.3).

2.4.1 Bulk Water and Isotropic Motion

One component of the dipolar relaxation of protons on a water molecule results from the intra-molecular dipolar interaction between the two protons on the same water molecule. In the bulk (i.e., free water) the water molecules reorient isotropically. For this random isotropic motion of spins the correlation function $G^{(q)}(t)$ is assumed to be of the form (Bloembergen *et al.*, 1948; Abragam, 1961):

$$G^{(q)}(\tau) = \overline{\left|S^{(q)}(0)\right|^2}\, e^{-\tau/\tau_c}, \tag{2.26}$$

where τ_c is the reorientational correlation time. Roughly, it can be taken as the time required for the molecule to rotate ~1 radian (Homans, 1989). According to Eq. 2.26 the spatial correlation of spins vanishes with time, i.e., $G^{(q)}(\tau) \Rightarrow 0$ as $\tau \Rightarrow \infty$. Thus, the longer is τ_c, the slower are the spin motions, and the longer the spins retain memory of their previous positions. In evaluating Eq. 2.19 the motion is averaged over the whole solid angle. Substituting Eq. 2.26 into Eq. 2.19 gives,

$$J_q(q\omega_o) = \overline{\left|S^{(q)}(0)\right|^2}\, \frac{\tau_c}{1 + (q\omega_o)^2\tau_c^2}, \tag{2.27}$$

where $\overline{\left|S^{(q)}(0)\right|^2} \propto r^{-6}$. Using Eq.'s 2.26 and 2.27, the resulting relaxation rates for intra-molecular relaxation of water molecules are (Bloembergen *et al.*, 1948; Solomon, 1955):

$$\frac{1}{T_1} = \frac{3}{10}\frac{\hbar^2\gamma^4}{r^6}\left[\frac{\tau_c}{1 + \omega_o^2\tau_c^2} + \frac{4\tau_c}{1 + 4\omega_o^2\tau_c^2}\right], \text{ and} \tag{2.28}$$

$$\frac{1}{T_2} = \frac{3}{20}\frac{\hbar^2\gamma^4}{r^6}\left[3\tau_c + \frac{5\tau_c}{1 + \omega_o^2\tau_c^2} + \frac{2\tau_c}{1 + 4\omega_o^2\tau_c^2}\right]. \tag{2.29}$$

The dependence of the spin relaxation times on the time scale of the motions, characterized by their correlation times τ_c, is indicated in Fig. 2.1. The figure shows the spectral densities for three different τ_c values and also curves relating T_1 and T_2 to the correlation times (commonly called Bloembergen, Pound and Purcell (BPP) plots (Bloembergen *et al.*, 1948)). The BPP plots were calculated from Eq.'s 2.28 and 2.29 for $\nu_o = \omega_o/2\pi = 20$ MHz. There are three main regimes for the molecular dynamics as observed by the spin relaxation:

i) $\tau_c\omega_o \ll 1$: Here the relative motions between spins are fast, the values of the spectral density at 0, ω_o and $2\omega_o$ are small, T_1 and T_2 are long and $T_2 \sim T_1$. Motions in this regime are often called white non-dispersive motions since the relaxation times are not strongly dependent on the value of ω_o.

ii) $\tau_c\omega_o \geq 1$: As $\tau_c\omega_o$ increases, the molecular dynamics slow and $J_1(\omega_o)$ and $J_2(2\omega_o)$ increase so that T_1 ($\propto J_1(\omega_o) + J_2(2\omega_o)$) decreases and becomes a minimum when $\tau_c\omega_o \sim 1$. Furthermore, $J_0(0)$ increases so that T_2^{-1} ($\propto J_0(0) + J_1(\omega_o) + J_2(2\omega_o)$) exceeds T_1^{-1}.

iii) $\tau_c\omega_o \gg 1$: In the rigid lattice regime, the dipolar interactions are no longer motionally averaged as in the other two regimes, $\tau_c > T_2$, T_2 is independent of temperature and spin-lattice relaxation is extremely inefficient.

Note that the actual spin-relaxation of bulk water is somewhat different than the relaxation idealized in Fig. 2.1. First, the correlation time does not decrease continuously from $\tau_c \sim 10^{-12}$ to 10^{-4} s since, at some point,

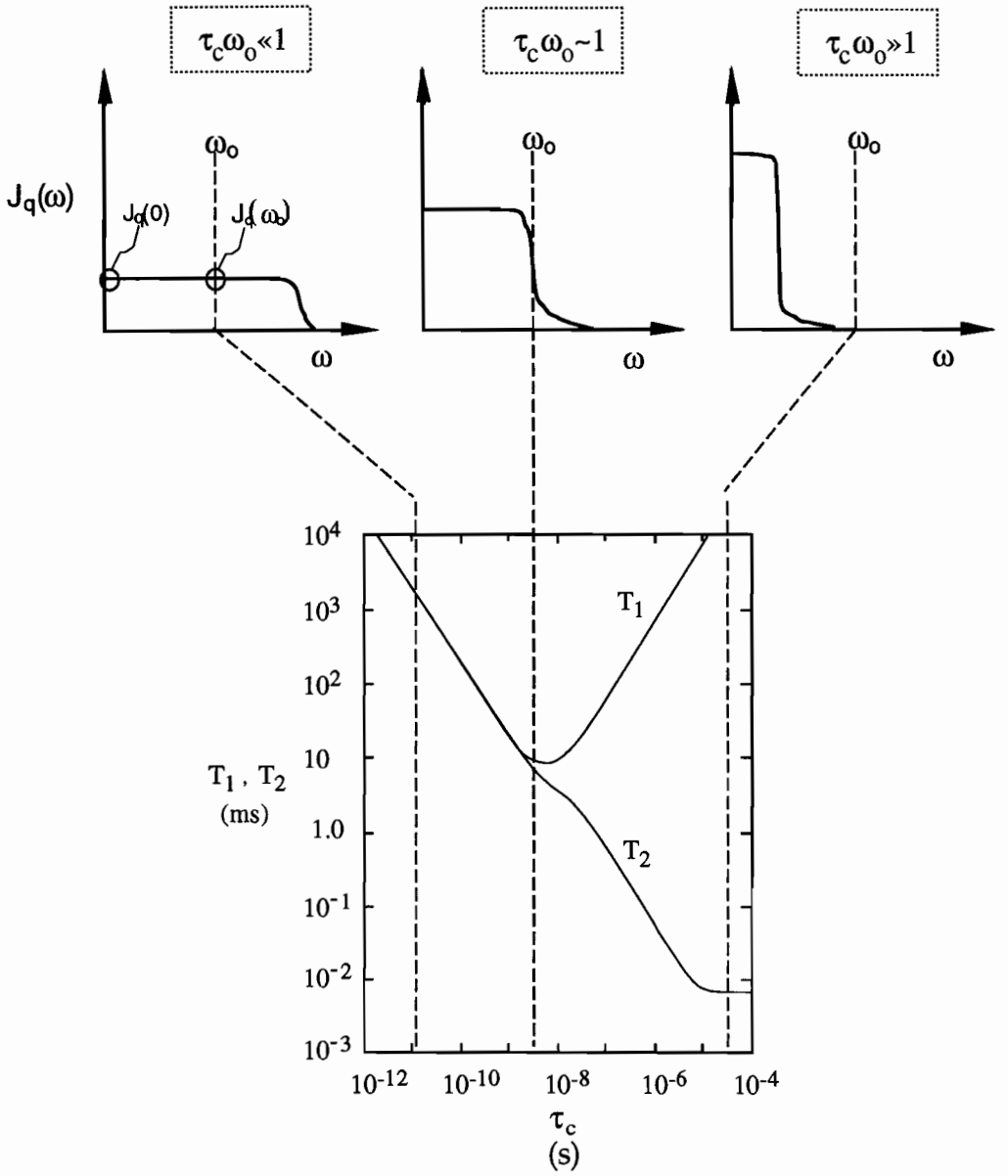

Figure 2.1 The top figures illustrate the change of the spectral density functions, $J_q(\omega)$, as the lattice dynamics slow down (left to right figures) and are characterized by longer τ_c's. The effect of changes in $J_q(\omega)$ with τ_c on the spin relaxation times is shown in the bottom plot.

there is a freezing transition which produces an abrupt change in τ_c and hence discontinuities in the T_1 and T_2 curves. Second, in bulk water there is an additional contribution to the spin relaxation resulting from inter-molecular interactions between protons on different water molecules as the molecules undergo translational diffusion (Bloembergen *et al.*, 1948; Abragam, 1961). The observed relaxation rate is the sum of the intra-molecular and inter-molecular terms:

$$\frac{1}{T_{1,2}} = \left(\frac{1}{T_{1,2}}\right)_{rot} + \left(\frac{1}{T_{1,2}}\right)_{trans}, \qquad (2.30)$$

where the rotation term is given by the relaxation rates in Eq.'s 2.28 and 2.29. In general the translational term does not have the same form as $(1/T_{1,2})$rot. However, if this motion is describable through an Arrhenius law, a BBP plot for bulk water in which both isotropic rotational and translational motions exist is similar to that shown for the isotropic reorientation. At room temperature, the diffusion and rotation correlation times are both of the order of 10^{-12} - 10^{-11} s^{-1}, $\tau_c\omega_o \ll 1$, and the values of T_1 and T_2 are both of the order of seconds.

2.4.2 Hydration Water and Anisotropic Motion

The water in many aqueous systems is not all bulk water, but is hydrating sites on large molecules or surfaces. This hydration water may be hydrogen bonded to the large molecule so that the molecular dynamics are modulated by this bonding; in particular, the reorientation of the water molecule becomes anisotropic. The anisotropic motion of hydration water can be broken down into a fast rotation about the axis of a hydrogen bond described by a correlation time, τ_f, and a much slower reorientation of the fast

rotation axis described by correlation time, τ_s (Woessner, 1962; Shirley and Bryant, 1982; Schreiner *et al.*, 1991).

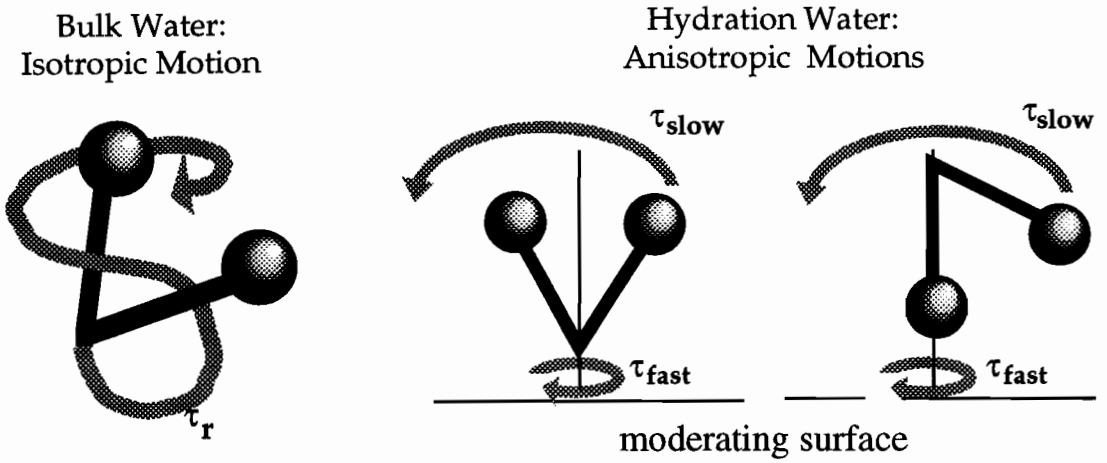

Figure 2.2 Schematic of bulk and hydration water undergoing isotropic and anisotropic motion, respectively (the spheres represent the hydrogen atoms or protons on the water molecule). Anisotropic motions include fast rotation about the hydrogen bond and slower tumbling of the molecule. A water proton may rotate about the hydrogen bond such that the angle Δ between the intra-proton vector and the bond (represented by the vertical line) is 90° (middle schematic) or about 38° (schematic on the right).

The spin-relaxation for hydration water experiencing anisotropic motion differs from that for spins undergoing isotropic motion for many reasons. First, the correlation function for the anisotropic motion reflects the more complex dynamics (Woessner, 1962):

$$\begin{aligned} G^{(q)} &= \overline{S^{(q)}(t)\ S^{(q)}(t+\tau)}, \\ &= k_q\left(A e^{-\tau/\tau_s} + B e^{-\tau/\tau_1} + C e^{-\tau/\tau_2} \right). \end{aligned} \tag{2.31}$$

The correlation times τ_1 and τ_2 are weighted sums of inverse slow and fast correlation times: $\tau_1^{-1} = \tau_f^{-1} + \tau_s^{-1}$ and $\tau_2^{-1} = 4\tau_f^{-1} + \tau_s^{-1}$. The k_q's are constants (i.e., $k_0 = 4/5$, $k_1 = 2/15.$, $k_2 = 8/15$). The A,B and C are geometric

factors that depend on the angle, Δ, of the intra-proton vector with the axis of fast rotation (i.e., $\Delta = 90°$ or 38°; see Fig. 2.2). For example, $A = \frac{1}{4}(3\cos^2\Delta\text{-}1)^2 = 1$ for $\Delta = 90°$. The geometric factors are determined by averaging the spatial operators over these portions of the solid angle covered by motion specific to each correlation time. They differ from the $\overline{|S^{(q)}(0)|^2}$ factors for isotropic motion (Eq. 2.26) which are averaged over the whole solid angle. The spectral densities $J_q(q\omega_o)$ are calculated from the Fourier transforms of the $G^{(q)}$'s (see Eq. 2.19) and also contain three components, one for each correlation time, weighted by the geometric factors. The relaxation rates are again given by Eq.'s 2.24 and 2.25 for the new $J_q(q\omega_o)$. The rates are (Woessner, 1962; Shirley and Bryant, 1982; Schreiner *et al.*, 1991):

$$\frac{1}{T_1} = \frac{3}{10}\frac{\gamma^4\hbar^2}{r^6}\left[\, A\, \mathbf{D}_1(\tau_s) + B\, \mathbf{D}_1(\tau_1) + C\, \mathbf{D}_1(\tau_2)\,\right], \text{ and}$$
$$\frac{1}{T_2} = \frac{3}{20}\frac{\gamma^4\hbar^2}{r^6}\left[\, A\, \mathbf{D}_2(\tau_s) + B\, \mathbf{D}_2(\tau_1) + C\, \mathbf{D}_2(\tau_2)\,\right]' \qquad (2.32)$$

where $\mathbf{D}_1(\tau)$ and $\mathbf{D}_2(\tau)$ designate the Debye terms:

$$\mathbf{D}_1(\tau) = \frac{\tau}{1+\tau^2\omega_0^2} + \frac{4\tau}{1+4\tau^2\omega_0^2}, \text{ and}$$
$$\mathbf{D}_2(\tau) = 3\tau + \frac{5\tau}{1+\tau^2\omega_0^2} + \frac{2\tau}{1+4\tau^2\omega_0^2}. \qquad (2.33)$$

Figure 2.3 shows the resulting BPP plots for the spin relaxation times of the anisotropically reorienting water along with the isotropic case for comparison. The anisotropic times were calculated using Eq. 2.32 with $\nu_o = \omega_o/2\pi = 20$ MHz. The probability between the 90° and 38° orientations of the intra-proton vector were assumed to be equal (see Fig. 2.2) and τ_s was taken to be $100\tau_f$. Unlike the curve for isotropic motion, the curve for anisotropic motion possesses two minima due to the large discrepancy in the

magnitude of τ_s and the magnitudes of τ_1 and τ_2 which are of the same order of magnitude as τ_f. These minima illustrate the superposition of effects of different motions on T_1^{-1}.

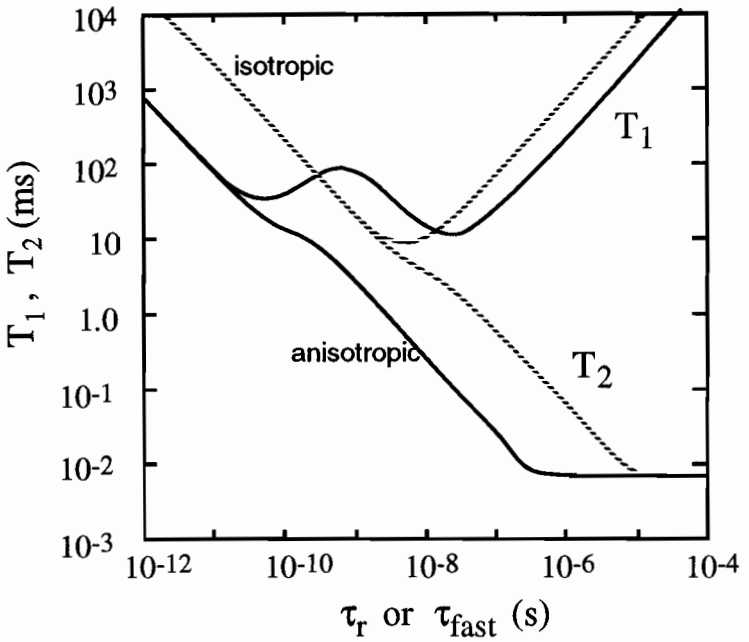

Figure 2.3 BPP plots for spin lattice and spin-spin relaxation of intra-molecular water protons undergoing isotropic and anisotropic reorientation.

It is also apparent from Figure 2.3 that spin-lattice relaxation for hydration water undergoing anisotropic motion is more efficient (i.e., T_1 is less) than that for bulk water. This is a result of the increased efficiency of the spin-lattice relaxation due to the slower correlation time τ_s. While the above BPP plots are again somewhat idealized, this T_1 behavior is, in fact, observed. At room temperature bulk water has a T_1 of ~ 1-2 s while hydration water has T_1 of ~ 100 ms in low hydration samples of DNA (Schreiner, 1985) and polyacrylamide (Zhang, 1990), and T_1 ~ 350 ms in tissue (Sobol and Pintar, 1987). Note that at room temperature, the τ_{fast} of water undergoing anisotropic motion is actually ~3 orders of magnitude longer than the τ_c of bulk water (Schreiner *et al.*, 1991).

Figure 2.3 also shows the spin-spin relaxation to be more efficient for hydration water than for isotropically reorienting bulk water. Spin-spin relaxation is more efficient for slow motions in general, since T_2^{-1} is proportional to τ (see Eq.'s 2.29 and 2.33) and in particular, for anisotropic systems in which the dipolar interactions are not averaged out completely. The T_2's of bulk water are of the order of 1-20 seconds whereas the T_2's of water undergoing anisotropic motion can be as short as 100 μsec (Schreiner *et al.*, 1991; Zhang, 1990).

2.4.3 Polymers

Polymers are macromolecules consisting of repeating units or monomers. The dipolar relaxation of protons along the polymer can be modeled by considering three types of polymer motions (Kimmich, 1977a,b). These motions are 1) the anisotropic motion of short segments whose ends are defined by kinks or defects in the polymer molecule and perhaps by side chains, 2) the longitudinal diffusion of defects along the molecule, and 3) the fluctuations in the overall configuration of the polymer molecule. These are characterized by the correlation times τ_s, τ_l and τ_f, respectively. The first motion is a fast local motion whereas the last two are slower and are determined by the long range dimensions of the molecule. The longitudinal diffusion correlation time is often assumed to be the average of a distribution of such correlation times. The correlation times have the following dependencies on the polymer molecular weight, M_W: τ_s = constant, $\tau_l \alpha M_W$ and $\tau_f \alpha M_W^3$. The relative magnitudes of the correlation times are $\tau_f > \tau_l > \tau_s$ (Kimmich *et al.*, 1977b). Each component of motion is considered to be largely independent of the others and, as a result, the total correlation function can

be taken as the product of the correlation functions for the three motions (Kimmich, 1977b):

$$G_T^{(q)} = G_s^{(q)} G_l G_f . \qquad (2.34)$$

The total spectral density, the Fourier transform of the total correlation function will equal the sum of the spectral densities for the component correlation functions. Hence, the contributions of each type of motion to the relaxation rates will be superimposed. Furthermore, for a specific frequency ω_o, spin-lattice relaxation will be dominated by those motions that best satisfy the condition $\tau\omega_o \sim 1$ while spin-spin relaxation will be determined primarily by the slowest motion (i.e., the longest τ). This condition for efficient spin-lattice relaxation is best satisfied by slower motions if the T_1's fall on the left side of the T_1 minimum in a BPP plot (i.e., $\tau\omega_o < 1$). Conversely, the condition is best satisfied by faster motions if the T_1's fall on the right side of the T_1 minimum in a BPP plot (i.e., $\tau\omega_o > 1$).

Experimental BPP plots for polymer protons are shown in Fig. 2.4 in terms of inverse temperature, β=1000/T, which is related to τ (see Section 2.2.2). It is evident that at higher temperatures, T_2 depends strongly on the molecular weight of the polymer whereas T_1 does not. This behavior indicates that transverse relaxation is dominated by the slower long range motions whereas longitudinal relaxation is dominated by the faster local motions. The BPP plot for T_1 exhibits a single broad minimum even though the polymer motions are described by several correlation times. This is typical for motions characterized by distributions of correlation times since the result of superimposing many minimums is a single broad minimum (Noack, 1971).

Also apparent in Fig. 2.4 is a decrease in the temperature dependence of T_2 with molecular weight. This indicates that molecular entanglements introduce a solid phase in which dipolar interactions cannot be motionally averaged. This is particularly pertinent to polyacrylamide gels. They possess physical crosslinks similar to entanglements that can restrict the motion of the polymer and contribute to transverse relaxation through dipolar broadening.

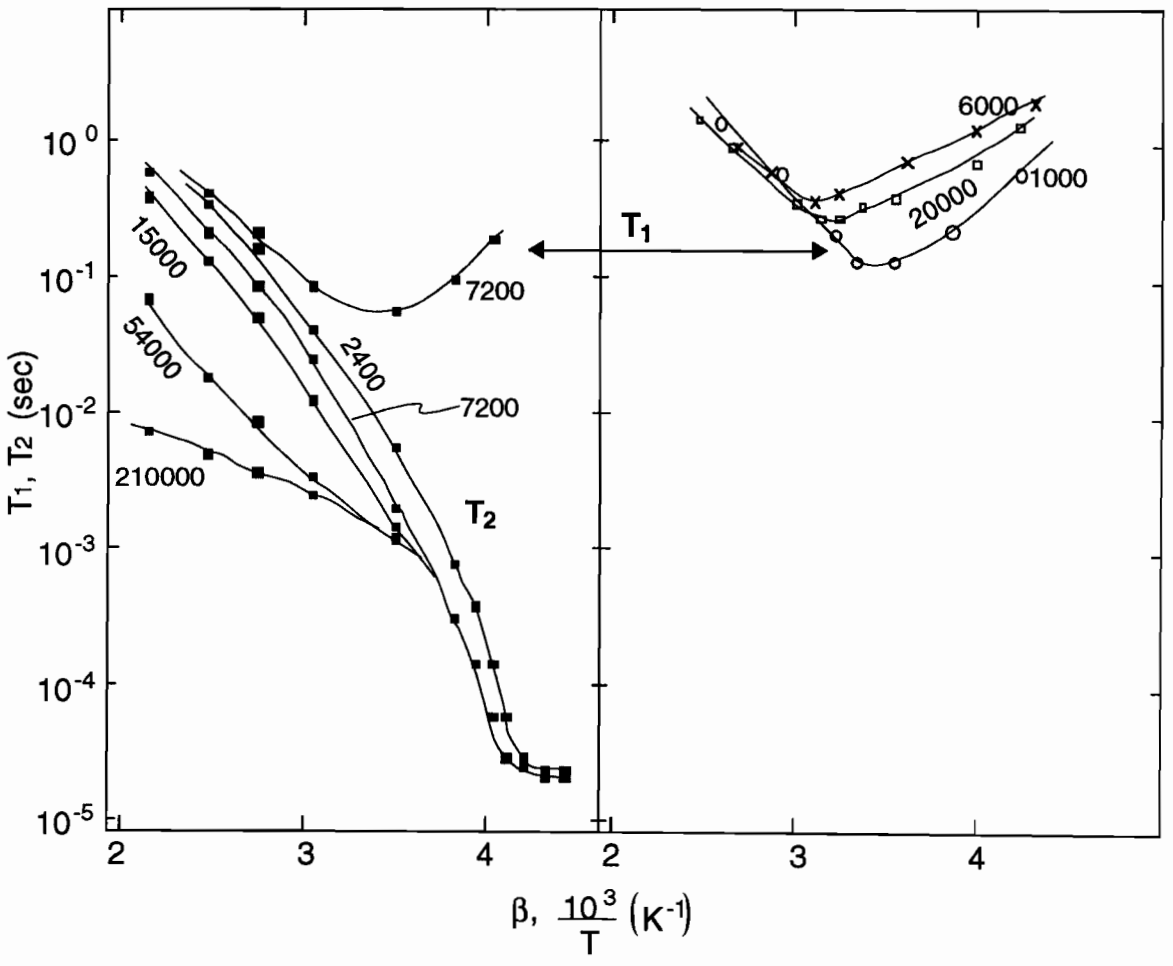

Figure 2.4 The BPP plots for different molecular weight samples of a) cis-polyisoprene (adapted from Charlesby and Folland, 1980) and b) poly(ethylene oxide) (adapted from Allen, 1967). The numerical labels on the curves indicate the molecular weight of the polymer.

2.5 Paramagnetic Relaxation of Water Protons

Early in the development of NMR it was noted that the proton spin-relaxation of many systems could be enhanced considerably by the introduction of paramagnetic centers (Bloembergen *et al.*, 1948; Pound, 1953). The relaxation mechanism for these systems remains a dipolar interaction, however, it is between a proton and the large magnetic moment of the unpaired electron associated with the paramagnetic center ($\gamma_e = 658\,\gamma_p$). For water hydrating a paramagnetic ion (with spin S), the protons (with spin I) relax with rates (Solomon, 1955):

$$\frac{1}{T_1} = \frac{2}{15}\frac{\hbar^2\gamma_I^2\gamma_S^2\,S(S+1)}{r^6}\left[\frac{\tau_c}{1+(\omega_I-\omega_S)^2\tau_c^2}+\frac{3\tau_c}{1+\omega_I^2\tau_c^2}+\frac{6\tau_c}{1+(\omega_I+\omega_S)^2\tau_c^2}\right], \qquad (2.35)$$

$$\frac{1}{T_2} = \frac{1}{15}\frac{\hbar^2\gamma_I^2\gamma_S^2\,S(S+1)}{r^6}\,x \qquad (2.36)$$

$$\left[4\tau_c+\frac{\tau_c}{1+(\omega_I-\omega_S)^2\tau_c^2}+\frac{3\tau_c}{1+\omega_I^2\tau_c^2}+\frac{6\tau_c}{1+\omega_S^2\tau_c^2}+\frac{6\tau_c}{1+(\omega_I+\omega_S)^2\tau_c^2}\right],$$

where ω_S and ω_I are the resonant frequencies for electrons and protons, respectively, and r is the ion to proton distance. Equations 2.35 and 2.36 account only for the dipolar interaction between the proton and the electron, and neglect the contact hyperfine interaction. The latter interaction may be important for the spin-spin relaxation of ferric and ferrous ions (Duzenli, 1995), but can be neglected for spin-lattice relaxation (Gore *et al.*, 1984).

Recalling that the correlation time τ_c reflects the temporal persistence of the spins we can write:

$$\frac{1}{\tau_c} = \frac{1}{\tau_r}+\frac{1}{\tau_h}+\frac{1}{\tau_s}, \qquad (2.37)$$

where τ_r is the rotational correlation time associated with the tumbling of the hydrated ion and τ_h is the correlation time accounting for the exchange of protons to and from the ion. The electron spin relaxation time, τ_s, characterizes the electron spin flip-flop rate resulting from the interaction between the paramagnetic centers themselves. According to Eq. 2.37, the value of τ_c is dominated by the fastest process. The exchange process is very slow, and may be neglected. The rotational correlation time τ_r is of the order of $\sim 10^{-11}$ s and does not vary much from one ionic species to the next. The electron spin relaxation time τ_s has similar order of magnitude as τ_r, however, it can vary greatly for different ions. Although the spin *S* and the distance r differ for different ions, it is the variation of τ_s that is largely responsible for the differences in the ability of different ions to enhance proton relaxation in aqueous solutions (Gore *et al.*, 1984).

The basis of the ferrous sulfate-doped gel dosimeters considered in this thesis relies on the difference in the ability of the Fe^{2+} and Fe^{3+} ions to relax hydrating water protons. Table 2.1 contains some of the parameters required to calculate the spin-spin and spin-lattice relaxation rates, ($R_1 = 1/T_1$ and $R_2 = 1/T_2$, respectively) for water hydrating the Fe^{2+} and Fe^{3+} ions (Eq.'s 2.35 and 2.36) and for bulk water (Eq.'s 2.28 and 2.29). The ratios of the rates are shown in Table 2.2 for comparison. Since the ionic radii and the radius of a water molecule are of the order of 1 Å and 2 Å, respectively, the ratios in Table 2.2 involving the ion to proton distances and the intra-molecular water proton distance will not change the magnitude of the ratios of the rates significantly. It is apparent that Fe^{3+} ions are more efficient at relaxing hydration water than Fe^{2+} ions, the efficiency being greater for spin-spin relaxation than spin-lattice relaxation. The main reason for the greater efficiency of Fe^{3+} ions is that $\tau_c^{3+}/\tau_c^{2+} = 34$. The ratios of relaxation rates for

hydrating water to that for bulk water are very high, indicating that dipolar relaxation between electron spins and protons is much more efficient than that between water protons.

Table 2.1 The spin and characteristic correlation times for the different dipolar species.

	spin	τ_c (sec) at 27°C
Fe^{2+}	S=2	[b] 1.5×10^{-12}
Fe^{3+}	S=5/2	[b] 5.1×10^{-11}
[a] H_2O	I=1/2	[c] 1.7×10^{-11}

[a] for simplicity, only the isotropic contribution to relaxation is considered (Eq.'s 2.26, 2.27 and 2.31); the diffusion contribution, which is of the same order of magnitude, is neglected for the purpose of the qualitative intercomparison of rates.
[b] Eisinger *et al.*, 1962
[c] Schreiner, MSc thesis 1978

Table 2.2 Different inherent relaxation rate ratios for $\nu_o = 25$ MHz and 27°C. The r^{2+} and r^{3+} are the distances between the ferrous and ferric ions, respectively and the water protons, and b is the intramolecular proton-proton distance.

	Ratios of Relaxation Rates		
spin-lattice relaxation	$\frac{R_1^{3+}}{R_1^{2+}} \sim 14.8\left(\frac{r^{2+}}{r^{3+}}\right)^6$	$\frac{R_1^{2+}}{R_1^{water}} \sim 10^5\left(\frac{b}{r^{2+}}\right)^6$	$\frac{R_1^{3+}}{R_1^{water}} \sim 10^6\left(\frac{b}{r^{3+}}\right)^6$
spin-spin relaxation	$\frac{R_2^{3+}}{R_2^{2+}} \sim 18.6\left(\frac{r^{2+}}{r^{3+}}\right)^6$	$\frac{R_2^{2+}}{R_2^{water}} \sim 10^5\left(\frac{b}{r^{2+}}\right)^6$	$\frac{R_2^{3+}}{R_2^{water}} \sim 10^6\left(\frac{b}{r^{3+}}\right)^6$

2.6 Relaxation in Heterogeneous Spin Systems

Thus far, the discussion of spin relaxation has been limited to homogeneous spin systems in which all the spins are considered to be in identical environments, e.g., protons on bulk water molecules. In fact, most spin systems are heterogeneous, and the spins exist in environments where they may experience different interactions or undergo different motions on different time scales. The protons in the ferrous sulfate doped gelatin gel dosimeters exist in four distinct spin groups: 1) on the gelatin macromolecule, 2) on water molecules hydrating the ions and 3) the gelatin, and 4) on free or bulk water molecules. The aqueous solutions of polyacrylamide and gelatin contain polyacrylamide protons, gelatin protons, water protons hydrating the polyacrylamide and gelatin, and bulk water. As noted above, these different groups of protons will have very different relaxation properties.

Each of the spin groups has inherent relaxation properties determined by the molecular dynamics and spin couplings experienced by the spins. If the spin groups are not isolated, an exchange of magnetization information may occur between the spin groups so that the observed or apparent relaxation may differ from the inherent relaxation. The simple Bloch equations (Eq. 2.9) may no longer express the magnetization evolution of the heterogeneous spin system wherein some form of exchange occurs. This exchange may proceed in a number of manners. There may be a physical transfer of spins from one spin group to another (i.e., water molecules diffusing from the hydration layers around macromolecules or paramagnetic ions to the bulk environment). Protons may actually be mixed between environments through the chemical exchange between different molecules (i.e., an NH group and a water molecule may exchange protons) (Schreiner *et al.*, 1991;

and Lynch *et al.*, 1983). Also, magnetic coupling may occur arising from the simultaneous spin flips induced by the dipolar interaction between two nuclei of different spin groups. The spin flips are analogous with the action of the spin operator $A^{(0)}$ (see Eq. 2.23).

The influence of exchange on the observed spin relaxation can be illustrated by considering the simple example of a heterogeneous system with spins existing in two different environments (a and b). The fraction of spins in each environment is p_i and the inherent relaxation rate for that environment is R_i. When exchange occurs there are additional terms in the Bloch equation to account for the loss or gain of the magnetization caused by the exchange (Zimmerman and Brittin, 1957; Schreiner, 1985). For example, the longitudinal Bloch equation (Eq. 2.11) for the 'a' group becomes:

$$\frac{dM_{za}}{dt} = R_{1a}\left(M_{oa} - M_{za}(t)\right) - k_a M_{za}(t) + k_b M_{zb}(t)\,, \qquad (2.38)$$

with a corresponding equation for M_{zb}. The k_a and k_b are the exchange rates specifying the rate at which the magnetization is exchanged between the two groups. Thus, the magnetization evolution of the two groups is described by two coupled differential equations. The observed total magnetization will evolve as:

$$\frac{M_z - M_o}{M_o} = C^+ e^{-\lambda^+ t} + C^- e^{-\lambda^- t}\,. \qquad (2.39)$$

The total magnetization ($M_{az} + M_{bz}$) still evolves as a two component magnetization. However, the apparent rates λ^+ and λ^- are complex functions of inherent spin-relaxation rates and of the exchange rates (Zimmerman and Brittin, 1957):

$$\lambda^{\pm} = \frac{1}{2}\left(R_a + R_b + k_a + k_b\right) \pm \left(\left(R_a - R_b + k_a - k_b\right)^2 + 4k_a k_b\right)^{1/2}\,. \qquad (2.40)$$

Similarly the apparent magnetization fractions C^+ and C^- of the evolution associated with λ^+ and λ^- are complex functions of p_a, p_b, R_a, R_b, k_a and k_b.

The effects of the exchange will depend on the efficiency of the exchange processes, i.e., on the magnitude of k_a and k_b. The exchange can be categorized into three regimes i) slow, ii) intermediate and iii) fast (see Fig. 2.5):

i) If the exchange rates are slow compared to the inherent relaxation rates (i.e., $k_{a,b} \ll R_{a,b}$) then the observed relaxation rates are equivalent to the inherent relaxation rates (i.e., $\lambda^+ = R_a$ and $\lambda^- = R_b$), $C^+ = p_a$ and $C^- = p_b$. Thus, the parameters characterizing the observed magnetization evolution are the inherent magnetization fractions and relaxation rates.

ii) For the intermediate exchange regime, $k_{a,b} \sim R_{a,b}$, and the observed rates and magnetization fractions remain complicated functions of the inherent relaxation rates and exchange rates. It is apparent from Fig. 2.5 that the exchange causes the apparent relaxation rates to increase relative to the inherent rates.

iii) For the fast exchange regime, $k_{a,b} \gg R_{a,b}$, the magnetization equations reduce to a single exponential form:

$$M(t) - M_o = (p_a + p_b)\, e^{-\lambda^- t} \quad . \tag{2.41}$$

The observed rate becomes the average of the inherent relaxation rates

weighted according to the relative sizes of the two spin groups, p_a and p_b, that is,

$$\lambda^- = p_a R_a + p_b R_b \ . \tag{2.42}$$

This solution may easily be extended to more than two spin groups as follows:

$$\lambda^- = \sum_i p_i R_i \ , \tag{2.43}$$

in which the p_i is the fraction of spins in each of the environments in the system.

In the above discussion it has been assumed that both spin groups resonate at the same frequency, and that there is no chemical shift between the two groups (i.e., $\Delta\omega = \omega_a - \omega_b = 0$). In the presence of a chemical shift the expressions for the magnetization evolutions are cumbersome and difficult to interpret. However, under the fast exchange regime spin-lattice relaxation is identical to that in the absence of a shift (Eq. 2.42), and spin-spin relaxation is described by (Zhong *et al.*, 1989),

$$\lambda_2^- = p_a R_{2a} + p_b R_{2b} + \frac{p_a p_b k_a k_b}{k_a + k_b} (\Delta\omega)^2 \ . \tag{2.44}$$

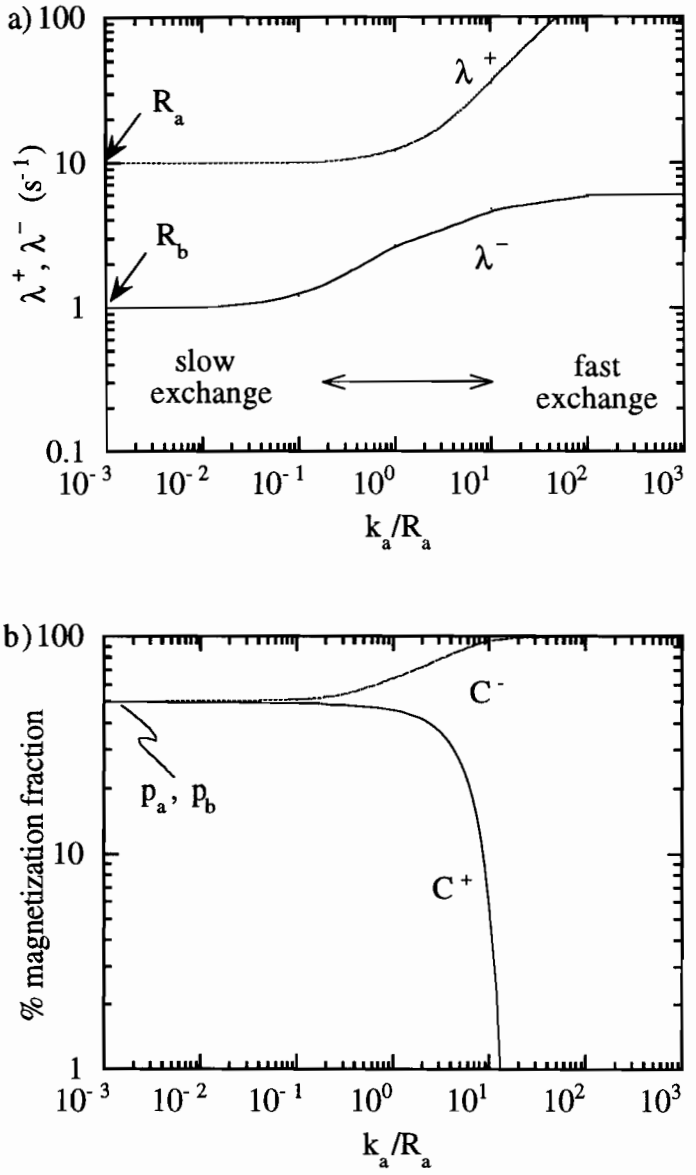

Figure 2.5 Apparent relaxation rates (a) and magnetization fractions (b) for a two spin group system as a function of the exchange rate k_a between the groups (normalized to R_a). the inherent conditions were taken as $R_a=1s^{-1}$, $R_b=10s^{-1}$ and $p_a=p_b=50\%$. At low k_a the relaxation parameters are identical to the inherent relaxation parameters. In the fast exchange limit ($k_a \gg R_a$) only one magnetization component is observed with $\lambda^{-1}=p_aR_a + p_bR_b$ since the value of C+ approaches zero.

2.7 Summary

In this chapter , the relationships between proton NMR spin relaxation times and molecular motions have been outlined. This relationship was derived from the time dependence of the spatial operators describing the dipolar interaction between spins. It was shown that spin-spin relaxation is more efficient for protons experiencing slower and/or anisotropic motions mainly because $T_2^{-1} \alpha J_0(0) \alpha \tau$ and because the slow motion component of anisotropic motion dominates spin-spin relaxation. Spin-lattice relaxation is most efficient for motions satisfying the condition $\tau\omega_o \sim 1$. For the systems studied in this thesis the molecular motions are relatively fast at room temperature such that the inherent T_1's are found on the left side of the T_1 minimum in a BPP plot (i.e., $\tau\omega_o < 1$). Hence, within the range of fast motions, the slower and/or anisotropic motions dominate spin-lattice relaxation. All of these aspects of relaxation have a number of implications for the dosimeter systems studied in this work.

Consider the BANG polymer gel dosimeter studies made at ν_o=25 MHz in the temperature range of 5-40°C. One can expect that bulk water protons, monomer protons and water protons hydrating the monomer to all have relatively long T_1's and T_2's because these are all small molecules undergoing relatively fast and isotropic reorientation. For the protons on water hydrating the gelatin and polymer, shorter T_1's and T_2's can be expected as the motions are slower and more anisotropic. The T_1's and T_2's of gelatin and polymer protons are expected to be even shorter. In the presence of the exchange between the different proton groups the relaxation rate observed for bulk water (the major constituent of the dosimeter) will be increased. The basis for the BANG polymer gel dosimeter is that the monomer and polymer affect the

relaxation of the bulk water differently and that the relaxation rate of bulk water will change with dose as monomer is converted to polymer. Spin relaxation in the BANG polymer gel dosimeter will be discussed and studied in more detail in Chapters 3 and 6.

It was also shown that spin relaxation is enhanced by paramagnetic species. Furthermore, the spin relaxation of water hydrating Fe^{3+} ions is greater than that of water hydrating Fe^{2+} ions. This provides the basis of the ferrous sulfate-doped gel dosimeter since the Fe^{3+} and Fe^{2+} ions affect the bulk water relaxation differently so that the apparent relaxation rates of the dosimeter will change with dose as Fe^{2+} ions are converted to Fe^{3+} ions. The spin relaxation of the ferrous-sulfate doped gelatin dosimeter will be discussed in more detail in Chapters 3 and 5.

CHAPTER THREE

Background: Gel Dosimeters

The background necessary to understand the gel dosimeters used for the MR imaging of three dimensional (3-D) dose distributions is presented in this chapter. Section 3.1 introduces some radiation dosimetry concepts common to chemical dosimeters, in general, and to the gel dosimeters, in particular. The chemistry and physics of the 3-D gel dosimeters of interest, the ferrous sulfate doped gel dosimeters and the polymer gel dosimeters, are described in Sections 3.2 and 3.3, respectively.

3.1 Radiation Dosimetry

3.1.1 Chemical Dosimetry

When radiation interacts with a medium it loses some of its energy producing highly unstable ionized and excited atoms and molecules in the medium. These products can further react with the other molecules in the medium to produce free radicals and secondary ions. The radicals and ions may then react to form stable chemical products.

Chemical dosimetry is the determination of absorbed dose from a quantification of the radiation induced chemical changes. The sensitivity of a chemical dosimeter is gauged by the radiation chemical yield G(x) for a

product, x, and is analogous to the inverse of the mean energy absorbed per ion pair, 1/W, used in ionization chamber dosimetry. The chemical yield as defined in ICRU Report No. 33 (1980) is the mean amount of product divided by the mean energy imparted to the dosimeter, and its SI units are mol J^{-1}. However, the traditional definition for yield employed in this thesis for the ferrous sulfate-doped gels is the mean number of product entities produced per 100 eV (1 entity/100 eV = 9.65×10^6 mol J^{-1}); this is termed the G-value. A practical yield is introduced in Chapter 6 (Section 6.2.2) for the polymer formed in the BANG polymer gel dosimeter. For reasons that will become evident, this yield is defined in terms of the percent weight fraction of polymer formed per unit dose (%w/Gy).

Ideally, a chemical dosimeter should satisfy the following requirements (Makhlis, 1972):

1) The dosimeter should be equivalent to tissue in terms of dose absorption characteristics (see Section 1.2.2). One of the unique advantages of chemical dosimeters is that their composition and phase can be varied to match that of any tissue of interest. Tissue equivalence greatly simplifies the calculation of dose which would otherwise require correction factors that can decrease the precision of the dosimeter (see Section 1.3.1).
2) The reaction cell (glass, polyethylene, quartz) within which many dosimetric substances are contained must also be considered to assure electronic equilibrium in the dosimetric substance. Without this electronic equilibrium the absorbed dose is perturbed by the cell wall (Johns and Cunningham, 1953). For irradiations in air, electronic equilibrium is accomplished if the cell wall is thicker than the range of the secondary electrons produced in it. For irradiations in thin-walled

cells imbedded in phantoms, the depth of measurement should exceed the range of electrons in phantom.

3) The dose response must be known. A linear dose response is preferred to simplify relative dose determinations. A single valued nonlinear response is acceptable, but requires that the detector response for the entire dose range of interest be calibrated (Attix, 1986).
4) The dose response should be independent of the energy and the intensity (i.e., dose rate) of the radiation, the temperature and environment, as well as the presence of impurities in the detecting medium.
5) The measurements should be reproducible over a wide dose-range, possess a high sensitivity, and be stable over time.
6) The dosimeter should be easy to prepare and use.

3.1.2 R_1 and R_2 Dose Response

A typical dose response of the spin-lattice and spin-spin relaxation times, R_1 and R_2, respectively, of the systems considered herein is shown in Fig. 3.1. The dose response is linear over a certain dose range and saturates at a maximum rate, $R_{1,2}^{max}$, and at a saturation dose, D_{sat}. According to the general dose response characterization described in Section 1.2.3, the dynamic range is $R_{1,2}^{max} - R_{1,2}(0Gy)$, the dose sensitivity, d, is given by the slope of the linear portion of the response, and the dose range is given by D_{sat}. The saturation dose can be defined as the dose at which the response begins to deviate from linearity. It can be alternatively approximated as follows:

$$D_{sat} = \frac{R_{1,2}^{max} - R_{1,2}(0Gy)}{d}. \qquad (3.1)$$

Hence, the D_{sat} is simply the dose at which an extrapolation of the linear portion of the dose response intercepts the value of $R_{1,2}^{max}$. It is evident from Eq. 3.1 that the three response characteristics are interrelated, however, for the studies in this thesis they will be dealt with individually to illustrate the effects of various parameters on the dose response. A second reason to deal with the dose response parameters separately is that the best dose resolution can be obtained for the greatest dose sensitivity or the greatest dynamic range for relative dose determinations (see Section 1.2.3.).

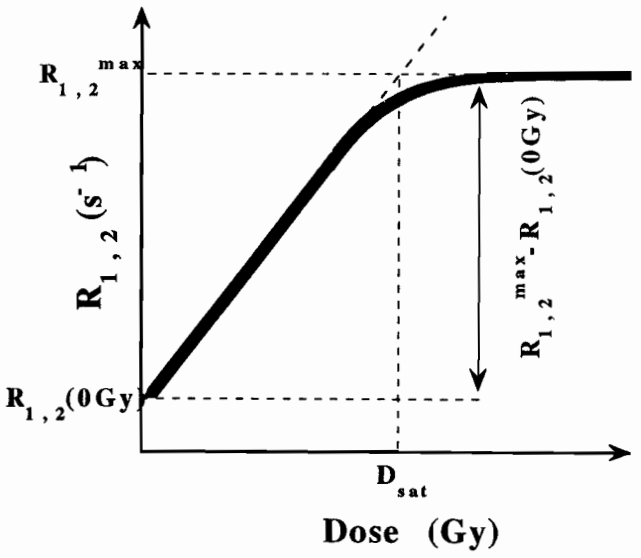

Figure 3.1 Typical R_1, R_2 dose response for ferrous sulfate gel and BANG polymer gel dosimeters.

3.1.3 Water Radiolysis

Water radiolysis is the study of the chemical response of both the ferrous sulfate doped gels and BANG polymer gel dosimeters (since both systems are between 87-96% water by weight). Radiolysis of water is the study of the molecular and radical products formed in irradiated water, and has been extensively studied (Draganic and Draganic, 1971; Allen, 1961; Spinks and Woods, 1964). Because water is tissue equivalent, the majority of chemical dosimeters are dilute aqueous solutions in which the radiation energy is absorbed primarily by water (typically present in molar concentrations) and not the solutes (typically present in mM concentrations). The chemical changes observed in aqueous chemical dosimeters result from the indirect action of the products of water radiolysis on the solutes.

In the first stage of water radiolysis the water molecules are either ionized to produce an electron (e^-) and a water cation (H_2O^+) or an excited species (H_2O^*),

$$H_2O \rightarrow e^- + H_2O^+, H_2O^* . \tag{3.2}$$

In the next stage the following reactions occur:

$$e^- + nH_2O \rightarrow e^-_{aq} , \tag{3.3}$$

$$H_2O^+ + H_2O \rightarrow H_3O^+ + OH\bullet , \text{ and} \tag{3.4}$$

$$H_2O^* \rightarrow H\bullet + OH\bullet . \tag{3.5}$$

In Reaction 3.3, the secondary electrons become thermalized and then hydrated by n water molecules to produce aqueous electrons. In the next Reaction 3.4 a hydronium ion (H_3O^+) and a hydroxyl radical ($OH\bullet$) are

produced. In Reaction 3.5 the excited water molecule decomposes into a hydrogen radical (H•) and a hydroxyl radical.

In the last stage of water radiolysis the primary species (e_{aq}^-, OH•, H_3O^+ and H•) diffuse from their point of origin and react with either themselves, water molecules or solutes, i.e.,:

$$e_{aq}^- + H_2O \rightarrow H\bullet + OH^- \text{ (high pH)}, \quad (3.6)$$

$$e_{aq}^- + H_3O^+ \rightarrow H\bullet + H_2O \text{ (low pH)}, \quad (3.7)$$

$$2e_{aq}^- + 2H_2O \rightarrow H_2 + 2\,OH^-, \quad (3.8)$$

$$e_{aq}^- + OH\bullet \rightarrow OH^-, \quad (3.9)$$

$$e_{aq}^- + H\bullet + H_2O \rightarrow H_2 + OH^-, \quad (3.10)$$

$$H\bullet + H\bullet \rightarrow H_2, \quad (3.11)$$

$$H\bullet + OH\bullet \rightarrow H_2O, \text{ and} \quad (3.12)$$

$$OH\bullet + OH\bullet \rightarrow H_2O_2. \quad (3.13)$$

3.2 Ferrous Sulfate-Doped Gel Dosimeter

The ferrous sulfate-doped gel dosimeters for the MR imaging of three dimensional radiation dose distributions were first proposed in 1984 by Gore *et al.*. The aqueous Fricke dosimeter upon which this gel dosimeter is based was developed in 1927 by Fricke and Morse and is described in Section 3.2.1. The R_1-dose response of aqueous Fricke dosimeters is described in terms of a previously developed physical model (Podgorsak and Schreiner, 1992) in Section 3.2.2. The composition and chemical response of the ferrous sulfate

gel dosimeter are described in Sections 3.2.3; previous investigations of the dosimeter are reviewed in Section 3.2.4.

3.2.1 Fricke Dosimetry

Of the many chemical dosimeters that have been developed, only the aqueous Fricke dosimeter developed in 1927 by Fricke and Morse has gained widespread use. The standard Fricke solution consists of 1 mM ferrous ion, Fe^{2+} (obtained from ferrous ammonium sulfate or ferrous sulfate) and 0.4 M sulfuric acid (H_2SO_4). The standard solution must be aerated, and can be modified by the addition of 1 mM NaCl to counteract perturbations to the response of the dosimeter caused by organic impurities.

When the aqueous Fricke solution is irradiated, the ferrous ions are oxidized to form ferric ions, Fe^{3+}. The amount of Fe^{3+} ions produced in the Fricke solution is proportional to the absorbed dose. The Fricke solution is 96% water by weight; therefore, the radiation chemistry is dominated by water radiolysis. The products of water radiolysis oxidize the Fe^{2+} ion through a series of reactions:

$$H\bullet + O_2 \rightarrow HO_2\bullet\,, \tag{3.14}$$

$$Fe^{2+} + HO_2\bullet \rightarrow Fe^{3+} + HO_2^-\,, \tag{3.15}$$

$$HO_2^- + H_3O^+ \rightarrow H_2O_2 + H_2O\,, \tag{3.16}$$

$$Fe^{2+} + H_2O_2 \rightarrow Fe^{3+} + OH\bullet + OH^-\,, \text{ and} \tag{3.17}$$

$$Fe^{2+} + OH\bullet \rightarrow Fe^{3+} + OH^-\,. \tag{3.18}$$

The three chemical species produced by water radiolysis that can cause the oxidation of Fe^{2+} ions are the hydrogen radical, H•, the hydroxyl radical, OH•, and the peroxide molecule, H_2O_2. The hydrogen radical is indirectly

responsible for the oxidation of three ferrous ions, through Reactions 3.14, 3.15, 3.17 and 3.18. Each peroxide molecule formed results in the oxidation of two ferrous ions by Reactions 3.17 and 3.18. Each hydroxyl radical oxidizes one ferrous ion by Reaction 3.18. The G-value for the ferric ion, $G(Fe^{3+})$, can be given in terms of the G-values for the water radicals as follows:

$$G(Fe^{3+}) = 2\ G(H_2O_2) + 3\ G(H\bullet) + G(OH\bullet). \qquad (3.19)$$

The individual G-values for H_2O_2, H• and OH• are 0.78, 3.7 and 2.92 ions per 100 eV, respectively for ^{60}Co γ-rays (cited in Attix, 1966). The yield of 15.8 ions/100 eV calculated using Eq. 3.19 agrees very well with the measured yield of 15.5±0.3 ions/100 eV recommended in ICRU Report No. 14 (1969) for maximum photon energies ranging from 0.6 to 50 MeV and that of 15.6 ± 0.6 ions/100 eV recommended in ICRU Report No. 37 (1984) for 1 to 30 MeV electrons (Kahn, 1984).

The Fricke dosimeter meets most of the requirements for an ideal chemical dosimeter listed in Section 3.1.1. It can provide dose measurements to within an accuracy of 1% (Fricke and Hart, 1966). Its response is independent of photon energy above 1 MV (Greening, 1981). The Fe^{3+} ion G-value drops to 12.5 ± 0.3 ions/100 eV for 5 keV photons (Greening, 1981). The G-value is constant in the temperature range of 15°C to 30°C. The practical dose range of the Fricke dosimeter is limited to ~ 400 Gy at which point the yield drops to 8.2 ions/100 eV (Spinks and Woods, 1964) because of oxygen depletion (see Reaction 3.14). The dose range can be significantly improved by aerating the dosimeter during irradiation; however, 400 Gy is large enough for most dosimetry applications. The response of the aqueous Fricke dosimeter is independent of dose rate between 10^{-3} to 10^{6} Gy/sec (Attix, 1986).

Because of its elemental composition (~10.8 %H, 1.2 %S and 88% O_2 by weight) the aqueous Fricke solution is essentially tissue equivalent (10.2% H, 88.7% C+O+N) over most photon energies of interest. At 50 keV the photoelectric effect cross-section of the sulfur present in the aqueous Fricke solution in the form of sulfuric acid becomes important, and the dose absorbed by the Fricke solution can exceed that absorbed by tissue by as much as 13%.

There are two main disadvantages of the Fricke dosimeter. The dose response of the dosimeter is very sensitive to impurities in the solution. Hence, stringent requirements on the purity of the chemicals and on the procedures used in the preparation of the aqueous Fricke solutions are necessary. Even trace amounts of impurities on the glassware (Podgorsak and Schreiner, 1992) can affect the dose response of the system. In addition, the spontaneous oxidation of ferrous ions imposes a constraint on the time elapsed between sample preparation and irradiation and between irradiation and analysis.

The dose, D, absorbed by a Fricke dosimeter can be calculated from a measurement of the change in ferric ion concentration, $\Delta[Fe^{3+}]$, using the following expression (Johns and Cunningham, 1953):

$$\Delta\left[Fe^{3+}\right] = D\, G\left(Fe^{3+}\right) \frac{10\,\rho}{N_A\, e}\,, \qquad (3.20)$$

where $\Delta[Fe^{3+}]$ is in mM, $G(Fe^{3+})$ is the G-value in #ions/100 eV, D is in Gy, ρ is in kg/liter, N_A is Avogadro's number and 'e' is the number of Joules per electron volt. Different experimental techniques may be used to measure the concentration. Fricke originally monitored ferric ion production using a titration method (Fricke and Morse, 1927). The most widely used method is spectrophotometry which will be discussed in more detail in Section 4.4.

Basically it involves measuring the dose-induced change in optical density of the dosimeter solution at a particular wavelength. An alternative for Fricke dose quantification has been introduced that involves nuclear magnetic resonance spin relaxation techniques.

3.2.2 NMR Dosimetry Using Aqueous Fricke

In 1984, Gore *et al.* proposed that the radiation induced changes in ferric ion concentration of a Fricke dosimeter could be measured using proton Nuclear Magnetic Resonance (NMR) methods. Although these methods are less precise than spectrophotometry, they were deemed important since they opened up the prospect of a three dimensional (3-D) radiation dosimetry using MRI, an imaging modality based on NMR.

The NMR methods exploit the differences in the abilities of Fe^{2+} and Fe^{3+} to enhance proton relaxation in water arising from the dipolar coupling between the magnetic moments of the water protons and the paramagnetic ions (see Section 2.5). The relaxation enhancement is greater for Fe^{3+} than for Fe^{2+} so that the spin-spin and spin-lattice relaxation rates, R_2 and R_1, respectively, of an irradiated Fricke solution increase with absorbed dose. The relationship between the proton R_1 and the concentration of ions and hence the absorbed dose is well understood and is discussed below (Gore *et al.*, 1984; Podgorsak and Schreiner, 1992). The relationship was derived by assuming fast exchange (see Section 2.6) between the water found in three different environments in the irradiated dosimeter: the bulk water and the water hydrating the Fe^{2+} and Fe^{3+} ions. The longitudinal magnetization recovery for a system in fast exchange is characterized by a single exponential and apparent relaxation rate R_1. A general expression for the apparent R_1 of a

heterogeneous system in terms of the inherent rates of the protons in each environment or group was presented earlier (Section 2.6). For the aqueous Fricke dosimeter the equation for R_1 becomes,

$$R_1 = p^{3+} R_1^{3+} + p^{2+} R_1^{2+} + \left(1 - p^{3+} - p^{2+}\right) R_1^{water}, \qquad (3.21)$$

where $R_1{}^i$ (i = 2+, 3+, water) is the inherent rate for the respective environments of water protons and p^i is the fraction of all the protons in each environment. The proton fractions can be expressed in terms of solute concentrations as follows:

$$p^{3+} = k^{3+}[Fe^{3+}] \text{ and } p^{2+} = k^{2+}[Fe^{2+}], \qquad (3.22)$$

where k^i is the fraction of water protons per unit solute concentration and [i] is the concentration of the solute.

Regrouping the terms in Eq. 3.21 one obtains:

$$R_1 = k^{3+}\left(R_1^{3+} - R_1^{water}\right)\left[Fe^{3+}\right] + k^{2+}\left(R_1^{2+} - R_1^{water}\right)\left[Fe^{2+}\right] + R_1^{water}, \qquad (3.23)$$

where the coefficients of the concentrations are the relaxivities of the respective solutes. The relaxivities are a measure of the ability of a solute to enhance spin-lattice relaxation of water protons, and can be determined from the slopes of plots of R_1 versus [i]. Expressing the relaxivities as,

$$r^i = k^i (R_1{}^i - R_1{}^{water}), \qquad (3.24)$$

and noting that the sum of the Fe^{2+} and Fe^{3+} concentrations is always equal to the original Fe^{2+} concentration prior to irradiation (i.e., $[Fe^{2+}] + [Fe^{3+}] = [Fe^{2+}]_o$), Eq. 3.23 becomes:

$$R_1 = \left(r^{3+} - r^{2+}\right)\left[Fe^{3+}\right] + r^{2+}\left[Fe^{2+}\right]_o + R_1^{water}, \qquad (3.25)$$

where the last two terms are independent of dose. It is the difference in the Fe^{2+} and Fe^{3+} relaxivities which enables R_1 to be used as a probe for dose.

Using Eq. 3.25, a change in ferric ion concentration, $\Delta[Fe^{3+}]$, can be expressed in terms of the measured change in the longitudinal relaxation rate, ΔR_1, as:

$$\Delta\left[Fe^{3+}\right] = \frac{\Delta R_1}{\left(r^{3+} - r^{2+}\right)} \quad . \quad . \tag{3.26}$$

Substituting Eq. 3.26 into Eq. 3.20, the following expression is obtained for the absorbed dose in terms of the longitudinal relaxation rate:

$$D = \frac{\Delta R_1 \, 9.64 \times 10^9}{\left(r^{3+} - r^{2+}\right) G(Fe^{3+}) \, \rho} \quad . \tag{3.27}$$

A fast exchange model will be presented for a ferrous sulfate doped gelatin system in Chapter 5.

3.2.3 Ferrous Sulfate-Doped Gel Dosimeter

The reactants and radiation products (Fe^{3+}) in an aqueous Fricke solution diffuse freely throughout the volume of the solution. Thus, a Fricke dosimeter only provides a measure of the average dose absorbed within the container holding it. A ferrous sulfate solution can be prepared in a gel matrix to limit diffusion so that the ferric ions remain close to their point of production, and better maintain the spatial integrity of the dose distribution in the dosimeter. In addition to spatially stabilizing dose information, the gel also contributes to the oxidation of ferrous ions during irradiation, thus enhancing the chemical yield of ferric ions and increasing the dose sensitivity of the dosimeter.

Since the initial proposal of the aqueous Fricke NMR dosimeter, most dosimeters investigated have been gels infused with ferrous sulfate. A ferrous sulfate-doped gel (or Fricke gel) typically consists of 1 mM ferrous

ammonium sulfate, 1 mM NaCl (optional), 0.05 M H_2SO_4 and 1-2% agarose or ~5% gelatin by weight. The reasons for this composition, and the effect of the gel dosimeter's composition on various practical aspects of the gel dosimeter, will be reviewed in Section 3.2.4.

Gel Matrix

A gel is a 3-D network or matrix of crosslinked polymer molecules that retains the solvent in which it is swollen (Encyclopedia of Polymer Science and Eng., 1985). Without the solvent the matrix would collapse. A polymer on the other hand is a macromolecular chain of repeating monomer units. The polymer may be natural or synthetic, and may be crosslinked by strong chemical covalent bonds or weak bonds such as hydrogen bonds. Covalently bonded gels are insoluble in solvents that do not degrade the gel. Hydrogen bonded gels will dissolve or undergo a transition from the gel phase to a liquid phase as they are heated beyond their melting point. Typically ferrous sulfate-doped gel dosimeters contain either agarose or gelatin gel. Both substances are crosslinked mainly by hydrogen bonds, and both are natural polymers. Agarose, a polysaccharide with the repeating unit $C_{12}H_{14}O_5(OH)_4$, is extracted from the agar found in red algaes (Olsson, 1991). Gelatin is a polypeptide chain of amino acids obtained from denatured collagen. It does not have a single particular repeating unit, but its average formula is given by, $C_{3.44}NO_{2.22}H_{6.9}$ (Kron *et al.*, 1993; Keller, 1993).

Reaction Scheme

A radiation reaction scheme, based on that for aqueous Fricke solutions in the presence of organic additives, (Spinks and Woods, 1976) was proposed for ferrous sulfate gels by Appleby *et al.* (1988). The scheme can be divided

into three steps: the initiation, propagation and termination of gel macroradicals (Olsson, 1991).

The initiation step, involves the production of gel macroradicals, R•, from the reaction of some products of water radiolysis with gel macromolecules RH, i.e.:

$$e^-_{aq} + H_3O^+ \rightarrow H\bullet + H_2O\,, \tag{3.28}$$

$$OH\bullet + RH \rightarrow R\bullet + H_2O\,, \text{ and} \tag{3.29}$$

$$H\bullet + RH \rightarrow R\bullet + H_2\,. \tag{3.30}$$

Reaction 3.29 competes for OH• with Reaction 3.18 seen previously in the aqueous Fricke reaction scheme in which Fe^{2+} is converted to Fe^{3+}. However, Reaction 3.29 dominates, because [RH] is much higher than $[Fe^{2+}]$. Hence, Reactions 3.14 to 3.17 describing the oxidation of Fe^{2+} for aqueous Fricke solutions, still occur in the presence of gelatin whereas Reaction 3.18 is superseded by Reaction 3.29.

The propagation step involves a chain reaction whereby macroradicals are continuously being produced:

$$R\bullet + O_2 \rightarrow RO_2\bullet\ , \tag{3.31}$$

$$Fe^{2+} + RO_2\bullet + H_3O^+ \rightarrow Fe^{3+} + RO_2H + H_2O\,, \tag{3.32}$$

$$RO_2H + Fe^{2+} \rightarrow Fe^{3+} + RO\bullet + OH^-\,, \text{ and} \tag{3.33}$$

$$RO\bullet + RH \rightarrow R\bullet + ROH\,. \tag{3.34}$$

Reaction 3.31 indicates that oxygen is required for the chain reaction to take place. The chain reaction occurs because the gel macroradicals, R•, required for Reaction 3.31 are continuously produced in Reaction 3.34 of the propagation step.

The chain reaction is terminated by the following reactions:

$$Fe^{3+} + R\bullet + H_2O \rightarrow Fe^{2+} + RX + H_3O^+ , \quad (3.35)$$

$$Fe^{3+} + H_2O + RO_2\bullet \rightarrow Fe^{2+} + H_3O^+ + O_2 + RX , \quad (3.36)$$

$$Fe^{2+} + R\bullet \rightarrow Fe^{3+} + R^- , \quad (3.37)$$

$$Fe^{2+} + H_3O^+ + RO\bullet \rightarrow Fe^{3+} + H_2O + ROH , \quad (3.38)$$

$$Fe^{2+} + OH\bullet \rightarrow Fe^{3+} + OH^- . \quad (3.39)$$

where RX and ROH are the reduced and oxidized forms of RH, respectively. Termination occurs because each reaction eliminates a radical.

The above reaction schemes indicate that the gel provides additional pathways to those observed in aqueous Fricke for the conversion of ferrous ion to ferric ion, and thus, increases the ferric ion yield.

3.2.4 Literature Review: Fe^{2+}-Doped Gel Dosimeters

Gore *et al.* (1984) were the first to propose the combined use of ferrous sulfate doped gel dosimeters and magnetic resonance imaging to detect and measure 3-D radiation dose distributions. Past investigations of the applications and practical aspects of the dosimeter are reviewed below. However, few studies have dealt with modeling the dose response of proton relaxation in ferrous sulfate-doped gel dosimeters. Such studies are presented in Chapter 5.

Applications

Ferrous sulfate-doped gel dosimeters have been used in basic studies involving rectangular beams of high energy x-rays or γ-rays and electrons. As early as 1986, Hiraoka *et al.* produced MR images of dose distributions produced by photon and electron beams in homogeneous and

inhomogeneous ferrous sulfate-doped Sephadex gel phantoms. They also presented two other electron beam studies involving ferrous sulfate-doped Sephadex gels (Hiraoka *et al.*, 1992 and 1993). However, the resulting MR images of the complex isodose distributions were not verified by comparisons with other dosimetry techniques or with calculated treatment plans. Hiraoka *et al.* (1993) did show excellent agreement between simple central axis percent depth doses (PDDs) determined using both MRI methods and an ion chamber. In another study, sophisticated chest and head anthropomorphic phantoms containing actual bone, and lung substitutes were used (Hiraoka *et al.*, 1992). Thomas *et al.* (1992) also looked at the effect of lung inhomogeneities on the isodose distributions using an agarose-based ferrous sulfate-doped gel dosimeter irradiated with a ^{60}Co beam. Slight discrepancies (~3%) were found under the lung inhomogeneity between MR isodose curves and isodose curves calculated using a treatment planning algorithm. These were thought to arise from susceptibility artifacts in the MR images. Both Appleby *et al.* (1987) and Olsson *et al.* (1990) employed agarose based gel dosimeters and found qualitative agreement between MR PDD data for high energy photon and/or electron beams and PDDs determined using ionization chamber or diode detectors; the MR PDD data with 20% scatter was well centered about the alternately determined PDDs. However, the MR determined doses near the surface of the gel were found to be too high (Olsson *et al.*, 1990). Prasad *et al.*, (1991) found qualitative agreement between MR-determined and calculated isodose contours in an axial plane through the dose distribution produced by a 6 MV rectangular photon beam. In a low energy x-ray study (Kron and Pope, 1994) the central axis PDD data obtained by MRI with agarose-based dosimeters were within 10% of calculated PDDs.

Furthermore, difficulties were encountered trying to determine the maximum dose at the surface of the dosimeter.

Other applications for which the high spatial resolution and the 3-D MRI gel dosimetry are particularly well suited include radiosurgery and brachytherapy; both techniques are characterized by high dose gradients and can provide complex dose distributions. Radiosurgery involves the irradiation of lesions (usually cerebral) using narrow beams that intersect at the lesion, but originate from many directions. This technique usually involves a stereotactic frame for localization of the target volume. Olsson *et al.* (1991) employed a gamma knife (consisting of 201 hemispherically distributed and collimated ^{60}Co sources) to irradiate a head-shaped phantom containing a ferrous sulfate agarose dosimeter and produce a spherical dose distribution 10 mm in diameter at 50% relative dose. The measured isodose contours were in good agreement with those calculated using a treatment planning system, however, the measured center of the dose distribution differed by 1 mm from the localized center determined using the stereotactic frame. Schulz *et al.* (1993) obtained agreement within 1 mm between the position of the localized target center and that of the measured center of a spherical dose distribution; the distribution was produced in a head phantom containing ferrous sulfate gelatin using McGill technique dynamic rotation of the couch and gantry. Rousseau *et al.* (1994) presented a more elaborate study where an anthropomorphic skull phantom of agarose-based gel was irradiated with a double isocenter to give an asymmetric dose distribution. The MRI isodose contours agreed with the calculated isodose contours to within 1 mm. Similarly, an agreement to within 5% was found for a skull phantom of gelatin gel irradiated with five narrow intersecting non-coplanar beams (Chan and Ayyangar, 1995a). The resulting dose distributions were

viewed in 3-D, and evaluated in 3-D with the use of a cumulative dose volume histogram (fraction of the total irradiated volume irradiated from 100% of the total dose to x% of the total dose versus x%). Three dimensional views of brachytherapy radiation dose distributions have also been produced (Schreiner *et al.*, 1995).

Ferrous-sulfate doped gel dosimeters are practical for detecting dose distributions of High Dose Rate (HDR) brachytherapy procedures where the irradiation times are relatively short compared to the diffusion of ions and concurrent loss of dose information (see below). Diffusion problems have been observed for a ten hour irradiation of an eyeball phantom with a low dose rate ^{106}Ru eye applicator (Olsen and Hellesnes, 1994). Very good agreement between PDD data measured by MR gel techniques and calculated PDD data or PDD data measured by alternate methods has been observed for HDR irradiations of ferrous sulfate-doped gelatin gels (Olsen and Hellesnes, 1994; Parker *et al.*, 1994; Schreiner *et al.*, 1994b) . In the two latter references a novel method was used for determining the MR dose distributions directly from MR intensities. Magnetization to dose calibration curves relating MR intensity for specific pulse sequences to dose were used. Previous MRI dose determinations typically involved converting multiple MR image sets to R_1 or R_2 maps which could be related to dose using established or calibrated relaxation rate dose responses.

Practical Aspects

In Section 3.1.1 it was stated that an ideal dosimeter should have a number of features. The studies addressing these requirements for ferrous sulfate doped gels are reviewed below.

i) *ease of preparation and use / impurities* Aside from using precise quantities of dosimeter constituents, certain precautions must be taken when preparing the gel dosimeters. For instance, the oxygen in agarose-based dosimeters that is lost when the gel is heated beyond its melting point (~95°C) must be replaced since it is required for the oxidation of Fe^{2+} ions to Fe^{3+} ions (Appleby *et al.*, 1988; Olsson *et al.*, 1989). This does not pose as great a problem for gelatin-based dosimeters which have a much lower melting point (~45°C).

It has been observed that the response of agarose-based dosimeters was affected by the cooling rate (Olsson *et al.*, 1991), heating duration (Gambriani *et al.*, 1994; Kron *et al.*, 1993) and by the time between heating and addition of the ferrous ion solution (Kron *et al.*, 1993). Thus, the heating history of a dosimeter during preparation must be regulated in order to obtain reproducible responses. This may be difficult to achieve for large volumes of agarose-based gels and variable dose responses may exist throughout the volume of the gel because of nonuniform cooling. Also, storage temperature and light may affect R_1 and R_2 through the spontaneous oxidation of ferrous ions in the dosimeter.

Impurities appear to have little effect on the dose response of ferrous sulfate-doped gels. Appleby *et al.* (1987) originally believed that the high yield of ferric ions observed in an agarose gel containing benzoic acid impurities arose from the impurities. More recent studies revealed that benzoic acid had little effect on the dose response of ferrous sulfate-doped agarose (Gambriani *et al.*, 1994) and gelatin gels (Duzenli *et al.*, 1994; Keller, 1993).

ii) *energy /dose rate* The dose response of the ferrous sulfate-doped gel dosimeters has been found to be independent of dose rate over a range of at least 0.4 to 24 Gy min^{-1}. It was also independent of radiation energy for high energy photons over a 6 - 18 MV range and high energy electrons over a 6-18 MeV range (Olsson, 1991) as well as low energy photons over a range of 30 - 70 keV (Kron *et al.*, 1993).

iii) *temporal stability* The dose information in a ferrous sulfate-doped gel dosimeter is not stable over long periods of time because of the spontaneous oxidation of ferrous ions and the diffusion of ions. The diffusion coefficient of ions has been found to be about 2 mm^2 hr^{-1} for agarose-based gels (Schulz *et al.*, 1990; Olsson *et al.*, 1992; Kron *et al.*, 1994) and polyacrylamide-based gels (deGuzman *et al.*, 1989). In other studies the effect of diffusion was observed on the shape and width profiles through imaged dose distributions (Hiraoka *et al.*, 1986; Appleby *et al.*, 1987; deGuzman *et al.*, 1989; Olsson *et al.*, 1992; Hiraoka *et al.*, 1992; Gambriani *et al.*, 1994; Hiraoka *et al.*, 1993; Schreiner *et al.*, 1994b). The general consensus is that the dosimeter should be imaged within at most a few hours after being irradiated. Ayyangar and Chan (1995) have found that diffusion effects were less for dose distributions having low dose gradients and hence low ferric ion concentration gradients, and that the dosimeters may be imaged much later.

The spin relaxation times have been found to decrease a few ms per hour because of the spontaneous oxidation of ferrous ions (Olsson *et al.*, 1989; Kron *et al.*, 1993; Keller *et al.*, 1993; Duzenli *et al.*, 1994). In addition, spontaneous oxidation caused the R_1 and R_2 dose response of gelatin gels to shift upwards with time without changing the shape of the dose

response curves (Keller *et al.*, 1993; Duzenli *et al.*, 1994). This is contrary to findings by Gambriani *et al.* (1994) which indicated that the dose sensitivity of agarose-based gel dosimeters changed with time. It is possible that the rate of spontaneous oxidation rate may be affected by the storage temperature of the dosimeters.

Thus, the temporal instability of the ferrous sulfate gel dosimeters places constraints on the time elapsed between preparation and irradiation, on the duration of the irradiation and the time delay between the irradiation and an imaging of the gel. While this makes the dosimeters inappropriate for low dose rate irradiations, the constraints can be met for most high dose rate applications.

iv) *reproducibility and resolution* The degree of reproducibility of the dose response observed in several studies appears to depend on the preparation procedure. Appleby *et al.* (1988) found that their results were reproducible within 15%; the greatest deviations were observed when the O_2 content of the gels was varied. Studies in which the heating and oxygenation protocols were relaxed indicated a 50% variability in the dose sensitivity of agarose-based dosimeters (Kron *et al.*, 1993; Rousseau *et al.*, 1994). However, by using strict preparation procedures, Gambriani *et al.* (1994) achieved a variability in dose sensitivity of less than 1%.

The reproducibility of doses measured by MR imaging is difficult to assess for ferrous sulfate-doped gels because the temporal instability of the dose information does not allow repeated imaging of an irradiated gel. However, the MR reproducibility may be evaluated by using the polymer gel dosimeters in which dose information is permanent.

The minimum detectable dose or dose resolution quoted for ferrous sulfate-doped gel dosimeters typically ranged from 0.5 to 1 Gy (Hiraoka *et al.*, 1986; Olsson *et al.*, 1989). Spatial resolutions of 1 mm are readily available for MR images with fields of view of about 24 x 24 cm^2 and composed of 256 x 256 pixels. The spatial resolution may be improved by decreasing the field of view or increasing the number of pixels.

v) *tissue equivalence* The tissue or water equivalence (see Section 1.2.2) of various ferrous sulfate-doped gel dosimeters has been established using different methods. Olsson and Mattsson (1991) compared the calculated mass attenuation coefficients and mass stopping power ratios (see Section 1.2.1) of an agarose-based dosimeter to those of water, and found that the quantities agreed within 1% over an energy range of 0.01 to 50 MeV. Kron *et al.* (1993) investigated the tissue equivalence of various gel dosimeters for a low energy photon range. The effective atomic number (see Eq. 1.1) and CT numbers (x-ray computed tomography parameter related to the linear attenuation coefficient, electron cross sections and electron density) compared very closely to that of water. Also the R_1-dose response was found to be independent of photon energy over a low energy range. Chan and Ayyangar (1995b) used Monte Carlo simulations to calculate the gel to water energy deposition ratio for different gel dosimeters, and for both electrons and photons of varying energies. The ratios were determined along the central axis, an off-centered axis and a profile of the dose distribution produced by a 10 x 10 cm^2 radiation field. The variability in energy deposition was typically < 2%, and the gel dosimeters were classified as water equivalent for the photon and electron beams used in radiotherapy.

Dose Response Studies

A number of studies have investigated the effect of different variables on the R_1 and R_2 dose response of ferrous sulfate-doped gel dosimeters. It is difficult to compare the results of these investigations since many variables, such as the gel, ferrous ion concentration, sulfuric acid concentration and oxygen concentration, change from one study to the next. Also, the studies were not usually performed with the direct goal of optimizing the dose response in terms of dose sensitivity, dose range and dynamic range (See Section 3.1.2). Nevertheless some general observations can be made. To assist in this discussion the dose sensitivities, dose ranges and dynamic ranges reported by various workers, are extracted from their data, and presented in Table A1-1 in Appendix 1.

Three main gels have been studied for MR-based dosimetry: agarose, gelatin and Sephadex (see Table A1-1). The dose response of these gels differed significantly. The Fe^{3+} G-values of the agarose-based dosimeters (~ 100 ions/100 eV) were about twice those of the ferrous sulfate gelatin (~ 50 ions/100 eV) which in turn were about three times that of aqueous Fricke (~ 15.8 ions/100 eV). The R_1-dose sensitivity in turn was of the order of 0.1-0.2 $s^{-1}Gy^{-1}$, 0.04 $s^{-1}Gy^{-1}$ and 0.1 $s^{-1}Gy^{-1}$ for the agarose, gelatin and Sephadex-based dosimeters, respectively (at 20 MHz).

The sensitivity of the Fricke-gel dosimeters has also been measured as a function of other preparation parameters. The dose sensitivity has been found to decrease with increasing gel concentration in both agarose (Olsson *et al.*, 1989) and gelatin (Olsson *et al.*, 1989; Duzenli *et al.*, 1994) based dosimeters. Schulz *et al.* (1990), on the other hand, reported that the dose response remained constant with agarose concentration. Contradictory

results have been observed for the dependence of the ferrous sulfate gel dosimeters on initial ferrous ion concentration $[Fe^{2+}]_o$. Appleby *et al.* (1988), Olsson *et al.* (1990) and Kron and Pope (1994) all reported a decrease in chemical yield and dose sensitivity with increasing $[Fe^{3+}]_o$ (from 0.1 - 2 mM). Schulz *et al.* (1990) and Hazle *et al.* (1991), on the other hand, reported no dependence of the response on Fe^{2+} ion concentration above 0.5 mM although it did decrease for $[Fe^{3+}]_o < 0.5$ mM. The dependence of the dose sensitivity on $[H_2SO_4]$ seems to vary with the gel system. In agarose-based dosimeters the sensitivity was essentially constant for $[H_2SO_4]$ ranging from 0.05 to 0.4 M (Schulz *et al.*, 1990; Olsson *et al.*, 1990). In gelatin-based dosimeters the chemical yield and dose sensitivity increased with increasing $[H_2SO_4]$ (Duzenli *et al.*, 1994).

Most studies have focused on the effect of variables on the $R_{1,2}$-dose response as a whole when, in fact, the response is governed by two separate mechanisms, the chemical response of the dosimeter to radiation as expressed by chemical yields and the response of R_1 and R_2 to the ferric ions. This breakdown becomes evident when physical models relating $R_{1,2}$ to dose are considered such as those for aqueous Fricke dosimeters (Gore *et al.*, 1984; Podgorsak and Schreiner, 1992) or ferrous sulfate-doped gelatin dosimeters (Audet *et al.*, 1993; Duzenli *et al.*, 1994). The ability of $R_{1,2}$ to respond to radiation-induced increases in ferric ion concentration has been gauged by the ratio of the ferric ion relaxation rates to the ferrous ion relaxation rates, $R_{1,2}{}^{3+}/R_{1,2}{}^{2+}$ (recall Section 2.6). In aqueous Fricke systems, calculated and measured $R_1{}^{3+}/R_1{}^{2+}$ ratios have been found to vary from about 17 to 19 for frequencies ranging from 20 to 64 MHz (Gore *et al.*, 1984; Podgorsak and Schreiner, 1992; Prasad *et al.*, 1991). The ferric and ferrous ion relaxivities,

$r_{1,2}^{3+}$ or $r_{1,2}^{2+}$ can also be used to gauge the response of $R_{1,2}$ to dose (see Section 3.2.2); some published values are listed in Table 3.1.

Table 3.1 Published relaxivity data for different dosimeter systems and NMR resonant frequencies. The relaxivities r_1 and r_2 correspond to the spin-lattice and spin-spin relaxation rates R_1 and R_2, respectively.

	ν_o	r_1^{2+}	r_1^{3+}
Aqueous Fricke			
(Gore et al., 1984) (37°C)	20 MHz	0.43	8.37
(Prasad et al. 1991)	64 MHz	0.5	9.6
		r_2^{2+}=0.4	r_2^{3+}=10.2
(Podgorsak and Schreiner , 1992)	25 MHz	0.45	7.98
	9 MHz	0.45	12.1
12% Gelatin *(Duzenli et al. , 1994)*	100 MHz	r_2^{2+}=1.71	r_2^{3+}=15

The resonance frequency at which R_1 is measured affects the dose response (see Table A1-1). Schulz *et al.* (1990) found that in agarose dosimeters the dose sensitivity and dynamic range both increase with an increase in frequency from 20 MHz to 85 MHz whereas the opposite was observed in an aqueous Fricke dosimeter for an increase in frequency from 9 MHz to 25 MHz (Podgorsak and Schreiner, 1992). Duzenli *et al.* (1994) observed an increase in the R_2 of ferrous sulfate gelatin dosimeters with frequency.

In addition to being essential for the dose response of ferrous sulfate-doped gels, oxygen can also affect the dose sensitivity, dose range and dynamic range of the dose response. Olsson *et al.* (1989) found that oxygenation was necessary in agarose gels to obtain a linear dose response, and that the dose sensitivity increased with oxygen content. Appleby *et al.* (1988) found that the ferric ion G-value and the dose range of agarose-based gels increased with oxygenation. Recent studies indicate that the dose response of gelatin-based dosimeters may also improve somewhat with additional oxygenation. Keller (1993) found that by oxygenating the gel, the gel's dose range increased from 40 to 80 Gy and its dynamic range increased from 1.7 to 3.5 s^{-1} whereas its dose sensitivity remained unchanged. Duzenli *et al.* (1994) found that smaller samples in which air could easily penetrate the whole volume, had a dose range of 120 Gy and a dynamic range of 7 s^{-1} instead of the 50 Gy dose range and 3 s^{-1} dynamic range observed for larger, less aerated samples.

Conclusion

The chemical dosimeter systems providing the best response can be determined from the data compiled in Table 3.1. The greatest dynamic range and dose range was found for gelatin gels and seemed to be limited by oxygen depletion since not all the ferrous ions have been converted when the response saturates (Keller, 1993; Duzenli *et al.*, 1994). The greatest dose sensitivity observed was about 0.2 $s^{-1}Gy^{-1}$ for the R_2-dose response of an oxygenated agarose-based gel dosimeter (Gambriani *et al.*, 1994).

Gelatin-based dosimeters, although less sensitive to dose, were chosen for the ferrous sulfate gel dosimeter studies in this thesis (Chapter 5). Gelatin is inexpensive (Sephadex ~$4000/kg; agarose~$2000/kg; gelatin $40/kg) and the gelatin-based dosimeters are easier to prepare. As mentioned previously,

agarose gels must be heated to higher temperatures during preparation thus necessitating reoxygenation procedures. Also, the higher temperatures will create greater cooling gradients that could affect the uniformity of the dose response throughout the gel's volume. R_1-dose responses of the ferrous sulfate gelatin dosimeters were studied instead of R_2-dose responses because the response is easier to model.

3.3 Polymer Gel Dosimeters

Three dimensional radiation dosimetry by MRI can also be performed with polymer gel dosimeters which offer certain advantages over the ferrous sulfate-doped gel dosimeters (see Section 3.3.3). The basis for the polymer gel dosimeter is that radiation induces the polymerization and crosslinking of monomers in a gel matrix. Section 3.3.1 introduces some general concepts of polymerization, and some specific concepts that will be used later in Chapter 6 when polymerization in the presence of a gel matrix is discussed. The monomers used for the polymer gel dosimeter studied in this thesis are acrylamide and Bis monomers which form crosslinked polyacrylamide gels in the absence of a gel matrix. The composition and structure of crosslinked polyacrylamide gels are described in Section 3.3.2. Finally, a review of the literature on polymer dosimeters, and their radiation response is given in Section 3.3.3.

3.3.1 Polymerization

General

While, the subject of polymerization is well covered in standard textbooks (e.g., Odian, 1991) a brief review is presented here. A polymer is a macromolecule consisting of a larger number of repeated units or monomers. The process by which polymers are synthesized from monomers are termed polymerization. In general, there are two types of polymerization: step and chain polymerization. In step polymerization, two reactive monomers can combine to form a dimer, and a third monomer can react with the dimer or another monomer to form a trimer or another dimer, respectively, and so on. Any two molecular species can react with each other, hence the polymer grows in a stepwise fashion. Chain polymerizations, on the other hand, involve the formation of a reactive center from a monomer. The reactive center can be either a free radical, cation or anion. As monomers successively bond to the reactive center, the polymer molecule grows, increasing in chain length by one unit each time. For chain polymerization, the monomers cannot react with one another as they do for step polymerization. Chain polymerizations that involve two kinds of monomers or co-monomers are called co-polymerizations. Important in the study of polymer gels are chain co-polymerizations in which the reactive center is formed by a free radical rather than by an ion.

Reaction Schemes

The reaction scheme for radical chain co-polymerizations consists of three steps: the initiation, propagation and termination steps. These are the same steps listed earlier for the reactions occurring in the ferrous sulfate gels

(see Section 3.2.3). In the initiation step an initiator or primary radical, I•, reacts with the co-monomers, M_1 and M_2, to form monomer radicals:

$$I\bullet + M_1 \rightarrow M_1\bullet, \text{ and} \tag{3.40}$$

$$I\bullet + M_2 \rightarrow M_2\bullet. \tag{3.41}$$

There are several methods available to produce the primary radicals. By applying heat to a monomer solution, thermal initiation produces monomer radicals directly and causes the dissociation of an additional compound into two primary radicals. Redox initiation produces primary radicals by oxidation-reduction reactions. In photochemical initiation, a compound in the system is excited by the absorption of UV or visible light, and either decomposes into radicals or interacts with a second compound to form radicals. For the studies in this thesis, initiation is achieved by ionizing radiation which excites and ionizes the monomers, water molecules or gelatin in the BANG polymer gel dosimeter to form primary radicals. Since the dosimeter is mainly composed of water, most monomer radicals are expected to be formed indirectly by the action of primary water radicals.

For radical chain polymerizations in general, the propagation step involves the reaction of a polymer radical, $M_n\bullet$, consisting of 'n' monomers with a monomer, M, to form a polymer radical that is one unit longer, i.e.:

$$M_n\bullet + M \xrightarrow{k_p} M_{n+1}\bullet, \tag{3.42}$$

where k_p is the propagation rate constant. The co-polymerization of two monomers, M_1 and M_2, is more complex, and will depend on the monomer at the propagating end as follows:

$$M_1\bullet + M_1 \xrightarrow{k_{p11}} M_1\bullet, \tag{3.43}$$

$$M_1\bullet + M_2 \xrightarrow{k_{p12}} M_2\bullet, \tag{3.44}$$

$$M_2\bullet + M_1 \xrightarrow{k_{p21}} M_1\bullet, \text{ and} \tag{3.45}$$

$$M_2\bullet + M_2 \xrightarrow{k_{p22}} M_2\bullet, \tag{3.46}$$

where the subscripts of $M_1\bullet$ and $M_2\bullet$ refer to the monomer found at the propagating end of the polymer and not to the length of the polymer. The overall propagation rate is given by:

$$R_p = k_{p11}[M_1\bullet][M_1] + k_{p12}[M_1\bullet][M_2] + k_{p22}[M_2\bullet][M_2] + k_{p21}[M_2\bullet][M_1]. \tag{3.47}$$

In the termination step, two polymer radicals can combine to form non-reactive dead polymer. The three possible reactions for the radicals ending in different monomers are:

$$M_1\bullet + M_1\bullet \xrightarrow{k_{t11}} \text{dead polymer}, \tag{3.48}$$

$$M_2\bullet + M_2\bullet \xrightarrow{k_{t22}} \text{dead polymer}, \text{ and} \tag{3.49}$$

$$M_1\bullet + M_2\bullet \xrightarrow{k_{t12}} \text{dead polymer}, \tag{3.50}$$

where k_t is the termination rate constant. The resulting rate of termination is given by:

$$R_t = 2k_{t11}[M_1\bullet]^2 + 2k_{t12}[M_1\bullet][M_2\bullet]^2 + 2k_{t22}[M_2\bullet]^2. \tag{3.39}$$

It is possible that in the BANG gel dosimeter the gelatin radicals may also participate in the termination process.

Chain Transfer and Inhibition

There are two other types of reactions which can affect polymerization: chain transfer and inhibition. During chain transfer a substance XA prematurely terminates a propagating radical by transferring species X to the polymer macroradical, $M_n\bullet$, as follows:

$$M_n\bullet + XA \xrightarrow{k_{tr}} M_n\text{-}X + A\bullet \quad . \tag{3.52}$$

The radical A• might re-initiate more polymerization however with a different initiation efficiency. In the inhibition reactions, a substance Z reacts with initiating and propagating radicals to produce non-radical species, M_n, or radicals with very low reactivity, Z• or $M_nZ\bullet$, i.e.,

$$M_n\bullet + Z \xrightarrow{k_Z} M_n + Z\bullet \text{ or } M_nZ\bullet \quad . \tag{3.53}$$

For example, oxygen is a powerful inhibitor that can react with the radicals to form a relatively non-reactive peroxy radical,

$$M_n\bullet + O_2 \rightarrow M_n\text{-}OO\bullet \quad . \tag{3.54}$$

This peroxy radical in turn reacts with other radicals to form non-reactive species. The radiation response of the BANG polymer gel dosimeter is inhibited unless it is purged of oxygen during preparation.

Kinetic Chain Length and Autoacceleration

It is necessary to address two polymerization concepts for the explanations proposed in Chapter 6 on radical chain co-polymerization in the BANG gel. The kinetic chain length, ν, is defined as the average number of monomer molecules consumed per radical formed. Alternatively, ν can be considered to be the number of growth steps between initiation and termination of the polymer reaction. The kinetic chain length can be written

in terms of the propagation and termination rates defined earlier (Odian, 1991),

$$\nu = R_p/R_t . \tag{3.55}$$

The kinetic chain length is useful for relating the polymerization dynamics to the amount of polymer formed. Also, as apparent from its definition, the kinetic chain will be instrumental in defining the polymer yield for the BANG dosimeter (see Chapter 6).

Autoacceleration is a process in which the rate of radical chain polymerization increases rapidly as more monomer is converted to polymer. As polymerization proceeds, the viscosity of the solution increases and the diffusion of the reacting species decreases. The diffusion of the larger macroradicals through the solution is more inhibited than that of the smaller monomers. Hence, the termination reaction rate involving two large radicals decreases more than the propagation rate involving a large radical and a small monomer. According to Eq. 3.55, this implies that the kinetic chain length (R_p/R_t) or amount of monomer converted per radical increases with the extent of monomer conversion. Eventually, after large conversion of monomer to polymer, the supply of monomers is exhausted and the value of the kinetic chain length levels off.

3.3.2 Polyacrylamide Gels

The radical chain co-polymerization of acrylamide and Bis co-monomers to form crosslinked polyacrylamide gels is the basis for radiation dosimetry using the BANG gel. Crosslinked polyacrylamide gels have been extensively investigated in the past because of their use in gel permeation

chromatography and gel electrophoresis (Hsu and Cohen, 1984; Richards and Temple, 1971; Weiss and Silberberg, 1977; Hsu *et al.*, 1983; Geissler *et al.*, 1982; Ruchel and Brager, 1975). Both these techniques exploit the sieving action of the porous gels to separate mixtures of macromolecules into components with different sizes or net charge.

The polyacrylamide gels consist of two types of repeating units, the acrylamide monomers and the crosslinking monomers or crosslinkers, N,N'-methylenebisacrylamide (Bis or Bisacrylamide). Polyacrylamide gels are formed by the radical co-polymerization of these co-monomers. During the co-polymerization process (see Section 3.3.2), the carbon double bonds of monomers are broken as the monomers bind to the reactive site of a polymer macroradical and extend the macroradical. Because acrylamide monomers only have one reactive carbon double bond, they form linear chains. The Bis monomer, however, is a diene with two carbon double bonds. Both bonds can link chains when activated and hence form a crosslink (see Fig. 3.2). Note that in polyacrylamide the crosslinks are established through chemical covalent bonds as opposed to the weaker hydrogen bonds which occur in agarose or gelatin gels.

Polyacrylamide gels are characterized by the concentrations of co-monomers in the solution prior to the synthesis of the gel. The specifications most commonly used are the percent weight fraction of the gel that is co-monomer (acrylamide and Bis), %T, and the percent weight fraction of all the co-monomer that is crosslinker Bis, %C:

$$\%T = 100\,\frac{\text{mass of acrylamide + Bis}}{\text{total mass of solution}} \tag{3.44}$$

$$\%C = 100\,\frac{\text{mass of Bis}}{\text{mass of acrylamide + Bis}} \tag{3.45}$$

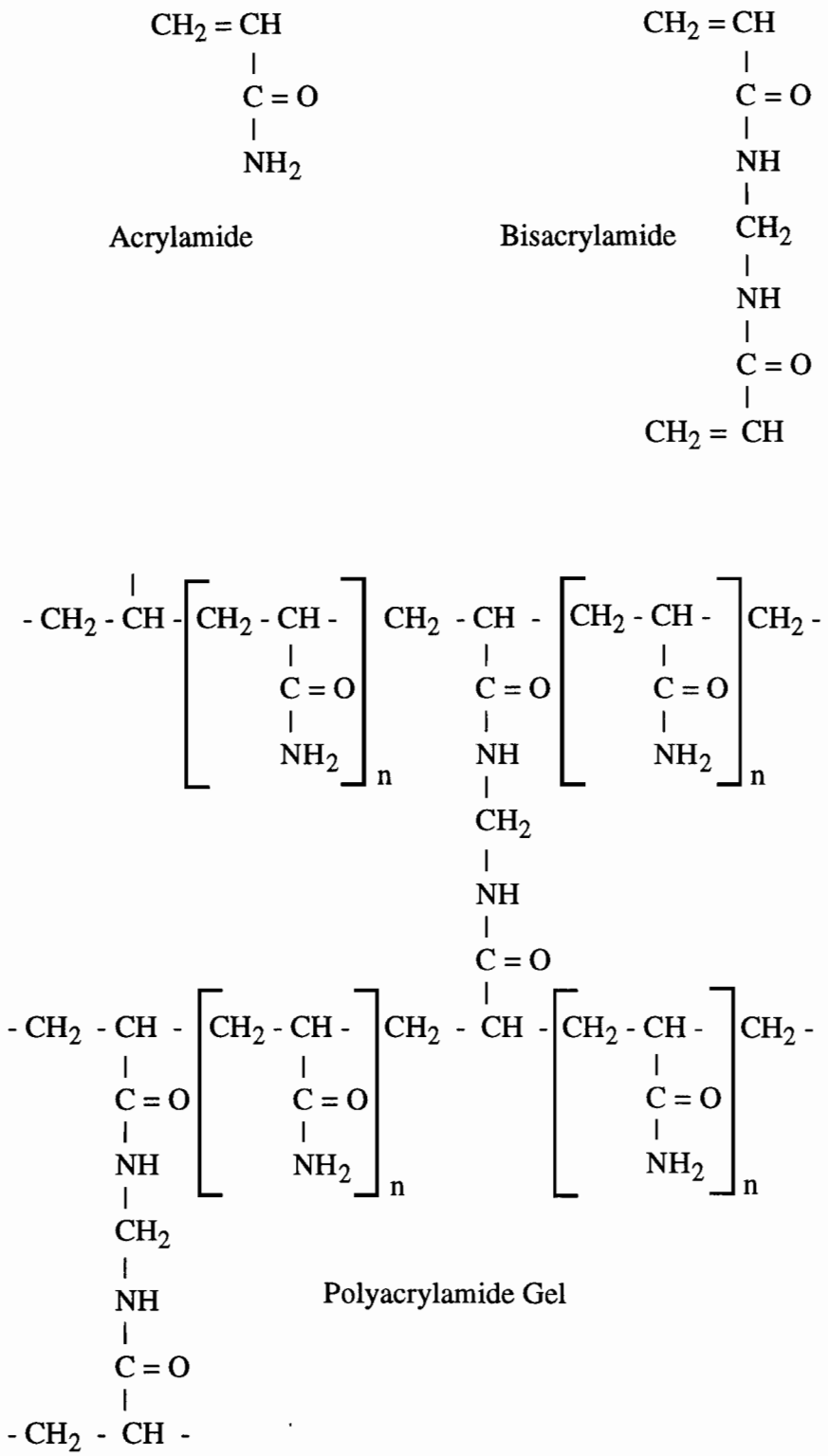

Figure 3.2 Chemical structure of acrylamide, Bis and crosslinked polyacrylamide gel.

Hence, 100 grams of gel containing 6 grams of co-monomer and 3 grams of crosslinker is characterized as 6%T and 50%C. The upper limits of %T and %C that can be used practically are defined by the solubility of the Bis (~3g/100g of water). Both %C and %T affect the structure and properties of the gel. Many studies have been performed to determine the effect of the gel's composition on the physical properties of the gel, i.e., porosity, structure, sieving action, etc. A review of these studies, partially outlined below, is given by Zhang (1990).

In the early 1970's, it was believed that the structure of polyacrylamide gels was formed by a homogeneous network of connected acrylamide chains defining the boundaries of the pores (Calvert, 1975). According to this model, the size of the pores is of the order of tens of angstroms which agrees with the size of the macromolecules normally fractionated by the gel. However, further studies have indicated that the polymer gel structure consists of a heterogeneous network of two phases, the polymer phase and the water phase (Hsu and Cohen, 1984; Richards and Temple, 1971; Weiss and Silberberg, 1977; Hsu *et al.*, 1983; Geissler *et al.*, 1982; Ruchel and Brager, 1975). This result is consistent with a model proposed in 1958 by Kilb in which each reactive center is taken to form a cluster of high co-monomer concentration. If the concentration of co-monomers is too low, the clusters do not crosslink, and system remains in the liquid-like, sol phase. As the concentration of co-monomer increases so does the number of clusters accrued and, at a high enough co-monomer concentration, the clusters crosslink together to form a gel phase.

Electron micrograph studies of polyacrylamide gels have established the structure of the heterogeneous gel as the gel composition is varied. The main findings are reviewed here (Ruchel and Brager, 1975; Ruchel *et al.*, 1978). The pores containing the water phase, are much larger, than originally predicted by

the model for homogeneous gels and are of the order of microns. The pore size initially decreases with %C until a minimum size is reached at 5%C after which it increases. The pore size decreases with %T. The pore limits are defined by the polymer phase. The polymer phase may reach thicknesses of the order of tens of microns. The walls thicken with %T. The structure of polyacrylamide is mostly affected by %C, and varies from parallel leaflets of polymer at low %C to random aggregation of highly condensed polymer beads at high %C. The beads are large enough to scatter light and are responsible for the increase in opacity of the gels with increasing %C. The scanning electron micrographs of polyacrylamide gels were also found to be independent of the temperature of polymerization, and of the motion of the system during polymerization.

The formation of beads at high %C is pertinent to some results presented in Chapter 6, and merits further attention. Gelfi and Righetti (1981a) found that the polymerization kinetics slow down with increasing %C. They attributed this to the formation of highly condensed gel regions into which unreacted monomers have difficulty penetrating. They also found that above 30% C of Bis (at 20°C) the gel regions are condensed enough to form beads causing the gel to become opaque and hydrophobic. In another study (Gelfi and Righetti, 1981b), it was found that lower %C gels became opaque if the polymerization temperature was reduced low enough. This result was attributed to regions of higher Bis concentration arising from the hydrogen bonding of the Bis molecules. The hydrogen bonding hypothesis was supported by the lack of opacity observed for a gel in which an anti-hydrogen bonding solvent was used.

3.3.3 Literature Review

Polymer gel dosimeters were developed for 3-D radiation dosimetry using MRI by Maryanski *et al.* (1993) in search of a solution to the main limitation of ferrous sulfate doped gels: the diffusion of the ions and concurrent loss of spatial dose information over time. Other dosimeters involving polymers or polymerization have been proposed in the past. Some of the dosimeters consisted of dilute solutions of high molecular weight polymer that degraded upon irradiation (Alexander and Fox, 1954; Feng, 1958; Boni, 1961; Weisner, 1961; Audet, 1991). The absorbed dose was usually determined from the resulting decreases in the systems' viscosity although the dose could also have been determined by measuring the changes in NMR transverse relaxation times (Audet, 1991). One dosimeter, an aqueous monomer solution, involved the radiation induced polymerization of the monomers, and was used to detect the threshold dose at which the solution gelled (Hoecker and Watkins, 1958). These dosimeters, however, have never gained widespread use, and are not eligible for 3-D radiation dosimetry since the radiation-induced changes are spatially uncorrelated. Spatial correlation has been achieved for polymer gel dosimeters by introducing acrylic monomers into a gel matrix (Maryanski *et al.*, 1993, 1994 and 1995) which moderated the polymerization and crosslinking reactions of the monomers so that the reactions did not propagate throughout the volume of the irradiation cell. Thus, the amount of polymer formed was related to the dose absorbed locally.

The BANANA (Bis Acrylamide Nitrous oxide ANd Agarose) polymer gel dosimeter was the first to be developed (Maryanski *et al.*, 1993). As indicated by its name, the dosimeter was an agarose gel whose aqueous phase

contained Bis and acrylamide monomers. The gel was saturated with nitrous oxide gas during preparation to purge oxygen which could inhibit the polymerization of monomers (see Section 3.3.1). Agarose was later substituted by gelatin as a gel matrix because the lower R_2 of gelatin broadened the dynamic range of the resulting 'BANG' dosimeter (Maryanski *et al.*, 1994; US Patent No. 5,321,357, 1994). A new polymer gel consisting of acrylic acid monomers instead of acrylamide monomers produced improved dose responses (see Table A1.2; Maryanski *et al.*, 1995). Sodium hydroxide which acted as a buffer, was added to the system to maintain a neutral pH.

The tissue equivalence of polymer gel dosimeters in terms of dose absorption was assumed based on the density, atomic composition, electron density and effective atomic number of the dosimeter (Maryanski *et al.*, 1995). Direct verification of the tissue equivalence by determination of the dose absorption properties of the polymer gel dosimeters has not yet been performed.

A compilation of published dose response data for polymer gel dosimeters is presented in Table A1.2. The data indicates that R_2 is at least ten times more sensitive to absorbed dose than R_1 (Maryanski, 1993). Hence, R_2 has been used for most polymer gel studies including the ones presented in this thesis. In addition, the R_2-dose response is independent of irradiation temperature. Furthermore, the R_2-dose response can be improved by decreasing NMR measurement temperature and increasing measurement of frequency (Maryanski *et al.*, 1993 and 1994). The best dose response, observed at 85 MHz and 20°C for the BANANA polymer gel dosimeter, demonstrated a dose sensitivity of 0.67 $s^{-1}Gy^{-1}$, a dynamic range of 10 s^{-1} and a dose range of 15 Gy (Maryanski *et al.*, 1993). These values, although they show improvement over the 0.2 $s^{-1}Gy^{-1}$ dose sensitivity and 7 s^{-1} dynamic range

observed for ferrous sulfate-doped gel dosimeters (see Section 3.2.4), could be improved by lowering the NMR measurement temperature, or varying the composition of the gel (see Chapter 6).

The main advantages of the polymer gel dosimeters over the ferrous sulfate-doped gel dosimeters are their temporal stability, neutral pH, high sensitivity and their visually observable dose response (Maryanski *et al.*, 1994). The crosslinked polyacrylamide formed in the polymer gels is spatially fixed by the gel matrix and does not diffuse through the dosimeter volume as do the ions in ferrous sulfate-doped gels. It was found that the R_1-dose response of the polymer gel dosimeters did not vary significantly over the span of several months (Maryanski *et al.*, 1993; Wong *et al.*, 1995). The neutral pH of polymer gels prevents the MR imaging artifacts arising from rf attenuation. These artifacts have been observed for Fricke solutions of large enough volume (Maryanski *et al.*, 1994). The polymer gels become opaque when they are irradiated to an extent that is related to the dose through the amount of polymer formed. Thus, the polymer gels can provide immediate qualitative visual information.

Dosimetry applications of the polymer gels have demonstrated very good quantitative agreement with measured or calculated dose data. Irradiations of polymer gels that have been performed with high energy electron and photon beams (Maryanski *et al.*, 1993, 1994; and 1995), Iridium-192 HDR remote after brachytherapy (Maryanski *et al.*, 1994 and 1995) and stereotactic radiosurgery (Maryanski *et al.*, 1995). The use of polymer gels as part of a dosimetry service, where dosimeters are shipped to remote sites, and their use for quality assurance procedures for various clinical irradiation modalities, have also been investigated (Ibbott *et al.*, 1995).

The BANG gel studies presented in Chapter 6 investigate in greater detail the effects of NMR measurement temperature and gel composition on the R_2-dose response of BANG gel dosimeters (data presented in Chapter 6 and reported in concurrent publications have not been included in this review). The results are used to determine how the R_2-dose responses can be optimized in terms of dosimeter composition and measurement temperature. They are also used to investigate a preliminary model of the R_2-dose response, and to better understand the mechanisms governing the dose response of the BANG dosimeter.

CHAPTER FOUR

Methods and Materials

The methods and materials pertaining to the two gel dosimeters are presented separately since the studies on each were performed at different institutes. All the procedures for the ferrous sulfate-doped gelatin dosimeters were performed in the Medical Physics Department, McGill University situated at the Montreal General Hospital, Montreal, Quebec whereas those for the polymer BANG gel dosimeters were performed in the NMR Research Group, Department of Diagnostic Radiology, Yale University, New Haven, CT.

4.1 Measurement of T_1 and T_2

4.1.1 The Free Induction Decay (FID)

As mentioned in Chapter 2, a bulk sample of spins placed in a homogeneous magnetic field, $\mathbf{H}=(0, 0, H_o)$, has a net, macroscopic equilibrium magnetization oriented parallel to $\mathbf{H}$ along the z-axis, $\mathbf{M}=(0, 0, M_o)$. The pulsed NMR methods used to measure the relaxation times of the gel dosimeters involve perturbing the equilibrium magnetization through irradiation with rf pulses and detecting the signal associated with the evolution of the magnetization back to equilibrium.

An NMR spectrometer produces and transmits the rf pulses to the sample by way of a coil or antenna oriented perpendicular to the main magnetic field which is taken to be along the z-axis (see Fig. 4.1). The samples are irradiated by a train of rf pulses commonly called a pulse sequence. The duration of each pulse in a sequence is conventionally specified by its action on the macroscopic magnetization. A 90° pulse, for instance, rotates the magnetization by 90°. If the 90° pulse is acting on the equilibrium magnetization $\mathbf{M} = (0, 0, M_0)$, it will rotate **M** away from the z-axis until it lies in a perpendicular plane. Similarly, a 180° pulse will invert $\mathbf{M} = (0, 0, M_0)$ to $\mathbf{M} = (0, 0, -M_0)$.

After the application of a pulse the magnetization components relax to their equilibrium values. For example, after a 90° pulse, M_{xy} approaches zero as it rotates about the z-axis at a frequency of ω_0 (see Eq.'s 2.9a and 2.9b). This oscillating and decaying magnetization induces a signal in the rf coil that is directly proportional to M_{xy}:

$$M_{xy}(t) = M_{xy}(0) \exp\left(-t/T_2^*\right), \tag{4.1}$$

where T_2^* is the decay constant. The detected signal is known as the Free Induction Decay, FID (see Fig. 4.2).

The decay constant of the FID, T_2^*, is not governed solely by the spin-spin relaxation time, T_2, determined by the structure and dynamics of the spin system (see Chapter 2). It is also affected by the presence of static magnetic field inhomogeneities, ΔH in H_0. The field inhomogeneities produce a spread in the Larmor frequency of $\Delta\omega=\gamma\Delta H$. Hence, some of the magnetic moments will be precessing faster than others. The range of the

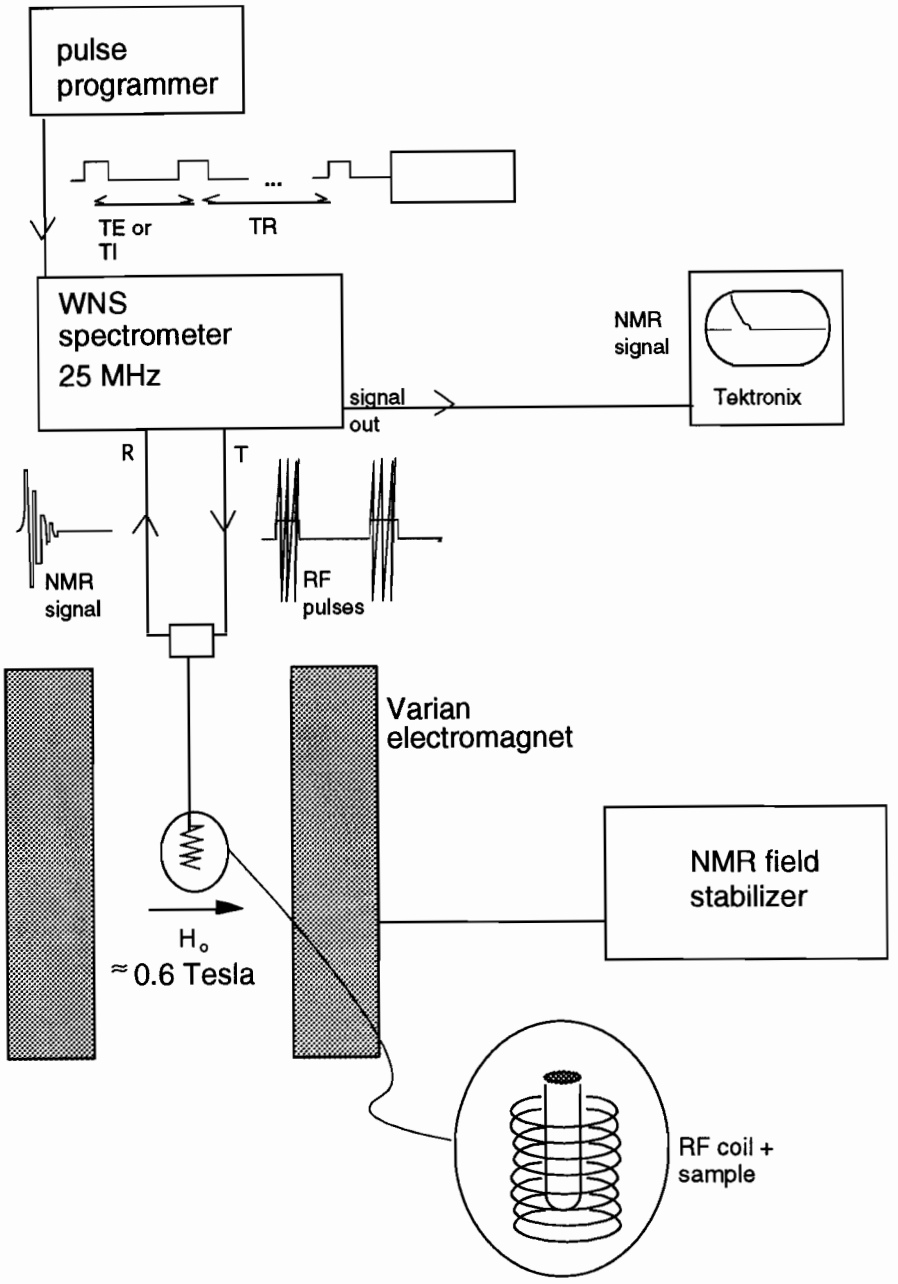

Figure 4.1 Schematic Diagram of the 25 MHz NMR system. The T and R represent the transmitter output and receiver input of the spectrometer, respectively.

precession frequencies may contribute to the dephasing of the magnetic moments and hence to spin-spin relaxation. The resulting decay constant of the FID signal is given by (Farrar and Becker, 1971),

$$\frac{1}{T_2^*} = \frac{1}{T_2} + \frac{1}{2}\gamma\Delta H . \qquad (4.2)$$

4.1.2 RF Pulse Sequences: T_2

While the FID is not characterized by the true T_2 decay, T_2 may still be determined by using special rf pulse sequences. The effects of the pulses may be described in terms of their effect on isochromats, i.e., the macroscopic magnetizations of groups of spins precessing in phase. These sequences refocus the isochromats dephased with respect to one another by using additional 180° echo generating pulses. Thus, the spin-echo pulse sequence (Hahn, 1950) consists of two pulses (see Fig. 4.2). The first pulse is a 90° pulse which brings the magnetization into the transverse plane. The second pulse, a 180° pulse, is applied a time, t = TE/2, later. On a microscopic level the 180° pulse has the effect of flipping the isochromats 180° about the x-axis. Before the 180° pulse the faster precessing isochromats are preceding the slower ones and the shaded area depicted in Fig. 4.2 is increasing. After the pulse, the faster precessing isochromats are behind the slower ones and the shaded area is decreasing. Thus, a time, t = TE, after the 90° pulse the isochromats rephase. As they do so, a signal or echo with a height proportional to $M_{xy}(t = TE)$ is produced. Unlike the field inhomogeneities which are temporally stable, the dephasing arising from inherent T_2 processes is not undone by the 180° pulse because these processes are random in time. By repeating the sequence with different TE's the $M_{xy}(t)$ curve corresponding to

the real spin-spin relaxation can be established and T_2 can be determined. It should be noted, however, that if there is significant diffusion in the system, the echo amplitude will be affected somewhat (see below).

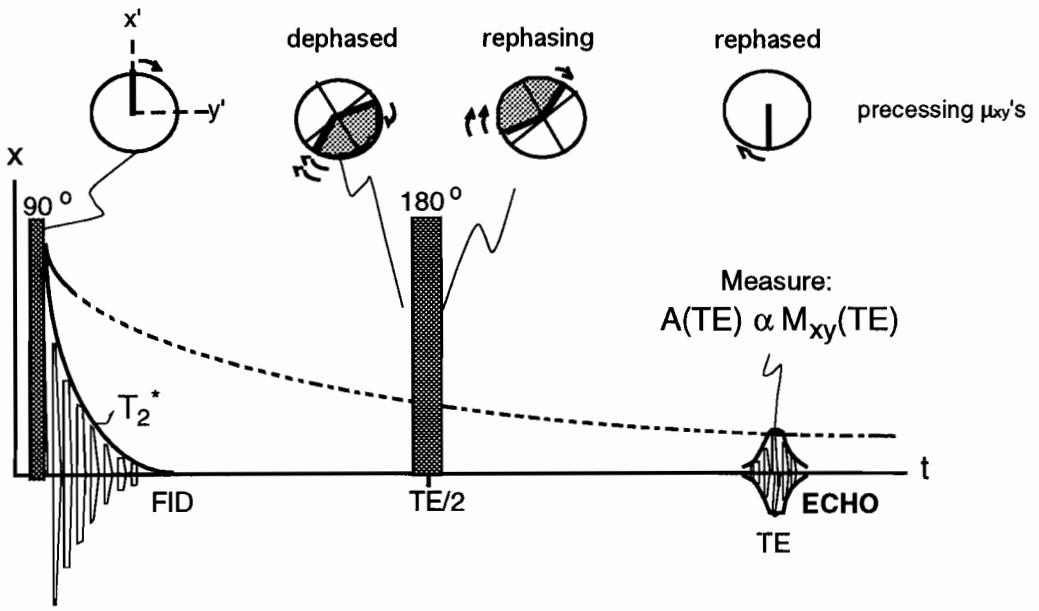

Figure 4.2 Schematic depiction of the Hahn spin-echo pulse sequence, and the creation of a spin echo induced by the rephasing of the precessing magnetic moments by the 180° pulse. The dashed curve represents the decay of $M_{xy}(t)$ according to Eq. 4.1 with T_2^* replaced with T_2. The x' and y' axes in the sketch show the precessing magnetic moments in a reference frame rotating at ω_0. The double and single arrows represent precession that is faster and slower than ω_0, respectively.

A more practical pulse sequence than the spin-echo sequence is the Carr-Purcell (CP) sequence (Carr and Purcell, 1954) which consists of a 90° pulse followed a time, TE/2, later by a series of 180° pulses each separated by a time t = TE. The single CP sequence produces a train of Hahn echoes. This decreases the acquisition time drastically from that needed for the several separate spin-echo sequences to produce the same number of echoes. The amplitude of the n^{th} echo in the CP train is given by,

$$A(nTE) = A(0)\exp\left(\frac{-nTE}{T_2} - \frac{1}{12} n \gamma^2 G^2 D\, TE^3\right). \qquad (4.3)$$

The additional term in the exponent in Eq. 4.3 accounts for losses in the transverse magnetization decay arising from the diffusion of protons, D, through magnetic field gradients, G. The diffusion effects can be minimized by reducing, as much as possible, the time TE over which diffusion can occur. The true T_2 can thus be determined directly from the negative inverse of the slope in a semi-log plot of the magnitude of the echo heights versus time (see Fig. 4.5). The echoes in the train are alternately positive and inverted because of phase differences. A variation of the CP sequence involving rf pulses with alternating phases is the Carr-Purcell-Gill-Meiboom (CPMG) pulse sequence (Meiboom and Gill, 1958; Farrar and Becker, 1971) that produces only positive echoes in the train. The CPMG sequence has the added advantage that even if the duration of the 180° pulses is slightly misadjusted, such errors are not accumulative over the echo train.

4.1.3 RF Pulse Sequences: T_1

The spin-lattice relaxation time, T_1, characterizes the recovery of the longitudinal magnetization M_z after perturbation. However, M_z can not be probed directly by the rf coil and, therefore, a pulse sequence which incorporates a read pulse must be employed to monitor the recovery of the longitudinal magnetization. In this work, T_1 was measured using the inversion recovery pulse sequence consisting of two rf pulses (see Fig. 4.3).

The first rf pulse is a 180^o preparation pulse immediately after which $M_Z(t=0) = -M_0$. A time TI later, a 90^o read pulse is applied; immediately after this read pulse, $M_{XY}(TI) \approx M_Z(TI)$. The signal amplitude A(TI) corresponding to the ensuing FID's peak, is proportional to $M_Z(TI)$. A(TI) is measured as early as possible on the FID, typically 40 μsec in this work, to avoid any signal decay from T_2 effects. One can define a reduced magnetization signal '[A(∞)-

A(TI)]/2A(∞)' which gives the difference of the recovered magnetization signal A(TI) from the equilibrium magnetization signal, A(∞), measured by a single 90° pulse. The reduced magnetization signal evolves as :

$$\ln\left(\frac{A(\infty) - A(TI)}{2A(\infty)}\right) = -\frac{TI}{T_1}, \qquad (4.4)$$

and T_1 can be determined from the reduced magnetization curve (see Fig. 4.4). Before repeating a pulse sequence for the different TI's, one must wait for a time of about $TR = 5T_1$ so that the magnetization can return to its equilibrium value before the next rf excitation. In fact, this condition applies for any pulse sequence.

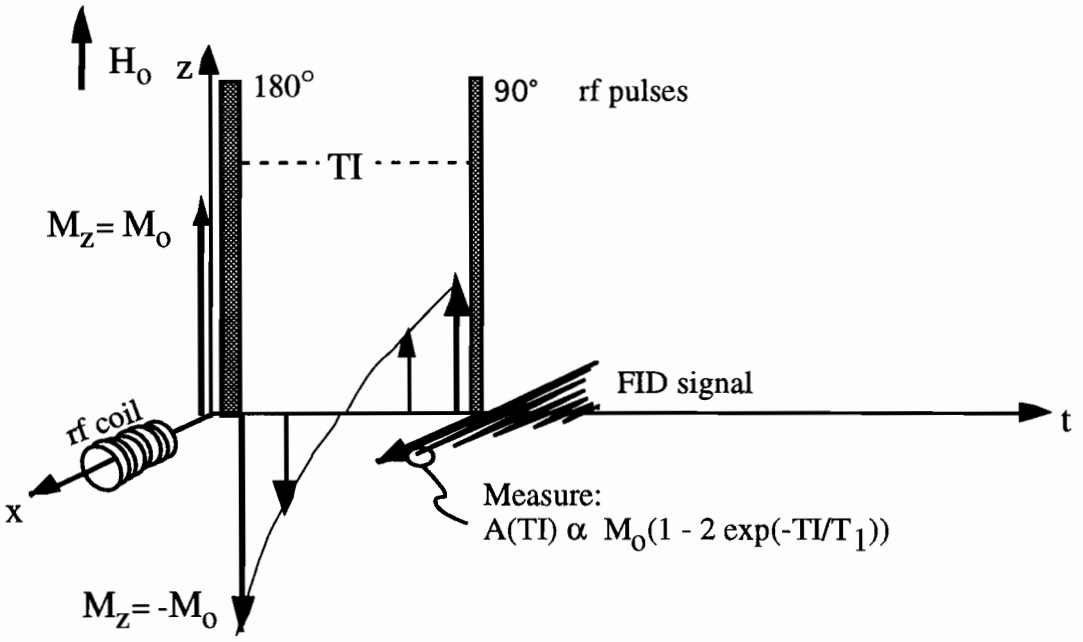

Figure 4.3 Shown is a schematic of an inversion recovery pulse sequence. The sample is placed in the rf coil whose axis is perpendicular to the direction of H_0. The arrows representing the magnetization vectors increase exponentially with time. The 180° rf pulse prepares the magnetization and the 90° rf pulse at time TI rotates the evolved M_Z into the transverse plane so that an FID (proportional to $M_Z(TI)$) can be detected by the rf coil.

4.2 NMR Apparatus and Data Acquisition

4.2.1 Ferrous Sulfate-Doped Gels

The ferrous sulfate-doped gelatin dosimeters were analyzed with an NMR system consisting of a Varian electromagnet (Varian Associates, Palo Alto, CA), and a WNS (Waterloo NMR Spectrometers Inc., Waterloo, ON) spectrometer operating at 25 MHz.

An inversion recovery pulse sequence was used to measure the T_1 of the ferrous sulfate-doped gelatin dosimeters. The FID signal amplitudes were measured using a Tektronix 2221 60 MHz digital storage oscilloscope (Beaverton, Oregon, USA). The FID height, A(TI), was measured 40 μsec after the read pulse to avoid the receiver dead time of 15 μsec between the end of the pulse and the start of the FID. The FID decay signal did not decay appreciably in the 40 μsec interval since 40 μsec « T_2. Typically, 6 to 10 TI's ranging from 200 ms to 5 sec. were used to characterize the longitudinal magnetization decay, and TR was about 5 sec. The signal for each TI was averaged about 10 times. The longitudinal magnetization decays for all the samples were exponential over a one decade range (see Fig. 4.4). The spin-lattice relaxation times were determined using an exponential least squares fit; the uncertainties quoted for the relaxation times are the standard deviations obtained by the fits. All T_1's were measured at 20°C within one day of sample preparation. The T_1's for any sample containing Fe^{2+} were measured 2 hours after preparation to avoid variations in T_1 brought about by the spontaneous oxidation of Fe^{2+}.

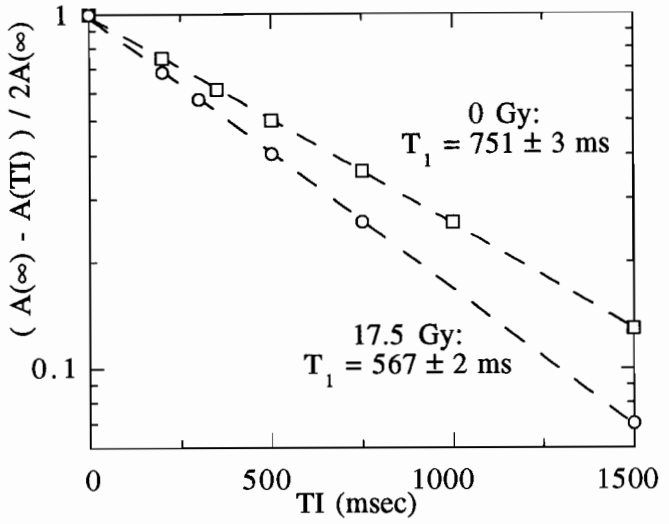

Figure 4.4 Typical reduced longitudinal magnetization evolution measured for samples of ferrous sulfate-doped gelatin dosimeters irradiated with a ^{60}Co beam at a dose rate of 3.18 Gy/min. The decays were obtained with an inversion recovery pulse sequence. The longitudinal relaxation time, T_1, is given by the negative inverse of the slope of the decay.

The gelatin protons accounted for about 3% of the total magnetization for the 10% gelatin solution. The contribution of the gelatin's magnetization to the total magnetization was considered negligible, and the T_1 of water protons was determined directly from the total magnetization.

4.2.2 Polymer BANG gels

The polymer BANG gel dosimeters were analyzed on a desktop Bruker IBM minispec desktop relaxometer (Bruker Instruments, Billerica MA) operating at 20 MHz and 40°C. The system consists of a permanent magnet and a built-in pulse programmer and data acquisition system. The transverse relaxation times were measured using a CPMG pulse sequence with TE = 500 μs and TR = 15 s since the T_1's of the samples were at most 2-3 s. Only every 8th echo was sampled, and the maximum number of echoes allowed by the system was 140. For samples measured at 40°C the signals of the echo train were averaged 16 times. For the temperature dependence

studies, the samples were equilibrated for 1 hour in an automated water bath (Haake A81, Karlsruhe, Germany) at temperatures ranging from 5°C to 40°C prior to analysis. Although the relaxometer operated at 40°C, the temperature of a sample did not appear to change significantly over the 1 to 2 s duration of a CPMG measurement. The T_2's reported for the temperature studies are the average of 4 separate measurements made after the sample temperature was re-established in the water bath. The uncertainty quoted for T_2 is the standard deviation in the 4 separate measurements.

The T_2's were calculated from the transverse magnetization decay using an exponential least squares fit. Figure 4.5 shows some typical transverse magnetization decays for BANG gel samples irradiated to different doses. The minimum normalized echo amplitude measured was usually 20%. The mono-exponentiality of the transverse magnetization decay over a greater range was verified by separate measurements on a 85 MHz NMR system which allowed a longer echo train to be sampled (i.e., > 140 echoes).

A small but very quickly relaxing magnetization from the polymer and gelatin protons was thought possible. However, no such component was observed and all decays were mono-exponential. This is not unusual considering that the first echo is acquired at 8 ms and the transverse relaxation time for polyacrylamide protons in a 10%T and 1%C solution is ~ 13 μs (Zhang, 1990) and that for gelatin protons is expected to be of similar magnitude. Under such conditions the polymer and gel proton magnetization should decay to zero by the time of the first echo.

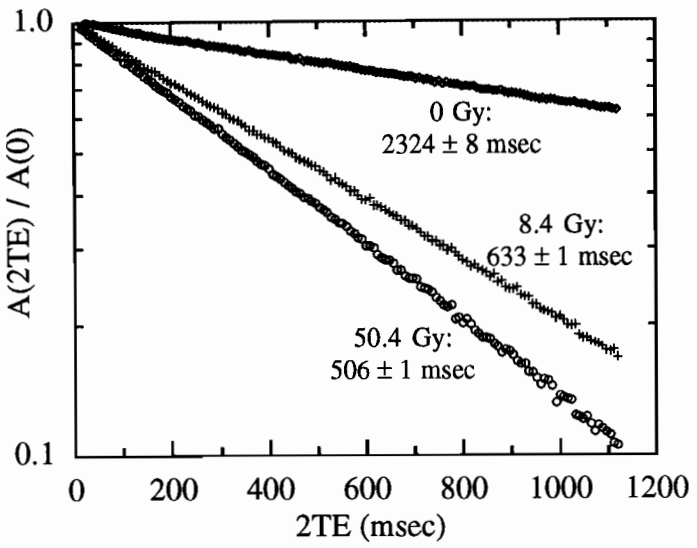

Figure 4.5 Typical transverse magnetization decays for BANG gel samples irradiated to different doses with a 250 kVp x-ray beam. The decays were measured using a CPMG pulse sequence with an inter-pulse spacing of 8 ms.

4.3 Sample Preparation and Irradiation

4.3.1 Ferrous Sulfate-Doped Gels

All the Fe^{2+} and Fe^{3+} solutions were prepared by dissolving ferrous and ferric ammonium sulfate salts (99%+ purity, Aldrich Chem. Co., Milwaukee, WI), respectively, in triply distilled water containing 1 mM NaCl (reagent grade, Aldrich) and either 0.05 M or 0.19 M H_2SO_4 (reagent grade, Baker Analyzed Reagent, Phillipsburg, NJ). All the solutions used for the dose response studies contained 1 mM Fe^{2+}. The Fe^{3+} ion concentrations were not calculated using the molecular weight of ferric ammonium sulfate salt alone, because of the unstable hydration of the salt (i.e., $FeNH_4(SO_4)_2 \cdot xH_2O$ where x is variable). Instead, the Fe^{3+} concentration of a 0.4 M H_2SO_4 solution of Fe^{3+} ion containing a known mass of the salt was determined from a spectrophotometric absorbance measurement in Optical

Density Units (ODU) assuming an extinction coefficient of 2205 ODU $M^{-1}cm^{-1}$ at 25°C (ICRU Report No.'s 17 (1970) and 21 (1972)). The appropriate molecular weight was determined to be 351 instead of 482 corresponding to hydration by 4.7 water molecules instead of a nominal 12 water molecules.

Acid-cured swine skin gelatin (Type A, 300 bloom, Aldrich) was slowly stirred into the ion solutions, and heated to about 45°C at which point the gelatin appeared to be completely melted. The solution was then quenched to room temperature (~21°C) by immediately dispensing µl quantities into NMR sample tubes of 5 mm I.D. or ml quantities into UV-grade, methacrylate, spectrophotometry cuvets with a 1 cm path length. The gelatin concentrations varied from 5% to 15% by weight.

All ferrous sulfate gel samples were irradiated in phantom with a Theratron 780 ^{60}Co γ-ray unit (AECL, Kanata, Ontario) in the Department of Radiation Oncology, Montreal General Hospital. The radioactive source is housed in a standard treatment head which is mounted to a rotating gantry with an isocenter 80 cm from the source. The output dose rate of the T-780 was calibrated with an NPL secondary standard ionization chamber and reader (Nuclear Enterprises Ltd., Beenham, England) calibrated for ^{60}Co γ-rays at the standardization laboratories of the National Research Council (Ottawa, Canada). The dose rate at the depth of dose maximum, d_{max} = 0.5 cm, in tissue equivalent phantom for a 10x10 cm^2 field at a source to surface distance (SSD) of 80 cm was measured as 1.32 Gy/min on Oct. 1, 1992. Dose rates on subsequent dates were calculated using the known exponential decay of ^{60}Co with a half-life of 5.26 years.

Different irradiation setups were used for the NMR samples in tubes and the spectrophotometry samples in cuvets. The cuvets were placed with their center at the depth of dose maximum in tissue equivalent media, and

surrounded with tissue equivalent Lucite sheets. They were irradiated with the same setup used for calibrating the output (i.e., 10x10 cm^2 field, 80 SSD). The other setup for the gels in NMR sample tubes consisted of a phantom mounted on a Lucite tray that fit into the accessory rails of the treatment head (51.2 cm from the source). Three samples were fitted into holes spaced 3 cm apart at a depth of 1.5 cm in a Lucite block mounted on the source side of the tray. The dose rates at the three sample positions were determined using thermoluminescent dosimetry with lithium fluoride crystals (TLD-100's). The TLD's responses were first calibrated to known doses by placing them at d_{max} in phantom in a 10x10 cm^2 field at an SSD of 80 cm. The light output from the crystals was read using a Harshaw Model 2000 Thermoluminescence Analyser (Harshaw Chemical Co., Solon OH). The calibrated TLDs were then used to determine the average dose rate for all three sample hole positions centered in a 17x17 cm^2 field. An average dose rate of 3.18 Gy/min was found for each position on March 18, 1993.

4.3.2 Polymer BANG Gels

All BANG gel samples were prepared using acid-cured swine skin gelatin (300 bloom, Sigma Chem. Co., St. Louis, MO), electrophoresis grade acrylamide monomer and N,N'-methylene-bisacrylamide crosslinker (Bis) (Bio-Rad, Richmond, CA) and water purified by ion exchange.

The gels were prepared in 100 ml quantities. The gelatin was dispersed in the water at room temperature, and dissolved by heating the mixture to 60°C. First the acrylamide and then the Bis were added and dissolved by stirring the mixture constantly at 60°C. Two milliliter quantities were poured directly into the test tubes (13 mm O.D.) used for NMR analysis, and the test

tubes were kept in a 60°C water bath. The samples were deoxygenated by blowing heated and humidified argon or carbon dioxide containing less than 10 ppm O_2 over the surface of a sample at a flow rate strong enough to agitate the solution without causing it to foam. The samples were bubbled for 2 minutes before hermetically sealing and refrigerating them.

The BANG gel dosimeter compositions varied depending on the R_2-dose response study. The gelatin concentrations ranged from 4% to 6% by weight, the percent total monomer weight fraction varied from 4%T to 8%T, and the percent weight fraction of Bis monomer ranged from 16%C to 83%C. The most widely used compositions were of 5% gelatin, 6%T at 50%C or 67%C.

The BANG gel samples were irradiated at room temperature (~21°C) with 250 kVp x-rays using a Siemens Stabiliplan Orthovoltage unit (Department of Radiotherapy, Yale New Haven University Hospital). The samples were irradiated in a Lucite phantom that fit into the collimator collar on the output port of the unit. The dose rate at the samples was calibrated using Fricke dosimetry and found to be 16.8 Gy/min and 3.5 Gy/min, for an unfiltered beam and a beam filtered with 2 mm of Al, respectively. The higher dose rate was more practical for delivering large doses on the order of 300 Gy. It was verified that the R_2-dose response was the same for both dose rates.

4.4 Spectrophotometry

When visible light passes through aqueous solutions of transition metal ions, some frequencies can cause transitions to occur between the electronic energy levels of the ions and photon can be absorbed in the process (Segal, 1985). Different ionic solutions are characterized by different absorption spectra. The fraction of incident radiation that is absorbed by a sample is proportional to the concentration, [x], of the absorbing species in the sample and can be measured with a spectrophotometer. This fraction is known as the absorbance or optical density and for a particular wavelength (λ) is given by (Johns and Cunningham, 1953),

$$A_\lambda = \varepsilon_\lambda \, l \, [x], \tag{4.5}$$

where A_λ is in Optical Density Units (ODU), [x] is the molar concentration of species x, ε_λ is the extinction coefficient in ODU M^{-1} cm^{-1} and l is the optical path length through the sample cell in cm.

The dose absorbed by a ferrous sulfate-based dosimeter can be related to the change in the optical density of the dosimeter arising from the conversion of Fe^{2+} to Fe^{3+} since the extinction coefficient for the two ions differ. According to Eq. 4.5 and Eq. 3.20 the dose in Gy to the dosimeter can be related to the change in absorbance, ΔA_λ, in ODU as follows:

$$\begin{aligned} D &= \Delta[Fe^{3+}] \, \frac{100 \, N_A \, e}{\rho \, G(Fe^{3+})}, \\ &= \frac{\Delta A_\lambda}{\varepsilon_\lambda \, l} \, \frac{100 \, N_A \, e}{\rho \, G(Fe^{3+})}, \end{aligned} \tag{4.6}$$

where $\Delta[Fe^{3+}]$ is the change in the molar ferric ion concentration, ρ is the density of the dosimeter in kg/l, $G(Fe^{3+})$ is the G-value for the ferric ion in

#/100 eV, N_A is Avogadro's number, and 'e' is the number of Joules per electron volt.

The response of the optical density to dose and to Fe^{2+} and Fe^{3+} ion concentrations was measured for the various Fe^{2+} and Fe^{3+} ion gelatin systems mentioned in Section 4.3.1. These data provided the $\Delta A_\lambda/D$ and ε_λ necessary to determine the $G(Fe^{3+})$ for the different systems. All these optical density measurements were made at a wavelength of 304 nm and at 25°C using a Spectronic 1001 spectrophotometer (Bausch and Lomb Canada, Longueuil, Québec). This wavelength corresponds to one of the two peaks in the absorption spectrum of a 0.4 M H_2SO_4 and Fe^{3+} solution which has a corresponding extinction coefficient of 2205 ODU M^{-1} cm^{-1} at 25°C (ICRU Reports No. 17 (1970) and 21 (1972)). The extinction coefficient for the Fe^{2+} ion at 304 nm is negligible.

The dose rate calibration of the BANG gel irradiation setup was accomplished with Fricke dosimetry by irradiating the aqueous Fricke samples for a known time and measuring the optical density of the Fricke solution in a quartz cuvet with a 1 cm path length. The optical densities were measured at 304 nm and 25°C on a Beckman dual beam spectrophotometer (Fullerton, CA) with a Gilford adaptation (heated chamber). The dose absorbed by the sample was then determined using Eq. 4.6, with ε_λ = 2205 ODU M^{-1} cm^{-1} and $G(Fe^{3+})$ = 15.5 ions/100 eV (Attix, 1986).

CHAPTER FIVE

Results and Discussion: Ferrous Sulfate-Doped Gels

While some of the radiation chemistry and practical aspects of the ferrous sulfate-doped gel dosimeters have been investigated in the past (see Section 3.2.4), a physical model for the R_1-dose response of the water protons in gel dosimeters has not been developed. Such a model is presented for gelatin-based dosimeters. It extends the three-site fast exchange model for the aqueous Fricke system (see Section 3.2.2) by including a term for water hydrating the gelatin. While this extension may seem trivial, it is complicated by effects of the gelatin on the iron ion hydration. Furthermore, a model for the R_1-dose response also allows for an absolute dosimetry whereby the absorbed dose can be derived from fundamental physical variables instead of a calibration of the dosimeter's response.

The model for the R_1-dose response allows for a better understanding of the two mechanisms governing the dose response: the chemical response of the dosimeter to dose and the response of R_1 to the ferric (Fe^{3+}) ion produced by radiation-induced oxidation of the ferrous (Fe^{2+}) ion in the dosimeter. The chemical response and the R_1-response are described by the ferric ion G-value ($G(Fe^{3+})$) and the ion relaxivities (r^{2+} and r^{3+}), respectively. The effects of gelatin concentration and sulfuric acid concentration on $G(Fe^{3+})$ and $r^{2+,3+}$ are studied, and the results are examined for possible ways of optimizing the dosimeter. The fast exchange model is verified in two ways. First, it is

compared to the r^{2+} and r^{3+} data. Second, the $G(Fe^{3+})$ or *NMR G-value*, determined using the NMR model, is compared to the $G(Fe^{3+})$ determined by standard spectrophotometry techniques (see Section 4.4). (Note that the conclusions to this chapter are presented in Chapter 7).

5.1 Results

In order to establish the model relating the NMR spin-lattice relaxation rate to dose, two categories of data were obtained. One category of data established the dependence of R_1 on the Fe^{3+} and Fe^{2+} ion concentrations; for a linear dependence, the relaxivity of the ions was determined as the slope of a fit through the data. The other category of data established the dose dependence of R_1; the dose sensitivity was determined as the slope of the linear portion of these data. The plots of the data used to determine relaxivities and dose sensitivities are referred to as *relaxivity plots* and *dose sensitivity plots*, respectively. The dose sensitivities and relaxivities were then used to calculate the NMR G-values for the Fe^{3+} ion. Spectrophotometry G-values were also determined for comparison using measured absorbance dose sensitivities and extinction coefficients. The G-value results are summarized later in Table 5.1. While many of the results have appeared in previously published works (Audet *et al.*, 1993; Audet and Schreiner, 1994; Audet and Schreiner, 1995), they were all based on this thesis work and are presented here for the first time in a complete and comprehensive fashion.

Figure 5.1 gives relaxivity plots in which longitudinal relaxation rates, R_1, are shown as a function of the Fe^{2+} and the Fe^{3+} ion concentrations for various gelatin concentrations (in percent weight fraction). The measurement error for all relaxation rate data shown in Fig.'s 5.1 to 5.4 is <1% which is

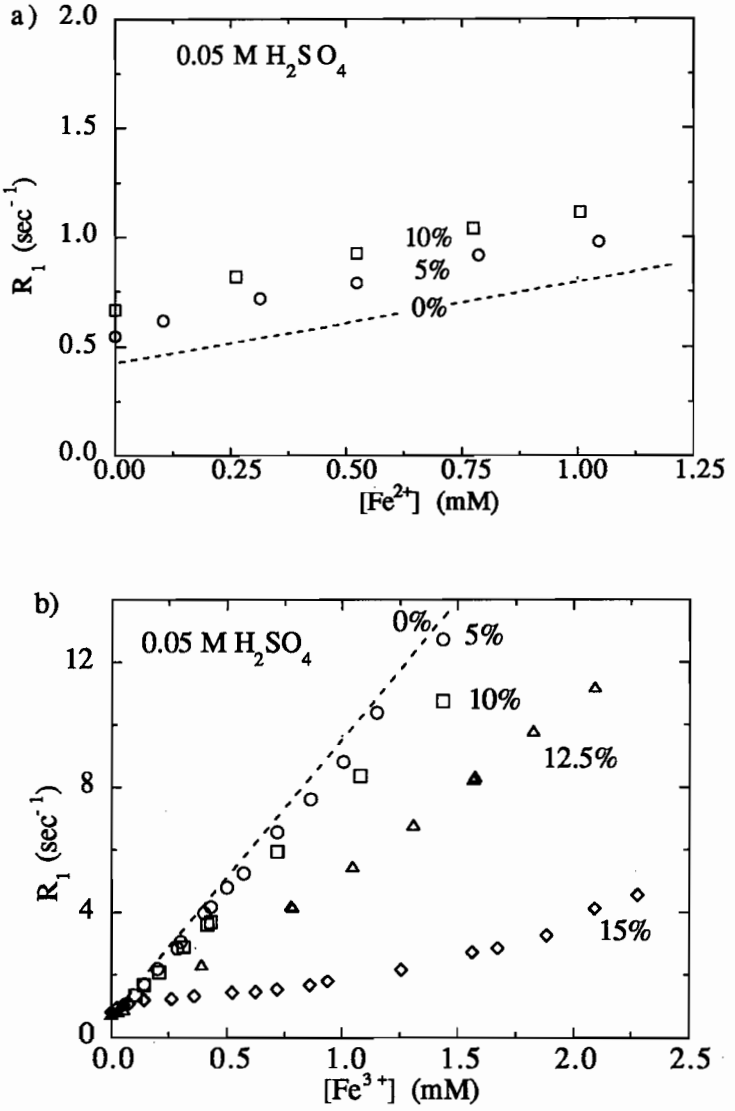

Figure 5.1 The spin-lattice relaxation rate dependence on the paramagnetic ion concentration in gels having different gel concentrations labeled on the graph (in % by weight). The data are shown for both a) ferrous ions, Fe^{2+} and b) ferric ions, Fe^{3+}. All samples contained 0.05 M sulfuric acid. The measurement error for the relaxation rates is < 1% which is smaller than the data symbols.

smaller than the data symbols. The solvent used to make the samples contained 0.05 M sulfuric acid according to the established preparation protocol (Appleby *et al.*, 1988; Olsson, 1991; Hazle *et al.*, 1991). The Fe^{2+} ion data for the different gelatin concentrations follow parallel lines whose intercepts increase with increasing gelatin concentration. The slopes of the three lines give an average relaxivity, r^{2+}, of $0.41 \pm 0.02\ s^{-1}mM^{-1}$ for the Fe^{2+} ion. (Note that unless stated otherwise all uncertainties presented are the standard deviations determined from least squares fits). The intercepts of the lines seem to overestimate the rates measured for the 0 mM Fe^{2+} ion concentration which were not included in the fits.

The behavior for the Fe^{3+} ion is quite different from that of the Fe^{2+} ions; in particular the Fe^{3+} relaxivity seems to vary with gelatin concentration. The data for the 5% and 10% gel concentrations are essentially linear; the measured zero Fe^{3+} ion concentration is slightly greater than the intercept of the linear fit. The slopes decrease with increasing gelatin concentration and give relaxivities, r^{3+}, ranging from 7.12 to 8.99 $s^{-1}mM^{-1}$ for gelatin concentrations ranging from 0% to 10% For the higher gelatin concentrations, 12.5% and 15%, the data are no longer linear, and the R_1 values are not stable over time.

Figure 5.2 shows the effect of increasing the sulfuric acid concentration, from 0.05 M (see Fig. 5.1) to 0.19 M, on r^{2+} and r^{3+} for the 5% and 10% gelatin concentrations. The Fe^{2+} ion data for 0.19 M H_2SO_4 follow the same behavior as that observed for 0.05 M H_2SO_4, and r^{2+} remains 0.41 $s^{-1}mM^{-1}$. For a given gelatin concentration, the r^{3+} increases with sulfuric acid concentration. For 0% gelatin, r^{3+} ranges from 8.99 $s^{-1}mM^{-1}$ to 9.17 $s^{-1}mM^{-1}$ for an increase in sulfuric acid concentration of 0.05 M to 0.19 M. For 10% gelatin, r^{3+} ranges from 7.12 $s^{-1}mM^{-1}$ to 8.73 $s^{-1}mM^{-1}$ for an increase in sulfuric acid

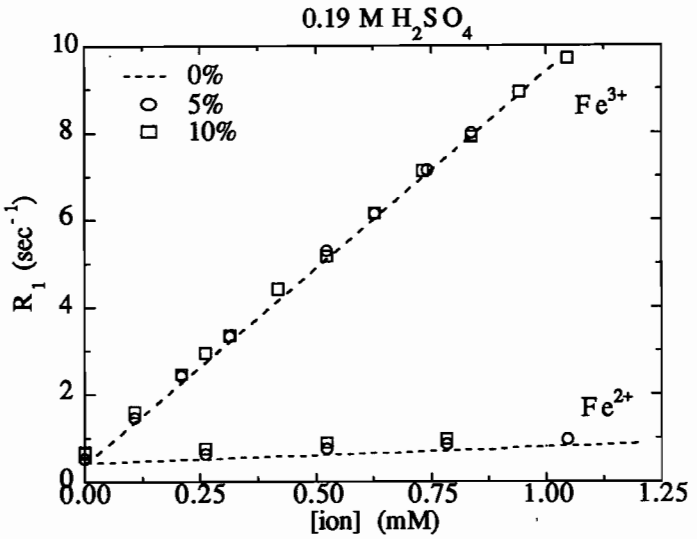

Figure 5.2 Ferrous and ferric ion relaxivity plots for various gelatin concentrations (% by weight) and 0.19 M H_2SO_4.

concentration of 0.05 M to 0.19 M. Also, at 0.19 M H_2SO_4 discrepancies no longer exist between the rates for the zero Fe^{3+} ion concentration and those predicted by the fit intercepts.

As the ferrous sulfate-doped gelatin dosimeter is irradiated the ratio of the Fe^{3+} to Fe^{2+} ion concentrations increases while the sum of the two quantities remains fixed at the initial ferrous ion concentration. This radiation effect was mimicked by preparing samples with varying ratios of Fe^{3+} to Fe^{2+} ion concentrations while keeping the sum of the two concentrations constant at 1 mM. The spin-lattice relaxation rates of such samples (5% gelatin and 0.19 M H_2SO_4) are plotted in Figure 5.3 as a function of increasing Fe^{3+} ion concentration and decreasing Fe^{2+} ion concentration. The resulting slope of $8.43 \pm 0.05\ s^{-1}mM^{-1}$ agrees very well with the difference in the measured ion relaxivities, r^{3+}-r^{2+}, of $8.54 \pm 0.07\ s^{-1}mM^{-1}$ represented by the dashed line.

The R_1-dose dependence of the ferrous sulfate-doped gelatin dosimeter was investigated. Figure 5.4 shows R_1 as a function of dose for samples containing 0.05 and 0.19 M H_2SO_4, and 5% and 10% gelatin. The data show a linear behavior until about ~ 40 Gy, where the rates begin to level off. The R_1-dose sensitivities are listed in Table 5.1 for the various acid and gelatin concentrations, and the dynamic range is ~ 1.6 s^{-1}. The results in Table 5.1

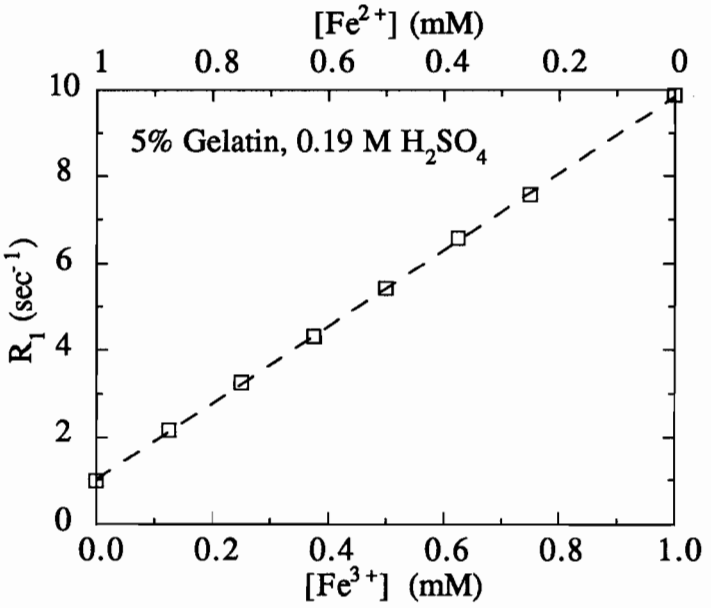

Figure 5.3 Effect of increasing the ratio of ferric to ferrous ion concentrations (left to right) on the spin-lattice relaxation rate of a 5% gelatin and 0.19 M H_2SO_4 solution, the total ion concentration is maintained at 1 mM (= $[Fe^{2+}]$ + $[Fe^{3+}]$). This variation of ion concentrations mimics radiation effects. The slope of the dashed curve is the difference in the Fe^{3+} and Fe^{2+} relaxivities ($r^{3+} - r^{2+} \sim 8.54\ s^{-1}mM^{-1}$).

indicate that the NMR dose sensitivity decreases with decreasing sulfuric acid concentration and with increasing gelatin concentration.

Spectrophotometric measurements, including extinction coefficients and spectrophotometric dose sensitivities, were also made to support the NMR observations. The extinction coefficient ε, the spectrophotometric analog of ion relaxivity, is defined as the change in absorbance in Optical Density Units (ODU) per unit increase in Fe^{3+} ion concentration in mM and per unit optical path length in cm (ODU mM^{-1} cm^{-1}). The spectrophotometric dose sensitivities, given in ODU Gy^{-1}, are determined as the slope of the linear

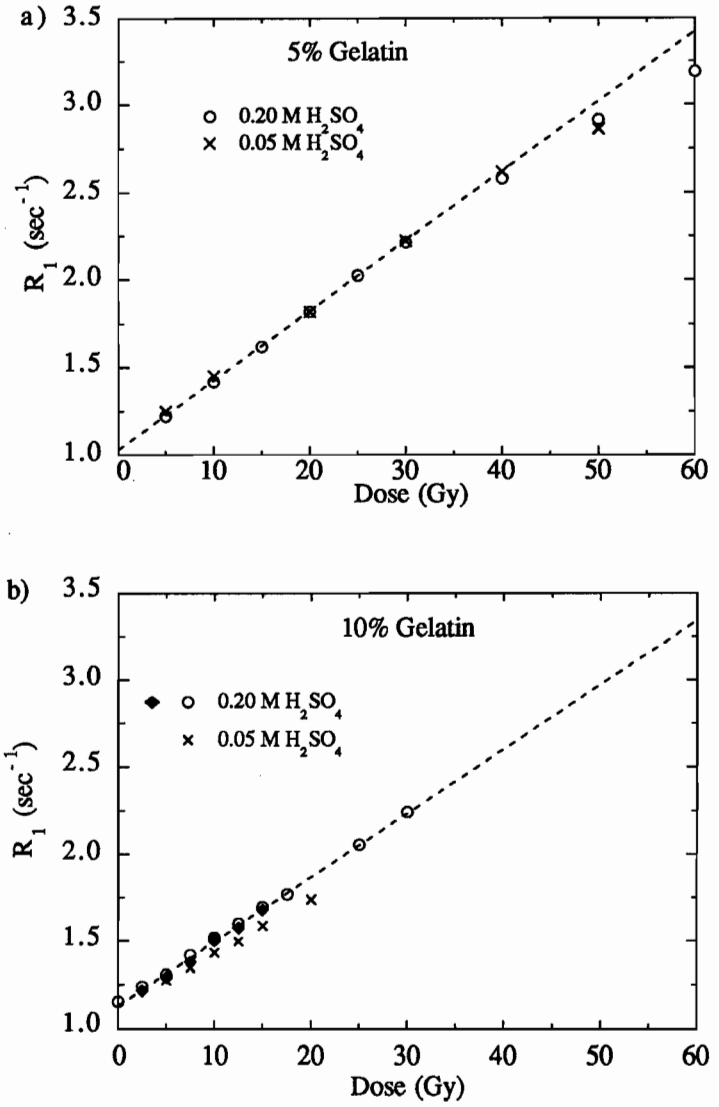

Figure 5.4 R_1-dose responses for a) 5% gelatin and b) 10% gelatin and 0.05 M and 0.19 M H_2SO_4. The dose sensitivities (slopes) decrease with increasing gelatin concentration and decreasing sulfuric acid concentration. The dashed lines represent fits to the linear portion of the R_1 dose-response for 0.19 M H_2SO_4. Saturation of the R_1-dose response begins at about 40 Gy because of the depletion of oxygen in the dosimeter.

portion of absorbance versus dose data. Dose sensitivity plots are shown in Fig 5.5 for 0.19 M H_2SO_4 ferrous sulfate doped-gelatin samples containing a) 5% gelatin and b)10% gelatin. The extinction coefficients and spectrophotometric dose sensitivities decrease with increasing gelatin concentration and decreasing acid concentration; this is the same behaviour which was observed in the relaxivity studies.

The NMR and spectrophotometry data along with the derived G-values are reviewed in Table 5.1.

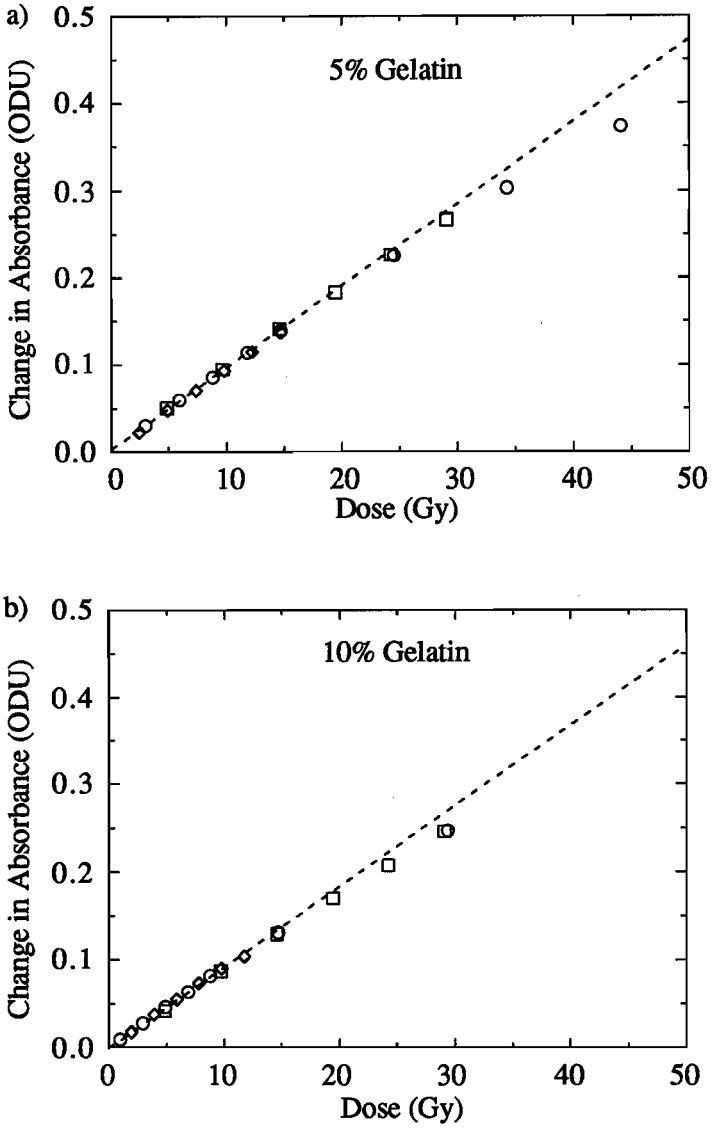

Figure 5.5 The spectrophotometric absorbance-dose response for a) 5% gelatin and b) 10% gelatin at 0.19 M H_2SO_4. The different points represent samples from different batches, and their agreement indicate very good reproducibility. The dashed lines represent fits to the linear portion of the responses. The slopes of the lines are 0.0093 and 0.0091 ±`0.0001 ODU Gy^{-1} for 5% and 10% gelatin, respectively.

Table 5.1

Calculated NMR and spectrophotometric G-values for various sulfuric acid and gelatin concentrations. The $r^{2+}=0.41 \pm 0.01\ s^{-1}mM^{-1}$ for all samples. The NMR G-values were derived using Eq. 5.14 presented in Section 5.2.5.

		NMR		
$[H_2SO_4]$ (M)	[gelatin] (% by wt.)	r^{3+} ($s^{-1}mM^{-1}$)	dose sensitivity ($s^{-1}Gy^{-1}$)	G #Fe^{3+}/100eV (± 4%)
0.05	0	8.99 ± 0.04		
	5	8.50 ± 0.07	0.0390 ± 0.0003	45.9
	10	7.12 ± 0.06	0.0309 ± 0.0006	43.4
0.19	0	9.17 ± 0.09		
	5	8.95 ±0.05	0.0399 ± 0.0002	44.4
	10	8.73 ± 0.06	0.0370 ± 0.0006	42.9
0.40	0	9.82 ± 0.09	0.0154 ± 0.0002	15.8
0.036	0	7.46 ± 0.07		

		Spectrophotometry		
$[H_2SO_4]$ (M)	[gelatin] (% by wt.)	extinction coefficient (ODU $mM^{-1}cm^{-1}$)	dose sensitivity (ODU Gy^{-1}) ± 0.0001	G #Fe^{3+}/100eV (± 4%)
0.05	0			
	5	2.080 ± 0.014	0.0097	44.6
	10	1.955 ± 0.013	0.0085	41.7
0.19	0			
	5	2.063 ± 0.014	0.0097	44.8
	10	1.998 ± 0.029	0.0091	43.1
0.40	0	†2.205 ± 0.033	0.0035	15.3
0.036	0	1.932 ± 0.028		

† extinction coefficient suggested by ICRU Reports No. 17 (1970) and 21 (1972);

5.2 Discussion

The fast exchange model relating the measured spin-lattice relaxation rate of the water protons to dose is presented (Section 5.2.1). The model is then compared to the relaxivity data (Section 5.2.2) and subsequently modified to account for the anomalous behavior observed for the ferric ion relaxivity data (Section 5.2.3). The R_1-dose sensitivity data are discussed in Section 5.2.3. To verify the model, the NMR G-values, determined using the model and the relaxivity and dose sensitivity data, are compared to the spectrophotometric G-values (Section 5.2.5).

5.2.1 Four-Site Fast Exchange Model for the R_1-Dose Response

The spin-lattice relaxation of water protons in an irradiated ferrous sulfate doped-gelatin dosimeter depends on the four groups of water existing in their associated environments: the bulk water, the water hydrating the Fe^{2+} and Fe^{3+} ions, and the water hydrating the gelatin. More specifically, it depends on the inherent relaxation rate of each group, R_1^i, where i=2+, 3+, gel or water, and the exchange of magnetization occurring between the groups and the protons fraction in each group (recall Section 2.6). The water is expected to exchange quickly between the four environments so that relaxation in the ferrous sulfate doped gelatin dosimeter should fall under the fast exchange regime. Fast exchange is expected, because it exists in both the aqueous Fricke (Gore *et al.*, 1984; Podgorsak and Schreiner, 1992) and the aqueous gelatin systems (Maquet *et al.*, 1986). In the limit of fast exchange, the magnetization recovery is characterized by a single exponential and hence by

single apparent longitudinal relaxation rate, R_1, where R_1 is equivalent to λ^- in Eq. 2.43, Section 2.6. Different expressions for the apparent rate can be derived along the same lines as in Section 3.2.2. To begin with, R_1 is simply the sum of the inherent rates each weighted by the fraction of protons, p^i, in their respective groups, i.e.,

$$R_1 = p^{3+} R_1^{3+} + p^{2+} R_1^{2+} + p^{gel} R_1^{gel} + \left(1 - p^{3+} - p^{2+} - p^{gel}\right) R_1^{water}. \qquad (5.1)$$

The proton fractions can be expressed in terms of solute concentrations as follows:

$$p^{3+} = k^{3+}[Fe^{3+}],\ p^{2+} = k^{2+}[Fe^{2+}],\ \text{and}\ p^{gel} = k^{gel}[gel], \qquad (5.2)$$

where k^i is the fraction of water protons hydrating solute i, per unit solute concentration [i]. Regrouping the terms in Eq. 5.1 the following is obtained:

$$R_1 = k^{3+}\left(R_1^{3+} - R_1^{water}\right)\left[Fe^{3+}\right] + k^{2+}\left(R_1^{2+} - R_1^{water}\right)\left[Fe^{2+}\right] + k^{gel}\left(R_1^{gel} - R_1^{water}\right)[gel] + R_1^{water}. \qquad (5.3)$$

The coefficients of the concentrations in Eq. 5.3, $k^i(R_1{}^i - R_1{}^{water})$, specify the ability of a solute to enhance spin-lattice relaxation of water protons, and are the relaxivities, r^i, of the respective solutes. As mentioned previously, the relaxivities can be measured as the slopes of R_1 versus [i] plots. Expressing Eq. 5.3 in terms of relaxivities and noting that the sum of the Fe^{2+} and Fe^{3+} concentrations is always equal to the Fe^{2+} concentration prior to irradiation, $[Fe^{2+}]_o$, the following is obtained (Audet *et al.*, 1993; Audet and Schreiner, 1995):

$$R_1 = \left(r^{3+} - r^{2+}\right)\left[Fe^{3+}\right] + R_o, \qquad (5.4)$$

where R_o is a constant for a given gelatin concentration and is given by,

$$R_o = \left\{ r^{2+}\left[Fe^{2+}\right]_o + r^{gel}[gel] + R_1^{water} \right\}. \qquad (5.5)$$

A similar fast exchange model has been proposed for the R_2-dose response of ferrous sulfate-doped gelatin dosimeters by Duzenli *et al.* (1994). However, the term accounting for the chemical shift between hydration water and bulk water protons, which could influence R_2, was not considered (see Eq. 2.44 for λ_2^- ($\equiv R_2$)). This term does not affect R_1.

The basis for using spin relaxation as a probe for radiation dose in general, and R_1 in particular, is indicated by Eq. 5.4. R_1 depends on dose because of the difference in the relaxivities of the Fe^{2+} and Fe^{3+} ions, and the dependence of the Fe^{3+} ion concentration on dose. The relaxivity difference is a more suitable parameter than the ratio R_1^{3+}/R_1^{2+} for quantifying the ability of R_1 to detect variations in Fe^{3+} concentration.

The radiation induced change in concentration of Fe^{3+} in mM as a function of dose is,

$$\Delta\left[Fe^{3+}\right] = \left[Fe^{3+}\right] - \left[Fe^{3+}\right]_o = D\, G\left(Fe^{3+}\right) \frac{10\,\rho}{N_A\, e}, \qquad (5.6)$$

where $G(Fe^{3+})$ is in number of ions per 100 electron volts, N_A is Avogadro's number, ρ is the density in kg/liter and e is the number of Joules per electron volt. Substituting Eq. 5.6 into Eq. 5.4 and assuming that initially $[Fe^{3+}]_o=0$, one obtains,

$$\begin{aligned} R_1 &= \left\{ G\left(Fe^{3+}\right)\left(r^{3+} - r^{2+}\right) \frac{10\,\rho}{N_A\, e} \right\} D + R_o \,, \\ &= d\, D + R_o \,, \end{aligned} \qquad (5.7)$$

where the coefficient of the dose, d, is the dose sensitivity of the dosimeter. The fast exchange model for the R_1-dose response suggests a linear

relationship between R_1 and D for constant d. A linear dependence over a dose range has been established experimentally for various ferrous sulfate-doped gel dosimeters (see Sections 3.2.4 and 5.1) indicating that the dose sensitivity is constant with dose. Beyond the linear dose range the response eventually saturates to a certain R_1-value because oxygen depletion decrease the G-value (Duzenli *et al.*, 1994; Keller, 1993). The dose sensitivity is determined experimentally as the slope of the linear portion of the R_1 versus dose plot. Equation 5.7 indicates that the dose sensitivity is governed by two mechanisms: the response of the dosimeter to radiation as described by $G(Fe^{3+})$ and the response of R_1 to the ions as described by $(r^{3+}-r^{2+})$.

5.2.2 Relaxivity Determination and the Effect of pH

Gelatin systems containing Fe^{3+} or Fe^{2+} ions, separately, were used to determine r^{3+} and r^{2+}, respectively. For these systems, Eq. 5.4 simplifies to,

$$R_1 = r^i\left[Fe^i\right] + \left\{r^{gel}[gel] + R_1^{water}\right\}, \qquad (5.8)$$

where i=2+ or 3+. The fast exchange model represented by Eq. 5.8 assumes that ion relaxivities, r^i, are not affected by the presence of gelatin, and are the same as those in pure aqueous solutions, i.e., [gel]=0. Hence, for both the Fe^{2+} and Fe^{3+} ions the R_1 versus ion concentration data for different gelatin concentrations should follow parallel lines of identical slope ($=r^i$). Also, the intercepts of these lines should increase with increasing gelatin concentration by an amount r^{gel} [gel] (see Eq. 5.8).

For the Fe^{2+} data, the expected behavior is observed although a slight non-linearity exists at 0 mM Fe^{2+} where the linear fits to the data slightly overestimate R_1 (see Fig. 5.1a). Similar behavior was observed by Hazle *et al.*,

(1991), and may be attributed to a slight spontaneous oxidation of the Fe^{2+} ion in the time between preparation and NMR measurement. The r^{2+} was measured as 0.41 $s^{-1}mM^{-1}$ for all gelatin concentrations. The Fe^{3+} ion data on the other hand does not follow the expected behavior (see Fig. 5.1b). The R_1 values decrease with increasing gelatin concentration, the r^{3+} are not constant but increase with [gelatin] and for gelatin concentrations exceeding 12% the R_1 dependence on [Fe^{3+}] is no longer linear.

An alternate comparison of NMR data and the fast exchange model are shown in Figure 5.6 in which the R_1 of various Fe^{2+} and Fe^{3+} gels is plotted versus gelatin concentration (Keller, Audet and Schreiner, 1993). The predicted R_1 dependences on gelatin concentration (See Eq. 5.8) for the various gels are shown as lines. They were determined using values for r^{2+}, r^{3+} and r^{gel} measured for separate aqueous Fe^{2+}, Fe^{3+} and gelatin systems, respectively. The data for samples with a constant Fe^{2+} ion concentration (~1 mM) and for samples with constant gelatin concentration agree with the model whereas those for samples with a constant Fe^{3+} ion concentration (~0.137 mM) do not. A lower Fe^{3+} concentration was used in order to obtain R_1 values comparable to those of the other two gel systems.

The disagreement observed in Fig.'s 5.1b and 5.6 between the R_1 data for the Fe^{3+} ion-doped gelatin and the R_1's predicted by the fast exchange model suggests a break down of the model. The model may misrepresent the spin-lattice relaxation in the Fe^{3+} ion and gelatin system for a number of reasons: fast exchange may not exist between the water hydrating the Fe^{3+} ion and bulk water, or fast exchange may exist but the presence of the gelatin may affect the

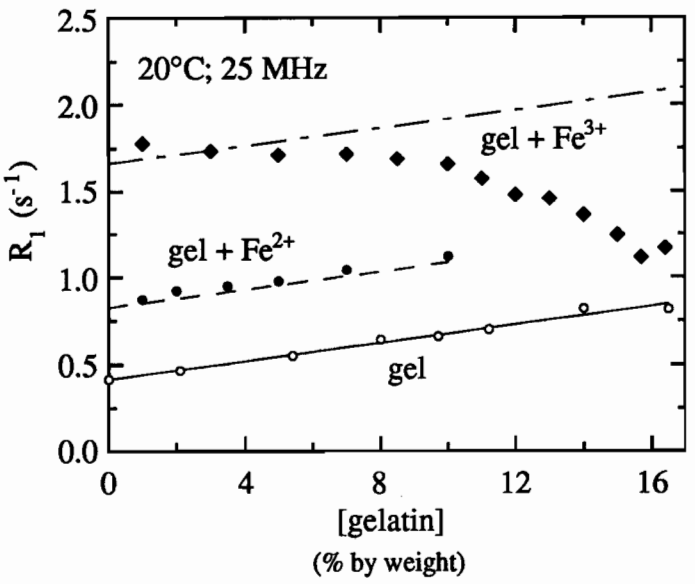

Figure 5.6 Effect of gelatin concentration on R_1 for three different systems: 1) gelatin + water, 2) gelatin + water + 1mM Fe^{2+} and 3) gelatin + water + 0.137 mM Fe^{3+} (Keller *et al.*, 1993). The samples contained 0.05 M sulfuric acid and 1 mM sodium chloride. The solid line is a fit to the data whereas the dashed lines represent the predictions of the model expressed in Eq. 5.8.

system so that the fraction of water protons hydrating the ferric ions (k^{3+}), or the inherent rate of the water hydrating the ion ($R_1{}^{3+}$) vary with Fe^{3+} ion concentration. Fast exchange probably exists for the ferric ion and gelatin system because it exists separately in both the pure aqueous ferric ion solution (Gore *et al.*, 1984; Podgorsak and Schreiner, 1992) and in the gelatin systems (Maquet *et al.*, 1986). Also, it is highly unlikely that the fast exchange would occur for the Fe^{2+} ion, whose data in Fig.'s 5.1a and 5.6 supports the fast exchange model, but not the Fe^{3+} ion. It is much more likely that the gelatin perturbs the influence of the Fe^{3+} ion on R_1 by altering k^{3+} and/or $R_1{}^{3+}$, but does not perturb the influence of Fe^{2+} on R_1. Any parameter affecting the normal hexaquo hydration configuration of the Fe^{3+} will affect k^{3+} since k^{3+} is the fraction of protons hydrating Fe^{3+} per unit concentration of Fe^{3+}. Also any parameter affecting the dynamics or correlation time of the water hydrating the Fe^{3+} ion will affect $R_1{}^{3+}$ (see Section 2.4).

The gelatin can affect k^{3+} or R_1^{3+} either indirectly, by changing the initial pH of the solvent, or directly, by binding with the ion (Audet *et al.*, 1993; Duzenli *et al.*, 1994; Audet and Schreiner, 1995). The pH changes occur because gelatin is amphoteric, meaning that the gelatin can act as a base in an acidic solvent with its amino groups gaining hydrogen ions or as an acid in a basic solvent with its carboxyl groups losing hydrogen ions. When gelatin was added to a 0.05 M H_2SO_4 solvent, a change in pH of 1 to 2 was observed for concentrations ranging from 0 to 12.5% by weight. Similar results were observed by Duzenli *et al.*, 1994. An increase in pH causes an increase in the formation of ferric ion hydroxide complexes. The following reaction represents complexing,

$$\left(Fe(H_2O)^6\right)^{3+} \Leftrightarrow \left(Fe(H_2O)^5OH\right)^{2+} + H^+ \qquad (5.9)$$

Equation 5.9 shows how, according to LeChatelier's principle, an increase in pH (or a decrease in hydrogen ion concentration) will force the reaction to the right so that more ion complexes are produced. The possible complexes that can form are $FeOH^{2+}$, $Fe(OH)_2^+$, $Fe_2(OH)_2^{4+}$ and $Fe(OH)_4^-$. The Fe^{3+} ions are able to form complexes at a pH of 3 or less whereas the Fe^{2+} ions, having a lower charge, only complex extensively above neutral pH (Koenig *et al.*, 1985). Figure 5.7 shows how complexing of the Fe^{3+} ion affects the number of water molecules hydrating the ion, that is, k^{3+}.

The binding of ferric ion onto the gelatin matrix may also affect k^{3+} and R_1^{3+}. The binding of Fe^{3+} occurs between the negative carboxylate groups (COO-) on gelatin molecules. As mentioned previously, the number of carboxylate groups existing in gelatin solutions is low in acidic environments and high in basic environments. Thus, extensive binding is not expected for the gelatin systems studied in this work. To verify this, additional

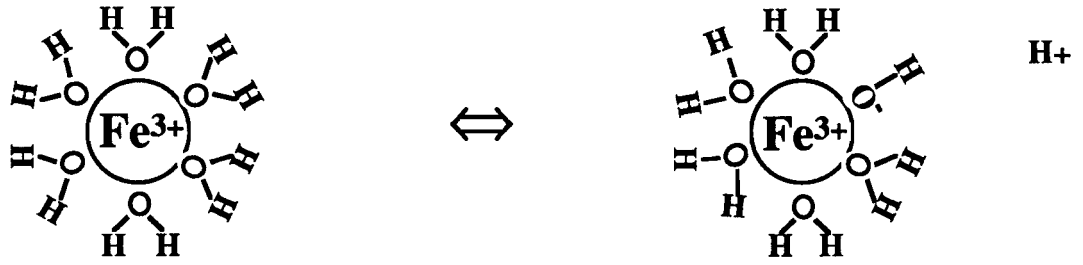

Figure 5.7 The schematic depicts the formation of a ferric ion hydroxide complex (right) from a ferric ion in its hexaquo form (left). The complexes are characterized by a decrease in the number of hydrogen atoms (protons) found in the hydration sphere of the ion.

experiments were performed on the 10% gelatin and 0.05 M H_2SO_4 solution. In particular the r^{3+} for the Fe^{3+}-doped gelatin was compared to that for an aqueous Fe^{3+} solution having identical pH. The 0.05 M H_2SO_4 gel has a pH of ~ 1.38 as extrapolated from a plot of pH versus H_2SO_4 concentration (Duzenli *et al.*, 1994) for a 10% gelatin. The pH of 1.38 corresponds to a sulfuric acid concentration of 0.036 M in an aqueous solution. The ferric ion relaxivity in a 0.036 M H_2SO_4 aqueous solution was measured as 7.46 $s^{-1}mM^{-1}$. Given the error introduced by using the pH versus H_2SO_4 data by Duzenli *et al.* (1994), this relaxivity compares very well with the relaxivity of 7.12 $s^{-1}mM^{-1}$ measured for the 10% gelatin solution. Thus, complexing is also observed in the aqueous solution where no Fe^{3+} binding can occur, and hence it is largely responsible for the discrepancy between the ferric ion relaxivity for 10% gelatin and that predicted by the fast exchange model.

In order to reduce complexing, the gelatin induced pH increases were countered by increasing the concentration of H_2SO_4 to 0.19 M. The results in Fig. 5.2 show an increase in the ferric ion relaxivities for the 5% and 10% gelatin concentrations. However, unlike the ferrous ion data, the relaxivities are still less than that for the 0% gelatin indicating that complexing and pH increases still occur. Differing Fe^{3+} ion relaxivities are observed in the absence

of gelatin for varying H_2SO_4 concentrations (Table 5.1). Again this indicates that complexing and not binding is responsible for the observed r^{3+} behavior.

The gelatin relaxivity, r^{gel}, albeit for spin-spin relaxation, has also been found to vary with pH and the gelatin concentration (Duzenli *et al.*, 1994), however, this does not modify the model greatly. The increase of R_1 with dose depends on the dose sensitivity which is related to the difference of the relaxivities of the iron species in the dosimeter (recall the dose sensitivity is given by the terms in brackets in Eq. 5.7). The r^{gel} contributes only in establishing the zero dose intercept, R_0, which only shifts the R_1-dose response by a fixed amount. Thus, r^{gel} drops out of any calculation of absorbed dose in terms of changes in R_1.

5.2.3 Effective Fast Exchange Model for R_1

When the Fe^{3+} ion complexes, a number of water molecules are displaced from the hydration sphere of the ferric ion such that the hexaquo configuration assumed by the model is no longer maintained (see Fig. 5.6). A decrease in hydration water and thus, in k^{3+} (see Eq. 5.3), is consistent with the lowering of R_1, observed in Fig. 5.1, with the addition of gelatin for a particular Fe^{3+} concentration. The fast exchange model for R_1 expressed in Eq. 5.4 can be modified to take the various Fe^{3+} complexes into account. Each form 'j' may represent a different water environment with its own proton fraction p_j^{3+} and inherent spin-lattice relaxation rate, $R_{1,j}^{3+}$. The expression for the apparent relaxation rate, R_1, becomes,

$$R_1 = \sum_j p_j^{3+} R_{1,j}^{3+} + p^{gel} R_1^{gel} + \left(1 - \sum_j p_j^{3+} - p^{gel}\right) R_1^{water}, \qquad (5.10)$$

where $p_j^{3+} = k_j [Fe^{3+}]_j$. In terms of relaxivity, r_j^{3+} ($= k_j^{3+}(R_{1,j}^{3+} - R_1^{water})$), Eq. 5.10 becomes,

$$R_1 = \sum_j r_j^{3+} \left[Fe^{3+}\right]_j + \left\{r^{gel}[gel] + R_1^{water}\right\}. \qquad (5.11)$$

Equation 5.11 cannot be verified experimentally since it is difficult, if not impossible, to know what the concentrations and the relaxivities of the different Fe^{3+} complexes are for systems of a given pH, total ferric ion concentration and gelatin concentration. Equation 5.11 can be simplified for the Fe^{3+}-gelatin systems which exhibit a linear dependence of R_1 on Fe^{3+} (i.e., 5% and 10% gelatin and 0.19 M H_2SO_4 solutions). It can be assumed for these systems that because the relaxivity is constant with Fe^{3+} concentration, the fractions, f_j, of the different Fe^{3+} complexes are also constant with Fe^{3+} concentration. It then follows that,

$$\left[Fe^{3+}\right]_j = f_j \left[Fe^{3+}\right], \qquad (5.12)$$

where f_j is a pH-dependent fraction. Substituting Eq. 5.12 into Eq. 5.11, the following is obtained (Audet and Schreiner, 1994; Audet and Schreiner, 1995),

$$R_1 = \left(\sum_j r_j^{3+} f_j\right)\left[Fe^{3+}\right] + \{...\}, \qquad (5.13)$$

where the term in brackets, ($\Sigma r_j^{3+} f_j$), is an effective relaxivity, r_{eff}^{3+}, which is constant for given H_2SO_4 and gelatin concentrations. An important result of Eq. 5.13 is that the effective relaxivities may be determined experimentally, and that they are equivalent to the measured relaxivities reported in Table 5.1. Furthermore, the fast exchange model for the R_1-dose response expressed in Eq. 5.7 still holds. The decrease in r_{eff}^{3+} with increasing gelatin concentration and decreasing H_2SO_4 concentration (see Table 5.1) is consistent with

complexing-induced decreases in hydration water, and hence, in k_j^{3+}. Although less obvious, the complexing of Fe^{3+} ions may also cause the $R_{1,j}^{3+}$ to decrease. Decreases in both k_j^{3+} and $R_{1,j}^{3+}$ will cause the component r_j^{3+}'s ($= k_j^{3+}(R_{1,j}^{3+} - R_1^{water})$) of r_{eff}^{3+} to decrease also.

Duzenli *et al.*, (1994) have also determined the ion relaxivities of ferrous sulfate-doped gelatin dosimeters, but from 100 MHz R_2 data instead of 25 MHz R_1 data. The r_2^{2+} and r_2^{3+} for a 0.15 M H_2SO_4 and 12% gelatin system were 1.71 $s^{-1}mM^{-1}$ and 15.0 $s^{-1}mM^{-1}$, respectively. These relaxivities exceed those presented in Table 5.1 because the inherent rates are greater for spin-spin relaxation than spin-lattice relaxation at high frequencies (Duzenli *et al.*, 1994). The r_2^{3+} was also found to decrease with gelatin concentration to a value of 14.2 $s^{-1}mM^{-1}$ for an aqueous Fe^{3+} solution.

5.2.4 Dose Sensitivity Determination and the Dose Response

The ferrous sulfate gelatin dosimeter and R_1 were chosen to study dose response model because the dosimeter is easier to prepare and R_1 is easier to measure. Although these studies were not meant to optimize ferrous sulfate gel dosimetry and the measured dose responses are far from the best reported in the literature, the studies can still provide information on the effect of pH and gelatin concentration on the dose sensitivity, dynamic range and dose range.

Dose Sensitivity

The dose sensitivities for the different ferrous sulfate-doped gelatin systems were measured to determine the NMR G-value which was used to verify the dose response model. A dose sensitivity of 0.0399 $s^{-1}Gy^{-1}$ for the 5%

gelatin concentration agrees with previous measurements (Olsson, 1991; Hazle *et al.*, 1991). The dose sensitivities listed in Table 5.1 are much less than the 0.2 $s^{-1}Gy^{-1}$ observed by Gambriani *et al.* (1994) for the R_2-dose response of oxygenated agarose-based dosimeters and the 0.091 $s^{-1}Gy^{-1}$ observed by Duzenli *et al.*, (1984) for the R_2-dose response of oxygenated gelatin-based dosimeters. These dose sensitivities are greater because the gels are oxygenated, the Fe^{3+} G-values for agarose are greater, and the spin-spin relaxation is more sensitive to ferric ion concentration than spin-lattice relaxation (Duzenli *et al.*, 1994).

The decrease in dose sensitivity with increasing gelatin concentration indicated by the results agrees with previous observations made by Olsson *et al.* (1989) for agarose and gelatin-based dosimeters, and Duzenli *et al.* (1994) for gelatin-based dosimeters. However, Schulz *et al.* (1990) found that the dose sensitivity was independent of agarose concentration, and ascribed the discrepancy with Olsson's data to preparation procedures and agarose brand.

The increase in dose sensitivity with H_2SO_4 concentration indicated by the results summarized in Table 5.1 agrees with previous studies on gelatin-based gels (Duzenli *et al.*, 1994), but not those on agarose-based gels (Olsson *et al.*, 1990; Schulz *et al.*, 1990). The reason for this discrepancy in behavior for the two gel systems is not well understood and could be the subject of future research.

Dynamic Range and Dose Range

It has been shown that the dynamic range and dose range in ferrous sulfate gelatin dosimeters are limited by the saturation of the dose response due to oxygen depletion (Keller *et al.*, 1993; Duzenli *et al.*, 1994). The dynamic range and dose range indicated by Fig. 5.4 are ~ 1.5 s^{-1} and ~ 40 Gy, respectively. This data supports saturation by oxygen depletion, i.e., for the 5% gelatin and

0.19 M H_2SO_4 solution (Fig. 5.4a), the relaxivity of 8.9 $s^{-1}mM^{-1}$ and dynamic range of 1.5 s^{-1}, indicate a ferric ion concentration of about 0.17 mM at 40 Gy. Therefore, at 40 Gy, there is still 0.83 mM of Fe^{2+} available in the dosimeter for conversion. By oxygenating the dosimeters Keller (1993) and Duzenli *et al.* (1994) were able to extend the dynamic range to 3.5 s^{-1} and 7 s^{-1}, respectively, and the dose range to 80 Gy and 120 Gy, respectively. A greater dose range of 400 Gy and dynamic range of 7 s^{-1} was observed for the aqueous Fricke dosimeter (Podgorsak and Schreiner, 1992) than for the gelatin dosimeter. This is probably because more oxygen was lost in the gelatin dosimeter by reactions with the gelatin macroradicals (see Section 3.2.3, Eq. 3.24) and by the heating of the gel during preparation.

The spectrophotometric dose response of the ferrous sulfate gelatin dosimeters appears to saturate earlier than the NMR dose response. It is believed that the considerably smaller sample sizes used for the NMR studies accounts for this. For small samples, a large fraction of the volume is comprised of the surface area exposed to air and reoxygenation of the sample may be enhanced. Comparing surface area to volume ratios, 2.45 cm^{-1} is obtained for 80 µl samples in 0.5 cm I.D. NMR sample tubes and 0.22 cm^{-1} is obtained for 4.5 ml samples in cuvets with 1 cm^2 cross-sections.

The spectrophotometric dose responses measured for different batches of the 5% (Fig. 5.5a) and 10% (Fig. 5.5b) solutions, represented by the different symbols, agree well indicating good reproducibility. This result contradicts claims of poor reproducibility assumed for the Fricke-gelatin by some previous workers (Gambriani *et al.*, 1994; Prasad *et al.*, 1991).

5.2.5 NMR G-Values

The four-site effective fast exchange model for R_1 is verified in these studies by measuring the dose sensitivity and the relaxivities, calculating the NMR G-value and comparing it to that determined using spectrophotometry. Equation 5.7 can be used to express the NMR G-value in terms of the measurable quantities d and r^i as follows:

$$G(Fe^{3+}) = d \frac{1}{(r_{eff}^{3+} - r^{2+})} \frac{N_A e}{10 \rho} \quad . \tag{5.14}$$

This expression for the NMR G-value, first proposed by Audet *et al.* (1993), is similar in form to that presented by Gore *et al.* (1984) and Podgorsak and Schreiner (1992) for aqueous Fricke solutions. However, it is based on the effective fast exchange model for R_1 involving r_{eff}^{3+}, the effective relaxivity of the Fe^{3+} ion complexes in a particular gel dosimeter. The calculation of an NMR G-value, by Gambriani *et al.* (1994), for an agarose-based dosimeter using the r^{2+} and r^{3+} determined for aqueous Fricke solutions by Prasad *et al.* (1991) is questionable.

The G-values summarized in Table 5.1 show that the calculated NMR G-values and the spectrophotometric G-values agree within error, thus supporting the effective fast exchange model for the R_1-dose response in ferrous sulfate doped-gelatin dosimeters containing 0% to 10% gelatin and 0.05 M to 0.19 M H_2SO_4. The NMR G-value of $15.8 \pm 4\%$ ions/100eV determined for the aqueous Fricke dosimeter agrees very well with the independently established value of 15.6 ions/100 eV (ICRU Report No. 14, 1969). The G-value study excludes both the higher gelatin concentrations, characterized by complicated nonlinear relaxivity plots (see Fig. 5.1a), and acid

concentrations greater than 0.2 M, because the gels degrade and become too soft for clinical use.

The yields decrease slightly with gelatin concentration decreasing by about 5% for an increase in gelatin concentration of 5% to 10%. This result suggests that the R_1-dose response of the dosimeter is insensitive to slight variations in gelatin concentration. It contradicts claims made by Prasad *et al.* (1991) and Gambriani *et al.* (1994) that $G(Fe^{3+})$ is irreproducible for ferrous sulfate gelatin dosimeters. Organic impurities, such as gelatin, can cause irreproducible dose responses when they are present in a Fricke solution in small uncontrolled amounts (Allen, 1961). The stability of the ferric ion yield at high impurity concentrations has been observed by others. Studies on the ethanol doping of pure Fricke solutions (Podgorsak and Schreiner, 1992) show that the yield increases with ethanol concentration, and eventually saturates at a high enough concentration. Adding benzoic acid to ferrous sulfate doped-gelatin dosimeters has been shown to have little effect on the yield (see literature review; Section 3.2.4) for dosimeters already containing enough gelatin.

The NMR G-values do not change significantly when the H_2SO_4 concentration is varied from 0.05 M to 0.19 M. This result is at odds with the increase in G-value of 55 ions/100eV to 62 ions/100eV observed by Duzenli *et al.* (1994) for a 4% gelatin dosimeter in which the H_2SO_4 concentration was increased from 0.05 M to 0.15 M. However, it should be noted that in determining these G-values Duzenli *et al.*, assumed that r^{3+} remained constant with increasing $[H_2SO_4]$. This assumption is not the case and so the constant G may be inaccurate.

The conclusions derived from the studies presented in this chapter will be discussed in Chapter 7, Section 7.1.

CHAPTER SIX

Results and Discussion: BANG Polymer Gels

A novel polymer gel dosimeter for three dimensional radiation dosimetry using MRI has recently been introduced (Maryanski *et al.*, 1993). It is based on changes in the NMR relaxation properties of the water protons in the gel as the radiation induces polymerization and crosslinking of the monomers. The composition of the dosimeter was determined by considering the following: the dosimeter had to be tissue equivalent, rigid enough for handling, contain very reactive monomers and it had to have a sufficiently high crosslinking density to produce significant changes in the transverse relaxation rate upon irradiation (Maryanski *et al.*, 1994). While few compositional modifications and some practical applications have been reported previously (Maryanski *et al.*, 1994 & 1995, see Section 3.3.3), systematic studies of the effect of different composition, preparation and measurement parameters on the dose response of BANG gels have not yet been undertaken. These studies have been undertaken in this thesis. They enable the performance of the dosimeter to be optimized, and are required to better understand the underlying radiation response mechanisms and NMR behavior of the dosimeter. Of particular interest is the dose response of the spin-spin relaxation rate, R_2, of the water protons in the BANG gel dosimeter.

A practical preparation protocol was designed especially for these studies. Additional studies were performed to establish the reproducibility of the R_2-dose response for dosimeters prepared by this protocol (Section 6.1). A

physical model for the R_2-dose response of the BANG polymer gel dosimeter has been developed (Section 6.2). The model relates the R_2-dose response to the fundamental physical radiation and NMR parameters. Results of the effects of gelatin concentration, crosslinker fraction (%C), total monomer fraction (%T), and NMR measurement temperature on the R_2-dose response are reported and discussed in Section 6.3. The results were analyzed in terms of the effects on the physical parameters of the model and the parameters of the R_2-dose response to be optimized (i.e., dynamic range, dose sensitivity and dose range; Section 3.1.2). The studies presented in Section 6.3 were not intended to provide a comprehensive understanding of the mechanisms governing the dose response. Nonetheless, the resulting insight was deemed useful especially with regards to suggesting future research directions. (Note that the conclusions to this chapter are presented in Chapter 7).

6.1 Reproducibility Studies

The studies of polymer gel dosimeters published to date have been restricted to large volume phantoms containing liters of gel. These studies either involved measuring dose distributions in 3-D (Maryanski *et al.*, 1994 and 1995) or studying the dosimeter's R_2-dose response (Maryanski *et al.*, 1993 and 1994). For the R_2-dose response studies presented, it was considered more practical and less costly to prepare and irradiate small volumes (~ml) in the test tubes suitable for NMR analysis by the desk top spectrometer. The small volume dosimeters better accommodate, for example, the studies of the effect of gel composition on the R_2-dose response since a different dosimeter batch is required for each composition, and many batches are required to cover a range of compositions. The use of large volume gels would either have

involved the impractical extraction of samples for spectrometer analysis or the NMR characterization of whole gels using the MR imager. The use of the MR imager for the basic relaxation studies was avoided, because:

1) The availability of the imager is limited, and the complete characterization of composition effects would be very time consuming (in terms of imaging time for individual dosimeters and total time to analyze many samples). The study of the effect of the duration between irradiation and R_2-measurement on the R_2-dose response (Section 6.1.2) requires flexible access to the imager at hourly intervals over the period of days.

2) MR imagers are less precise than spectrometers for R_2-measurements (Rosen *et al.*, 1984; Johnson *et al.*, 1987). For spectrometers, the samples are in immediate contact with the rf transmitting and receiving coil, and the magnetization can be detected and analyzed directly with a good signal/noise ratio. For MR imaging, the magnetization data is spatially encoded using magnetic field gradients and the data is processed using reconstruction algorithms to produce image intensities. Since the intensities are a more indirect measure of magnetization data, the signal to noise ratio is much lower and the R_1 and R_2 determined using these intensities are less precise. MR images can also contain artifacts arising from rf attenuation and concurrent variations in flip angle throughout large sample volumes (Maryanski *et al.*, 1994). Other geometric distortions in MR images may also arise (Sumanaweera *et al.*, 1993 as cited in Duzenli, 1995).

The desktop spectrometer on the other hand was very accessible and was designed specifically to determine conveniently, quickly and accurately the spin relaxation rates of samples. It was more convenient than an MR imager

for the measurement temperature dependence study, because the long MR imaging times would have required a temperature controlled environment to keep a sample volume at a temperature other than room temperature.

The use of small sample volumes not only simplifies the NMR measurements, but also simplifies the preparation procedure. The main difference in procedure for the small and large volume gels was that the deoxygenation step was performed at different times. For the large volume gels, the monomer solution was deoxygenated prior to the addition of the gelatin powder and to the subsequent distribution into irradiation containers. The small volume gels on the other hand were purged of oxygen in the irradiation containers, i.e., test tubes, after the addition of the gelatin powder.

Although it was apparent that small samples were more appropriate for detailed R_2-dose response studies, they had not been used in the past because reproducible R_2-dose responses could not be achieved (Maryanski, 1994). The aim of the studies presented in this section was to establish reproducible R_2-dose responses for the small samples. Reproducibility is essential for the composition studies (Section 6.2) if the variations observed for the R_2-dose response as a function of composition are to be attributed to composition and not some unknown preparation factor. The reproducibility of the R_2-dose response for separately prepared polymer gel dosimeters had been demonstrated for a limited set of large volume phantoms (Maryanski *et al.*, 1994). Hence, it was expected that reproducible responses for small volume samples was feasible.

Figure 6.1 shows the radiation response of the water proton spin-spin relaxation rate for several batches of small volume gels prior to establishing a preparation protocol. The different symbols represent different batches of BANG gel, and the error bars represent a 2% measurement error applicable to

all points (this applies to the error bars in Fig.'s 6.2, 6.3, 6.4 and 6.6 as well). The error excludes any possible error due to preparation. As for all the studies in this section, the dosimeters were composed of 5% gelatin by weight, 67%C (unless stated otherwise) and 6%T; the NMR measurements were performed at 40° C (unless stated otherwise).

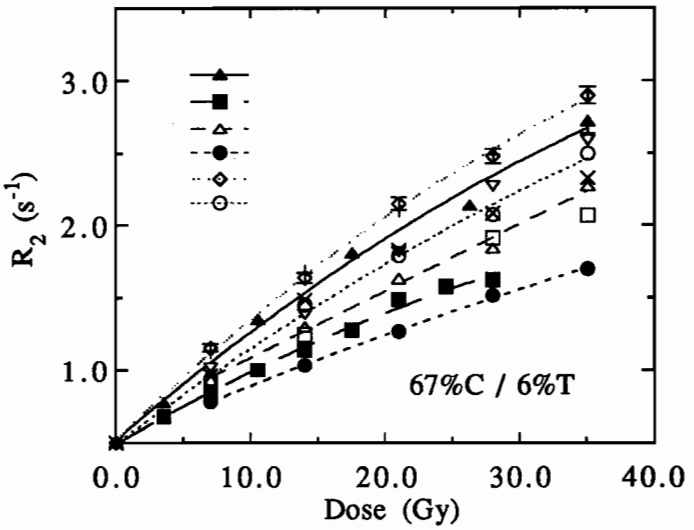

Figure 6.1 The pre-study reproducibility of the R_2-dose response is shown for several batches BANG gel dosimeter each represented by a different symbol. The error bars represent a 2% measurement error applicable to all points.

It is clear from Fig. 6.1 that the response of the different dosimeter batches varies drastically, with R_2 values of identically irradiated samples differing by as much as 100% at higher doses. Despite the variation it is encouraging that the data for each batch lie on a smooth curve with little scatter. This suggests that for each particular batch the dose response is well behaved and reproducible.

To determine the source of inter-batch irreproducibility the effect on the R_2-dose response of the bubbling gas, the temperature of irradiation, the cooling procedure prior to irradiation and the time delay between irradiation and measurement were investigated. The results are presented and discussed in the following sections.

6.1.1 Effects of Some Preparation and Irradiation Conditions

The preparation of small volume BANG gel dosimeters (see Section 4.2.2) involved mixing the gel, pouring them into separate test tubes, and then purging the melted samples of oxygen by bubbling them with gases such as nitrogen, argon or carbon dioxide. To avoid foaming during the bubbling of the gas through the gel, the purging gas was blown over the surface of the melted sample at a flow rate high enough to agitate the sample. Once deoxygenated, the samples were hermetically sealed and then cooled by immersion in a water bath for two hours to either 2° C or 20° C. The samples were then irradiated at these temperatures.

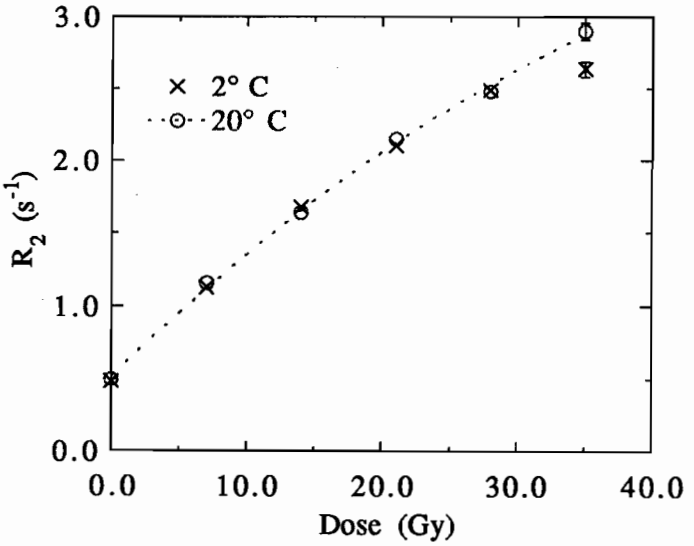

Figure 6.2 The effect of cooling and irradiation temperature on the R_2-dose response of BANG gel dosimeters.

Figure 6.2 shows the effect of the cooling and irradiation temperatures on the R_2-dose response of BANG gel dosimeter purged of oxygen with argon. The data observed at the two temperatures agree very well. This result agrees with those previously observed for the large volume BANG dosimeters irradiated at temperatures of 0°C and 25°C (Maryanski *et al.*, 1994). The

cooling temperatures in this study were not specified. Thus, it may be concluded that possible changes in the cooling and irradiation temperatures are not the source of the inter-batch irreproducibility observed in Figure 6.1.

Figure 6.3 shows the effect on the radiation response of using different gases to purge the oxygen from the dosimeter. The data for the argon bubbling gas and that for CO_2 do not differ significantly. Hence, the R_2-dose response seems unaffected by the choice of gases used to purge the oxygen from the gel.

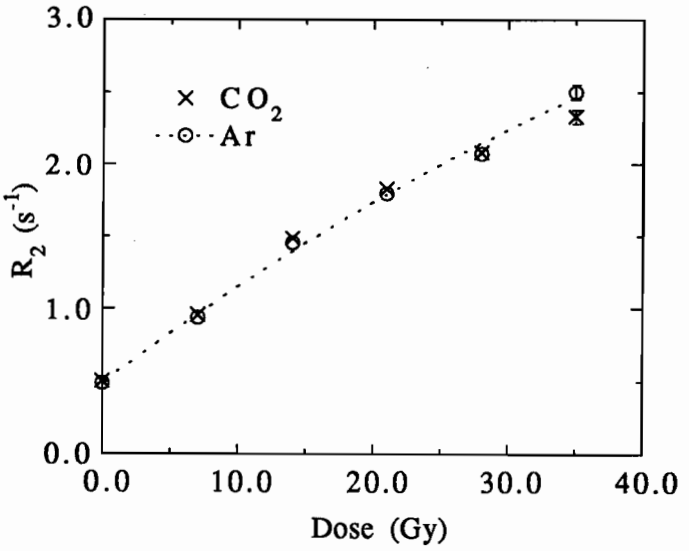

Figure 6.3 The effect of using different bubbling gases, CO_2 and argon, on the R_2-dose response of BANG gel dosimeters. The data for the two gases agree very well.

6.1.2 Effects of the Post-Irradiation Time

Figure 6.4 shows the spin-spin relaxation rate for two identical BANG gel samples irradiated to 33.6 Gy as a function of the time delay between irradiation and the NMR measurement of the samples. For one sample the R_2 was measured 3 hours after irradiation whereas for the other, designated longer-cured, R_2 was measured 2 days later. Subsequent measurements of R_2 yielded constant values, however, the value was greater for the longer-cured

sample (i.e., 2.5 s^{-1} instead of 1.4 s^{-1}). The longer-cured sample also appeared more opaque, indicating more crosslinked polyacrylamide had formed. These observations suggest that the polymerization and crosslinking reactions proceeded for some time after irradiation until the R_2 of the sample was measured. The stabilizing effect of the R_2 measurement probably has to do with the preparation of the samples for analysis. The preparation of any irradiated sample in these studies involved uncapping the sample and removing the amount of sample in excess of 1 ml (this volume is the limit allowed by the size of the rf coil in the spectrometer). In the process, the sample was exposed to oxygen which can inhibit crosslinking and polymerization (recall Section 3.3.1). Hence, oxygen can "fix" post-irradiation reactions before they terminate naturally. The 3 hour sample was exposed to oxygen sooner after irradiation, had less time for complete polymerization to occur and contained less polymer and had a lower R_2 than the longer-cured sample. The slow reaction kinetics will be discussed in further detail shortly.

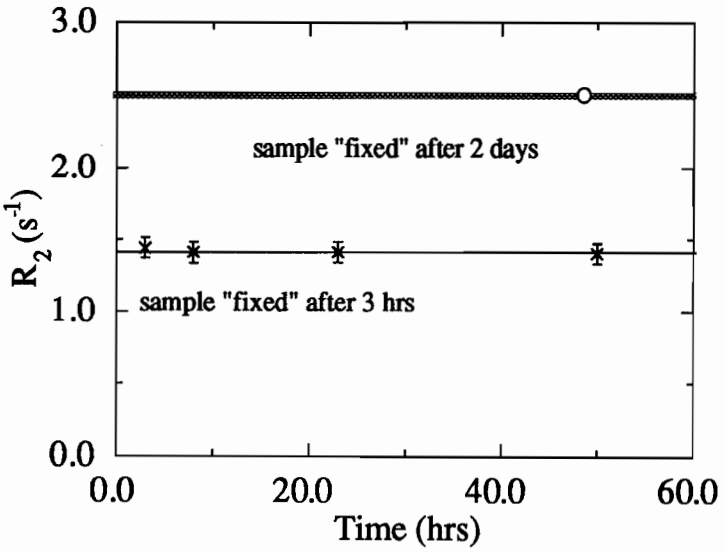

Figure 6.4 R_2 is shown as a function of the post-irradiation time for two 67%C samples irradiated to 33.6 Gy. R_2 was measured at 40°C. For one sample the analysis began 3 hours after irradiation whereas for the other analysis began two days later.

It may be argued that the post-irradiation reactions are not polymerization and crosslinking processes, but the progressive precipitation of insoluble polymer. Precipitation, however, cannot account for the constant R_2-value of a sample after it is exposed to oxygen since precipitation is not affected by oxygen.

Figure 6.5 shows the results of a more detailed post-irradiation time study of R_2 using a set of identical samples exposed to oxygen, or fixed, at different times. Two sets of R_2-data obtained at 20°C are shown for 67%C samples irradiated to 16.8 Gy, and 50% C samples irradiated to 7 Gy. The spin-spin relaxation rate increases with time and saturates at about 20 and 55 hours for the 50%C and 67%C BANG gels, respectively. The curves are meant as an aid to the eye.

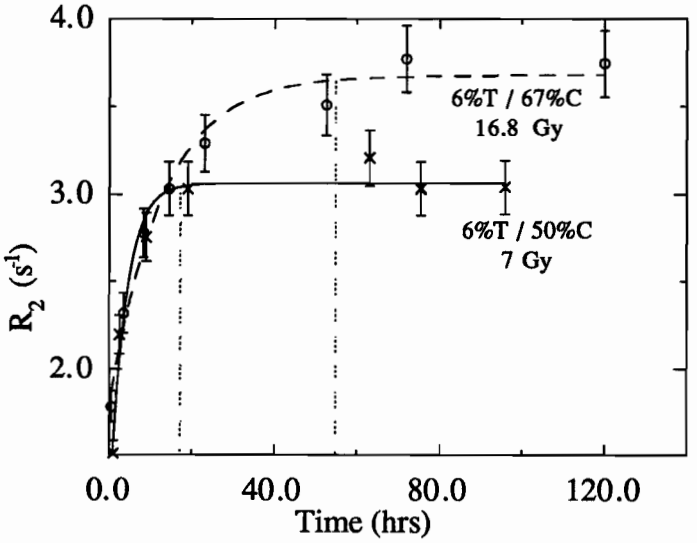

Figure 6.5
The detailed R_2-time responses are shown for a 67%C gel sample irradiated to 16.8 Gy and a 50%C gel irradiated to 7 Gy. R_2 was measured at 20°C. The response was obtained by exposing individual, identical samples to oxygen at different times. R_2 increases with time, and saturates at about 20 hours and 55 hours for the 50%C and the 67%C gels, respectively.

The results of Fig. 6.5 confirm that the radical polymerization and crosslinking reactions continue to propagate after irradiation. They also give a more precise determination of the duration of the reaction. The post-irradiation reaction explains the lack of agreement between the R_2-dose

responses in Fig. 6.1 for different batches of BANG gels, because the responses were measured at different post-irradiation times. It can also explain why the dose responses agree, for example, within Fig. 6.2 for differing irradiation temperatures, but disagree between Fig.'s 6.2 and 6.3. The times between fixation were the same for samples within each figure, but were different for the two studies. One can see from the data in Fig. 6.5 that periods of one and two days should be allowed to elapse before fixation and analysis for the 50%C and the 67%C gels, respectively.

The post-irradiation reactions observed in Fig. 6.5 may occur because the polymerization propagation and termination rates discussed in Section 3.3.1 decrease in the presence of gelatin. Both propagation and termination reactions are diffusion controlled reactions, and are likely to be affected by the high viscosity of the gelatin solvent. As the viscosity increases the diffusion of monomers and macroradicals is impeded, and the propagation and termination rates decrease.

Slow propagation and termination have been observed previously in other viscous polymer systems. For example, in the later stages of polymerization in a liquid solvent when most of the monomer has been converted to high molecular weight polymer, the system becomes viscous and the reaction kinetics slow down (Odian, 1991). Electron spin resonance studies of polymerization kinetics have shown the presence of long-lived macroradicals in viscous solvents (Sato *et al.*, 1984). Long-lived radicals are also thought to be responsible for the edge-enhancement effects observed in regions of high dose gradients in a BANG gel (Maryanski *et al.*, 1994). The Bis and acrylamide monomers from low dose regions diffuse and react with macroradicals found at the edges of high dose regions causing additional polymerization not expected from the dose at that point alone.

The longer stabilization time observed for the 67%C BANG gel than for the 50%C gel is consistent with the slower reaction kinetics observed using spectrophotometry by Gelfi and Righetti (1981a) for pure polyacrylamide gels with high %C. As %C increases the polymer becomes more rigid and condensed and the viscosity of the solution increases. The increase in viscosity is thought to decrease the reaction kinetics because the reactants have more trouble diffusing through the polymer (Gelfi and Righetti, 1981a,b).

One might argue that the difference in the stabilization time observed in Fig. 6.5 may be attributed to the difference in absorbed dose, 16.8 Gy for the 67%C gel versus 7 Gy for the 50%C gel. However, dose is not expected to be a factor since it should only determine the number of actively polymerizing radical centers throughout the gel. The centers, being fixed should not "see" each other and affect each other's polymerization dynamics until very high doses where the density of centers is large.

While it would have been interesting to perform further studies of the effect of factors such as %C, %T and gelatin concentration on the time course of the polymerization and crosslinking in the BANG gel dosimeter, such studies are considered to be beyond the scope of the present study. Preliminary observations indicate that heating samples slightly to 26°C after irradiation brought the samples to full opacity and perhaps termination within hours instead of days. This probably arises from a decrease in viscosity of the gelatin, and a concurrent increase in the diffusion of reactants. Also, reaction rates are usually considered to be thermally activated (i.e., through an Arrhenius relation) and so the rates themselves increase with temperature. This phenomena brings up the interesting concept of using heat to "develop" the irradiated BANG gel. A parallel may be drawn between the BANG gel dosimeter and a 3-D photography insofar as an irradiated gel

could be "developed" using heat and "fixed" with oxygen. The possibility of reducing the time of analysis by reducing the time required for R_2 values to stabilize using development by heat is encouraging, and would increase the clinical practicality of 3-D dosimetry with polymer gels.

6.1.3 Post-Study Reproducibility

Having found that the post-irradiation time delay is a possible source of the irreproducibility of the R_2-dose response, the reproducibility was reassessed for irradiated dosimeters analyzed with adequate time delays. Figure 6.6 shows the reproducibility of R_2 for 50% C samples irradiated to 8.4 Gy and analyzed one day after irradiation once curing was complete. The three different symbols represent dosimeters prepared in separate batches. The standard deviation of R_2-values for each of the batches is about 5%. This error exceeds the 2% measurement error in the R_2-values indicated by the error bars. The additional error may be explained by variations in the concentration of polymer formed in the presence of spurious amounts of oxygen and impurities that remain despite preparation precautions. The error in data presented in the remainder of this chapter is taken as ± 5%. The error propagates as a percentage of any R_2-value since R_2 is proportional to polymer concentration (see Section 6.2.2).

The average spin-spin relaxation rates for each batch agree quite closely indicating good inter-batch reproducibility. Neglecting the encircled outlying point the averages for each batch are 1.47, 1.47 and 1.48 s^{-1}. The line in Fig. 6.6 represents the 1.47 s^{-1} average value. These averages for the different batches agree much better than the R_2 data, measured after insufficient time delays, for the different batches shown in Fig 6.1. The shaded area in Fig. 6.6 roughly

indicates the range of inter-batch R_2's from Fig. 6.1 before reproducibility was established. Thus, reproducible R_2-dose responses can be obtained from different batches of small volume BANG gels with the appropriate preparation protocol and post-irradiation time delay prior to NMR measurement. The outlying data point in Fig. 6.6 indicates that an odd sample may be improperly prepared and have an exceptionally high error.

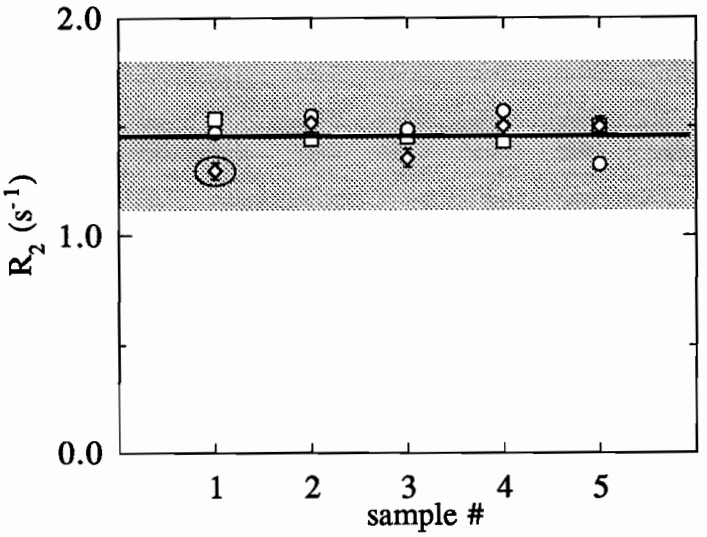

Figure 6.6 The reproducibility of R_2 is shown for several 50%C samples irradiated to 8.4 Gy. R_2 was measured at least one day after irradiation to assure completion of the polymerization and crosslinking reactions. The different symbols represent different batches. The average R_2 for each batch was about 1.47 ± 0.08 s^{-1}.

Once the reproducible R_2-dose responses were achieved for different batches of BANG gel dosimeter, studies of the effect of composition on the R_2-dose responses of the dosimeter were made possible. Before these studies are presented, it is interesting to note the clinical implications of reproducible dose responses. Of concern is the reproducibility of the R_2-dose responses for BANG gel dosimeters prepared from a single batch and that for dosimeters prepared separately from different batches. For different dosimeters prepared from a single batch of gel, the preparation protocol may be relaxed if the R_2-dose response to known doses can be calibrated. Since all gels within a batch are considered identical, the dose response of one dosimeter could be applied

to any of the remaining gels in the batch. Such a calibration procedure is characteristic of dosimeters such as film in which H&D curves (named after F. Hurter and V.C. Driffield who first published such a curve in 1890) are used to relate optical density to absorbed dose for a given batch of film and specific dosimetric and film processing conditions. Similarly, M&D curves (Magnetization to Dose curves) have been used to relate MR intensity to dose for ferrous sulfate-doped gels irradiated to known doses and for specific scan parameters (Schreiner *et al.*, 1994). Inter-batch reproducibility, however, allows for an absolute dosimetry and one would not be restricted to a dosimetry requiring a calibration step. For the studies presented in the following sections, different batches of gel were required for each variation in composition.

6.2 Dose Response Mechanisms of the BANG Polymer Gel

The BANG gel dosimeter is based on the premise that radiation induced conversion of monomer to crosslinked polymer affects the NMR relaxation properties of the water protons in the dosimeter. To establish this connection, the spin-spin relaxation in the BANG gel dosimeter is now discussed. A preliminary model relating the water proton spin-spin relaxation rate to the dose absorbed by the dosimeter is proposed in Section 6.2.2. Also introduced are the model parameters and optimization parameters used to characterize the R_2-dose responses presented in Section 6.3.

6.2.1 Spin-Spin Relaxation in the BANG gel

Before describing the model relating the proton spin-spin relaxation rate, R_2, to the dose it is important to establish what the measured R_2 for the BANG gel actually represents. The protons in the BANG gel dosimeter exist in a number of groups: on the monomer, polymer, gelatin and water molecules. The protons in each group exist in a different environment, and each group can be characterized by an inherent or intrinsic relaxation rate; these rates are those that would be observed in the absence of all the other groups (see Section 2.6). The intrinsic rates directly reflect the molecular dynamics and structure of each proton group. However, since the groups are not isolated from each other, the observed relaxation of the system will most likely be modulated by the exchange of information between the groups (recall Section 2.6). The observed spin relaxation (the observed relaxation rates and magnetization fractions) are functions of the inherent spin relaxation (the inherent relaxation rates and magnetization fractions) and the exchange rates. The observed quantities cannot be interpreted directly to give fundamental information about the spin system such as, the fraction of protons in, or the molecular motions of the different spin groups.

Because the BANG gel dosimeters consist mostly of water (proton fraction $\geq 92\%$) the description of the observed relaxation for the dosimeter is based on how the radiation-induced structural changes in the monomers and polymers affect the relaxation of the water protons. These effects are mediated by the water at the interface, i.e., by the water hydrating the molecules.

Monomer Hydration Water

The exchange scheme between water protons hydrating monomers and the monomer protons has not been investigated specifically in these studies. However, it was observed that the R_2 of pure water did not change significantly when typical amounts of Bis or acrylamide monomer (~6%T) were added to it. The intrinsic R_2's of dilute small oligomers are very similar to that of bulk water (Liu and Ullman, 1968; Schreiner *et al.*, 1991b; Schreiner *et al.*, 1994c), because the dynamics of the small molecules are very similar to that of water. That is, these molecules also undergo fast isotropic reorientation. Thus, in the dilute aqueous monomer system the spin relaxation of all water and monomer protons is dominated by intra-molecular and inter-molecular dipolar interactions characterized by short correlation times, τ_c. Since the spin relaxation of water hydrating the monomers is not expected to be very different from that of the bulk water, the water hydrating the monomers was omitted as a separate spin group in the treatment of spin-spin relaxation in the BANG gel dosimeter.

Polyacrylamide Hydration Water

Previous studies (Zhang, 1990) of crosslinked polyacrylamide gels at low water content have indicated that, on the scale of the spin-spin relaxation times, the exchange processes between the polymer and hydration water protons are in, or very close to, the slow exchange regime. That is, the exchange rate of polymer and water protons << R_2 of polymer and water protons (see Section 2.6). Thus, the measured or observed R_2's and magnetization fractions corresponded to the intrinsic R_2's and actual proton fractions of the polymer and water. This behaviour has also been observed for other large molecule systems of low water content (Schreiner *et al.*, 1991).

Since equal, if not stronger, coupling is expected between polymer and hydration water protons in low-hydration systems than in the highly hydrated polyacrylamide gels used in this work, the effects of exchange are also assumed negligible in the spin-spin relaxation of the polymer dosimeters.

It should be noted, however, that the slow exchange regime for water and polyacrylamide protons is not applicable to the spin-lattice relaxation, because the R_1's of the water and polymer protons are much smaller than the R_2's, and may be comparable to the exchange rates. Thus, exchange between polymer protons and hydration water protons would have to be considered in any analysis of the R_1-dose response of the polymer gels (Zhang, 1990; Shirley and Bryant, 1982; Schreiner *et al.*, 1991; Stanley and Peemoeller, 1991; Sobol and Pintar, 1987; Lynch, 1983 and references therein).

Gelatin Hydration Water

Whether or not the spin-spin relaxation of water protons hydrating the gelatin is inherent or affected by exchange of magnetic information with the gelatin protons is not an issue for the preliminary treatment of the spin-spin relaxation of the BANG dosimeter being presented. The treatment assumes that the gelatin or its relaxation properties are not affected by the formation of the polymer (results will be shown later that support this assumption). Hence, the gelatin is not expected to contribute to the R_2-dose response of the BANG gel dosimeter via its effect on hydration water.

Resulting R_2 for Water

According to arguments presented above the observed R_2's of the hydration water in the BANG gel dosimeter are assumed to be the intrinsic spin-spin relaxation rates, R_2^i, where i=p or g for the polymer or gelatin, respectively. In the BANG gel dosimeter there is also a third water proton group, the bulk water with an intrinsic rate, R_2^w. At room temperature the physical exchange of bulk and hydration water typically proceeds very rapidly (Resing, 1972; Lynch, 1983; Sobol and Pintar, 1987 and references therein) and an exponential transverse magnetization decay characterized by a single R_2 is observed. As for proton groups undergoing fast exchange, the observed R_2 for the water protons is just the sum of the inherent water R_2's weighted by the fraction of protons, p^i, in their respective group, i.e.,

$$R_2 = p^p R_2^p + p^g R_2^g + \left(1 - p^p - p^g \right) R_2^w \qquad (6.1)$$

This expression is similar to that for the spin-lattice relaxation of the ferrous sulfate-doped gel dosimeters in which the different water proton groups were the water hydrating the ions and the gelatin, and the bulk water (recall Eq. 5.1).

As noted in Chapter 2, the inherent R_2 of the water protons hydrating the polyacrylamide in the BANG gel dosimeter, or macromolecules in general, is greater than the R_2 of bulk water protons (i.e., $R_2^p > R_2^w$). This is the result of the modulation of the dynamics of the hydration water by the hydration: the reorientation becomes anisotropic and the motions slow down (Lynch, 1983; Schreiner et al., 1991; Shirley and Bryant, 1982). The rigorous analysis of the R_2 of the polymer gel would require one to establish the dynamics of the hydration water (Zimmerman and Brittin, 1957; Schreiner et al., 1991; Shirley and Bryant, 1982; Zhang, 1990) and perhaps account for

distributions of correlation times associated with different hydration sites (Lynch, 1983). This is beyond the scope of this study. However, it is clear that the increase in polymer hydration water fraction, p^p, in the dosimeter as monomer polymerizes and crosslinks will result in an increase in the R_2 of the BANG polymer gel dosimeter with dose. A model for the R_2-dose response in the dosimeter based on Eq. 6.1 is presented below.

6.2.2 Model for R_2 vs Dose

As the weight fraction of the polymer, [p], in the dosimeter increases with dose so does the fraction of water protons that are hydrating the polymer, p^p. The two quantities are related as follows,

$$p^p = k^p [p] \tag{6.2}$$

where k^p is the fraction of water protons hydrating the polymer per weight fraction of polymer in the dosimeter. The following is obtained by substituting Eq. 6.2 into Eq. 6.1,

$$R_2 = k^p \left(R_2^p - R_2^w\right)[p] + \left\{p^g R_2^g + \left(1-p^g\right) R_2^w\right\} \tag{6.3}$$

As the dosimeter is irradiated, the last term in parantheses is assumed to be constant with dose; in fact, it is considered equivalent to $R_2(0\,Gy)$, the spin-spin relaxation rate for the unirradiated dosimeter for which [p]=0. The term multiplying the polymer concentration is the polymer transverse relaxivity, r^p, defined as the ability of the polymer to enhance the observed transverse relaxation rate of the water protons. Thus, Eq. 6.3 may be rewritten as

$$R_2 = r^p [p] + R_2(0Gy) \tag{6.4}$$

The percent weight fraction of polymer formed in the BANG gel can be given by:

$$[p] = G^P D \tag{6.5}$$

where G^P is the *polymer yield* in units of percent weight fraction of polymer formed per Gy (= J/kg).

The polymer yield differs from the *chemical yield* which is customarily expressed in units of moles per Joule. It is difficult to define a chemical yield for the polymer, because the polymer is a growing entity with an evolving molecular weight. Hence, the amount of polymer formed is difficult to describe in terms of moles. The chemical yield is appropriate for describing dosimeters in which there is a direct correspondence between the number of products formed and the number of reactants. The polymer yield as defined here, is an effective yield which is more easily related to the R_2-dose response of the polymer gel dosimeter.

The following expression relating R_2 to the dose is obtained by substituting Eq. 6.5 into Eq. 6.4,

$$R_2 = \{r^P G^P\} D + R_2(0\text{Gy}), \tag{6.6}$$

where the term in parentheses is the dose sensitivity, d. The dose sensitivity in Eq. 6.6 is similar in form to that written for the ferrous sulfate-doped gelatin dosimeters in Eq. 5.7: the radiation product is now polymer rather than Fe^{3+} and the disappearing species is monomer rather than Fe^{2+}. Equation 6.6 is a general expression that applies to BANG dosimeter systems in which r^P and G^P might vary with dose giving nonlinear R_2-dose responses.

There are the two processes considered in the model for the R_2-dose response of BANG gel dosimeters (Eq. 6.6). The response of the polymer gel requires the radiation induced polymerization of the system and a change in

hydration water relaxation as the monomers polymerize. The chemical response of the dosimeter to radiation is represented by the polymer yield, G^P, and the response of R_2 to the polymer formed is represented by the relaxivity, r^P.

6.2.3 Determination of r^P and G^P

In terms of the model presented, the R_2-dose response is governed by the polymer relaxivity r^P and the polymer yield G^P. Thus, these parameters will be used in the analysis of the effects of dosimeter composition and of measurement temperature on the dosimeter's R_2-dose response.

Ideally, the polymer relaxivity should be determined independently by measuring R_2 as a function of [p] much as the relaxivities of the iron ions in the Fricke solution were determined in the last chapter. However, this is not possible for two reasons. First, the dose variation of the exact structure and composition of the irradiated polymer is not known. Second, even if it were known, it would be difficult to produce these specific polymers independently so that they could be used in model solutions in the same way iron ions were used in the analysis of ferrous sulfate gels (see Fig.'s 5.1 and 5.2). However, values of R_2 for known amounts of polymer in BANG gels may be estimated from the measured R_2-dose responses, given certain assumptions. After saturation of the dose response, when sufficient curing times have passed and $R_2=R_2^{max}$, the amount of polymer formed is equivalent to the initial amount of monomer, i.e., [p]=%T, assuming that all the monomer has reacted. Given the high reactivity of the monomers this is a reasonable assumption since it is unlikely that some monomers remain unpolymerized in the presence of the excessive amounts of water or gelatin radicals created at high doses. Also, the

fact that R_2 does not change at all over a large range of doses after saturation (i.e., tens to hundreds of Gy's) suggests that no additional polymerization from slower reactions with low dose sensitivity occur. This observation is supported by the high monomer to polymer conversions ($\geq 98\%$) typically observed for pure, chemically crosslinked polyacrylamide.

Thus, the polymer relaxivity can be estimated by:

$$r^p \sim \frac{\left(R_2^{max} - R_2(0\%T)\right)}{\%T}, \tag{6.7}$$

where r^p is in units of s^{-1} per percent weight fraction of polymer formed in the dosimeter (i.e., $s^{-1}/\%w$) and $R_2(0\%T)$ is the apparent rate for water in the presence of the gelatin only.

The polymer yield was not determined directly since, as noted above, the weight fraction of polymer formed for a given dose could not easily be measured directly. However, G^p can be estimated from the dose at which saturation occurs and all of the monomer has polymerized so that the percent weight fraction of polymer formed is the initial %T. Thus,

$$G^p = \frac{\%T}{D_{sat}} \tag{6.8}$$

It is interesting to note that for the ferrous sulfate-doped gels, the concentration of Fe^{3+} after saturation is not equivalent to the initial concentration of Fe^{2+} because saturation is due to the depletion of oxygen not Fe^{2+}. Hence, the yield for Fe^{3+} could not be determined in the same manner as that for the polymer. However, oxygen, or any other compound for that matter, are not required in the polymer gel for the polymerizations to proceed, rather it inhibits polymerization.

The polymer relaxivity and yield are all interrelated with the parameters used to characterize the R_2-dose response (recall Section 3.1.2), i.e.,

the saturation dose D_{sat}, the dose sensitivity d, and the dynamic range (R_2^{max}-R_2(0 Gy)). The dose sensitivity, the slope of the linear portion of the R_2-dose response, and the dynamic range are both determined directly from the R_2-dose response. The relationships can be made evident by combining Eq.'s 6.7 and 6.8 and Eq. 3.1 to give:

$$D_{sat} = \frac{\left(R_2^{max} - R_2(0Gy)\right)}{d} = \frac{\%T}{G^p} = \frac{r^p \%T}{d}. \qquad (6.9)$$

Despite these connections, all five parameters will be dealt with independently so that the data can be more easily interpreted for information on both the dose response mechanisms (parameters r^p and G^p) and on the optimization of the R_2-dose response for practical use (parameters D_{sat}, d and dynamic range (R_2^{max}-R_2(0Gy))).

The linearity of the R_2-dose response for the BANG polymer gel dosimeter implies that the polymer yield and relaxivity determined using data from the saturation region of the response should apply throughout the whole dose range to saturation. Examples of the linear portions of R_2-dose responses for various BANG gel dosimeters are shown in Fig. 6.7. According to Eq. 6.6, a linear response of R_2 to dose implies that the dose sensitivity, d, is constant with dose. Hence, the relaxivities and polymer yield are probably also constant with dose so that their values determined using R_2^{max} and D_{sat} apply at any dose. It is highly unlikely that a linear dose response would be obtained, for example, by increases in polymer yield G^p with dose countered by concurrent and equivalent decreases in polymer relaxivity r^p with dose.

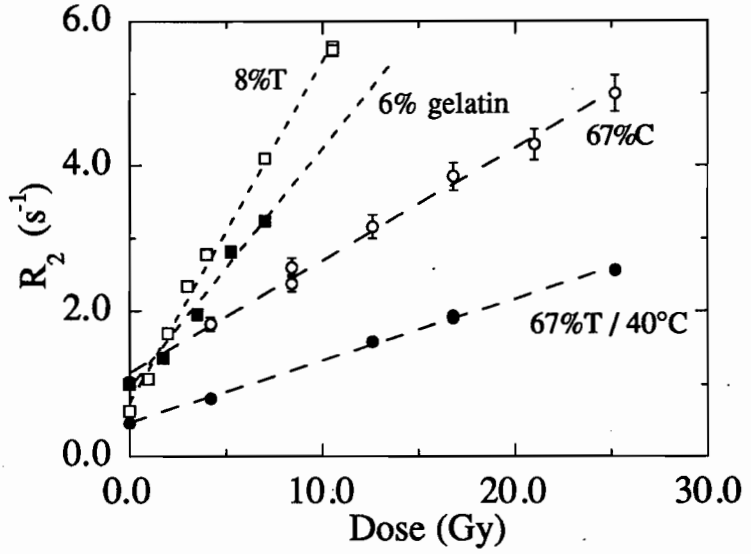

Figure 6.7 Examples of the linear portion of the R_2-dose responses for different BANG gel dosimeters. Unless specified otherwise, the dosimeters consist of 5% gelatin, 50%C and 6%T, and were measured at 20°C.

6.3 R_2-Dose Response Studies

The effects of a number of variables, such as the gelatin concentration, %T and %C and NMR measurement temperature on the R_2-dose response of BANG gel dosimeters are studied in Sections 6.3.1, 6.3.2 and 6.3.3, respectively. As noted in the previous section, the results will be analyzed in two different ways. One analysis deals with the effects of the variables on the polymer yield and relaxivity in order to better understand the dose response mechanisms. The other analysis deals with the effects of the variables on the dose sensitivity, dynamic range and saturation dose for the purpose of optimizing the dosimeter's response for practical applications.

6.3.1 Effect of Gelatin

Linearity of the R_2-Dose Response

The presence of gelatin in the BANG polymer gel dosimeter has a profound effect on the behavior of the radiation response of Bis and acrylamide monomer. Figure 6.8 shows two dose responses, one for the R_1 of a 50%C and 8%T solution of acrylamide and Bis without gelatin (adapted from Maryanski *et al*, 1993) and another for the R_2 of a 67%C and 6%T BANG gel dosimeter containing 5% gelatin by weight. All data were measured at 40°C.

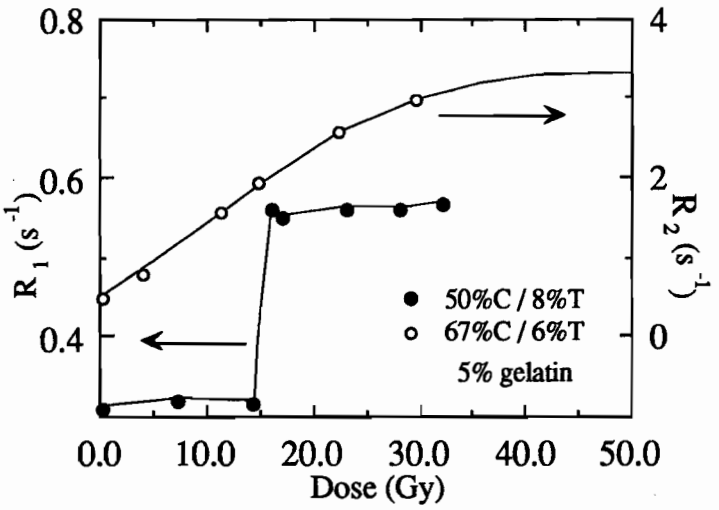

Figure 6.8 The effect of gelatin on the radiation response of BANG gel dosimeters. An R_1-dose response is shown for a 50%C and 8%T Bis and acrylamide solution without gelatin (adapted from Maryanski *et al.*, 1993) and R_2-dose response is shown for a 67%C and 6%T BANG gel dosimeter containing 5% gelatin.

In the absence of gelatin, the dose response of the longitudinal relaxation rate, R_1, was shown to be a step function; R_1 did not vary with dose until a threshold dose of about 15 Gy where R_1 suddenly increased to a saturation value (Maryanski *et al.*, 1993). This threshold behaviour is identical to the response of the "go-no-go" aqueous monomer dosimeters, proposed by Hoecker and Watkins (1958). The same behavior is expected for R_2 in the absence of gelatin since R_2 and R_1 respond similarly to dose in the

presence of gelatin; they both increase linearly with dose before saturating at a certain value (Maryanski *et al*, 1993). The similarity follows directly from the likelihood that R_1, like R_2, depends on polymer concentration.

The threshold behavior of the radiation dose response for Bis and acrylamide in the absence of gelatin is best described in terms of the kinetic chain length, ν, which is the average number of monomers consumed or polymerized per radical formed. As noted in Section 3.3.1 ν is equivalent to the ratio of the polymerization rate, R_p, to termination rate, R_t. Since the number of radicals formed is related to the dose absorbed by the system, ν is related to the number of monomers consumed per unit dose, a measure of the polymer yield, G^P, defined in Eq. 6.5. Hence, the important result that the polymer yield is related to the reaction dynamics through the parameter, ν, is obtained (i.e., $G^P \propto \nu \propto R_p/R_t$).

With the relationship between G^P and the reaction dynamics in mind, the threshold behavior may be explained as follows. As polymer is formed the viscosity of the system increases and the reactants and products diffuse less readily. Thus, both R_p and R_t decrease. However, R_t decreases more than R_p because termination, involving two large radicals, is more hindered than polymerization, involving a large radical and small monomer. The net effect is that ν and hence, the polymer yield G^P, increases with dose as more polymer is formed. This phenomena is referred to autoacceleration (recall Section 3.3.1).

In the presence of gelatin, the R_2-dose response of the polymer system is altered and the spin-spin relaxation rate increases linearly with dose until saturating at constant value R_2^{max} after the dose D_{sat} (see Fig. 6.8). Thus, it seems that the polymer yield G^P is constant with dose in the BANG gel dosimeter. It is postulated that the gelatin acts to control the viscosity of the

system so that the gelatin and not the polymerization alone determines the diffusion of reactants and products in the dosimeter. The polymerization and termination rates would be determined by the gelatin as well. Thus, in the presence of gelatin, R_p and R_t do not vary significantly as the amount of polymer increases, and ν and G^P remain constant throughout the whole dose range. By decreasing the diffusion of products, the gelatin also stabilizes the spatial dose information over time so that the gel dosimeters may be analyzed any time after irradiation for 3-D radiation dose distributions.

Also, in the absence of gelatin the polymerization propagates throughout the whole volume of the dosimeter container whereas in the presence of gelatin the amount and hence spatial extent of the polymer formed are limited. Thus, the distribution of effects observed in a large BANG gel are representative of the doses absorbed locally.

G^p and r^p

Preliminary data demonstrating the effect of gelatin concentration on the R_2-dose response of 50%C and 6%T BANG gel dosimeters are shown in Fig.'s 6.9a and 6.9b. The gelatin concentration was varied from 4 to 6% by weight and R_2 was measured at 20°C and 20 MHz. It is obvious that varying the gelatin concentration from 4 to 6% has little effect on the R_2-dose response. This supports the assumption in the model for the BANG gel's R_2-dose response that the gelatin relaxivity plays an insignificant role in the response.

The polymer relaxivity remains constant at about 0.67 ± 0.03 $s^{-1}/\%w$ when the gelatin concentration is varied from 4-6%. In so far as r^P is a measure of the composition and structure of crosslinked polyacrylamide (see Section 6.3.2), its insensitivity to gelatin concentration suggests that the

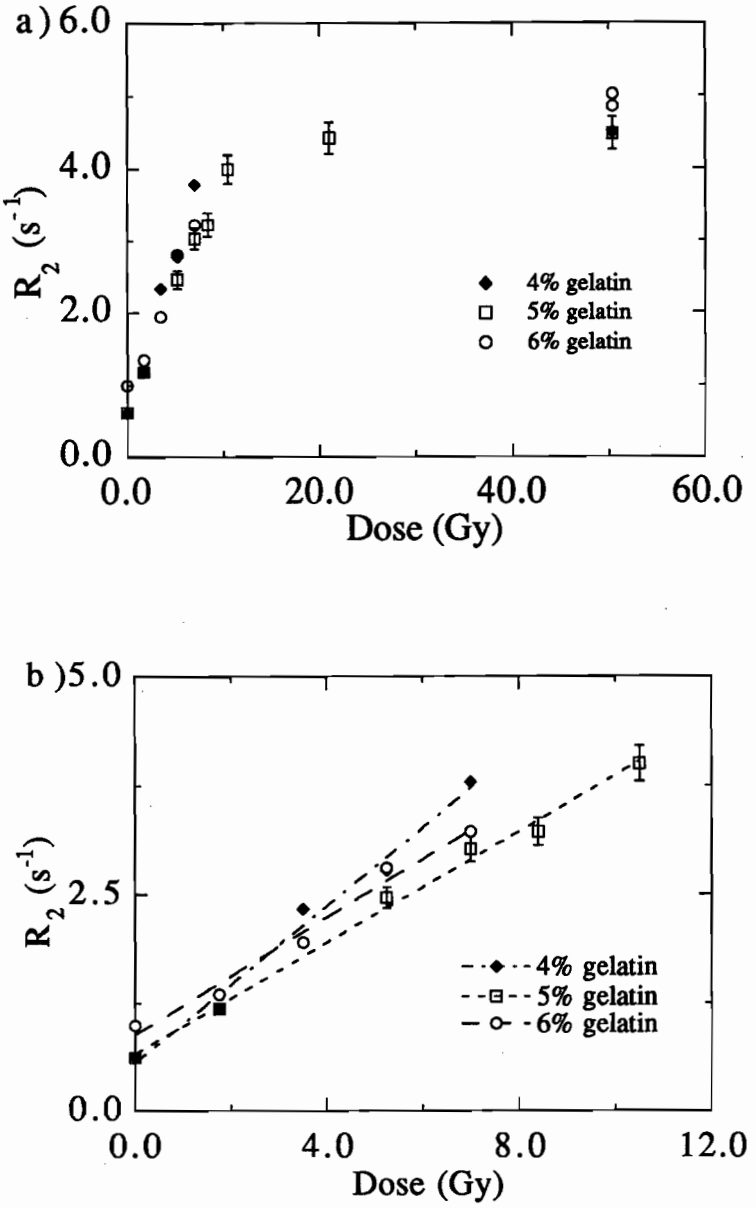

Figure 6.9 a) and b) The R_2-dose response curves for 50%C and 6%T BANG gels with different gelatin concentrations of 4%, 5% and 6% by weight. All measurements were made at 20°C. Figure 6.9b) is an exploded view of the lower dose region of Figure 6.9a).

gelatin does not affect the nature of the polyacrylamide formed significantly. It also suggests the reverse, the polyacrylamide formed has little effect on the gelatin and its relaxivity. This observation supports the assumption made in the model that the water hydrating the gelatin does not play a role in the R_2-dose response of the BANG gel dosimeter.

The polymer yield, as determined from the R_2-dose responses using Eq. 6.8, increases from 0.50±0.05 to 0.68±0.07 %w/Gy when the gelatin concentration is decreased from 6% to 4%. This behavior supports the proposition made earlier that the polymer yield is determined by the gelatin. It suggests that as the gelatin concentration is decreased, the diffusion of the monomers increases more than that of large radicals, and hence, ν ($=R_p/R_t$) and G^P also increase. If the gelatin concentration were to be decreased further, the linear response of R_2 to dose, characterized by a constant G^P, would be expected to revert to the nonlinear, threshold response observed in the absence of gelatin, characterized by a variable G^P.

Two additional sets of data supporting these observations are shown in Fig. 6.10. The data show r^P as a function of %C which determines polymer composition and structure. The variation in r^P with %C confirms that the value of r^P is a reflection of composition and structure. This aspect of the data is further discussed in the next section.

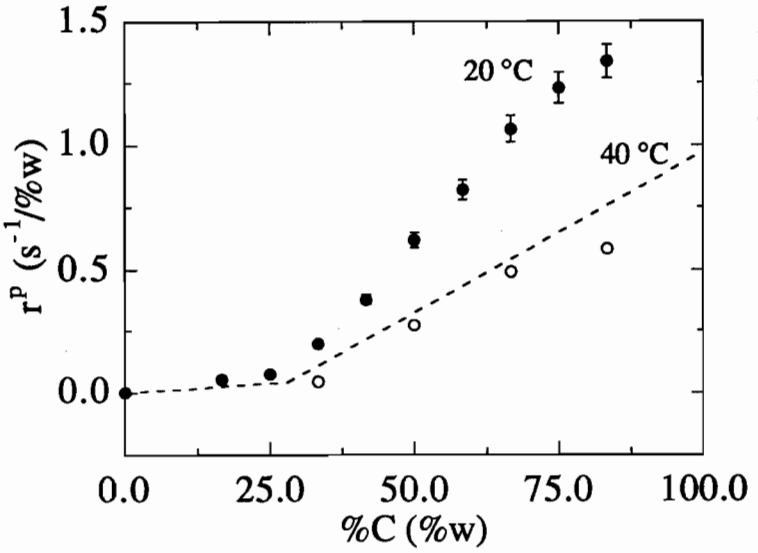

Figure 6.10 The polymer relaxivity, rP as a function of %C for a 6%T BANG gel samples measured at 20°C (filled circles) and 40°C (open circles). The dashed lines represent fits to data obtained at 40°C for chemically crosslinked samples of 5%T polyacrylamide without gelatin (Kennan *et al.*, 1995).

The first set of data, analyzed at 20°C, is for 6%T BANG gel dosimeters containing 5% gelatin. The behaviour of interest is the sudden increase in rP at about 30%C which coincides with the %C where the opacity of the BANG gel has been observed to change from transparent to milky in pure polyacrylamide systems containing no gelatin (Gelfi and Righetti; 1981a,b). The onset of opacity is associated with the formation of condensed regions of highly crosslinked, bead-like structures of polyacrylamide called "coagula" whose sizes are of the order of the wavelength of light. The agreement between the %C at which rP changes suddenly for polyacrylamide formed in 5% gelatin and where coagula begin to form for pure polyacrylamide seems to indicate that the gelatin does not affect the formation of coagula.

The second set of data shown in Fig. 6.10 were measured at 40°C for 6%T BANG gels containing 5% gelatin (empty circles) and for 5%T pure, chemically crosslinked polyacrylamide (dashed lines representing fits to data obtained by Kennan *et al.*; 1995). The data for the 6%T BANG gel and the 5%T

pure polyacrylamide agree closely, so to a large extent the gelatin does not affect the composition and structure of the polyacrylamide that would be formed in the absence of gelatin.

Dosimeter Optimization

According to the data in Fig. 6.9 the saturation dose increases slightly from 8.8 ± 0.9 Gy to 12.1 ± 1.2 Gy when the gelatin concentration is increased from 4 to 6%. The dynamic range ($=R_2^{max} - R_2(0Gy)$), however, remains constant at about 4.0 ± 0.2 s^{-1}. The dose sensitivity decreases with gelatin concentration (see Fig. 6.9b) and ranges from 0.45 to 0.32 ± 5% $s^{-1}Gy^{-1}$ when the gelatin concentration is increased from 4% to 6%. This decrease in dose sensitivity arises from a decrease in G^P since r^P remains constant over the 4% - 6% gelatin range (recall discussion above). However, gelatin concentrations below 5% are too low to provide adequate rigidity of the BANG gel. Also, if the gelatin concentration were lowered too much, the R_2-dose response might revert to the nonlinear step function form observed in the absence of gelatin .

Summary

The gelatin in the BANG gel dosimeter affects the polymer yield, G^P, of the polyacrylamide. It moderates the radiation response of polymerization so that G^P is constant with dose and a linear response of R_2 to dose results. Increasing the amount of gelatin in the dosimeter decreases the value of the polymer yield. The gelatin appears to have little effect on the relaxivity of the polymer. Thus, the structure and composition of the polymer formed seems unaffected by the gelatin. Significant improvement of the R_2-dose response by changing the gelatin concentration is not possible.

6.3.2 Effect of Polymer Composition (%T,%C)

The effect of the polymer composition and structure on the R_2-dose response of the BANG gel dosimeter was investigated by varying the monomer content in terms of either the total weight fraction of monomer (acrylamide + Bis) in the solution, %T, or the weight fraction of Bis crosslinker per total monomer, %C (recall definitions in Section 3.3.2). Figures 6.11a and 6.11b show that the R_2-dose response is affected by %C and %T, respectively, but that it keeps its general form, an initial linear response followed by a saturation of R_2. The effects of the polymer composition on the relaxivity and chemical yield of the BANG gel dosimeter, as well as the optimization of the R_2-dose response, are discussed below in terms of %C and %T.

Effect on the Polymer Relaxivity r^p

Figure 6.12 shows the variation of the relaxivity of the polymer as a function of the percent weight fraction of Bis (= %C x %T/100) and acrylamide (= (100 -%C) %T/100) in the gel. The rate measurements were made at 20°C and 20 MHz and the gel samples contained 5% gelatin. The data in Fig. 6.12 were plotted versus the weight fraction of Bis instead of %T or %C, because it allows two sets of data, one in which %C was varied while %T was fixed at 6%T and another in which %C was fixed at 50%C while %T was varied, to be compared directly. Both sets show an initial slow increase in r^p with % Bis followed by a sharper increase after about 2% Bis.

The increase in relaxivity with amount of crosslinker is not unexpected. Studies of pure crosslinked polyacrylamide show that separate increases in %C and %T make the polyacrylamide more rigid (Weiss and

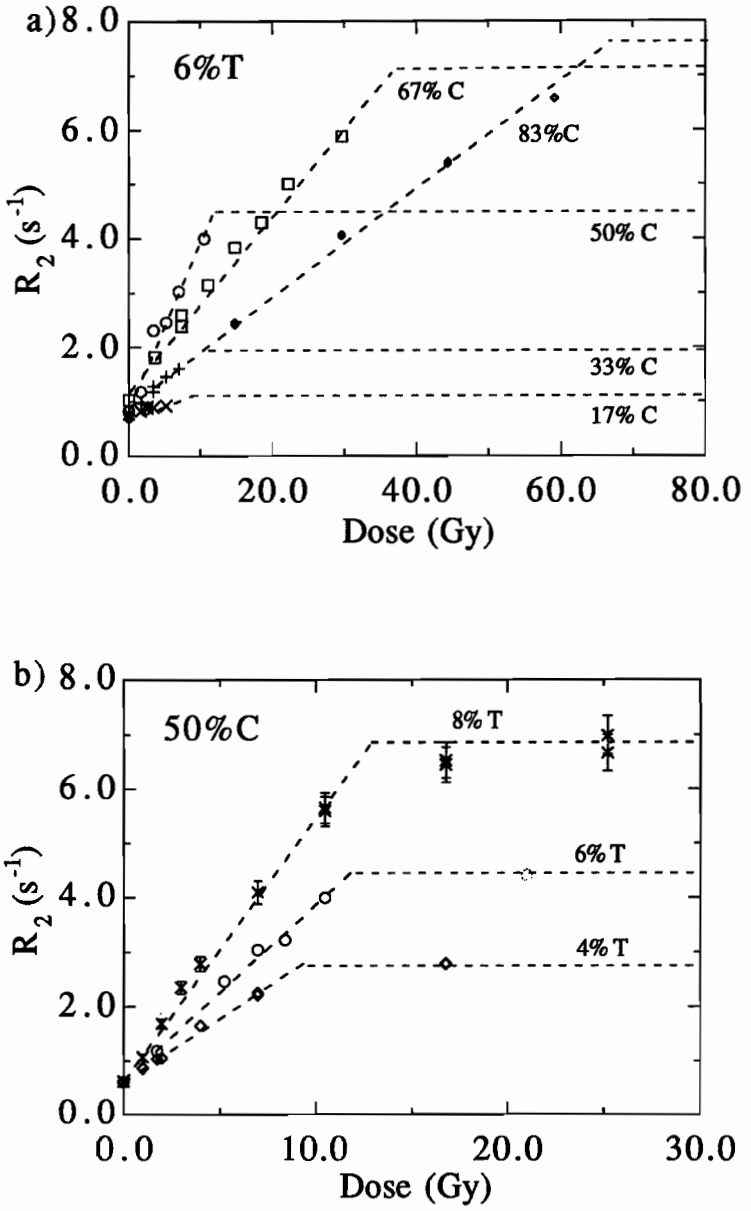

Figure 6.11 The R_2-dose responses for BANG gel with varying polymer composition:
a) %C varied and %T held constant at 6%T
b) %T varied and %C held constant at 50%C
All samples contained 5% gelatin; the NMR measurements were made at 20°C and 20MHz. R_2^{max} data at ~ 300 Gy from which most of the horizontal dashed lines extend are not shown in the graphs.

Silberberg, 1977). The same behavior is expected in the presence of gelatin since, according to the results of the previous section, the structure and composition of polyacrylamide do not seem to be affected significantly by gelatin. If the motions of the hydration water are indeed modulated by those of the polymer (recall Section 6.2.1), then as the polymer rigidity increases, the motions of hydration water should also be affected. This change in the hydration water dynamics should cause the inherent spin-spin relaxation rate of the hydration water, R_2P, and hence the polymer relaxivity, rP (= kP (R_2P - R_2^W)), to increase.

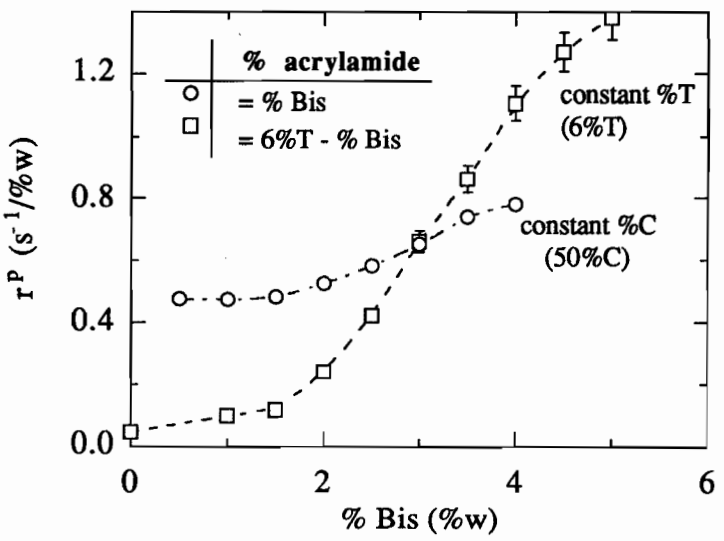

Figure 6.12 The polyacrylamide relaxivity plotted as a function of the absolute weight fraction of Bis crosslinker in the BANG gel. Data are shown for samples of constant %T (6%T) and varying %C, and for constant %C (50%C) and varying %T. The gelatin concentration was 5% for all samples and the NMR measurements were made at 20°C. The curves through the data are for visual guidance only.

Greater increases in the polymer relaxivity with %Bis are observed for the samples with varying %C and constant 6%T than those with varying %T and constant 50%C. This agrees with the greater increases in polymer rigidity observed for high %C than for high %T. For high %C polyacrylamide the acrylamide chain length between crosslinks is much shorter. The two sets of data intersect where the samples' compositions are equivalent, i.e., 3% Bis.

Before the crossover the constant %T samples contain more acrylamide and less Bis than the constant %C samples, hence the acrylamide chains between crosslinks are longer, and the polymer rigidity and relaxivity are lower. The reverse is true after the crossover. This behavior further supports that the spin-spin relaxation of polyacrylamide is determined by polymer rigidity and the water hydrating the polyacrylamide.

It is also interesting to note that the polymer relaxivity remains constant with %T until about 4%T or 2% Bis (see Fig. 6.12). Assuming that increases in the amount of polymer formed with dose can be mimicked by increases in %T, the constancy of r_P with %T supports the hypothesis proposed in Section (6.2.1) that r_P remains constant with dose throughout the linear portion of the R_2-dose response. The increase in r_P with %T beyond 2% Bis may be an indication of a change in phase of the polymer being formed. It may be possible that below 4%T the density of polymer is too low for the radical centers distributed throughout the gelatin to connect and gel. Hence, the polyacrylamide within the gelatin exists only in a sol phase whereas above 4%T it exists in a gel phase. An easy way to detect a change in phase would be to attempt to melt the samples since polyacrylamide in the gel phase does not melt.

Effect on the Polymer Yield G^P

Figure 6.13 shows the polymer yield as a function of the % weight fraction of Bis in the gel. As for Fig. 6.12, the data are shown for samples with constant %C (50%C) and varying %T, and for samples of constant %T (6%T) and varying %C. Although far from complete, the set of constant %C data, obtained from a preliminary study (see Fig. 6.11b) is informative nonetheless.

The chemical yield for the constant %T samples decreases with increasing %C whereas the G^P for the constant %C samples increases with increasing %T.

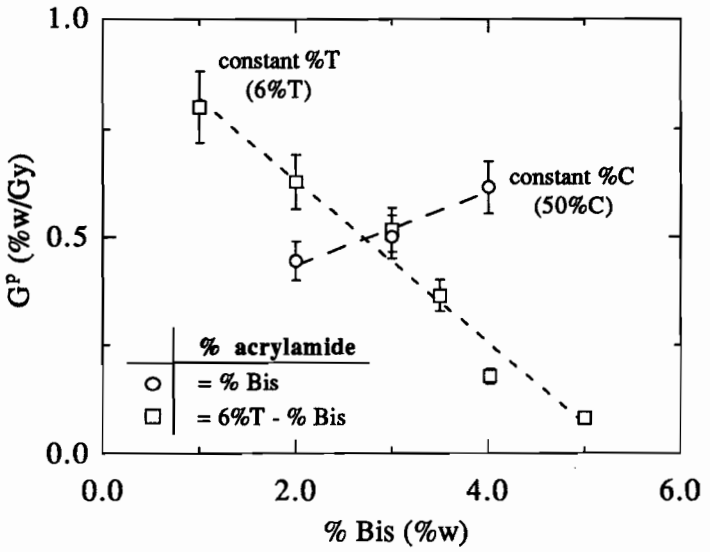

Figure 6.13 The polymer yield, G^P, as a function of the % weight fraction of Bis in the BANG gel. Data are shown for samples of constant %T (6%T) and varying %C, and for constant %C (50%C) and varying %T. The gelatin concentration was 5% and the measurements were made at 20°C. The lines are aids to the eye only.

As mentioned in Section 6.2.2 the polymer yield is related to the kinetic chain length ($\nu = R_p/R_t$) and hence the dynamics of the reaction. The decrease in the yield with increasing %C is consistent with the slower reaction kinetics observed spectrophotometrically by Gelfi and Righetti (1981a) for pure polyacrylamide gels with high crosslinker fractions. It is also consistent with the results of Section 6.1.3 where it was observed that the post-irradiation reactions last longer for the 67%C BANG gel than for the 50%C gel. The reaction kinetics are thought to decrease with %C because, as the structure of the polymer becomes more rigid and condensed, the reactants have more trouble diffusing through the polymer (Gelfi and Righetti, 1981a). The relative decrease in diffusion of the monomers is likely to be greater than that of the macroradicals. Hence, R_p should decrease more than R_t, and the polymer yield should decrease. So far it has been proposed that diffusion mediated changes in the polymer yield for an aqueous monomer system can arise from

the amount of polymer formed or by the addition of gelatin (see Section 6.3.1). It is also apparent that polymer yield changes can arise from changes in the structure of the polyacrylamide brought on by varying %C.

The increase in the polymer yield with %T observed for the constant %C samples can also be explained in terms of the kinetic chain length ($=R_p/R_t$). It was shown in Section 3.3.1 that the polymerization rate, R_p, depends linearly on the monomer concentration whereas the termination rate, R_t, does not. Hence, the kinetic chain length and the chemical yield should also increase linearly with monomer concentration. Although limited, the chemical yield data for constant %C in Fig. 6.13 supports a linear dependence of G^P on %T.

Effect on the Dose Sensitivity

Figure 6.14 shows plots of the dose sensitivity, d, versus the Bis weight fraction of the BANG gel for samples of constant %T (6%T) with varying %C, and of constant %C (50%C) with varying %T. The gelatin concentration was 5%, and the NMR measurement temperature was 20°C for all samples. The dose sensitivity was determined from the slope of the linear portion of the R_2-dose response. For the constant %T data, the dose sensitivity peaks at about 3% Bis (=50%C). The constant %C data, although limited, suggests a constant increase in dose sensitivity with increasing %T.

The behavior of the dose sensitivity with % Bis can be interpreted in terms of the basic dose response mechanisms described by the relaxivity (Fig. 6.12) and the polymer chemical yield (Fig 6.13). According to Eq. 6.6 the dose sensitivity for constant %T samples increases with %Bis because of an increase in the polymer relaxivity (see Fig. 6.12). However, a concurrent decrease in the polymer yield (see Fig. 6.13) eventually dominates the

relaxivity increase causing the dose sensitivity to peak and then decrease with increasing % Bis. The peak observed in Fig. 6.14 can essentially be reproduced by dividing the relaxivity data in Fig. 6.12 by yield data in Fig. 6.13. Similarly, the increase in dose sensitivity with %Bis for constant %C samples is a result of simultaneous increases in polymer relaxivity and yield with % Bis.

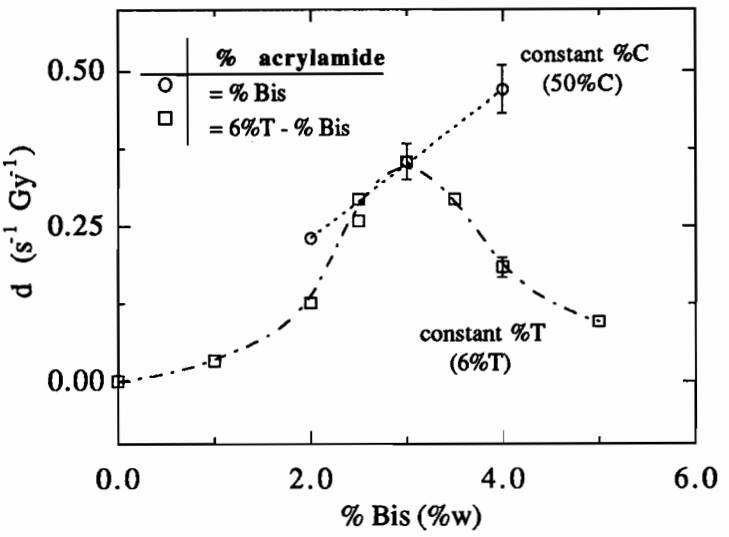

Figure 6.14 The effect of %weight fraction of Bis on the dose sensitivity. Data are shown for samples of constant %T (6%T) and varying %C, and for constant %C (50%C) and varying %T. The gelatin concentration was 5% and the measurements were at 20°C. The curves are for visual guidance only.

Dosimeter Optimization

The effects of polymer composition on the optimization parameters, i.e., the dynamic range (=R_2^{max}-R_2(0Gy)), dose range (D_{sat}) and dose sensitivity (d), are shown Figure 6.15. The polymer composition is expressed in terms of %T and %C as opposed to %Bis, because these are the standard variables used to describe the polymer composition. Presenting the data in this fashion provides easy reference when customizing the composition for the dose response requirements of a particular application. One must bear in mind that there is a practical limitation to the composition of the gel imposed

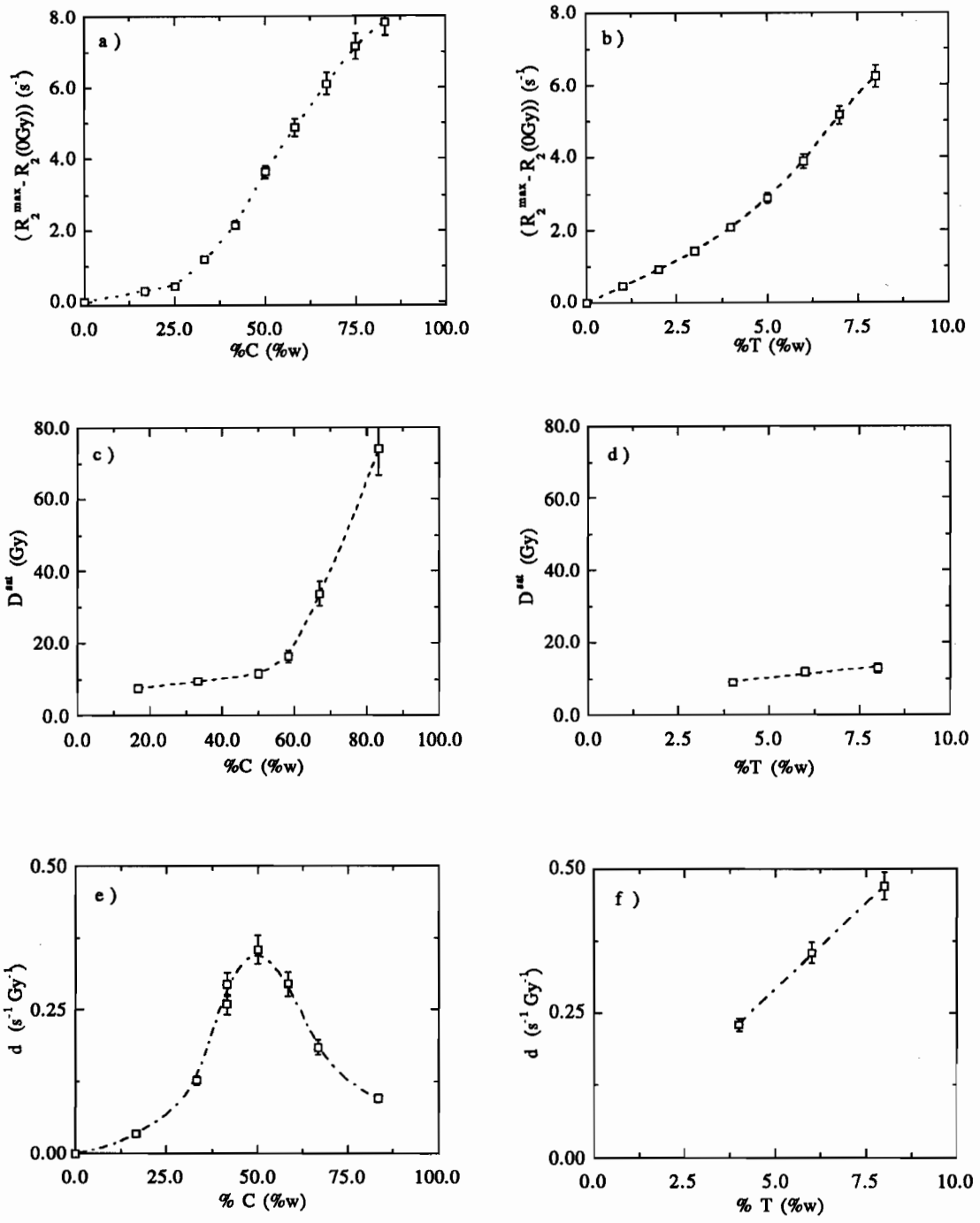

Figure 6.15 The dependence of various dose response parameters on the polymer composition (%C or %T). The parameters were the dynamic range (a,b), the dose range (c,d) and the dose sensitivity (e,f). The data in plots a), c) and e) are for 6%T dosimeters whereas the data in plots b), d) and f) are for 50%C dosimeters. All dosimeters contained 5% gelatin.

by the precipitation of Bis for Bis weight fractions exceeding 6% in the BANG gel.

Figures 6.15a and 6.15b indicate that the largest dynamic range is obtained for high %C and %T, respectively. Figure 6.15c indicates that the greatest saturation dose is obtained for high %C. This suggests that at high %C small variations in %C due to preparation may cause large fluctuations in D_{sat}. Figure 6.15d shows that, over the composition range studied, changes in %T have little effect on the dose range.

It is apparent from Fig.'s 6.15e and 6.15f that best high dose sensitivities are obtained for crosslinker concentrations of about 50%C and high total monomer concentrations, respectively. However, it is interesting to also note how preparation errors in %C might affect uncertainties in the dose sensitivity. The dose sensitivity varies least with %C at about 50%C where the slope is a minimum (see Fig. 6.15e). Hence, small errors in %C at 50%C will cause smaller errors in dose sensitivity than at higher or lower %C. Thus, not only is the sensitivity optimized at 50%C but, also, some of the preparation constraints may be relaxed for this composition.

The optimal crosslinker fraction producing the maximum dose sensitivity is about 50%C (Fig. 6.15e), however, beyond 50%C the dynamic range (Fig. 6.15a) and dose range (Fig. 6.15c) increase whereas the dose sensitivity decreases. Thus, a compromise must be made between the dose sensitivity, and the dynamic and dose ranges when choosing the best crosslinker fraction for a certain dosimetry application. This type of compromise is often encountered for other types of dosimeters such as the Fricke dosimeter where the addition of cupric ion can increase the dose range by a factor of 24, but decreases the dose sensitivity by the same factor (Attix *et al.*, 1966).

6.3.3 Effect of NMR Measurement Temperature

Previous results have indicated that the dose sensitivity of BANG gels varies with NMR measurement temperature (Maryanski *et al.*, 1993). Figure 6.16 shows the effect of NMR measurement temperature on R_2-dose response of a 67%C and 6%T BANG gel dosimeter containing 5% gelatin. It is obvious that both the dose sensitivity and the maximum spin-spin relaxation rate increase with decreasing temperature. Data such as that presented in Fig. 6.16 can be interpreted, as in previous sections, for effects on the various dose response parameters. The data can also be used to provide a preliminary interpretation of the molecular dynamics of the system although they were not acquired with this goal in mind.

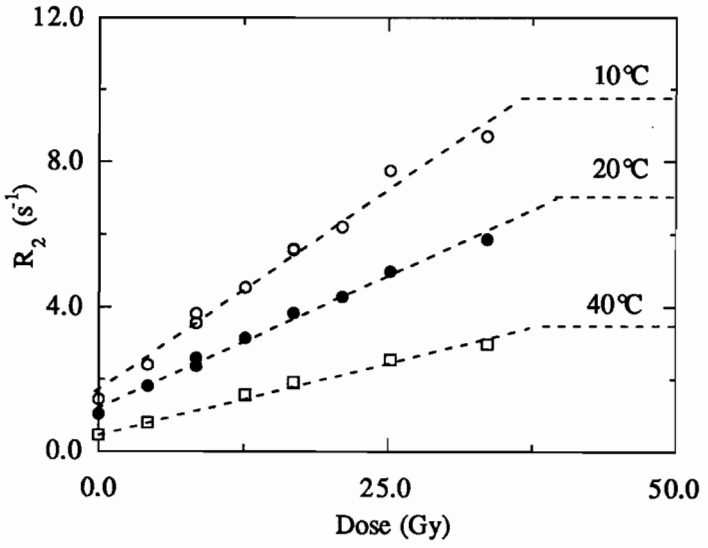

Figure 6.16 The effect of NMR measurement temperature on the R_2-dose response of a 67%C and 6%T BANG gel dosimeter containing 5% gelatin.

Molecular Dynamics

Temperature studies of relaxation times can yield information about the molecular dynamics in a system, in particular, the activation energies for the motions may be determined. As shown in Section 2.2.2, the relaxation times depend on molecular motions through the correlation times, τ, of the

motions. Because molecular motions are thermally activated processes, the following Arrhenius relation, given previously in Eq. 2.19b, is often assumed for the correlation times (Farrar and Becker, 1971):

$$\tau = \tau_0 \exp(E_a/kT), \tag{6.10}$$

where E_a is the activation energy and k is Boltzman's constant. For simple homogeneous systems whose motions and relaxation times are easily characterized in terms of correlation times, the activation energy may be determined from the R_2 versus temperature data (recall Eq. 2.33) shown on a BPP plot (see Section 2.4.1). However, for more complex systems where exact characterization in terms of τ's is not possible, effective activation energies may still be extracted from BBP plots to give qualitative information about molecular motions (Hsi *et al.*, 1976).

The temperature dependence of the observed spin-spin relaxation times of 5% gelatin, 67%C and 6%T BANG gels irradiated to different doses are shown in Fig. 6.17a along with the T_2's of pure water (Krynicki, 1966) and hydration water in low hydration polyacrylamide (Zhang, 1990). As discussed previously, the observed spin-spin relaxation is modulated by the exchange processes between the different water environments in the gel (Section 2.6). The inherent T_2^p's ($= 1/R_2^p$), independent of exchange processes, better characterize the temperature dependence of the spin-spin relaxation of the polymer hydration water protons. They are extracted from the observed T_2's using:

$$\frac{1}{T_2} = p^p\left(\frac{1}{T_2^p} - \frac{1}{T_2^w}\right) + \frac{1}{T_2(0Gy)}, \tag{6.11}$$

where polymer hydration water proton fraction, p^p, are determined from stoichiometry and the bulk water spin-spin relaxation time, T_2^w, is

determined from measurements at 20°C (T_2 = 2.38 s) using an activation energy of 4.2 kcal mol^{-1} appropriate for purified water (Krynicki, 1966).

The resulting T_2^P temperature dependencies of BANG gel dosimeters (67%C, 6%T and 5% gelatin) irradiated to different doses are given in Fig. 6.17b. Since the data for samples irradiated to different doses approximately follow parallel lines, the activation energies for the different doses are essentially the same. The average of these activation energies is about 6.2 ± 0.3 kcal mol^{-1}. A similar average activation energy of 6.7 ± 0.5 kcal mol^{-1} is found for 50%C, 6%T and 5% gelatin BANG gel dosimeters irradiated to different doses. These activation energies agree closely with that of the 6.5 kcal mol^{-1} associated with the hydrogen bonding of the hydration water in low water content polyacrylamide gels (Zhang, 1990). They are also greater than the activation of bulk water, 4.2 kcal mol^{-1}, and less than the activation energies of polymer motions (10-100 kcal mol^{-1}; McBrierty and Packer, 1993). These comparisons support the idea that the restricted motion of hydration water is involved in the spin-spin relaxation of BANG polymer gel dosimeters.

In addition, it can be deduced from the decrease in T_2^P with decreasing temperature that there is no chemical exchange occurring between the NH and NH_2 protons and the water protons over the 5°C to 40°C temperature range. The observed rates are expected to increase with temperature in the presence of chemical exchange. Similar behavior was observed for pure crosslinked polyacrylamide at neutral pH (Zhang; 1990), where R_2 decreased with temperature below 76°C and increased with temperature above 76°C indicating the onset of chemical exchange.

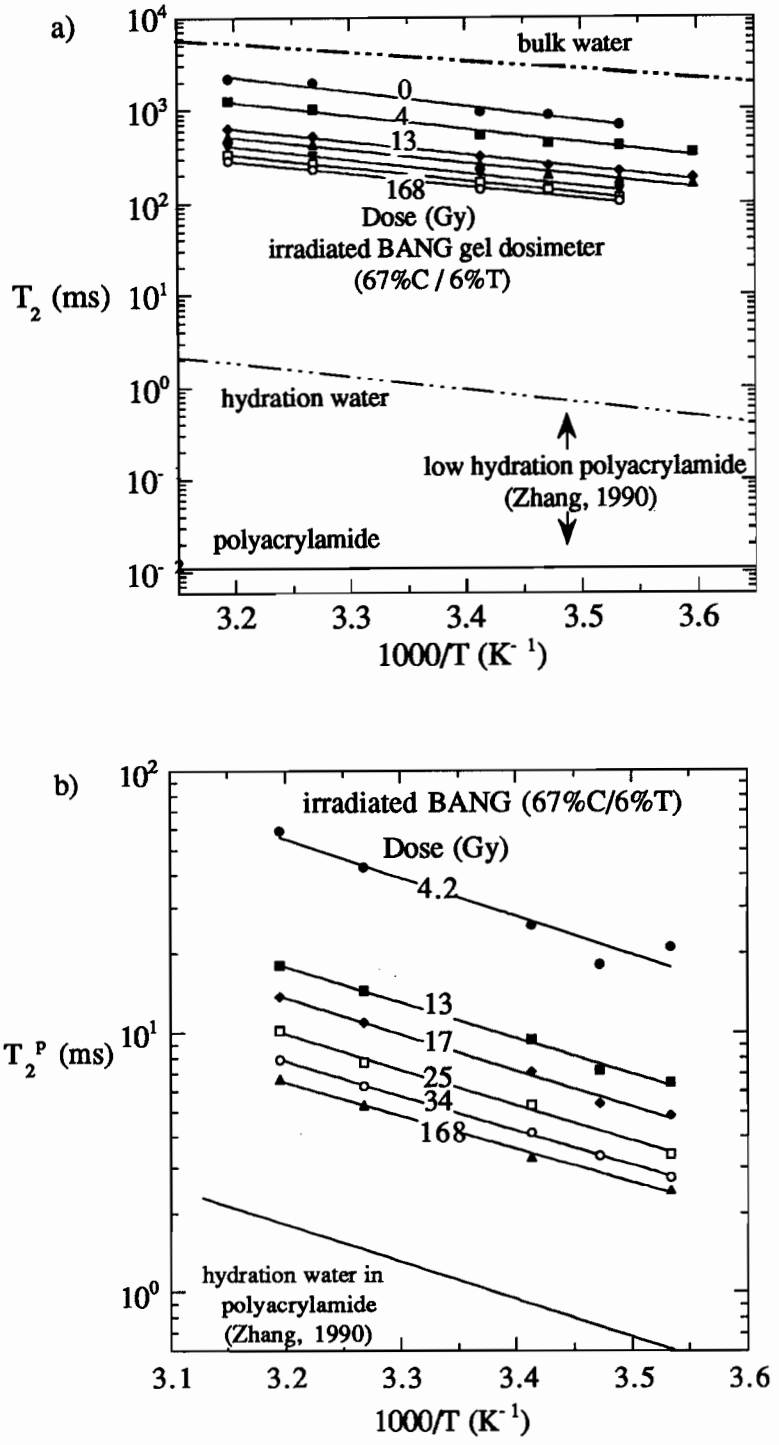

Figure 6.17 a) Temperature dependence of the spin-spin relaxation times of 5% gelatin, 67%C and 6%T BANG gel dosimeters irradiated to different doses along with the T_2's of pure water (Krynicki, 1966) and polyacrylamide and hydration water in low hydration polyacrylamide (Zhang, 1990). b) Temperature dependence of the T_2 of polyacrylamide hydration water in the BANG gel dosimeter (5% gelatin, 67%C and 6%T).

r^p an G^p

Figure 6.18a shows the effect of the NMR measurement temperature on the polymer relaxivity, rP, of 6%T and 5% gelatin BANG gels of varying %C. The relaxivity increases with decreasing temperature, the effect being more pronounced for higher %C. As discussed previously, this increase is expected to arise from the changes in the spin-spin relaxation resulting from the slowing of the hydration water dynamics (i.e., τ decreases with increasing temperature). Recalling that $r^P = kP\,(R_2{}^P - R_2{}^W)$, an increase in r^P with decreasing temperature is expected because $R_2{}^P$ changes more rapidly than $R_2{}^W$ as temperature decreases (E_a~6.2 and 4.2 kcal mol^{-1}, respectively).

It is apparent from Figure 6.18b that the NMR measurement temperature has no effect on the polymer yield regardless of the crosslinker fraction. This is to be expected since the amount of polymer formed is determined by the curing of the dosimeter before measurement occurs.

Optimization

The independence of polymer yield on temperature observed in Fig. 6.18 also indicates that D_{sat}, which is inversely proportional to yield (i.e., $D_{sat} = \%T/G^P$), should not be affected by the measurement temperature either. Hence, the dose range cannot be optimized by manipulating the measurement temperature.

Figure 6.19a shows that the general dose sensitivity dependence on %C does not vary with the measurement temperature. The dose sensitivity peaks at 50%C at 10°, 20° and 40°C, but the magnitude of the effect decreases with increasing temperature. The best dose sensitivities are obtained for low measurement temperatures. The increase in dose sensitivity with decreasing temperature is most pronounced for the 50%C BANG gel (see Fig. 6.29b). The

CHAPTER SEVEN
Conclusions

7.1 Ferrous Sulfate-Doped Gelatin Dosimeter

A physical model was proposed in Section 5.2.1 for the dose response of the spin-lattice relaxation rate of water protons in the ferrous-sulfate doped gelatin dosimeter. The model assumes fast physical exchange between the water hydrating the ions and gelatin and water in the bulk. It also assumes that the gelatin did not interact with the ions. Experimental testing of the model provided a better understanding of the dosimeter. The testing was accomplished in two ways: 1) by comparing the behavior of R_1 as a function of ion concentration for different gelatin concentrations with that predicted by the model and 2) by comparing NMR G-values for Fe^{3+} determined using the model for the R_1-dose response with the G-values for Fe^{3+} determined using spectrophotometry.

Agreement between the behavior observed for R_1 as a function of Fe^{2+} ion concentration for different gelatin concentrations supports the model. However, such agreement was not observed for the Fe^{3+} ion. It was found that in the ferrous-sulfate gelatin system the gelatin interacted with the Fe^{3+} ions indirectly by increasing the pH of the solution. This enhanced the ability of the Fe^{3+} ion to complex and, hence, to decrease the Fe^{3+} ion relaxivity. The gelatin-induced pH changes were not great enough to affect the ferrous ion relaxivity. Thus, the model correctly assumes fast exchange between all the

That is, absorbed dose can be directly determined for a given R_1 from the basic NMR and radiochemistry parameters r^{2+}, r^{3+} and $G(Fe^{3+})$.

7.2 BANG Polymer Gel Dosimeter

7.2.1 Reproducibility

The studies of Chapter 6 indicate that reproducible R_2-dose responses can be obtained for BANG gels prepared in small volumes and in separate batches. It has been shown that the reproducibility of the R_2-dose response is not affected by the gas (Ar or CO_2) used to purge oxygen from the gel and the cooling and irradiation temperature. However, the duration between irradiation and NMR measurement has to be taken into account since the R_2's of irradiated BANG dosimeters increase with time as post-irradiation polymerization and crosslinking reactions proceed. After sufficient time delays the reactions terminate and the R_2-value stabilizes. The R_2-dose responses are then temporally stable and reproducible at room temperature. About 1 and 2 days are required for the R_2-dose response to stabilize for the 50%C and 67%C samples (6%T), respectively. Assuming a given dosimeter composition and NMR measurement temperature, the main factors determining the reproducibility of the dosimeter are the presence of impurities and O_2 and the post-irradiation time delay.

It might be possible to reduce the post-irradiation time delay required for R_2 to stabilize by "developing" the gel by heating it slightly to accelerate the polymerization dynamics. This process would be interesting to investigate further.

7.2.2 Governing Mechanisms of the R_2-Dose Response

A model has been proposed for the dose response of the water proton R_2 in BANG polymer gel dosimeters. The model is based on the fast exchange of the water molecules between the water hydrating the polymer, that hydrating the gelatin and the bulk water. The model is given in terms of two parameters, the polymer relaxivity, r^P, and the polymer yield, G^P. The relaxivity essentially characterizes the greater inherent spin-spin relaxation rate of the water protons hydrating the polymer. The G^P indicates how the concentration of crosslinked polymer increases with dose.

The effects of dosimeter composition and NMR measurement temperature on r^P and G^P and the resulting effects on the dose sensitivity ($\alpha\ r^P G^P$; see Eq. 6.6) are summarized in Table 7.1 below.

Table 7.1 Effect of BANG gel dosimeter composition and NMR measurement temperature on G^P, r^P and d. The arrows indicate whether the parameters are increasing or decreasing. The thin and thick arrows represent weak and strong dependences, respectively.

	G^P	r^P	d
⇑[gelatin]	↓	constant	⇓
⇑%C	⇓	⇑	peak at 50%C
⇑%T	⇑	↑	⇑
⇑Temp.	N/A	⇓	⇓

One of the more interesting observations was the peaking of the dose sensitivity at 50%C arising from the opposing effects of increases in r^P and decreases in G^P with increasing %C. Future more thorough studies could involve acquiring data for a greater range of monomer compositions. The conclusions, derived from the above results, for r^P and G^P are summarized below.

Polymer Chemical Yield, G^P

It has been proposed in Section 6.2.2 that the polymer chemical yield is related to the polymerization dynamics through the kinetic chain length, ν, which is equivalent to the ratio of the polymerization rate to the termination rate, R_p/R_t. Thus, the effects of any variable on G^P can be explained in terms of effects of the variable on the reaction dynamics.

For gelatin concentrations exceeding 4% the R_2-dose response is linear and G^P is probably constant with dose. This linear response differs from the go-no-go polymer dosimeters developed previously (see Section 3.3.3). It seems that the gelatin moderates the polymerization by increasing the viscosity of the dosimeter so that the diffusion of reactants is moderated. In the absence of gelatin, the diffusion of reactants is determined by the amount of polymer formed and G^P varies with dose to produce a non-linear threshold dose response (Maryanski *et al.*, 1993). It would be interesting to investigate the effect of gelatin concentration on the R_2-dose response in more detail to better characterize the move from a step-function-like response to a linear one. However, this is of academic interest only since a threshold dose response is not practical for 3-D radiation dosimetry.

Both the percent weight fraction of Bis per total monomer, %C, and the percent weight fraction of monomer in the gel, %T, have been known to

supports the assumption made by the model that the gelatin does not play a significant role in determining the R_2-dose response of the BANG dosimeter.

Constant r^P and G^P

Several observations and results support the assumption that G^P and r^P are constant with dose. First of all the R_2-dose response of a particular polymer dosimeter is linear (see Fig. 6.7). Second, r^P may be constant with dose because it is constant with %T below 4%T (see Fig. 6.12). Third, a polymer yield that is constant with dose is well explained by the proposed theory relating G^P to the kinetic chain length and polymerization dynamics. Future studies could be used to verify that G^P is constant with dose by measuring the polymer proton magnetization fractions for samples irradiated to different doses. These magnetization fractions are proportional to the amount of polymer formed.

7.2.3 BANG Dosimeter Optimization

The results of the effect of BANG dosimeter composition and NMR measurement temperature on the optimization parameters of the R_2-dose are summarized in Table 7.2 below.

If one is only concerned with relative doses for a given dosimetry application and irradiations can be performed to span the dose range within a practical time frame, then the error in the maximum dose delivered can be minimized by maximizing the dynamic range (see Section 1.2.3). The dynamic range is greatest for high %C and %T and low NMR measurement temperatures. However, the post-irradiation R_2-time responses presented in Section 6.1 suggests that higher %C BANG gels may take longer to stabilize,

and that one may have to compromise greater dynamic ranges for quicker stabilization.

Table 7.2 Effect of dosimeter composition and NMR measurement temperature on the parameters characterizing the R_2-dose response. The arrows indicate whether the parameters are increasing or decreasing. The thin and thick arrows represent weak and strong dependence, respectively.

	dynamic range R_2^{max}-R_2(0Gy)	dose range D^{sat}	dose sensitivity d
⇑[gelatin]	constant	↑	⇓
⇑%C	⇑	⇑	peak at 50%C
⇑%T	⇑	↑	⇑
⇑Temp.	⇓	constant	⇓

For the determination of absolute doses the lowest minimum detectable dose and the highest dose resolution are obtained with dosimeters having the highest dose sensitivity (recall Section 1.2.3). The highest dose sensitivity is obtained for low measurement temperature, 50%C for 6%T and high %T for 50%C. The greatest %C and %T that can be used for either absolute or relative dosimetry applications is limited by the solubility of Bis (~3-4 g per 100 g of BANG gel). While the 50%C BANG gels exhibit the highest dose sensitivity, these gels are also the most sensitive to temperature. This emphasizes the importance of allowing the BANG gel dosimeters to equilibrate thoroughly to the ambient temperature prior to magnetic resonance imaging so that the R_2-dose response is uniform throughout the dosimeter.

The increases in dynamic range and dose sensitivity with decreasing measurement temperature suggest that it would be worth while designing a method for analyzing gels in an MR imager at temperatures below room temperature.

7.3 Ferrous Sulfate-Doped Gels vs Polymer gels

Three parameters, the dynamic range, dose sensitivity and dose range can be used to evaluate the performance of gel dosimeters studied herein and in the literature (see Section 1.2.3). For relative dose determinations in which the whole dynamic range of a dosimeter's dose response can be spanned within a practical time frame, the best dose resolution and minimum detectable dose are obtained for dose responses with the greatest dynamic range and the minimum measurement error (see Section 1.2.3). Similarly, for the determination of absolute doses, the best minimum detectable dose and dose resolution are obtained for the highest dose sensitivity (recall Section 1.2.3). Wide dose ranges are preferred for high dose irradiations such as those produced by brachytherapy treatments.

The best dynamic ranges for relaxation rates have been observed for the polymer gel dosimeters. The maximum dynamic ranges observed for any gel dosimeter were 9.6 s^{-1} for the R_2-dose response of a 67%C, 6%T and 5% gelatin BANG gel dosimeter measured at 5° C and 20 MHz (see Fig. 6.20) and ~10 s^{-1} for a 50 %C, 8%T BANANA gel measured at 20°C and 85 MHz (Maryanski *et al.*, 1993; see Fig. A1.2). These dynamic ranges could be further extended by

increasing the %T and the measurement frequency, and slightly decreasing the NMR measurement temperature.

The dynamic range of R_1 for the ferrous sulfate-doped gelatin dosimeter studied in Chapter 5 theoretically could reach 8 - 10 s^{-1}, however, the depletion of oxygen limits the range to about 2 - 3 s^{-1}. Greater R_2-dynamic ranges of ~ 6 s^{-1} and ~ 7 s^{-1} have been observed for well oxygenated ferrous sulfate agarose dosimeters (Gambriani *et al.*, 1994) and small aerated ferrous sulfate gelatin dosimeters (Duzenli *et al.*, 1994), respectively. However, the dynamic range observed for small aerated samples is not expected to apply to large volume dosimeters where enhanced aeration is hard to achieve beyond 3 mm depth from the surface (Duzenli *et al.*, 1994).

Greater dose sensitivities are observed for polymer gels than for ferrous sulfate gels. A maximum dose sensitivity of 0.52 $s^{-1}Gy^{-1}$ has been measured for a 50%C, 6%T and 5% gelatin BANG gel dosimeter measured at 5° C and 20 MHz (see Fig. 6.19). This compares closely to the dose sensitivity of 0.44 $s^{-1}Gy^{-1}$ reported for a gel of identical composition, prepared using a different protocol, and measured at 0°C and 64 MHz (Maryanski *et al.*, 1994). It is expected that the dose sensitivity could be increased further by increasing %T and decreasing the NMR measurement temperature. The highest dose sensitivity reported for a ferrous sulfate-doped gel system is 0.20 $s^{-1}Gy^{-1}$ for the R_2-dose response of an oxygenated 1% agarose-Seaplaque gel at room temperature and 63 MHz (Gambriani *et al.*, 1994). These dose sensitivities are much greater than those of ~ 0.04 $s^{-1}Gy^{-1}$ observed for the ferrous sulfate-gelatin gels (see Table 5.1). Results in Chapter 5 indicated that neither gelatin nor sulfuric acid concentration affected the dose sensitivity of the gelatin-based gel significantly enough.

The maximum dose range observed for any gel dosimeter is ~120 Gy for the small well aerated ferrous sulfate gelatin dosimeters, but again this dose range does not apply to large volume dosimeters (Duzenli *et al.*, 1994). The greater dose ranges that can be observed for larger volume dosimeters are ~ 80 Gy for a 83%C, 6%T and 5% gelatin BANG gel (see Fig. 6.15). This saturation dose is much higher than the ~ 10 Gy previously reported for polymer gel dosimeters (Maryanski *et al.*, 1993; see Table A1.2) and those of ~40 Gy for aerated ferrous sulfate gelatin dosimeters (see Chapter 5).

Overall, it would appear that the polymer gels provide the best spin relaxation dose responses, and hence, the best dose resolutions and minimum detectable doses for 3D radiation dosimetry using MRI. The resulting dose resolution and minimum detectable dose would depend on the resolution of the measurement, either intensity or relaxation rate, from the MR imager. Their actual determination for the optimal BANG gel dosimeter compositions and NMR measurement temperature could be the subject of future investigations. Other advantages of polymer gels mentioned in Section 3.3.3 include their temporal stability (after termination of post-irradiation reactions), neutral pH, and visually observable dose response (Maryanski *et al.*, 1994). The advantage of the ferrous sulfate-doped gel dosimeters remains their ease of preparation, low cost and availability of dose information immediately after irradiation. Both dosimeters offer the possibility of an absolute dosimetry given the physical models presented in Chapters 5 and 6 that relate R_1 and R_2 to dose.

Appendix A1

Compilation of dose response data taken from various sources in the literature. Table A1-1 reviews the results of studies on the various ferrous sulfate-doped gels while Table A1-2 presents the data for the polymer gel dosimeters. In some cases the various parameters have been taken directly from the literature, in others the parameters have been extracted by the author from published dose response curves.

All NMR measurements were at room temperature unless otherwise stated. Proton frequency specified in MHz. If the preparation of the dosimeter differs from the standard, the changes are specified in the Conditions Column.

The symbol ≥ indicates that the real dose range could not be obtained from the published dose response since the saturation dose was not reached.

The G^{NMR} and G^{spect} are the G-values found using NMR and spectrophotometric methods, respectively. If G is specified without a subscript then the yield was determined by some alternate method.

Any data presented in Chapters 5 or 6 of this thesis which may have been reported previously at conferences or in the literature are not included in these tables.

Table A1-1: Ferrous Sulfate (Fricke) Dosimeters

NMR frequency	Sample Condition	Dose Response: dose sensitivity ($s^{-1}Gy^{-1}$) (R1 unless specified)	dynamic range (s^{-1})	dose range (Gy)	G-value* (#Fe^{3+}/100eV)
Aqueous Fricke solution (1 mM Fe^{2+}, 1 mM NaCl, 0.4 M H_2SO_4)					
Gore et al., 1984					
20 MHz	37°C	0.0113			G^{NMR}=13.4
		0.0121 (R_2)			
Hiraoka et al., 1986					
4.2 MHz		0.0105			
Olsson et al., 1989					
10 MHz	0.05 M H_2SO_4	0.018			
	0.4 M H_2SO_4	0.016			
Podgorsak and Schreiner, 1992					
25 MHz		0.0182	7	400	G^{NMR}~23 (increased due to wall impurities)
9 MHz		0.0263	10	400	
Prasad et al., 1992					
64 MHz		0.018			
		0.019 (R_2)			
	1.32 mM benzoic	0.086			
Hiraoka et al., 1992					
		0.028			

Table A1-1 (con't)

NMR frequency	Sample Condition	Dose Response: dose sensitivity ($s^{-1}Gy^{-1}$) (R1 unless specified)	dynamic range (s^{-1})	dose range (Gy)	G-value* (#Fe^{3+}/100eV)
	Agarose Fricke gel				
Appleby et al., 1987 (1.5% agarose; 0.4 mM Fe^{2+}; 0.025 M H_2SO_4; 5 mM benzoic acid)				10	G^{spect} = 101
Appleby et al., 1988 (1% agarose; 0.025M H_2SO_4)					
20 MHz	air / 0.4 mM Fe^{2+}	0.090	≥1.5	8	G^{spect}=98.8
	air/ 0.9 mM Fe^{2+}			12	G^{spect}=61.7
	air/ 10 mM Fe^{2+}			-	G^{spect}=37.1
	O_2/ 0.4 mM Fe^{2+}			12	G^{spect}=134
	N_2/ 0.4 mM Fe^{2+}			4	G^{spect}=37
Olsson et al., 1989 (Agarose +)					
	1% agarose/air	-		not linear	
	1% agarose/ O_2	0.074	≥3	≥40	
	1.5% agarose/ O_2	0.020			
Olsson et al., 1990 (1.25% SeaPlaque Agarose + 0.25% Seagel)					
10 MHz	0.05-.4 M H_2SO_4	0.11-0.12			
	0.5 mM Fe^{2+}	0.2	3	15	
	1 mM Fe^{2+}	0.13	≥5	≥40	
	1.5 mM Fe^{2+}	0.12	≥ 4	≥ 40	G=94

Table A1-1 (Agarose Fricke gel con't)

NMR frequency	Sample Condition	Dose Response: dose sensitivity ($s^{-1}Gy^{-1}$) (R1 unless specified)	Dose Response: dynamic range (s^{-1})	Dose Response: dose range (Gy)	G-value* (#Fe^{3+}/100eV)
Schulz et al., 1990 (1% agarose; 1 mM Fe^{2+}; 0.5 mM NaI, oxygenated)					
20 MHz				20	150
	1-2% agarose + 0.5-5 mM Fe^{2+}	0.10	4	20	
	0.25 mM Fe^{2+}	0.07			
85 MHz		0.13	5.5	20	
	12-50 mM H_2SO_4	0.10	3.5	20	
	250 mM H_2SO_4	0.11	4	20	
Olsson et al., 1991 (1.5% agarose; 3 mM Fe^{2+}; 1mM NaCl; 50 mM H_2SO_4)					
10 MHz		0.108	≥4	≥40	G=93.9
Kron et al., 1993 (1.5% agarose; 0.125 M H_2SO_4; 0.5 mM Fe^{2+})					
63 MHz		0.084	1	10	
		0.09 (R_2)	1	10	
Gambriani et al., 1994 (1 mM Fe^{2+}; 1mM NaCl; 0.05 M H_2SO_4)					
64 MHz	1% agar-agar+O_2	0.09	≥1.5	≥15	
	1% Seaplaque O_2	0.2	6	35	G^{NMR}=185
Kron and Pope, 1994 (1.5% agarose; 0.5 mM Fe^{2+}; .125 M H_2SO_4)					
64 MHz		0.08	1.5	20	
Rousseau et al; 1994 (1 mM Fe^{2+}; 0.05 M H_2SO_4; 1% agarose; 1mM NaCl)					
20 MHz		0.039-0.058			

Table A1-1 (con't)

NMR frequency	Sample Condition	Dose Response: dose sensitivity ($s^{-1}Gy^{-1}$) (R1 unless specified)	Dose Response: dynamic range (s^{-1})	Dose Response: dose range (Gy)	G-value* (#Fe^{3+}/100eV)
	Gelatin Fricke gel				
Appleby et al., 1988 (1mM Fe^{2+}, 0.025M H_2SO_4)					
20 MHz	4% gelatin	0.041	≥1.5	≥40	
	8% gelatin	0.031	≥1	≥40	
Hazle et al., 1991 (5% gelatin; 0.05 M H_2SO_4; 1 mM NaCl)					
64 MHz	0.5-2 mM Fe^{2+}	0.04492	2.3	50	
	≤ 0.5 mM Fe^{2+}	< 0.045	< 2.3	< 50	
Keller et al., 1993 (5% gelatin; 1mM Fe^{2+}; 0.05 M H_2SO_4)					
25 MHz		0.04	2	50	
	aerated	0.041	1.7	40	
	oxygenated	0.043	3.5	80	
Duzenli et al., 1994 (4% gelatin; 1 mM Fe^{2+}; 0.05M H_2SO_4)					
100 MHz		0.077 (R_2)	≥3	≥40	G^{NMR}=55
	4% gel; 0.15M H_2SO_4	0.091 (R_2)	≥3.5	≥40	G^{NMR}=62
	8% gel "	0.082 (R_2)	≥3.3	≥40	G^{NMR}=54
	12% gel "	0.069 (R_2)	7	120	G^{NMR}=44
Chan and Ayyangar; 1995					
64 MHz	1 mM Fe^{2+}; 0.1N H_2SO_4; 7.5% gelatin; R_1 ;	0.031			

Table A1-1 (con't)

NMR frequency	Sample Condition	Dose Response: dose sensitivity ($s^{-1}Gy^{-1}$) (R1 unless specified)	dynamic range (s^{-1})	dose range (Gy)	G-value* (#Fe^{3+}/100eV)
	Sephadex Fricke gel				
Hiraoka et al., 1986					
	crosslinked Sephadex G-200	0.105		30	
Hiraoka et al., 1992					
	2-4% Sephadex G-200 gel;	0.107	3	30	
Hiraoka et al., 1993 (1 mM Fe^{2+}; 0.4 N H_2SO_4; 1% sephadex + 3.8% Sumikagel)					
		0.0476	1.5	30	

Table A1-2: Polymer-gel Dosimeters

NMR frequency	Sample Condition	Dose Response: dose sensitivity ($s^{-1}Gy^{-1}$) (R1 unless specified)	Dose Response: dynamic range (s^{-1})	Dose Response: dose range (Gy)
BANANA gel (4% Bis, 4% acrylamide, 1% agarose)				
Maryanski et al., 1993				
20 MHz	40°C	0.024	0.40	~ 15
		0.22 (R_2)	4 (R_2)	"
64 MHz	20°C	0.015	0.32	"
		0.28 (R_2)	5 (R_2)	"
85 MHz	20°C	0.014	0.25	"
		0.67 (R_2)	10 (R_2)	"
BANG gel				
Maryanski et al., 1994 (3% Bis, 3% acrylamide, 5% gelatin)				
64 MHz	irradiation temperature dependence	none	none	none
	25 ° C	0.25 (R_2)	3	8
	0° C	0.44 (R_2)	3.7	8
Maryanski et al., 1995 (3% Bis, 3% acrylic acid; 1% NaOH; 5% gelatin)				
64 MHz	20° C	0.335 (R_2)	> 4	> 10

Appendix A2:

List of Symbols

(Note that the page numbers also apply to the symbols that follow and have no page number indicated)

Symbol	Description	Page #
	CHAPTER ONE	
	Introduction	
MRI	Magnetic Resonance Imaging	1-3
CT	Computed Tomography	
HDR	High Dose Rate	1-4
Z_{eff}	effective atomic number	1-7
Z	atomic number	
A	atomic weight	
μ	linear attenuation coefficient	1-8
μ_{ab}	energy absorption attenuation coefficient	1-9
μ_{ab}/ρ	mass energy absorption attenuation coefficient	
ρ	mass density	
S	linear stopping power	1-10
S_{col}	collisional stopping power	
S_{rad}	radiative stopping power	
N_e	electron density	
S/ρ	mass stopping power	1-11
L/ρ	mass restricted collisional stopping power	
PDD	Percent Depth Dose	1-12
D	Dose	1-13
d	dose sensitivity	
TLD	Thermoluminescent Dosimeter	1-16

Fe^{2+}	ferrous ion	1-22
Fe^{3+}	ferric ion	

CHAPTER TWO
Nuclear Magnetic Resonance and Relaxation

NMR	Nuclear Magnetic Resonance	2-1
$\vec{\mu}$	magnetic moment of a nucleus with spin with components μ_x, μ_y, μ_z.	
$\hbar$	Plank's constant	
$\mathbf{I}$	spin operator with components operators I_x, I_y, I_z	
γ	gyromagnetic ratio	
I_2, I_z	spin operators with eigenvalues $I(I+1)$ and m, respectively, and eigenstates $\|Im\rangle$, where I is designated the spin of the nucleus	
$\mathbf{H}$	applied magnetic field	2-2
$\mathcal{H}_o$	Zeeman Hamiltonian	
Ψ	generalized wave function	
E_m	energy eigenvalue of the Zeeman Hamiltonian	
a_m	coefficients of the constituent eigenstates $\|m\rangle$ of Ψ	
I_+, L	raising and lowering operators, respectively	2-3
ω_o	Larmor frequency	
$\mathbf{M}$	macroscopic magnetization with components M_x, M_y, M_z	2-4
k	Boltzman's constant	
$\overline{\langle \vec{\mu} \rangle}$	the expectation value of the magnetic moment averaged over all spins	
θ	angle of rotation of M produced by an rf pulse	2-8
t_p	duration of the rf pulse	
T_1	spin-lattice or longitudinal relaxation time	
T_2	spin-spin or transverse relaxation time	

$\mathcal{H}_1$	perturbing Hamiltonian of the spin interaction	2-9
$S^{(q)}(t)$	spatial time dependent operators of $\mathcal{H}_1$	2-11
$A^{(q)}$	spin operators of $\mathcal{H}_1$	
q	difference in the states joined by $A^{(q)}$ (=Δm)	
$J_q(q\omega_o)$	spectral density functions	2-12
τ	correlation function	
$G^{(q)}$	Gentlemen's Quarterly or auto-correlation function of the spatial operators	
E_a	activation energy	
r	distance between two spins	2-16
$D_{1,2}$	Debeye terms describing spin relaxation of anistropically reorienting water	2-23
M_w	molecular weight of the polymer	2-26
$G_T^{(q)}$	total correlation function for protons on polymer molecules with components $G_s^{(q)}$, G_l and G_f for segmental, longitudinal diffusion and fluctuation motions of the polymer molecule	
S	electron spin	2-29
R_1	spin-lattic relaxation rate (=$1/T_1$)	2-30
R_2	spin-spin relaxation rate (=$1/T_2$)	
$p_{a,b}$	inherent fractions of spins in groups 'a' and 'b'	
$R_{a,b}$	inherent spin relaxation rates of two proton groups 'a' and 'b'	2-33
$k_{a,b}$	rates at which magnetization is exchanges between proton groups 'a' and 'b'.	
$\lambda^{\pm}$	apparent or observed relaxation rates	
$C^{\pm}$	apparent or observed magnetization fractions	2-34

CHAPTER THREE
Gel Dosimeters

$G(x)$	chemical yield or G-value for radiation product x	3-1
D_{sat}	dose at which a response saturates	3-3
$R_{1,2}^{max}$	maximum spin-lattice or spin-spin relaxation rate that a $R_{1,2}$-dose response saturates to.	
H_2O^*	excited water molecule	3-5
H_2O^+	water cation	
e_{aq}^-	hydrated electron	
H_3O^+	hydronium ion	
OH•	hydroxyl radical	
H•	hydrogen radical	3-6
H_2O_2	peroxide molecule	3-8
OH-	hydroxyl ion	
$\Delta[Fe^{3+}]$	change in ferric ion concentration	3-10
N_A	Avogadro's number	
e	number of Joules per electron volt	
p^i	i=2+, 3+; inherent fractions of water protons hydratine Fe^{2+} or Fe^{3+}	3-11
R_1^i	i=2+, 3+ or water; inherent spin-lattice relaxation rate for water hydrating ferrous or ferric ion and bulk water	
k^i	i=2+, 3+; fraction of water protons hydrating ions per unit ion concentration	
[x]	concentration of species x	
r^i	i=2+, 3+; ion spin-lattice relaxivity for ferrous sulfate gels	3-12
$[Fe^{2+}]_o$	ferrous ion concentration prior to irradiation	
R•	gel macroradicals; • denotes the radical form	3-14
RH	gel macromolecule	

RX	reduced form of RH	3-15
ROH	oxidized form of RH	
I•	initiator or primary radical	3-29
M_1, M_2	two co-monomers	
k_i	reaction rate constants	3-30
M_n	polymer molecule consisting of 'n' monomers	
R_p	propagation rate for polymerization reaction	
R_t	termination rate for termination reaction	3-31
v	kinetic chain length	3-32
BANG	Bis Acrylamide Nitrogen Gelatin dosimeter	
%T	percent weight fraction of a gel that is comonomer	3-34
%C	percent weight fraction of all the monomer that is crosslinker	
BANANA	Bis Acrylamide Nitrogen ANd Agarose dosimeter	3-38

CHAPTER 4
Methods and Materials

T_2^*	spin-spin decay constant of the FID	4-2
FID	Free Induction Decay	
TE	time between the application of a 90° rf pulse and the formation of an echo in a spin-echo rf pulse sequence	4-5
G	magnetic field gradient	
D	spin diffusion constant (otherwise dose in all other chapters)	
TI	time between the application of the 90° pulse and 180° pulse in the inversion recovery pulse sequence	4-6
A(t)	signal amplitude at time 't'	
ODU	optical density units	4-12
SSD	surface skin distance	4-13
A_λ	absorbance of a sample at wavelength λ	4-16

ε_λ	extinction coefficient at wavelength λ	
l	optical path length	

CHAPTER 5
Results and Discussion: Ferrous Sulfate-Doped Gels

R_1	observed spin-lattice relaxation rate of the water protons in ferrous sulfate-doped gel dosimeters	5-1
p^{gel}	fraction of water protons hydrating the gelatin	5-12
$R_1{}^{gel}$	inherent spin-lattice relaxation rate of the water protons hydrating the gelatin	
k^{gel}	fraction of water protons hydrating the gelatin per unit concentration of gelatin	
R_o	the spin-lattice relaxation rate of an unirradiated ferrous sulfate gelatin dosimeter	
p_j^{3+}	fraction of water protons hydrating the j^{th} complexed form of Fe^{3+}	5-19
$R_{1,j}^{3+}$	inherent spin-lattice relaxation rate of the water protons hydrating the j^{th} complexed form of Fe^{3+}	
f_j	fraction of the Fe^{3+} ions that is the j^{th} complexed form	5-20
r_j^{3+}	spin-lattice relaxivity of the water protons hydrating the j^{th} complex	

CHAPTER SIX
Results and Discussion: BANG Polymer Gels

R_2	observed spin-spin relaxation rate of the water protons in the BANG polymer gel dosimeter	6-18
R_2^p	spin-spin relaxation rate of the polymer hydration water protons	
R_2^g	spin-spin relaxation rate of the gelatin hydration water protons	
R_2^w	spin-spin relaxation rate of the bulk water protons	
p^p	fraction of the water protons hydrating the polymer	

p^g	fraction of the water protons hydrating the polymer	
k^p	fraction of the water protons hydrating the polymer per weight fraction of polymer in the dosimeter	6-19
Gp	polymer yield	
[p]	polymer weight fraction	
r^p	spin-spin relaxivity of the polymer	

References

Abragam, A., *The Principles of Nuclear Magnetism*, Clarendon Press, Oxford, England (1991).

Alexander, P. and Fox, M., "The degredation of polymethacrylic acid by x-rays," Trans. Faraday Soc. **50**, 605-612 (1954).

Allen, A.O., *The Radiation Chemistry of Water and Aqueous Solutions* (Van Nostrand, Princeton, NJ, 1961).

Allen, G., "Applications of NMR spectroscopy in polymer science," Rev. Pure and Appl. Chem. **17**, 67, (1967).

Andreo, P., Cunningham, J.R., Hohlfeld, K. and Svensson, H., "Absorbed dose determination in photon and electron beams," IAEA Technical Report Series **277**, 1-98 (1987).

Appleby, A., Christman, E.A. and Leghrouz, A., *Imaging of Spatial Radiation Dose Distribution in Agarose Gels Using Magnetic Resonance*, Med. Phys., **14** (3), 382-384 (1987).

Appleby, A., Leghrouz, A. and Christman, E.A., "Radiation chemical and magnetic resonance studies of aqueous agarose gels containing ferrous ions," Radiat. Phys. Chem. **32**, 241-244 (1988).

Attix, F.H., Roesch, W.C. and Tochilin, E., *Radiation Dosimetry*, Vol. 2, 2nd ed. (Academic Press, New York, NY, 1966).

Attix, F.H., *Introduction to Radiological Physics and Radiation Dosimetry* (John Wiley and Sons, New York, NY, 1986).

Audet, C., *NMR-Based Radiation Dosimetry Using Polymer Solutions*, M.Sc. thesis, McGill University, Montreal (1991).

Audet, C., Keller, B.M. and Schreiner, L.J., "NMR relaxation in the Fricke-gelatin dosimeter," Proceedings of the Society of Magnetic Resonance In Medicine, 12th annual scientific meeting, New York, NY, 736 (1993).

Audet, C. and Schreiner, L.J., "Multi-site fast exchange model for spin-lattice relaxation in the Fricke-gelatin dosimeter," Med. Phys. **21**, 1364 (1994).

Audet, C. and Schreiner, L.J., "NMR relaxation in the Fricke-gelatin dosimeter," Phys. Med. Biol. (submitted, 1995).

Ayyangar, K.M. and Chan, M.F., "Spatial verification of brachytherapy dose distributions by FeMRI dosimetry," Med. Phys. **22**(6), 924 (1995).

Bevington, P.R. and Robinsion, D.K., *Data Reduction and Error Analysis for the Physical Sciences*, 2nd ed. (McGraw-Hill, New York, NY, 1992).

Bloembergen, N. and Morgan, L.O., Proton relaxation times in paramagnetic solutions: Effects of electron spin relaxation," J. Chem. Phys. **34**, 842-50 (1961).

Bloembergen, N., Purcell, E.M., and Pound, R.V., "Relaxation effects in nuclear magnetic resonance absorption," Phys. Rev., **73**, 679-712 (1948).

Boni, A.L., "A polyacrylamide gamma dosimeter," Rad. Research **14**, 374-380 (1961).

Bortfeld, T. and Schlegel, W., "Optimization of beam orientations in radiation therapy: some theoretical considerations," Phys. Med. Biol. **38**(2), 291-304 (1993).

Bragg, W.H., *Studies in Radioactivity* (Macmillan, New York, NY, 1912).

Callaghan, P.T., *Principles of Nuclear Magnetic Resonance Spectroscopy* (Oxford University Press, New York, 1991).

Calvert, P., "Polyacrylamide gels," Nature **254**, 104 (1975).

Carr, H.Y. and Purcell, E.M., "Effects of diffusion on free precession in nuclear magnetic resonance experiments," Phys. Rev. **94**, 630-638 (1954).

Chan, M.F. and Ayyanger, M., "Confirmation of target localization and dosimetry for 3D conformal radiotherapy treatment planning by MR imaging of a ferrous sulfate gel head phantom," Med. Phys. **22**(7), 1171-1175 (1995a).

Chan, M.F. and Ayyanger, M., "Verification of water equivalence of FeMRI gels using Monte Carlo simulation," Med. Phys. **22**(4), 475-478 (1995).

Charlesby, A. and Folland, R., "The use of pulsed NMR to follow radiation effects in long chain polymers," Radiat. Phys. and Chem. **15**, 393-403 (1980).

Chawla, K.J., Jaffray, D.A., Yu, C.X. and Wong, C.W., "Two dimensional plastic scintillator for dosimetry of dynamic intensity modulation," Med. Phys. **22**, 995 (1995).

Chiu-Tsao, S.T., de la Zerda, A., Lin, J. and Kim J.H., "High-sensitivity GafChromic film dosimetry for ^{125}I seed," Med. Phys. **21**, 651-657 (1994).

Curtin-Savard, A., *Dose Delivery Uncertainty in Photon Beam Radiotherapy*, MSc Thesis, McGill University, Montreal (1995).

Dixon, R.L., Ekstrand, K.E. and Moran, P.R., "Physical Foundations of Proton NMR" in *NMR in Medicine: The Instrumentation and Clinical Aspects*, S.R. Thomas and R.L. Dixon, Ed.s (American Inst. of Physics Inc., New York NY, 1986).

Dorner, K.J., "A new realtime detector-array for dosimetry," Med. Phys. **22**, 995 (1995).

Draganic, I.G. and Draganic, Z.D., *The Radiation Chemistry of Water* (Academic Press, New York, NY, 1971).

Duzenli, C., Sloboda, R. and Robinson, D., "A spin-spin relaxation rate investigation of the gelatin ferrous-sulfate NMR dosimeter," Phys. Med. Biol. **39** (1994).

Duzenli, C., *Spin-Spin Relaxation Rate MRI Dosimetry using Ferrous Sulfate-Gelatin Materials*, Ph.D. thesis, University of Alberta, Edmonton, Alberta (1995).

Eisinger, J., Shulman, R.G. and Szymanski, B.M., "Transition metal binding in DNA solutions," J. Chem. Phys. **36**(7), 1721-1729 (1962).

Encyclopedia of Polymer Science, Vol. 7, 2nd ed., 514 (John Wiley and Sons, 1985).

Evans, R.D., *The Atomic Nucleus,* R.E. Krieger Ed., (McGraw-Hill, Malabar FL, 1982).

Feng, P.Y., "Polymer degradation - wide range dosimeter," Nucleonics **16**, 114 (1958).

Ferrar, T.C. and Becker, E.D., *Pulse and Fourier Transform NMR,* (Academic Press, New York, NY, 1971).

Fricke, H. and Morse, S., "The chemical action of Roentgen rays on dilute ferrosulphate solutions as a measure of dose," Am. J. Roent. Radium Ther. Nucl. Med. **18**, 430-432 (1927).

Fricke, H. and Hart, E.J., "Solid state integrating dosimeters" in Radiation Dosimetry, Vol. 2, F.H. Attix and W.C. Roesch, Ed.s (Academic Press, New York, NY, 1966).

Galvin, J.M., Chen, X.G., and Smith R.M., "Combining multileaf fields to modulate fluence distributions," Int. J. Radiat. Oncol. Biol. Phys. **27**, 697-705 (1993).

Gambriani, G., Arrigoni, S., Cantone, M.C., Molho, N., Facchielli, L. and Sichirollo, A.E., "Dose-response curve slope improvement and result reproducibility of ferrous-sulfate-doped gels analysed by NMR imaging," Phys. Med. Biol. **39**, 703-717 (1994).

Geissler, E., Hecht, A.M. and Duplessix, R., J.Polymer Sci. A-2 **20**, 225 (1982).

Gelfi, C. and Righetti, P.G., "Polymerization kinetics of polyacrylamide gels I. Effect of different crosslinkers," Electrophoresis **2**, 213-219 (1981).

Gelfi, C. and Righetti, P.G., "Polymerization kinetics of polyacrylamide gels II. Effect of temperature," Electrophoresis **2**, 220-228 (1981).

Glasgow , G.P., Bourland, J.D., Grigsby, P.W. et al, "Remote afterloading technology," AAPM Report No. 41, New York (AIP) (1993).

Gore, J.C., Kang, Y.S., and Schulz, R.J., "Measurement of radiation dose distributions by Nuclear Magnetic Resonance (NMR) Imaging," Phys. Med. Biol. **29**, 1189-1197 (1984)

Gray, L.H., "Absorption of penetrating radiation," Proc. Roy. Soc. **A122**, 647 (1929).

Gray, L.H., "Ionization method for the absolute measurement of gamma-ray energy," Proc. Roy. Soc. **A156**, 578 (1936).

Greening, J.R., *Fundamentals of Radiation Dosimetry*, 2nd ed. (Adam Hilger Ltd., Bristol, England, 1981).

deGuzman, A., Gore, J.C. and Schulz, R.J., *Dose-Response Curves for Gels Infused with Fricke Dosimeter by NMR*, Med. Phys., **16**(3), 457 (1989).

Hahn, E.L., "Spin Echoes," Phys. Rev. **80**, 580-594 (1950).

Harrison, R.M., "External beam treatment planning: Can we deliver what we plan?," Acta Oncological **32**, No. 4, 445-451 (1993).

Hazle, J.D., Hefner, L., Nyerick, C.E., Wilson, L. and Boyer, A.L., "Dose-response characteristics of a ferrous-sulphate-doped gelatin system for determining radiation absorbed dose distributions by magnetic resonance imaging (FeMRI)," Phys. Med. Biol. **36**, 1117-1125 (1991).

Hiraoka, T., Fukuda, N., Ikehira, H., Hoshino, K., Nakazawa, K., Tateno, Y. and Kawashima, K., "Digital imaging of dose distributions by magnetic resonance," Nippon Acta Radiologica **46**, 503-505 (1986).

Hiraoka, T., Fukuda, N., Ikehira, H., Hoshino, K., Tateno, Y. and Kawashima, K., "Digital imaging of dose distributions using NMR imager," Nipp. Acta. Radiol. **52**, 1177-1182 (1992).

Hiraoka, T., Hoshino, K., Kawashima, K., Kato, H. and Tateno, Y., "A new gel using super absorbent polymer for mapping the spatial dose distribution of electron beams by MR imager," Med. Dos. **18**, 73-79 (1993).

Hoecker, F.E. and Watkins, I.W., "Radiation polymerization dosimetry," Int. J. Appl. Rad. and Iso. 3, 31-35 (1958).

Homans, S.W., *A Dictionary of Concepts in NMR* (Oxford University Press, New York, NY, 1989).

Hsi, E., Mason, R. and Bryant, R.G., "Magnetic resonance studies of α-chymotrypsin crystals," J. Phys. Chem. **80** (23) 2592-2597 (1976).

Hsu T-P, Ma, D.S. and Cohen, C., Polymer **24**, 1273 (1983).

Hsu,T-P and Cohen, C., "Observations on the structure of a polyacrylamide gel from electron micrographs," Pqlymer **25**, 1419-1423 (1984).

Ibbott, G.S., Maryanski, M.J., Avison, R.G. and Gore, J.C., "Investigation of a BANG polymer gel dosimeter for use as a mailed QA device," Med. Phys. **22**(6), 951 (1995).

International Commission on Radiation Units and Measurements, *Radiation Dosimetry: X Rays and Gamma Rays with Maximum Photon Energies Between 0.6 and 50 MeV*, ICRU Report 14 (ICRU, Washington, DC, 1969).

International Commission on Radiation Units and Measurements, *Radiation Dosimetry: X-rays Generated at Potentials of 5 to 150 kV*, ICRU Report 17 (ICRU, Washington, DC, 1970).

International Commission on Radiation Units and Measurements, *Radiation Dosimetry: Electrons with Initial Energies Between 1 and 50 MeV*, ICRU Report 21 (ICRU, Washington, DC 1972).

International Commission on Radiation Units and Measurements, *Measurements of Low Level Radioactivity*, ICRU Report No. 22, (ICRU, Washington, DC, 1972).

International Commission on Radiation Units and Measurements, *Radiation Quantities and Units*, ICRU Report No. 33, (ICRU, Bethesda, MD, 1972).

International Commission on Radiation Units and Measurements, *Stopping Powers for Electrons and Positrons*, ICRU Report No. 37, (ICRU, Bethesda, MD, 1984).

Johns, H.E. and Cunningham, J.R., *The Physics of Radiology*, 4th ed. (Charles C. Thomas, Springfield Illinois, 1953).

Kaldoudi, E., and Williams, C.R., "Relaxation time measurements in NMR imaging . Part I: longitudinal relaxation time," Concepts in Mag. Res. **5**, 217-242 (1993).

Keller, B.M., *Characterization of the NMR-Based Fricke-Gelatin Radiation Dosimeter*, M.Sc. Thesis, Medical Physics Unit, McGill University, Montreal (1989).

Keller, B.M., Audet, C. and Schreiner, L.J., "NMR studies of the Fricke-gelatin dosimeter," Conf. Proc. COMP, Ottawa, 116-117 (Gloucester, Ont.: CMBES, 1993).

Kennan, R.P., Richardson, K.A., Zhong, J., Maryanski, M.J. and Gore, J.C., "A quantitative study of magnetization transfer in polyacrylamide gels: The role of crosslinking density and chemical exchange," Mag. Res. Med. (submitted, 1995).

Khan, F.M., *The Physics of Radiation Therapy* (Williams and Wilkins, Baltimore, 1984).

Khan, F.M., Doppke, K.P., Hogstrom, K.R., Kutcher, G.J., Nath, R., Prasad, S.C., Purdy, J.A, Rozenfeld, M. and Werner, B.L., "Clinical electron beam dosimetry: Report of AAPM Radiation Therapy Committee Task Group 25," Med. Phys. **18**, 73-109 (1991).

Kilb, R.W., J. Phys. Chem. **62**, 969 (1958).

Kimmich, R., "Molecular motion in polymer melts: 1. Description by components and NMR relaxation behavior," Polymer **18**, 233-238 (1977a)

Kimmich, R.and Schmauder, K, "Molecular motion in polymer melts: 2. Interpretation of relaxation data of polyethylene oxide," Polymer **18**, 239-243, (1977b).

Koenig, S.H., Baglin, C.M. and Brown, R.D. III, "Magnetic field dependence of solvent proton relaxation in aqueous solutions of Fe^{3+} complexes," Mag. Res. Med. **2**, 283 (1985).

Krynicki, K., "Proton-spin lattice relaxation in pure water between 0-100°C," Physica **32**, 167-178 (1966).

Kron, T., Metcalf, P. and Pope, J.M., "Investigation of the tissue equivalence of gels used for NMR dosimetry," Phys. Med. Biol. **38**, 139-150 (1993).

Kron, T. and Pope, J.M., "Dose distribution measurements in superficial x-ray beams using NMR dosimetry," Phys. Med. Biol. **39**, 1337-1349 (1994).

Kron, T., Rajanayagam, V. and Pope, J.M., "Fast T_1 imaging for the evaluation of diffusion in NMR dosimetry gels," Med. Phys. **21**, 909 (1994).

Kutcher, G.J., Fuks, Z., Brenner, H. et al., "Three dimensional photon treatment planning for carcinoma of the nasopharynx," Int. J. Rad. Oncol. Biol. Phys. **21**, 169-182 (1991).

Liu, K.J. and Ullman, R., "Proton magnetic relaxation in poly(ethylene oxide) solutions," J. Chem. Phys. **48**, 1158-1168 (1968).

LoSasso, T, Chui, C.S., Kutcher, G.J. *et al.*, "The use of a multileaf collimator for conformal radiotherapy of carcinomas of the prostate and nasopharynx," Int. J. Radiat. Oncol. Biol. Phys. **25**, 161-170 (1991).

Lynch, L.J., "Water Relaxation in Heterogeneous and Biological Systems," Mag. Res. **2**, 248 (1983).

Mackie, T.R., Holmes, T., Swerdloff, S., Reckwerdt, P., Deasy, J.O., Yang, J., Paliwal, B. and Kinsella, T., "Tomotherapy: a new concept for the delivery of dynamic conformal radiotherapy," Med. Phys. **20**, 1709-1719 (1993).

Makhlis, F.A., *Radiation Physics and Chemistry of Polymers* (John Wiley and Sons, New York, NY, 1972).

Maquet, J., Theveneau, H., Djabourov, M., Leblond, J. and Papon, P., "State of water in gelatin solution and gels: An 1H NMR investigation," Polymer **27**, 1103-1110 (1986).

Maryanski, M.J., Gore, J.C., Kennan, R.P. and Schulz, R.J., "NMR relaxation enhancement in gels polymerized and crosslinked by ionizing radiation: a new approach to 3D dosimetry by MRI," Mag. Res. Im. **11**, 253-258 (1993).

Maryanski, M.J., Private communications (1994).

Maryanski, M.J., Schulz, R.J., Ibbott, G.S., Gatenby, J.C., Xie, J., Horton, D. and Gore, J.C., "Magnetic resonance imaging of radiation dose distributions using a polymer-gel dosimeter," Phys. Med. Biol. **39**, 1437-1455 (1994).

Maryanski, M.J., Gore, J.C. and Schulz, R.J., US Patent No. 5,321,357 (1994).

Maryanski, M.J., Ibbott, G.S., Eastman, P., Schulz, R.J. and Gore, J.C., "Radiation therapy dosimetry using magnetic resonance imaging of polymer gels," Med. Phys. (in press, 1995).

Masterson, M.E., Barest, G., Chui, C.S. *et al.*, Interinstitutional experience in verification of external photon dose calculations, Int. J. Radiat. Oncol. Biol. Phys. **21**, 37-58 (1991).

McBrierty, V.J. and Packer, K.J, *Nuclear Magnetic Resonance in Solid Polymers*, E.A. Davis and I.M. Ward, Ed.s (Cambridge University Press, Cambridge, GB, 1993).

McCullough, E.C. and Holmes, T.W., "Acceptence testing computerized radiation therapy treatment planning systems: Direct utilization of CT scan data," Med. Phys. **12**, 237-242 (1985).

McLaughlin, W.L. and Chalkey, L., "Low atomic numbered dye systems for ionizing radiation measurements, " Photo. Sci. Eng. **9**, 159-165 (1965).

McLaughlin, W.L., Soares, C.G., Sayeg, J.A. *et al.*, "The use of radiochromic detectors for the determination of stereotactic radiosurgery dose characteristics," Med. Phys. **21**, 379-388 (1994).

Meiboom, S. and Gill, D., "Modified spin-echo method for measuring nuclear relaxation times," Rev. Sci. Instrum. **29**, 688-691 (1958).

Meigooni, A.S., Sanders, M., Ibott, G. and Szeglin S.R., "Dosimetric characteristics of an improved radiochromic film," Med. Phys. **22**, 952 (1995).

Michalski, J.M., Wong, J.W., Gerber, R.L. *et al.*, "The use of on-line image verification to estimate the variation in radiation therapy dose delivery," Int. J. Radiat. Oncol. Biol. Phys. **27**, 707-716 (1993).

Mohan, R., *Secondary field shaping, asymmetric collimators and multileaf collimators in Advances in Radiation Oncology Physics*, Purdy, J., Ed. (AIP, New York, NY, 1993).

Noack, F., "Nuclear magnetic resonance spectroscopy," in *NMR Basic Principles and Progress*, P. Diehl, E. Fluck and R. Kosfeld (Ed.s) Vol. **3**, 84-144 (Springer-Verlag, Berlin, 1971).

Odian, G., *Principles of Polymerization*, 3rd ed. (John Wiley and Sons Inc., New York, NY, 1991).

Olsen, D.R. and Hellesnes, J., "Absorbed dose distribution measurements in brachytherapy using ferrous sulphate gel and MRI," Brit. J. Radiol. **67**, 1121-1126 (1994).

Olsson, L.E., Petersson, S., Ahlgren, L. and Mattsson, S., *Ferrous Sulfate Gels for Determination of Absorbed Dose Distributions Using MRI Technique: Basic Studies*, Phys. Med. Biol., **34** (1), 43-52 (1989).

Olsson, L.E., Fransson, A., Ericsson, A. and Mattsson, S., "MR Imaging of absorbed dose distributions for radiotherapy using ferrous sulphate gels," Phys. Med. Biol. **35**(12), 1623-1631 (1990).

Olsson, L.E., *Radiation Dosimetry Using Magnetic Resonance Imaging*, PhD Thesis, Lund University, Malmö (1991).

Olsson, L.E. and Mattsson, S., "The interaction characteristics of a dosimeter gel based on agarose and ferrous sulfate solution" in *Radiation Dosimetry using Magnetic Resonance Imaging*, L.E. Olsson, PhD thesis, Lund University, Malmö (1991).

Olsson, L.E., Appleby, A. and Sommer, J., "A new dosimeter based on ferrous sulfate solution and agarose gel," Appl. Radiat. Isot. **42** (11), 1081-1086 (1991).

Olsson, L.E., Westrin, B.A., Fransson, A. and Nordell, B., "Diffusion of ferric ions in agarose dosimeter gels," Phys. Med. Biol. **37** (12), 2243-2252 (1992).

Parker, W.A., Schreiner, L.J., Evans, M.D.C. and Audet, C., "Imaging of HDR Brachytherapy dose distributions using MRI and Fricke-gelatin Dosimetry," Med. Phys. **21**, 1364 (1994).

Parker, W., *Brachytherapy dosimetry with Fricke-gelatin and MRI*, M.Sc. thesis, McGill University, Montreal (1995).

Perera, H., Williamson, J.F., Monthofer, S.P., Binns, W.R., Klarmann, J., Fuller, G.L. and Wong, J.W., "Rapid two-dimensional dose measurement in brachytherapy using plastic scintillator sheet: linearity, signal to noise ratio, and energy response characteristics," Int. J. Rad. Oncol. Biol. Phys. **23**(5), 1059-1069 (1992).

Perez, C.A. and Purdy, J., *Rationale for treatment planning in radiation therapy in Levtt and Tapley's Technological basis of Radiation Therapy: Practical Clinical Applications*, Levtt S.H., Khan, F.M. and Potish R.A., Ed.s (Lea and Febiger, Philildelpia PA, 1992).

Pfeifer, H., *Nuclear Magnetic Resonance and Relaxation - Basic Principles and Progress*, P. Diehl, E. Fluck and R. Kosfeld (Ed.s), Vol. **7**, 55-153 (Springer-Verlag, Berlin, 1972).

Pla, C., "A high speed interstitial intracavitary treatment planning system," Int. J. Oncol. Biol. Phys. **17**, suppl. 1, 199 (1989).

Pla, C., "A Macintosh-based treatment planning system for brachytherapy and stereotactic radiosurgery," in *Proceedings of the XIth International Conference on the Use of Computers in Radiation Therapy*, Hounsell AR, J.M. Wilkinson and P.C. Wilkinson, Ed.s (Medical Physics Publications, Madison WI, 1994).

Podgorsak, E.B., Olivier, A., Pla M. *et al.*, "Dynamic stereotactic radiosurgery," Int. J. Radiat. Onc. Biol. Phys. **14**, 115-125 (1988).

Podgorsak, M., *Fricke Radiation Dosimetry Using Nuclear Magnetic Resonance*, M.Sc. Thesis, Dept. of Phys., McGill University, Montreal (1989).

Podgorsak, M.B. and Schreiner, L.J., "Nuclear magnetic relaxation characterization of irradiated Fricke solution," Med. Phys. **19**, 87-95 (1992).

Pound, R.V., "Evidence of crystalline imperfection in nuclear magnetism," J. Phys Chem **57**, 743-748, (1953).

Powlis, W.D., Smith, A.R., Cheng E. *et al.*, "Initiation of multifleaf collimator confromal radiation therapy," Int. J. Radiat. Oncol. Biol. Phys. **25**, 171-179 (1991).

Prasad, P.V., Nalcioglu, O. and Rabbani, B., "Measurement of Three-Dimensional Radiation Dose Distributions Using MRI," Rad. Res. **128**, 1-13 (1991).

Ramani, R., Lightstone, A.W., Mason, D.L.D and O'Brien, P.F., "The use of radiochromic film in treatment verification of dynamic stereotactic radiosurgery," Med. Phys. **21**, 389-392 (1994).

Resing, H.A., "NMR relaxation of adsorbed molecules with emphasis on adsorbed water," Adv. Mol. Relax. Process 3, 199-226 (1972).

Richards, E.G. and Temple, C.J., Nature (Phys. Sci.) **22**, 92 (1971).

Rousseau, J., Gibon, D., Sarrazin, T.H., Doukhan, N. and Marchandise, X., "Technical note: Magnetic resonance imaging of agarose gel phantom for assessment of three-dimensional dose distribution in linac radiosurgery," Brit. J. Radiol. **67**, 646-648 (1994).

Ruchel, R. and Brager, M.D., "Scanning electron microscopic observations of polyacrylamide gels," Anal. Biochem. **68**, 415 (1975).

Ruchel, R., Steere, R.L. and Erbe, E.F, J. Chromatography **166**, 563 (1978)

Sato, T., Miyamoto, J. and Otsu, T., J. Polym. Sci. Polym. Chem. Ed. **22**, 3921 (1984).

Schreiner, L.J., *Muscle Molecular Dynamics by NMR*, M.Sc. thesis, University of Waterloo, Waterloo, Ontario (1978).

Schreiner, L.J., *Correlation Approach in Nuclear Magnetic Resonance Application to Hydrated NaDNA*, Ph.D. thesis, University of Waterloo, Waterloo, Ontario (1985).

Schreiner, L.J., MacTavish, J.C., Pintar, M.M. and Rupprecht, A., "NMR spin grouping and correlation exchange analysis," Biophys. J. **59**, 221-234 (1991).

Schreiner, L.J., Miljkovic, L. and Peemoeller, H., "A determination of hydration water stoichiometry," Polymer Comm. 32, 105-107 (1991b).

Schreiner, L.J., Parker, W., Evans, M.D.C., Audet, C., Roman, T.N. and Donath, D., "Brachytherapy dose verification using MRI and Fricke-gelatin: a quality assurance technique," Proceedings of Brachytherapy: Today and the Future, Scotsdale, AZ (1994).

Schreiner, L.J., Crooks, I., Evans, M.D.C., Keller, B.M. and Parker, W.A., "Imaging of HDR brachytherapy dose distributions using NMR Fricke-gelatin dosimetry," Mag. Res. Im. **12**(6), 901-907 (1994b).

Schreiner, L.J., MacTavish, J.C., Miljkovic, L. and Pintar, M.M., "Dynamical characteristics of aqueous PEG400: correlation of NMR spin grouping and NQES results," Molecular Phys. (submitted 1994c).

Schreiner, L.J., Parker, W., Henri, C., Evans, M.D.C. and Podgorsak, E.B., "3-D MRI dosimetry using the magnetization to dose (M&D) calibration technique," Med. Phys. **22**(6), 951 (1995).

Schulz, R.J., deGuzman, A.F., Nguyen, D.B. and Gore, J.C., "Dose-response curves for Fricke-infused agarose gels as obtained by nuclear magnetic resonance," Phys. Med. Biol. **35**, 1611-1622 (1990).

Schulz, R.J., Maryanski, M.J., Ibbott, G.S. and Bond, J.E., "Assessment of the accuracy of stereotactic radiosurgery using Fricke-infused gels and MRI," Med. Phys. **20** (6), 1731-1734 (1993).

Segal, B.G., *Chemistry: Experiment and Theory* (John Wiley and Sons, New York, NY, 1985).

Shirley, W.M. and Bryant, R.G., "Proton-nuclear spin relaxation and molecular dynamics in the lysozyme-water system," J. Am. Chem. Soc., **104**, 2910-2918 (1982).

Slichter, C.P., *Principles of Magnetic Resonance*, 2nd ed., Springer-Verlag, Berlin, West Germany (1978).

Sobol, W.T. and Pintar, M.M., "NMR spectroscopy of heterogeneous solid-liquid mixtures: spin grouping and exchange analysis of proton spin relaxation of tissue," Mag. Res. Med. **4**, 537 (1987).

Solomon, I., "Relaxation processes in a system of two spins," Phys. Rev. **99**, 559-565 (1955).

Spinks, J.W.T. and Woods, R.J., *An Introduction to Radiation Chemistry* (John Wiley and Sons, New York, NY, 1964).

Stanley, J.A. and Peemoeller, H., "Characterization of polyproline-water system by NMR spin grouping and exchange analysis," J. Phys. II France **1**, 1491-1503 (1991).

Task Group 21, Radiation Therapy Committee, AAPM, "A protocol for the determination of absorbed dose from high-energy photon and electron beams," Med. Phys. **10**, 1-31 (1983).

Thomas, S.J., Wilkinson, I.D., Dixon, A.K. and Dendy, P.P., "Magnetic resonance imaging of Fricke-doped agarose gels for the xisualization of radiotherapy dose distributions in a lung phantom," The British J. of Rad. **65**, 167-169 (1992).

Webb, S., *The Physics of Three-Dimensional Radiation Therapy: Conformal Radiotherapy, Radiosurgery, and Treatment Planning* (Institute of Physics Publ., Philidelphia PA, 1993).

Weisner, L., "The use of polyisobutylene solutions for measuring doses from 10^3 rad up to about 10^{10} rad," Proceedings of Symposium on Selected Topics in Radiation Dosimetry (Int. Atomic Energy Agency, Vienna, 1960).

Weiss, N. and Silberberg, A., "Inhomogeneity of polyacrylamide gel structure from permeability and viscoelasticity," Brit. Polym. J. **9**, 144 (1977).

Woessner, D.E., "Nuclear Spin Relaxation in Ellipsoids Undergoing Rotational Brownian Motion," J. Chem. Phys., **36**, 1-4 (1962).

Wong, J., Munro P. and Fenster A., *On-line radiotherapy treatment verification systems in Advances in Radiation Oncology Physics*, Purdy, J., Ed. (AIP, New York NY, 1993).

Wong, P.S., Clarke, G.D., McColl, R.W., Maryanski, M.J. and Glatsein, E., "Imaging the radiation dose in two different types of gel-based dosimeters: a comparison between FAX and BANG," Med. Phys. **22**(6), 951 (1995).

Zhang, D., *Characterization of Proton Spin Relaxation in a Polyacrylamide Gel*, M.Sc. thesis, University of Waterloo, Waterloo, Ontario (1990).

Zhong, J., Gore, J.C. and Armitage, I., "Relative contributions of chemical exchange and other relaxation mechanisms in protein solutions and tissues," Mag. Res. in Med. **11**, 295-308 (1989).

Zhu, Y., Williamson, J.F., Meigooni, A.S. and Mishra, V., "Quantitative radiochromic film dosimetry: uniformity, linearity and reproducibility," Med. Phys. **22**, 995 (1995).

Zimmerman, J.R. and Brittin,W.E., "Nuclear magnetic resonance studies in multiple phase systems: lifetime of a water molecule in an absorbing phase on silica gel," J. Phys. Chem. **61**, 1328-1333 (1957).